UNIVERSITY OF SOUTHAMPTON

THE SPECTROSCOPY OF HD^+, HeH^+ AND H_3^+ NEAR THEIR DISSOCIATION LIMITS

by

Richard Anthony Kennedy

Bachelor of Arts at the University of Oxford

A dissertation submitted in partial fulfilment
of the requirements for the degree of Doctor
of Philosophy at the University of Southampton

October 1983

ACKNOWLEDGEMENTS

My thanks go first to my ever enthusiastic supervisor, Prof. Alan Carrington. He has been a constant source of advice, ideas and encouragement. I am very grateful to Dr. Juliet Buttenshaw (Mrs. Leighton) and Mr. Timothy Softley for their help in obtaining some of the results presented in this thesis. I have benefitted greatly from conversations with them, and with the other members of the Chemical Physics Group at Southampton.

I wish to thank Dr. John Brown, Dr. Paul Fournier, Dr. Jeremy Hutson, Prof. L. Wolniewicz, Prof. Stewart Strickler, Prof. Mike Bowers, Mr. R. Bateman, Mr. Colin Young, Mr. Peter Francis and many others for their various contributions to my researches.

Financial support from the Science and Engineering Research Council and the University of Southampton is gratefully acknowledged.

Mrs. Sally Johnson, Mrs. Jane Thorp and Mrs. Jenny Murphy are thanked for their swift and accurate typing.

CONTENTS

Page

CHAPTER 4

BOUND TO QUASIBOUND VIBRATION-ROTATION SPECTRUM OF HeH^+ AND ISOTOPES

CHAPTER 5

INFRARED PREDISSOCIATION SPECTRUM OF THE H_3^+ ION

CHAPTER 6

THEORY OF THE HYDROGEN MOLECULAR ION

CHAPTER 1

SPECTROSCOPY OF MOLECULAR IONS

1.1 Introduction.

The past decade has seen the greatest revolution in spectroscopy since the development of quantum mechanics. This revolution is primarily due to the increasing availability of tunable lasers, with advances in computers and microelectronics playing an important role. Coherent, monochromatic radiation can now be obtained at almost any frequency, from radiofrequencies to the vacuum ultraviolet; although it must be admitted that some regions are only accessible to a limited few with extremely sophisticated apparatus. Allied to the development of lasers has come a formidable array of new experimental techniques, offering previously inconceivably high resolution and sensitivity. The way is now open, given sufficient time and funds, to obtain high resolution spectra of any molecule. This places a considerable burden of responsibility on those performing experiments in molecular spectroscopy. Molecular spectroscopists must be more than mere generators of molecular constants, we must be able to appraise the significance of our results, compare them with our current understanding, expose the limitations of our models and point the way forward. A number of specific reasons for studying the spectroscopy of a particular molecule may be conceived.

i) An increasing understanding of the dynamics of chemical reactions is being achieved through the study of state-to-state processes. Data from molecular spectroscopy play a vital role in permitting the selection of an initial state, and the specific detection of a final state.

ii) The most precise thermochemical data are frequently obtained through spectroscopic determinations of dissociation energies,

ionisation energies and electron affinities. The molecular potential energy functions, obtained by the inversion of spectroscopic data, can be used to calculate many molecular properties.

iii) Theoretical models for the structure and dynamics, both electronic and nuclear, of molecules are leading to accurate predictions of many molecular properties. In many cases the definitive tests of these models are provided by molecular spectroscopy. The resolution of nuclear hyperfine interactions can reveal the details of the electronic structure. Analysis of spectra to obtain parameters describing rotational and vibrational motion allows an investigation of the nuclear structure and dynamics. Finer details of molecular structure due to the interactions between the electronic and nuclear motions may also be revealed. The dynamics of dissociation and predissociation are amenable to study. Outstanding problems, such as the relative energies of different electronic states of a molecule, may be resolved by spectroscopic investigations.

iv) The identification of molecules in remote environments, such as interstellar molecular clouds, is only possible by recording spectra from these sources. Comparison of the observed transitions with laboratory data on known molecules can then reveal the presence of these species in the remote source. Observations of this type are leading to a detailed understanding of the behaviour and chemistry of interstellar molecular clouds.

Before describing our work in detail we shall briefly review the wide range of spectroscopic techniques that have been applied to molecular ions. A number of excellent reviews [1] have appeared recently, so that this survey makes no attempt at being a complete catalogue, but rather seeks to indicate the types of data which can be obtained about molecular ions. The review will be restricted to gas phase ions, although much interesting work is being performed on ions isolated in inert gas matrices by methods such as electron spin resonance [2], infrared absorption [1a], and laser excited fluorescence [3]. Limiting the field further to high resolution studies, implying the resolution of at least rotational fine structure, means

that photoelectron spectroscopy [1a] will not be covered. Investigations in which the resolution is limited to vibrational structure, such as the very elegant elucidation of the Jahn-Teller effect in the ground states of symmetrical halobenzene cations by Miller and coworkers [4] lie outside the scope of this review.

1.2 Radiofrequency Spectroscopy.

By irradiating H_2^+ ions held in a radiofrequency quadrupole trap under collision free conditions with an arc lamp polarised parallel to a small static magnetic field, it is possible to produce spatial ($|M_F|$) alignment of the ions [5]. If during the irradiation a radiofrequency magnetic field is applied perpendicular to the static field, driving $\Delta M_F = \pm 1$ transitions, the alignment is destroyed, and an increased photodissociation rate is observed. Various types of radiofrequency transitions in H_2^+ have been detected using this principle - magnetic resonance transitions between the Zeeman split sublevels of a single state [6], hyperfine transitions in para H_2^+ (N = 2) between states split by the electron spin-molecular rotation interaction [7], and also hyperfine transitions in ortho H_2^+ (N = 1) [8]. From the results of these experiments the hyperfine parameters for various vibration-rotation levels of the ground state of H_2^+ were determined to an accuracy of a few kiloHertz. These experiments were the first to reveal hyperfine structure in a molecular ion, but their prime importance comes from the tests they allowed of calculations on H_2^+; excellent agreement has been achieved [9, 10]. No attempts have been made to apply this technique to any other molecular ions, the distribution of the ions over many more rotational states than in H_2^+ would probably reduce the sensitivity too greatly.

1.3 Rotational Spectroscopy.

The plasmas formed by electric discharges through low pressure gases contain a great variety of transient species, including

molecular ions. By passing radiation of an appropriate frequency through liquid nitrogen cooled D.C. discharges, pure rotational transitions of a number of molecular ions have been observed in absorption. The factors influencing the sensitivity of this type of experiment have been considered in detail by Woods [11]. Two fundamental requirements are identified, an adequate column density of the ion of interest, and an accurate prediction of the transition frequency. Optimisation of the column density requires a sensitive means for monitoring the species present in the discharge, sampling by a mass spectrometer appears to be a promising method. The second requirement stems from the fact that high sensitivity searches are necessarily very slow. Accurate transition frequency predictions can be obtained from the analysis of high resolution optical spectra, radioastronomy and high quality ab initio calculations.

Using microwave radiation from klystrons, Woods and co-workers have observed rotational transitions in five linear molecular ions - CO^+ (N = 1 - 0) [12], HCO^+ (J = 1 - 0) [13], HN_2^+ (J = 1 - 0) [14], HCS^+ (J = 2 - 1) [15] and HOC^+ (J = 1 - 0) [16]. The vital initial predictions of transition frequencies came from optical data in the case of CO^+, radioastronomy supported by ab initio calculations for HCO^+, HN_2^+ and HCS^+, and ab initio calculations alone for HOC^+. By studying the spectra of isotopically substituted HCO^+, HN_2^+ and HOC^+, microwave substitution structures were obtained for these ions. Since the laboratory observation of HOC^+, this ion has been tentatively detected in an interstellar cloud [17]. For the ion CO^+, which has a $^2\Sigma^+$ ground state, a study of $^{13}CO^+$ revealed nuclear hyperfine structure in addition to the spin-rotation splitting of N = 1. Analysis of the observed transition frequencies yielded hyperfine parameters in excellent agreement with an optical determination [18].

Submillimeter radiation can be produced by harmonic generation and mixing of klystrons. Passing these higher frequencies through magnetically enhanced discharges [19], de Lucia and co-workers have detected higher rotational transitions in CO^+ (N = 2 - 1, 3 - 2, 4 - 3) [20], HCO^+ (J = 2 - 1 to 5 - 4) [21], HN_2^+ (J = 2 - 1 to 5 - 4) [22], HOC^+ (J = 2 -1, 3 - 2, 4 - 3) [23] and NO^+ (N = 2 - 1,

3 - 2) [24]. These observations have allowed very precise determinations of the rotational constants B and D for each of these ions in their vibrational ground states, as well as the nitrogen quadrupole coupling constant for NO^+.

Tunable radiation of still higher frequency can be generated by mixing the output of a far infrared (HCN) laser with microwaves from a klystron. Passing this radiation through the negative glow discharge in a hollow cathode has allowed the observation of high rotational transitions, such as J = 11 - 10 of HCO^+ [25], with excellent sensitivity. Such results may be particularly valuable as far infrared methods for probing interstellar clouds are being developed.

There is every prospect that rotational transitions of many more molecular ions will be observed. The results will provide valuable structural data, and lead to the identification of further molecular ions in interstellar clouds.

1.4 Far Infrared Laser Magnetic Resonance.

Optically pumped molecular gas lasers provide a dense forest of discrete frequencies across the whole of the far infrared region. Although it is possible to produce tunable radiation by mixing the output of these lasers with microwaves, it is much easier to tune molecules into resonance with their fixed frequencies. Components of pure rotational transitions of paramagnetic molecules can be tuned by a magnetic field through the Zeeman effect. If the cell containing the molecules is made an integral part of the laser cavity, absorption by magnetically tuned resonances can be detected with extremely high sensitivity [26].

Far infrared laser magnetic resonance has been successfully applied to two molecular ions - HBr^+ [27] and HCl^+ [28]. These ions both have inverted $^2\Pi$ ground states, various rotational transitions within the lower $^2\Pi_{\frac{3}{2}}$ manifold have been observed and assigned.

Detailed analysis of the spectra provides a wealth of information on the ions, notably on their electronic structure through the determination of magnetic hyperfine and electric quadrupole parameters. The influence of a net positive charge on the electron distribution can be investigated.

It is to be expected that far infrared laser magnetic resonance will prove as prolific in providing data on molecular ions as it has been for uncharged radicals. The extension to other frequencies, in particular the mid infrared, seems likely. A number of groups are actively searching for vibration-rotation transitions in DCl^+ using CO lasers.

1.5 Infrared Absorption Spectroscopy.

Recent developments in laser technology have provided several sources of broadly tunable coherent infrared radiation - diode lasers, colour centre lasers and difference frequency laser systems. Using these various sources, infrared absorption spectra of a number of molecular ions have been directly observed. The ions are usually produced in electric discharges, the only exception being the detection, using a diode laser, of a few vibration-rotation transitions in NO^+ formed by flash photoionisation [29].

Oka has observed the ν_2 (asymmetric stretch) fundamental band of H_3^+ [30, 31], using a difference frequency laser system, in which tunable infrared radiation is produced by mixing the output of a dye laser with that of a single mode argon ion laser in a lithium niobate crystal. Detection of the small H_3^+ absorption signals was achieved by passing the frequency modulated infrared radiation 16 times through a 2 m D.C. discharge in pure H_2. The observed spectrum was in acceptable agreement with the theoretical predictions [32], providing a test of both the calculated potential energy surface for H_3^+, and our understanding of the vibration-rotation dynamics of simple polyatomic molecules. Attempts are being made to detect H_3^+ in interstellar clouds by searching for

infrared absorption at the frequencies obtained experimentally [31]. H_3^+ plays a central role in current theories of interstellar chemistry as a protonator, but its presence is not yet confirmed. Further work with the difference frequency system has yielded spectra of HeH^+ [33] and NeH^+ [34]. Similar experiments by Davies and co-workers using a diode laser have led to the observation of a few transitions in HCl^+ [35].

The discharges used to produce the ions H_3^+, HeH^+ and NeH^+ were clean, in the sense that the only strong infrared absorber present was the ion of interest. In general this will not be the case, and techniques are required which will identify the carrier of a spectrum as being an ion. In a D.C. glow discharge the ions drift under the influence of a longitudinal electric field, under favourable conditions this causes a Doppler shift of similar magnitude to the thermal Doppler linewidth. Measurements of this shift can be used to investigate the mobility of ions in buffer gases, as in the study of ArH^+ in He using a diode laser by Haese, Pan and Oka [36]. While such quantum state selective studies of ion transport are of interest for the information they can provide about interactions between the ions and the buffer gas, their implications for ion selective spectroscopy are much more exciting. If a bipolar square wave voltage is used to maintain the discharge, the drift velocity of the ions will be synchronously reversed, giving Doppler frequency modulation of the laser in the rest frame of the ions. Detection of velocity-modulated infrared absorption has been used by Saykally and co-workers to observe vibration-rotation transitions in the ν_1 fundamental stretch bands of the ions HCO^+ [37] and HN_2^+ [38], using a colour centre laser. Enhancement of the sensitivity should be possible by multipassing, but the laser beam must always propagate through the discharge in the same direction; the Doppler-modulated signal cancels for a back reflected beam.

Infrared absorption spectroscopy is a technique of very general applicability and good sensitivity has been demonstrated, so that it seems likely that spectra of many more molecular ions will be obtained. There is considerable theoretical interest in

the vibration-rotation dynamics of H_3O^+ [39] and CH_2^+ [40], both are candidates for investigation by infrared spectroscopy. The influence of the net charge on the electric dipole moment of ions has attracted some attention [41], this could be studied by measurements of infrared absorption coefficients.

1.6 Infrared Emission Spectroscopy.

A variety of processes can produce vibrationally hot molecular ions - electron impact ionisation, ion-molecule reactions and Penning ionisation. If the emission is sufficiently strong high resolution infrared spectra can be obtained through the use of a Fourier transform spectrometer. Infrared emission by ArH^+ from a hollow cathode discharge through Ar has been recorded and analysed [42]. As well as providing spectroscopic information similar to that obtained by infrared absorption studies, the emission spectra can be used to probe the dynamics of ion-molecule reactions. An example is provided by the recent investigation of infrared chemiluminescence by NO^+ following the reaction between N^+ and O_2 [43].

1.7 Infrared Spectroscopy Using Ion Beams.

Ion beams provide an almost ideal medium in which to perform high resolution spectroscopy. The mass of the carrier of a spectrum is known, and the optimisation of its formation can easily be monitored. The essentially collision free environment through which the beam propagates preserves the initial population distribution, which frequently corresponds to a very high degree of internal excitation. The near unit efficiency with which ions can be detected makes it possible to devise extremely sensitive indirect methods for detecting the occurrence of transitions [44]. The high velocity of the ions gives a substantial Doppler shift for a collinear laser beam. This shift can easily be varied to bring transitions into resonance with a line tunable infrared laser. For light ions virtually complete frequency coverage can be achieved

over the ranges covered by fixed frequency CO and CO_2 lasers. The kinematic compression of the velocity distribution that occurs when the ions are accelerated from the source [45] gives limiting linewidths of a few megaHertz. In some cases it is possible to directly determine the position of a state with respect to a dissociation limit of the molecular ion. The only glaring disadvantage is the extremely slow scanning rate, ~0.1 cm^{-1}/hr., dictated by the inherent high resolution.

Wing and his co-workers have used charge exchange neutralisation as an indirect method for detecting transitions in a number of ions. The technique relies upon the fact that, even for collisions of very fast molecular ions with neutrals, the charge exchange cross-section does vary with the internal state of the ion. Thus the transfer of population between two initially unequally occupied quantum states that occurs on resonance produces a very small change in the attenuation of the ion beam, when it is subsequently passed through a gas target. Wing et al have detected a number of vibration-rotation transitions between the first few vibrational levels of HD^+ [46], Doppler tuned into resonance with lines from a CO laser. Theoretical calculations on this fundamental molecule have now achieved a level of accuracy comparable to the original experimental data, ~0.001 cm^{-1} [47, 48]. The transition frequencies are sensitive to radiative and relativistic effects, as well as to nonadiabatic couplings. They provide a test of our theories of these small corrections, and offer a potential method for examining the values of some of the fundamental constants. Some hyperfine structure was resolved in the transitions, and has been successfully accounted for by subsequent calculations [9]. The charge exchange technique has produced infrared spectra of several other simple molecular ions - HeH^+ [49], D_3^+ [50] and H_2D^+ [51]. The observed transitions of HeH^+ were assigned on the basis of a theoretical calculation [52], as were four of the D_3^+ transitions [32]. Interpretation of the remaining results for D_3^+ and all the H_2D^+ observations will require further work on the dynamics of the H_3^+ system, and its isotopic modifications.

Monitoring of the fragment ions formed by infrared photodissociation and photopredissociation is being developed by Carrington and his co-workers as a very sensitive method for studying transitions in molecular ions near their dissociation limits. For HD^+ photodissociation by a CO_2 laser is predominantly from v = 18. Resonant pumping of population into v = 18 from v = 16 with a second, Doppler-shifted CO_2 laser gives a substantial increase in the photofragment ion signal, providing a sensitive method by which to detect transitions in the v = 18 - 16 band [53]. Analogous experiments using a CO laser have led to the observation of transitions in the v = 17 - 14 band [54]. Comparison of these results with the best available theoretical predictions [48] has revealed significant, systematic discrepancies. The resolved hyperfine structure appears to be consistent with a symmetrical electron distribution. Nearer the dissociation limit the electron must start to localise around the deuteron, and experiments to detect this through the hyperfine structure are being attempted.

Doppler tuning transitions to predissociated vibration-rotation states into resonance with CO_2 laser lines has produced spectra of HeH^+ (and isotopes) [55, 56], CH^+ [57], H_3^+ (and isotopes) [58] and $HeNe^+$. In addition to providing high resolution spectroscopic data on these ions, the experiments have allowed a detailed investigation of their predissociation dynamics. While the predissociation of HeH^+ by tunnelling through a centrifugal barrier is well understood theoretically, the behaviour of CH^+ near its lowest dissociation limits, $C^+ (^2P_{\frac{1}{2},\frac{3}{2}}) + H$, is provoking considerable theoretical interest. The problem of describing the dynamics of a triatomic molecule, such as H_3^+, near its dissociation limits is closely related to quantum mechanical studies of atom-diatom collisions. Electronic predissociation is normally associated with a curve crossing, the observations on $HeNe^+$ have unequivocally demonstrated that this is not a necessary condition.

The charge exchange and photodissociation methods provide complementary data. The first yields data on highly populated, usually low, vibrational levels, while the latter can only probe

levels near a dissociation limit. Both are techniques of general applicability, and will certainly continue to produce fascinating data on molecular ions.

1.8 Fluorescence Excitation Spectroscopy.

The classical, photographic methods of recording electronic absorption spectra require much stronger absorption than the usually attainable column densities of molecular ions can provide. Much higher instantaneous densities can be achieved through the use of a flash discharge. A spectrum of C_2^- was first observed in CH_4 subjected to a high voltage pulse [59]. The extremely long path lengths provided by interstellar clouds has allowed the detection of CH^+ through its electronic absorption [60]. Indirect methods of recording electronic absorption, such as fluorescence excitation spectroscopy and ion beam techniques, offer much better sensitivity.

In fluorescence excitation spectroscopy the total light emission from a sample is recorded as a function of the exciting laser frequency. Such spectra have been obtained from ions held mass selectively in radiofrequency traps and ion cyclotron resonance cells. Studies of the time resolved fluorescence, excited by a pulsed laser, can provide accurate radiative lifetimes, which are normally difficult to obtain due to the very rapid dispersal of the ions from the detection volume under the influence of their mutual repulsion. These lifetimes provide a valuable test of the accuracy of electronic wavefunctions, and reliable oscillator strengths, which are required for the estimation of ion populations in remote environments. The experiments of Mahan and his co-workers on CH^+ [61] illustrate the capabilities of the method. The ions are trapped under collision free conditions, preserving frequently highly excited nascent internal state distributions. In the case of CH^+, transitions involving high rotational levels were observed, considerably extending the transition frequency data field, so allowing a refinement of some of the spectroscopic parameters. By admitting a buffer gas into the trap, the effect of a controlled

number of collisions on the internal state distribution can be investigated. Rotational excitation of N_2^+ in collisions with Ar has been studied in this way [62].

Fluorescence excitation spectra of ions in other environments have been reported. A study of CO^+ formed by Penning ionisation has revealed a small, previously undetected perturbation [63]. Analysis of the perturbation has refined the potential curves for CO^+, and provided a value for the electronic coupling matrix element [64], which may be compared with ab initio calculations. In a fascinating experiment Zare and his co-workers have studied the fluorescence excitation spectrum of very cold CO_2^+ in a supersonic molecular beam [65]. By applying optical-optical double resonance to the spectrum they were able to uniquely assign transitions in the $B^2\Sigma_u^+$ (000) - $X^2\Pi_g$ (000) band, which is very irregular due to perturbations in the $B^2\Sigma_u^+$ (000) state. The observations allowed the identification of three interacting vibronic bands, and gave considerable insight into the nature of the mixed states. Attempts have also been made to record fluorescence from fast beams of molecular ions, but the high velocity ($\sim 10^5 ms^{-1}$) of the ions limits the amount of fluorescence that may be collected. Nonoptical methods of detecting absorption can generally offer higher sensitivity. A successful very high resolution study of N_2^+ has been reported [66]. The very narrow linewidths that can be achieved with fast ion beams allowed the measurement of fully resolved hyperfine structure, which could be compared with theoretical predictions.

1.9 Electronic Emission Spectroscopy.

The recording of optical emissions from electronically excited molecular ions is the most prolific source of high resolution spectroscopic data. Emissions have been observed from ions formed by electric discharges, controlled electron-impact ionisation, Penning ionisation and exothermic ion-molecule reactions. Spectra of over fifty molecular ions have now been recorded and analysed. Although the resolution is not as high as can be achieved in laser-ion beam

experiments, this is compensated for by the ease and speed with which spectra covering wide frequency ranges can be recorded. Indeed the design and interpretation of many ion beam experiments have relied upon data from emission studies.

Some of the more recent investigations have been prompted by the need to refine existing data in the light of theoretical calculations and ion beam experiments. For BH^+ ab initio calculations of various spectroscopic parameters [67] demonstrated the need for further study of this ion; the original data was over forty years old. The BH^+ spectrum from a hollow cathode discharge has now been reinvestigated [68]. Carrington and Ramsay have improved and extended earlier measurements on CH^+ [69]. The emphasis was on observing higher vibrational levels, with the aim of extrapolating the spectroscopic constants to the high levels involved in ion beam predissociation experiments [44]. Unfortunately the data could not be adequately represented by a Dunham expansion, due to the shapes of the potentials. Following detailed work on $HeNe^+$ [70], emission spectra of $HeAr^+$ [71] have also been recorded. A comparison of the potential curves derived from the experimental data revealed details of the charge transfer bonding in these ions.

For many molecular ions the extensive overlapping of rotational transitions in different vibrational bands greatly confuses spectra, hindering assignment. The rotational congestion can be greatly reduced by cooling the parent molecule in a supersonic expansion, and then forming the ion by electron impact ionisation; very little rotational excitation occurs during direct ionisation by electrons. Dispersing the fluorescence from electronically excited ions formed in this way clearly reveals the underlying vibrational structure associated with an electronic transition. The recent work of Tuckett and co-workers on F_2^+ [72] provides a good illustration of the capabilities of this technique.

The reaction of active species of helium, He^+, He_2^+ and He^* (2^3S), with molecules provides another method by which electronically excited molecular ions can be generated. Many of the emissions

produced by Penning ionisation have not been reported from electric discharge sources. Recent examples, in which rotationally resolved emissions were recorded include S_2^+, formed from S_2Cl_2 [73], and GeH^+ from GeH_4 [74]. The data for S_2^+ confirmed the expected similarity to O_2^+. The GeH^+ emissions were assigned to the $a^3\Pi_{0^+} - X^1\Sigma^+$ and $a^3\Pi_1 - X^1\Sigma^+$ systems, which have not been detected for CH^+ or SiH^+.

1.10 Electronic Spectroscopy Using Ion Beams.

The advantages of fast beams of molecular ions for spectroscopy have already been mentioned. Transitions are detected indirectly [44], because the amount of radiation absorbed is far too small to be detected directly. Detection by recording total fluorescence is possible, but rather inefficient. The highest sensitivity is achieved by monitoring the production of fragment ions formed by laser-induced predissociation. More general methods rely on variations in the cross-sections for ion-molecule reactions, such as charge exchange, with the electronic state of the ion. These techniques will only be successful if the reactions are faster than deactivation by fluorescence.

Variations in the attenuation of a fast beam of $^{13}CO^+$ by charge exchange have been used to record transitions in the $A^2\Pi - X^2\Sigma^+$ system of this ion [18]. Transitions were excited by Doppler tuning the ions into resonance with the blue lines of a single mode argon ion laser. Analysis of the resolved ^{13}C nuclear hyperfine structure confirmed a simple picture of the electronic structure for the $^2\Sigma^+$ state of CO^+, in which the unpaired electron is in an sp hybrid orbital localised on the C nucleus. The experiment is analogous to the studies of Wing and co-workers on the infrared spectroscopy of molecular ions [46, 49-51], but charge exchange cross-sections are usually much more sensitive to electronic than vibrational excitation. Greater sensitivity to the quantum state of the ions can be achieved by slowing them down to near thermal velocities in the reaction cell. The feasibility of this method has been demonstrated

by Carrington and co-workers, who detected transitions in the $A^2\Pi - X^2\Sigma^+$ system of CO^+, by monitoring the formation of product ions from a number of ion-molecule reactions involving CO^+ [75]. Unfortunately the loss of beam intensity in retarding the CO^+ ions and then accelerating the product ions meant that the overall sensitivity was no better than in the charge exchange attenuation method using a fast beam of CO^+. Selected ion flow tube systems have been developed specifically for studying the reactions of thermalised molecular ions. By crossing the slowly drifting flow of ions with a tunable dye laser, and introducing a reagent into the interaction zone, reactions involving excited ions can be studied. A band of the $A^2\Pi_u - X^2\Sigma_g^+$ system of N_2^+ has been detected by monitoring Ar^+ ions formed by charge transfer between Ar and N_2^+ (A) [76]; the reaction is endothermic for N_2^+ ions in the lowest vibrational level of the X state. As well as providing valuable spectroscopic data these experimental techniques could also be used to study state-selected ion-molecule reactions.

Electronic transitions in about ten molecular ions have now been observed by monitoring the fragment ions produced by laser-induced predissociation. The excellent sensitivity of this detection method comes from the high probability of converting an absorbed photon into a fragment ion, which can then be detected with near unit efficiency. As well as allowing the resolution of nuclear hyperfine structure for some ions, the high instrumental resolution has permitted the determination of accurate lifetimes from transition linewidths. These lifetimes, together with experimentally measured fragment ion kinetic energies, can assist in assigning the observed transitions, and in identifying predissociation mechanisms.

The four lowest lying quartet states of O_2^+ have been extensively studied by ion beam predissociation methods. The various experiments performed have given a very detailed description of these states and the couplings that exist between them. The first high resolution studies were performed by Carrington et al, who Doppler tuned transitions from the metastable $a^4\Pi_u$ state to predissociated levels of the $b^4\Sigma_g^-$ state into resonance with a line from

an argon ion laser [77]. The transitions were assigned to the (4, 1) band of the $b^4\Sigma_g^-$ - $a^4\Pi_u$ system using constants obtained from the analysis of optical emission by O_2^+; a short extrapolation to the predissociated v = 4 level of the $b^4\Sigma_g^-$ state was required. An investigation of the variation of the linewidths with the upper state quantum numbers indicated that the predissociation of the $b^4\Sigma_g^-$ state at v = 4 is predominantly due to coupling with the continuum of the $d^4\Sigma_g^+$ state. By using tunable dye lasers, which offer much wider frequency coverage than a Doppler-tuned ion laser, many other bands of the $b^4\Sigma_g^-$ - $a^4\Pi_u$ system of O_2^+ have been observed and analysed [78, 79]. Linewidth investigations on transitions to higher vibrational levels of the $b^4\Sigma_g^-$ state, identified by the kinetic energy of the O^+ fragment ions, have revealed that by v = 8 the predissociation is dominated by coupling to the continuum of the $f^4\Pi_g$ state [80]. The presence of a potential maximum in the $f^4\Pi_g$ state had been suggested by theoretical calculations, and measurements of the kinetic energy distributions of O^+ ions formed by direct photodissociation from $a^4\Pi_u$ to the repulsive part of the $f^4\Pi_g$ potential [81]. Its existence has been confirmed by the observation of transitions from the $a^4\Pi_u$ state to two predissociated vibrational levels of the $f^4\Pi_g$ state, held behind the maximum [82]. The assigned predissociated transitions in the $b^4\Sigma_g^-$ - $a^4\Pi_u$ system can be used to monitor the population of a specific level in the $a^4\Pi_u$ state. Other transitions involving this level, including transitions to bound levels can then be identified. Optical-optical double resonance experiments of this type have been used to detect transitions from selected levels of the $a^4\Pi_u$ state to bound levels of the $f^4\Pi_g$ state [83].

A considerable amount of additional information can be extracted from measurements of the kinetic energy distributions of the fragment O^+ ions from selected predissociated levels. Careful fitting of the distributions, using Monte Carlo simulation techniques, gives the energy of the predissociated level above the dissociation limit, and the anisotropy parameter β, which describes the angular distribution of the fragments relative to the direction of polarisation of the laser [84]. For O_2^+ the energy of the

lowest predissociated level of the $b^4\Sigma_g^-$ state can be determined with respect to the O^+ (^4S) + O ($^3P_2$) limit to better than 2 cm^{-1} [85]. Combining this energy with various other spectroscopic data, the zero point dissociation energies of the $a^4\Pi_u$ and $b^4\Sigma_g^-$ states of O_2^+, and of the O_2 $^3\Sigma_g^-$ ground state can be obtained to a similar level of accuracy.

An understanding of the quantum dynamics of the dissociation process, in particular the influence of the radial motion of the nuclei on the electronic wavefunction, and the effects of angular momentum on the final angular distribution of the fragments, is required to fully explain the observed kinetic energy distributions. For some of the predissociated levels of the $b^4\Sigma_g^-$ state the higher fine structure dissociation limits, O^+ (^4S) + O ($^3P_1$) and O^+ (^4S) + O ($^3P_0$) are energetically accessible. However, at least for v = 4 the O^+ kinetic energies show that the only significant predissociation channel is to O^+ (^4S) + O ($^3P_2$) [85]. This nonstatistical behaviour indicates that the radial motion of the nuclei is sufficiently slow to allow the electronic motion to follow that of the $d^4\Sigma_g^+$ state, which correlates uniquely with the O^+ (^4S) + O ($^3P_2$) limit, when long range spin-orbit interactions are taken into account. This adiabatic behaviour also appears to occur for the predissociation of the $f^4\Pi_g$ state [82], although the situation is complicated by uncertainty as to the predissociation mechanism. This behaviour is to be contrasted with that observed in direct photodissociation of $a^4\Pi_u$ via the repulsive part of the $f^4\Pi_g$ potential. The rather faster fragments produced in this way are apparently statistically distributed over the three fine structure states of O ($^3P_{2,1,0}$) [86]. The predissociation of O_2^+ $b^4\Sigma_g^-$ (v = 4) is slow compared to rotation of the molecule, so that the angular distribution of the fragments, described by the anisotropy parameter β, is determined by angular momentum effects [85] rather than the parallel or perpendicular nature of the transition. The most important factor in determining β is found to be the P, R or Q character of the transition, because of the way these different types of transition differentially populate the M_J substates of the predissociated level. The predictions from angular momentum theory were in agreement with the experimental

determinations of β.

Predissociation of CH^+ has also received considerable attention [87], in part because of the astrophysical importance of the reverse process of radiative association [88]. Assignment and interpretation of the spectra present problems, because of the lack of any data from which to make reliable extrapolations to the levels involved in the predissociated transitions, and uncertainty as to how best to describe the interacting electronic states near the $C^+ (^2P_{\frac{1}{2},\frac{3}{2}}) + H$ dissociation limits. Some levels of the $A^1\Pi$ state can predissociate by tunnelling through the centrifugal barrier due to the rotational motion of the nuclear framework. Transitions to these levels from the $X^1\Sigma^+$ state have been identified by calculating their frequencies, widths and the kinetic energy distributions of the associated $C^+ (^2P_{\frac{3}{2}})$ fragment ions from empirical potentials for the $X^1\Sigma^+$ and $A^1\Pi$ states. These potentials were constructed from the available experimental and theoretical data, and have been greatly refined by adjusting them to reproduce the predissociation results. However the majority of the observed transitions remain unassigned. Many of them are believed to involve levels of CH^+ lying between the two fine structure dissociation limits $C^+ (^2P_{\frac{1}{2}}) + H$ and $C^+ (^2P_{\frac{3}{2}}) + H$, which can predissociate by coupling with the continuum of a state which correlates with the lower $C^+ (^2P_{\frac{1}{2}})$ limit. Theoretical calculations have confirmed the feasibility of this type of predissociation [89], but uncertainty as to the long range behaviour of the electronic states and the shape of the potentials has precluded any definite assignment of the transitions. These observations have brought into sharp focus the current lack of understanding of the behaviour of simple molecules near dissociation limits. The capabilities of predissociation spectroscopy of fast beams of molecular ions, and the problems encountered in interpreting the detailed results obtained, are further illustrated by the experiments performed on NO^+ [90], N_2^+ [91] and H_2S^+ [92].

Provided the predissociation is relatively slow ($\tau \geq 5\times10^{-9}$s) the high Doppler resolution can be exploited to study hyperfine splittings of transitions. With the transitions assigned, usually

by making short extrapolations from existing optical emission data, these splittings can be analysed to obtain hyperfine parameters, which provide a probe of the electronic structure of the ion. Preliminary investigations of hyperfine structure in transitions of SH^+, NH^+ and PH^+ Doppler tuned into resonance with a krypton ion laser have been reported [93].

Spectroscopic studies of the predissociation of molecular ions have not been limited to diatomics. Several vibrational bands of the $A^2\Sigma^+ - X^2\Pi$ system of N_2O^+ have been investigated at high resolution using Doppler-tuned ion beams [94, 95]. Attention has recently focused on the mechanism by which the A (100) level predissociates to N (^4S) + NO^+ ($X^1\Sigma^+(v)$). Measurements of the kinetic energies of the NO^+ fragment ions show that they are formed vibrationally excited, the distribution peaking at v = 4 [96]. The hyperfine splittings for $^{14}N^{15}NO^+$ and $^{15}N^{14}NO^+$, due to the unpaired electron localised on the terminal N nucleus in the A state, reveal that the predissociation occurs without scrambling of the N nuclei. For more complicated ions, such as CH_3I^+, the spectra are heavily congested, and only partial vibrational analyses have so far been achieved [97].

Fast beams of negative ions can also be generated, and high resolution spectra of C_2^- have been reported. Two techniques were used, sequential two photon photodetachment [98], and single photon autodetachment [99]. In both cases resonances could be detected by monitoring the production of fast C_2 neutrals. The first method is closely related to the two photon photodissociation technique applied to HD^+ [53], the latter is analogous to the many predissociation studies of positive molecular ions.

1.11 Conclusions.

We now have available methods for detecting transitions in molecular ions from radiofrequencies to the ultraviolet. Some of these techniques are simply extensions to ions of methods widely applied to neutral molecules. Others make use of the unique feature

of ions, their net charge, which allows the motion of ions to be controlled by electric and magnetic fields, and greatly facilitates their quantitative detection. The power of this second class of techniques is amply demonstrated by the range and quality of information obtained from ion beam experiments. However the great contributions made by other methods must never be overlooked, particularly since the success of many ion beam experiments has been in large part due to data obtained by more traditional means. The future will surely see the development of new techniques and the application of the existing methods to many further problems. The results already obtained have added significantly to our understanding of the properties and dynamics of molecules, and areas where a great deal of work still remains to be done have been identified.

The work described in this thesis has involved the study of three of the simplest molecular ions by infrared spectroscopy, using an ion beam. The ions HD^+, HeH^+ and H_3^+ have been studied near their dissociation limits, the most difficult region in which to accurately describe the molecular dynamics, but also the most interesting from a chemical viewpoint. HD^+ has been studied as the simplest possible molecule with an electric dipole moment. We have been able to provide a stringent test of the best theoretical treatment of this fundamental ion, and expose deficiencies in the calculations. The resolution of nuclear hyperfine structure has allowed us to investigate the electronic structure of the ion as it approaches the dissociation limit. HeH^+ has been described as the model heteronuclear diatomic molecule. Our results have tested the accuracy of recent calculations of the ground state potential energy curve, and probed the dynamics of rotational (tunnelling) predissociation in great detail. Finally our studies of the model polyatomic molecule H_3^+ in the region near its dissociation limits have revealed a totally unexpected wealth of fine detail. The interpretation of these results presents a great challenge, and will surely reveal many new facets of the behaviour of polyatomic molecules near their dissociation limits.

CHAPTER 2

EXPERIMENTAL PRINCIPLES AND METHODS

2.1 Introduction.

The material in this chapter describes our laser-ion beam apparatus, and the experimental techniques we are developing to obtain results such as those reported in subsequent chapters. We begin by outlining the principles of the methods by which spectroscopic transitions may be detected, and indicate the information we are seeking to obtain from our observations. The later sections describe how these concepts are made a practical reality.

2.2 Sequential Two Photon Photodissociation.

Figure 2.1 illustrates the principles of this method, which was first applied by Carrington, Buttenshaw and Roberts to detect vibration-rotation transitions in the v = 18 - 16 band of HD^+ [100]. XY^+ molecules in high vibrational levels, such as state b of the lower electronic state, can be photodissociated to $X^+ + Y$ by driving the allowed transition to the repulsive upper state with an infrared laser of frequency ν_2. This single photon photodissociation is selective, since only levels with energies no further below the $X^+ + Y$ dissociation limit than $h\nu_2$ may be photodissociated. The selectivity is usually rather greater than this, because of the way the photodissociation cross-section for a specific vibration-rotation state varies with ν_2 [101]. If a transition from state a to the state b is simultaneously pumped with a second laser of frequency ν_1, the population of state b will usually be changed, so modifying the rate of formation of X^+ ions, which we are monitoring. State a will usually be too far below the dissociation limit to be photodissociated by a single photon of energy $h\nu_2$. This method of detecting transitions

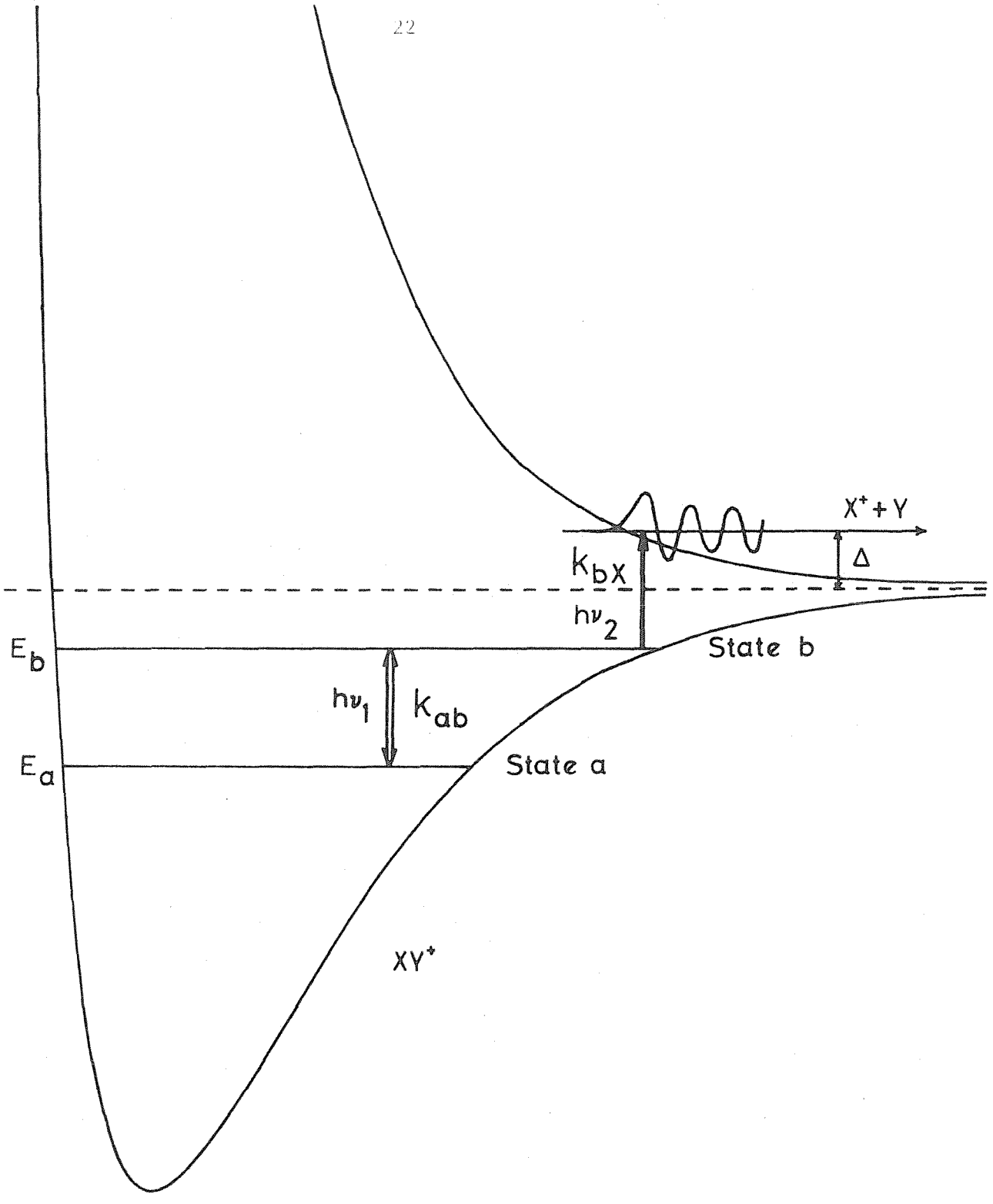

Figure 2.1

Sequential Two Photon Photodissociation

can be regarded as a type of double resonance; we are using one transition, photodissociation of state b, to monitor the occurrence of another, b - a. A simple kinetic analysis can be used to describe the technique, and illustrate some interesting features.

Let $n_a(t)$ and $n_b(t)$ be the number of XY^+ ions in states a and b after irradiation by the lasers for a time t, and let $n_X(t)$ be the number of X^+ ions formed by photodissociation. The sequential two photon photodissociation experiment can then be described by the coupled rate equations:

$$\frac{d}{dt}\begin{pmatrix} n_a \\ n_b \\ n_X \end{pmatrix} = \begin{pmatrix} -k_{ab} & k_{ab} & 0 \\ k_{ab} & -k_{ab} - k_{bX} & 0 \\ 0 & k_{bX} & 0 \end{pmatrix}\begin{pmatrix} n_a \\ n_b \\ n_X \end{pmatrix} \qquad (2.1)$$

or in matrix notation:

$$\frac{d}{dt}\ \underline{n} = \underline{\underline{R}}\ \underline{n} \qquad (2.2)$$

k_{ab} is the rate constant for the resonant transition b - a, it is proportional to the power of the ν_1 laser, and also to the transition probability, which peaks sharply at $\nu_1 = (E_b - E_a)/h$. k_{bX} is the rate constant for photodissociation, it is proportional to the power of the ν_2 laser, and is only weakly dependent on ν_2 (both lasers may contribute to the photodissociation of state b). When ν_1 is off resonance the number of X^+ ions detected after irradiation for a time t is immediately given by:

$$n_X(t) = n_b(0)\ \ [1 - \exp(-k_{bX}t)] \qquad (2.3)$$

where $n_b(0)$ is the number of XY^+ ions in state b before photodissociation. When ν_2 satisfies the resonance condition simple matrix methods can be used to solve (2.1), and obtain $n_X(t)$ from $\underline{n}(0)$. The rate matrix $\underline{\underline{R}}$ is transformed into diagonal form:

$$\underline{\underline{R}} = \underline{\underline{T}}\ \underline{\underline{\Lambda}}\ \underline{\underline{T}}^{-1} \qquad (2.4)$$

where $\underline{\underline{\Lambda}}$ is the diagonal matrix of the eigenvalues of $\underline{\underline{R}}$, $\underline{\underline{T}}$ is the matrix of eigenvectors of $\underline{\underline{R}}$ (columnwise) and $\underline{\underline{T}}^{-1}$ is the inverse of $\underline{\underline{T}}$ such that:

$$\underline{\underline{T}}^{-1} \underline{\underline{T}} = \underline{\underline{1}} \tag{2.5}$$

The coupled rate equations:

$$\frac{d}{dt} \underline{n} = \underline{\underline{T}} \underline{\underline{\Lambda}} \underline{\underline{T}}^{-1} \underline{n} \tag{2.6}$$

can now be decoupled by multiplying from the left by $\underline{\underline{T}}^{-1}$, giving:

$$\frac{d}{dt} \underline{n}^T = \underline{\underline{\Lambda}} \underline{n}^T \tag{2.7}$$

$$\text{where } \underline{n}^T = \underline{\underline{T}}^{-1} \underline{n} \tag{2.8}$$

The decoupled rate equations (2.7) can immediately be solved:

$$n_1^T(t) = n_1^T(0) \exp(\lambda_1 t) \quad \text{etc.} \tag{2.9}$$

and the values of $\underline{n}(t)$ obtained by back-transforming $\underline{n}^T$ using $\underline{\underline{T}}$:

$$\underline{n}(t) = \underline{\underline{T}} \underline{n}^T(t) \tag{2.10}$$

The change in $n_X(t)$ when ν_1 is brought into resonance is then:

$$\Delta n_X = n_X(t) - n_b(0) \quad [1 - \exp(- k_{bX} t)] \tag{2.11}$$

and we detect the transition b - a through Δn_X. In figure 2.2 we show the signal (Δn_X) obtained after irradiation for 10^{-6} secs, for $k_{ba} = 10^7$ sec^{-1} (b - a saturated) and k_{bX} increasing from 0 to 10^7 sec^{-1} as the initial populations are changed, keeping $n_a(0) + n_b(0) = 1$. At low photodissociation rates, the regime in which we operate, the signals depend linearly on the power of the photodissociating laser, and are proportional to the initial population difference $n_a(0) - n_b(0)$. If the photodissociation can be saturated the signal then tends to $[n_a(0) + n_b(0)] - n_b(0)$, we are able to convert all the XY^+ ions which can reach state b into X^+ fragment ions.

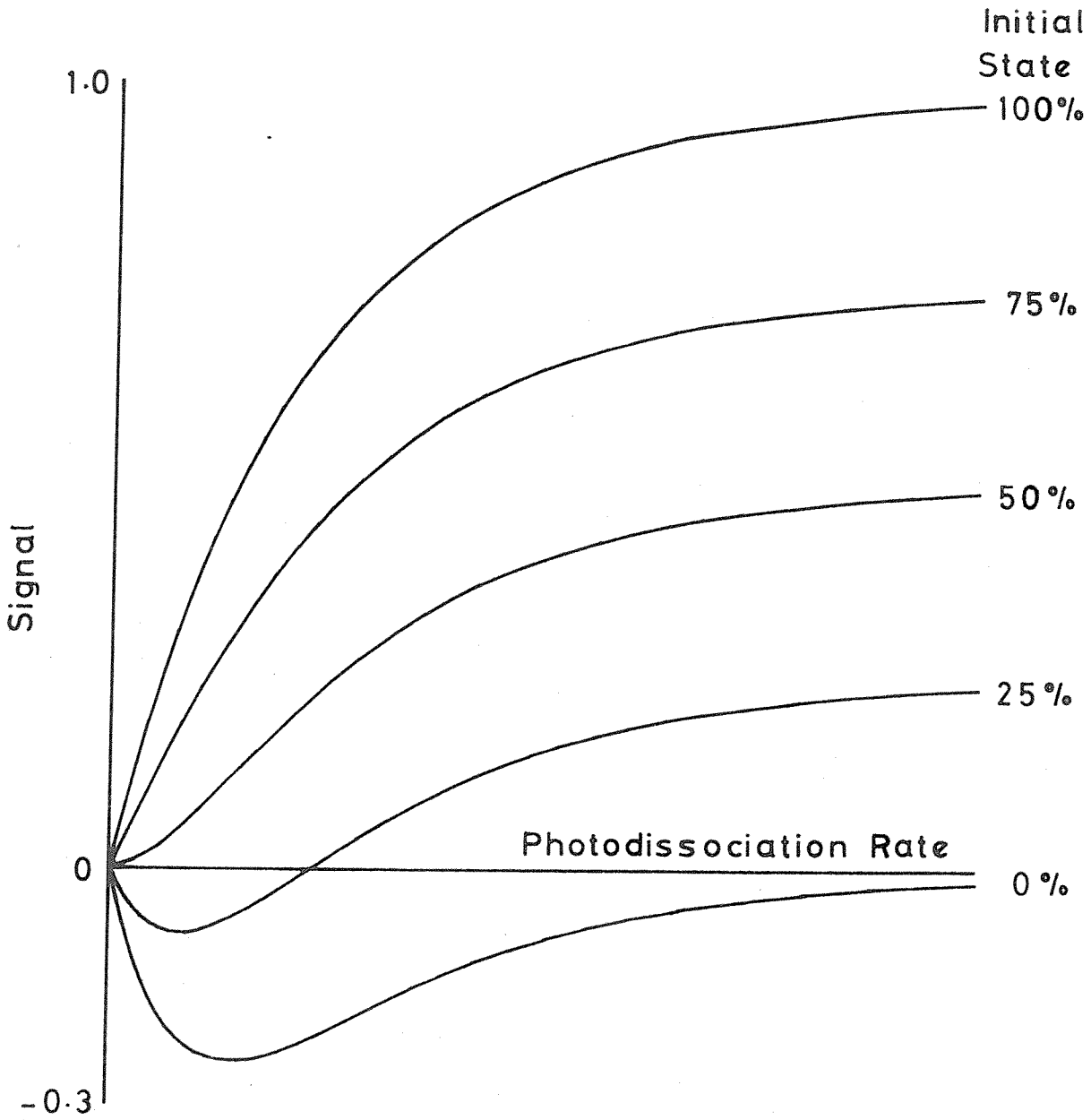

Figure 2.2

Results of Kinetic Modelling

Although in figure 2.1 we have shown state b, the photodissociated state, to be above state a, the analysis presented above makes no assumptions about the relative energies of the states. The technique only requires that the photodissociation is state selective; it would work just as well if a were above b, provided that the probability of photodissociation from state b is greater than for state a.

Electric dipole allowed bound to bound transitions, such as b - a, have high transition probabilities, and are easily saturated and power broadened. The resolution of small hyperfine splittings is aided by the use of low ν_1 laser powers, reducing power broadening to below the instrumental Doppler linewidth. The bound to free process of photodissociation has a much smaller probability, and high laser powers are required to obtain efficient photodissociation. It is possible to use the same laser to pump b - a and drive the photodissociation of b, but this arrangement leads either to a loss of resolution or to a reduced signal. The use of two lasers allows the optimum conditions to be achieved, and offers maximum experimental flexibility.

To summarise, the requirements for this type of experiment, in which the objectives are to accurately determine bound to bound transition frequencies, and to measure hyperfine splittings, are:

1) A source of molecular ions in which the high vibrational levels are populated.

2) A tunable laser of accurately known frequency with which to pump the bound to bound transition.

3) A high power laser with which to drive the state selective photodissociation.

4) A region in which to interact the lasers with the ions, and from which the fragment ions are to be extracted.

5) An efficient method for selectively detecting fragment

ions formed by sequential two photon photodissociation.

To achieve good signal to noise it is desirable to minimise the production of fragment ions by processes other than sequential two photon photodissociation, such as collision induced dissociation. There is also some interest in determining the energy Δ released into relative translational motion of the fragments; dissociation energies for the states a and b can be obtained from Δ.

2.3 Predissociation.

Figure 2.3 illustrates the principles of this method, which has been widely applied, an early example being the study of O_2^+ by Carrington and co-workers [77]. XY^+ molecules in state b predissociate to form $X^+ + Y$ with an energy Δ above a dissociation limit. We identify two broad classes of predissociation mechanism, tunnelling predissociation (figure 2.3a) and predissociation by coupling with the continuum associated with a lower dissociation limit (figure 2.3b). We can detect predissociated transitions such as b - a by monitoring the frequency dependent formation of X^+ ions. The maximum signal is $n_a(0)$, provided that the predissociation is sufficiently fast all the ions initially in state a can be converted to X^+ ions via b before the ions leave the laser interaction region. In practice instrumental effects on the collection efficiency for X^+ ions play a crucial role in determining the optimum signal, as our investigations on HeD^+ have shown. Time scales are important in determining the success of predissociation experiments. For detectable conversion of absorbed photons into fragment ions the final state predissociation lifetime must not be much longer than the flight time of the ions through the laser interaction region. If the predissociation rate is too fast the transitions will be too broad to be detected. The lifetime of the initial state must be longer than the time interval between formation and irradiation. To provide a complete characterisation of predissociated transitions, we have sought to determine the lifetime of the predissociated state from the low power linewidth (free of power broadening) and the energy

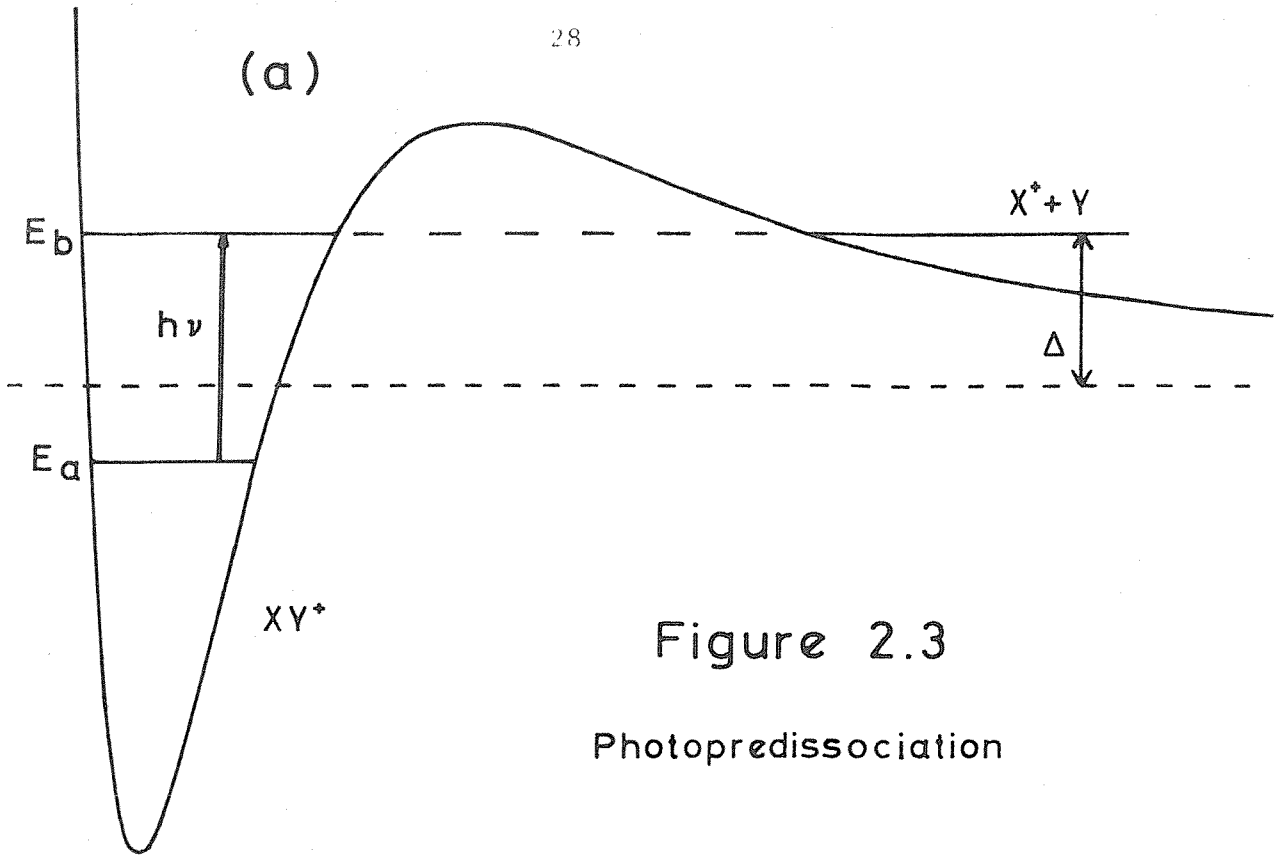

Figure 2.3

Photopredissociation

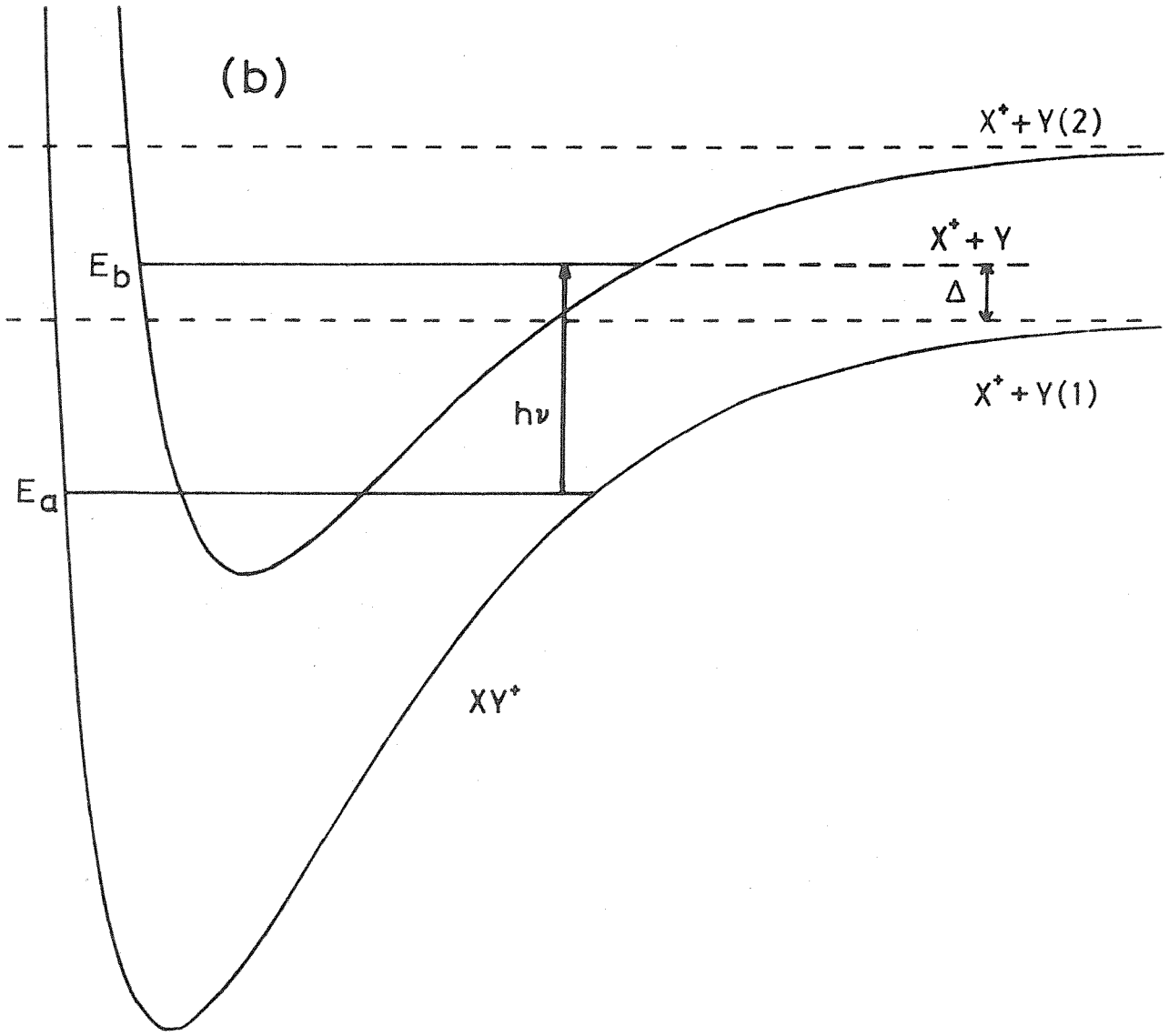

Δ released into relative translational motion of the fragments, in addition to the transition frequency. Our requirements for this type of infrared spectroscopy are very similar to those for the sequential two photon photodissociation experiment:

1) A source of molecular ions in which states close to a dissociation limit are populated.

2) A tunable laser of accurately known frequency with which to pump the bound to quasibound transitions.

3) A region in which to interact the ions with the laser, and from which the fragment ions are to be extracted.

4) An efficient method of selectively detecting the fragment ions formed by laser-induced predissociation.

5) A method for obtaining the value of Δ associated with a specific predissociated transition.

As in the case of the photodissociation method good signal to noise ratios require the minimisation of X^+ production by other processes, such as direct photodissociation, collision-induced dissociation and spontaneous predissociation of metastable ions. Finally we note that both techniques can be used to detect transitions between different electronic states, as well as vibration-rotation transitions within a single electronic state.

2.4 Doppler Tuning.

Our list of requirements includes "a tunable laser of accurately known frequency", we should also add that output powers of several Watts are needed. While the intracavity usage of continuous wave dye lasers can provide powers in excess of 20 Watts in the visible region, no continuously tunable infrared lasers of comparable performance are yet available. Diode lasers can provide at best 1 milliWatt,

which is totally insufficient for our experiments. There is also the problem of accurately determining the frequency of a continuously tunable laser. Spectral atlases of calibration molecules are being compiled, but they are not yet widely available. Interpolation to an observed transition is complicated by the nonlinear frequency scans of diode lasers. Fortunately it is not necessary to be able to continuously vary the frequency of the laser, instead we can tune the ions into resonance with a fixed laser frequency using the Doppler effect. The frequencies of the line tunable CO and CO_2 lasers we use are known very accurately [102, 103].

The first application of Doppler tuning to molecular ions was the measurement of transitions in HD^+ using a CO laser by Wing et al [46]. When a beam of fast ions is crossed by a laser of frequency ν and the angle between the directions of propagation of the ion and laser beams is θ, the Doppler-shifted frequency in the rest frame of the ions is given by the relativistic formula [104]:

$$\nu_{ion} = \nu \frac{(1 - \frac{v}{c}\cos\theta)}{[1 - (\frac{v}{c})^2]^{\frac{1}{2}}} \qquad (2.12)$$

where v is the speed of the ions in the rest frame of the laser, the laboratory, and c is the speed of light. If the laser and ion beams are collinear the formula simplifies to:

$$\nu_{ion} = \nu \left(\frac{1 - v/c}{1 + v/c}\right)^{\frac{1}{2}} \quad \theta = 0° \text{ (parallel propagation)} \qquad (2.13)$$

$$\nu_{ion} = \nu \left(\frac{1 + v/c}{1 - v/c}\right)^{\frac{1}{2}} \quad \theta = 180° \text{ (antiparallel propagation)} \qquad (2.14)$$

Small angular misalignments have a negligible effect, for:

$$\frac{d\nu_{ion}}{d\theta} = \nu \frac{(v/c)\sin\theta}{[1 - (v/c)^2]^{\frac{1}{2}}} = 0 \quad \text{for } \theta = 0° \text{ and } 180° \qquad (2.15)$$

Table 2.1 shows the Doppler shifts we can achieve at a laser wavenumber of 1000 cm^{-1} for an ion of mass 3 (a.m.u.) as we vary the ion beam potential V from 0 to 10.5 keV.

Table 2.1

Doppler Shifts at 1000 cm^{-1} for Mass 3 Ion

Beam Potential (eV)	Ion Speed ($\times 10^5$ ms^{-1})	Non-relativistic Shift (cm^{-1})	Relativistic Antiparallel Shift (cm^{-1})	Relativistic Parallel Shift (cm^{-1})	Doppler Width 1 eV spread (cm^{-1})
0	0	0	0	0	0.02675
500	1.7934	0.5982	+0.5984	-0.5980	0.00060
1000	2.5362	0.8460	+0.8463	-0.8456	0.00042
1500	3.1062	1.0361	+1.0367	-1.0356	0.00035
2000	3.5867	1.1964	+1.1971	-1.1957	0.00030
2500	4.0101	1.3376	+1.3385	-1.3367	0.00027
3000	4.3928	1.4653	+1.4664	-1.4642	0.00024
3500	4.7448	1.5827	+1.5839	-1.5814	0.00023
4000	5.0724	1.6920	+1.6934	-1.6905	0.00021
4500	5.3801	1.7946	+1.7962	-1.7930	0.00020
5000	5.6711	1.8917	+1.8935	-1.8899	0.00019
5500	5.9748	1.9840	+1.9860	-1.9820	0.00018
6000	6.2124	2.0722	+2.0744	-2.0701	0.00017
6500	6.4661	2.1568	+2.1592	-2.1545	0.00017
7000	6.7102	2.2383	+2.2408	-2.2358	0.00016
7500	6.9457	2.3168	+2.3195	-2.3141	0.00015
8000	7.1735	2.3928	+2.3957	-2.3900	0.00015
8500	7.3942	2.4664	+2.4695	-2.4634	0.00014
9000	7.6086	2.5380	+2.5412	-2.5347	0.00014
9500	7.8171	2.6075	+2.6109	-2.6041	0.00014
10000	8.0202	2.6752	+2.6788	-2.6717	0.00013
10500	8.2182	2.7413	+2.7451	-2.7376	0.00013

$$v = \left(\frac{2qV}{m}\right)^{\frac{1}{2}} \qquad (2.16)$$

where q is the charge on the ion. Values for the fundamental constants are taken from Cohen and Taylor [105]. For our ion beam apparatus the beam current falls off sharply at low potentials, and the practical lower limit is 1 keV. The upper limit of 10.5 keV is set by the power supply which provides the accelerating voltage. A total tuning range of about 3.8 cm^{-1} is available from each laser line, -2.7 to -0.8 cm^{-1} and +0.8 to +2.7 cm^{-1}. The Doppler shifts and tuning ranges are of course rather smaller for heavier ions. Table 2.1 also shows the nonrelativistic Doppler shifts ($\pm\nu\frac{v}{c}$), to demonstrate the need to allow for relativistic effects in obtaining experimental transition frequencies. We have also tabulated the Doppler width, assuming the ions exit the source with a kinetic energy spread of 1 eV. The large decrease in the Doppler width as the beam potential is increased is the result of the kinematic compression of the velocity distribution, that occurs during the acceleration of the ions from the source [45]. Considering two ions, c and d, of mass m which initially have velocity components along the direction of propagation of the ion beam (x) of:

$$\begin{aligned} v_c &= 0 \\ v_d &= \left(\frac{2q\delta V}{m}\right)^{\frac{1}{2}} \end{aligned} \qquad (2.17)$$

where δV is the kinetic energy difference (in eV) between ions c and d. This difference is preserved during the acceleration of the ions from the source by a potential difference V, so that the ions have final velocities along x of:

$$\begin{aligned} v_c' &= \left(\frac{2qV}{m}\right)^{\frac{1}{2}} \\ v_d' &= \left(\frac{2qV}{m} + \frac{2q\delta V}{m}\right)^{\frac{1}{2}} \\ &\simeq v_c' \left(1 + \frac{\delta V}{2V}\right) \end{aligned} \qquad (2.18)$$

The reduction in the velocity difference is:

$$\frac{v_d' - v_c'}{v_d - v_c} = \frac{1}{2}\left(\frac{\delta V}{V}\right)^{\frac{1}{2}} \qquad (2.19)$$

Figure 2.4 shows graphically how the compression arises, by plotting v against V, for m = 3 a.m.u. For a typical beam potential of 8 keV, and a kinetic energy spread of 1 eV the compression factor is 180. The Doppler limited linewidth at 1000 cm^{-1} is then about 5 MHz, before acceleration the width is about 800 MHz. If required, higher frequency resolution can be achieved by velocity selective saturation spectroscopy; in-flight Lamb-dip spectroscopy has been demonstrated [106].

2.5 Lasers.

Most of the experiments described in this thesis have been performed with continuous wave carbon dioxide gas discharge lasers. The efficient, near resonant transfer of vibrational energy from N_2 (v = 1) to CO_2 (00°0):

$$N_2\ (v = 1) + CO_2\ (00°0) + 18\ cm^{-1} \rightarrow N_2\ (0) + CO_2\ (00°1) \qquad (2.20)$$

produces a population inversion of the CO_2 (00°1) vibrational level over the (10°0) and (02°0) levels [107]. Lasing can then occur on individual molecular vibration-rotation transitions in the (00°1) - (10°0) and (00°1) - (02°0) bands. The frequencies of these transitions have been very precisely determined by heterodyne measurements [103], and are given in table 2.2 for $^{12}CO_2$ and $^{13}CO_2$. Recalling that from each laser line we have Doppler-shifted tuning ranges of -2.7 to -0.8 cm^{-1} and +0.8 to +2.7 cm^{-1} (mass = 3), we see that we have almost complete coverage from 875 to 1095 cm^{-1}; coverage is rather fragmentary for heavier, slower ions.

Our lasers were designed and constructed by Edinburgh Instruments. They exhibit good long term passive frequency (±1 MHz) and amplitude (±1%) stability. Their construction is very simple as can be seen from figure 2.5. The diffraction grating is mounted in

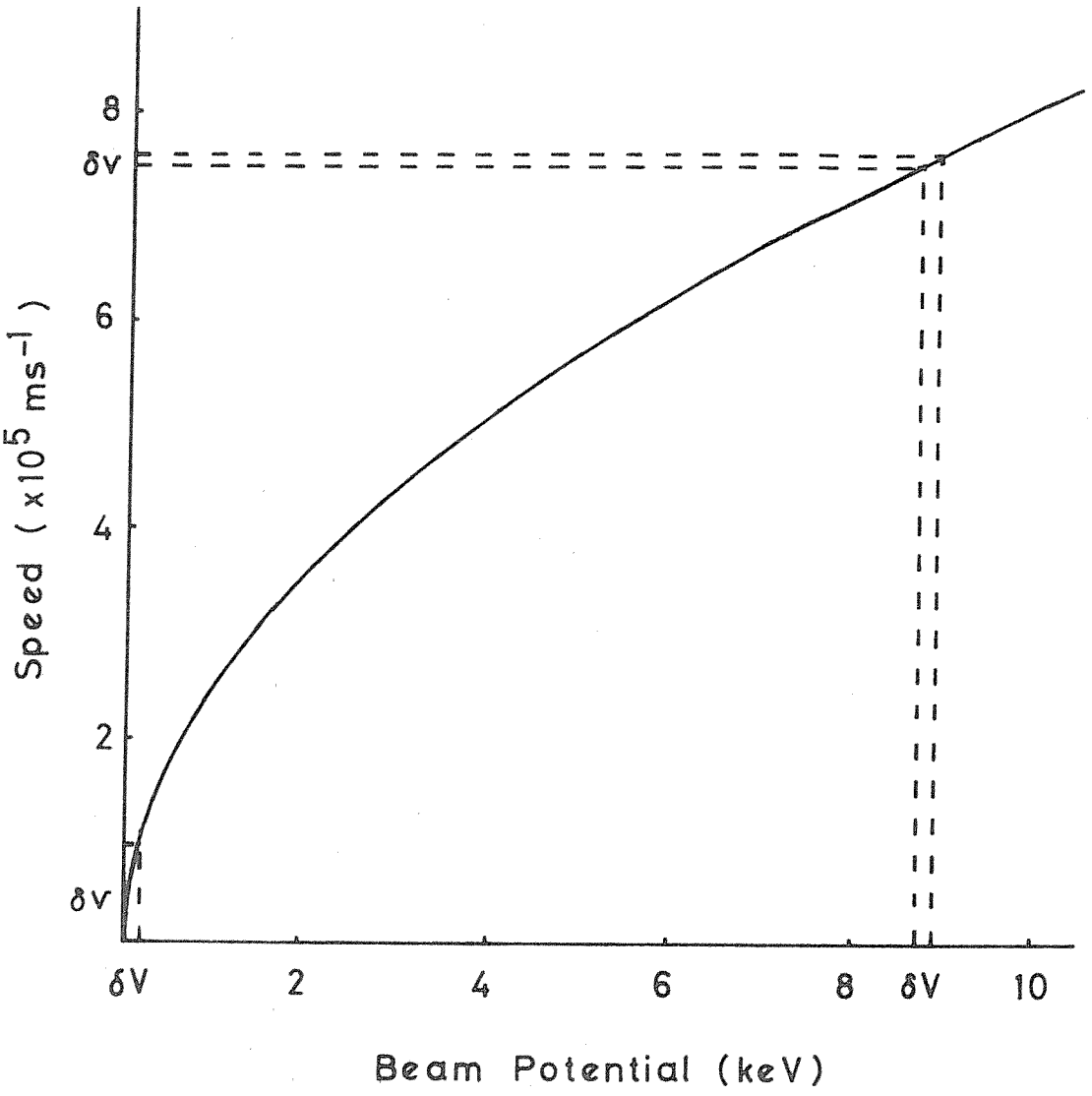

Figure 2.4

Kinematic Compression

Table 2.2

Vacuum Wavenumbers for $^{12}CO_2$ and $^{13}CO_2$ Infrared Lasers [103]

a) $^{12}CO_2$

00°1 - 10°0 Band

Transition	Wavenumber/cm^{-1}	Transition	Wavenumber/cm^{-1}
P(52)	912.2307	R(0)	961.7329
P(50)	914.4193	R(2)	963.2631
P(48)	916.5818	R(4)	964.7690
P(46)	918.7183	R(6)	966.2504
P(44)	920.8291	R(8)	967.7072
P(42)	922.9143	R(10)	969.1395
P(40)	924.9740	R(12)	970.5472
P(38)	927.0083	R(14)	971.9303
P(36)	929.0174	R(16)	973.2885
P(34)	931.0014	R(18)	974.6219
P(32)	932.9604	R(20)	975.9304
P(30)	934.8945	R(22)	977.2139
P(28)	936.8037	R(24)	978.4723
P(26)	938.6883	R(26)	979.7054
P(24)	940.5481	R(28)	980.9132
P(22)	942.3833	R(30)	982.0955
P(20)	944.1940	R(32)	983.2522
P(18)	945.9802	R(34)	984.3832
P(16)	947.7420	R(36)	985.4883
P(14)	949.4793	R(38)	986.5674
P(12)	951.1923	R(40)	987.6202
P(10)	952.8808	R(42)	988.6466
P(8)	954.5451	R(44)	989.6465
P(6)	956.1850	R(46)	990.6196
P(4)	957.8005	R(48)	991.5658
P(2)	959.3917	R(50)	992.4848

00°1 - 02°0 Band

Transition	Wavenumber/cm^{-1}	Transition	Wavenumber/cm^{-1}
P(52)	1014.5179	R(0)	1064.5089
P(50)	1016.7209	R(2)	1066.0374
P(48)	1018.9007	R(4)	1067.5391
P(46)	1021.0569	R(6)	1069.0141
P(44)	1023.1894	R(8)	1070.4623
P(42)	1025.2979	R(10)	1071.8838
P(40)	1027.3822	R(12)	1073.2785
P(38)	1029.4421	R(14)	1074.6465
P(36)	1031.4774	R(16)	1075.9878
P(34)	1033.4880	R(18)	1077.3025

P(32)	1035.4736	R(20)	1078.5906
P(30)	1037.4341	R(22)	1079.8523
P(28)	1039.3693	R(24)	1081.0874
P(26)	1041.2791	R(26)	1082.2962
P(24)	1043.1632	R(28)	1083.4788
P(22)	1045.0217	R(30)	1084.6351
P(20)	1046.8542	R(32)	1085.7654
P(18)	1048.6608	R(34)	1086.8698
P(16)	1050.4413	R(36)	1087.9483
P(14)	1052.1955	R(38)	1089.0011
P(12)	1053.9235	R(40)	1090.0284
P(10)	1055.6251	R(42)	1091.0302
P(8)	1057.3002	R(44)	1092.0068
P(6)	1058.9487	R(46)	1092.9582
P(4)	1060.5707	R(48)	1093.8847
P(2)	1062.1660	R(50)	1094.7865

b) $^{13}CO_2$

00°1 - 10°0 Band

Transition	Wavenumber/cm^{-1}	Transition	Wavenumber/cm^{-1}
		R(0)	914.1955
		R(2)	915.7340
limit of PL3 grating drive.		R(4)	917.2488
		R(6)	918.7440
P(44)	874.4993	R(8)	920.2195
P(42)	876.4766	R(10)	921.6753
P(40)	878.4336	R(12)	923.1113
P(38)	880.3705	R(14)	924.5276
P(36)	882.2874	R(16)	925.9239
P(34)	884.1844	R(18)	927.3003
P(32)	886.0614	R(20)	928.6567
P(30)	887.9187	R(22)	929.9930
P(28)	889.7562	R(24)	931.3092
P(26)	891.5739	R(26)	932.6051
P(24)	893.3721	R(28)	933.8807
P(22)	895.1506	R(30)	935.1358
P(20)	896.9095	R(32)	936.3704
P(18)	898.6488	R(34)	937.5844
P(16)	900.3686	R(36)	938.7776
P(14)	902.0689	R(38)	939.9499
P(12)	903.7497	R(40)	941.1012
P(10)	905.4110	R(42)	942.2314
P(8)	907.0528	R(44)	943.3403
P(6)	908.6752	R(46)	944.4278
P(4)	910.2780	R(48)	945.4936
P(2)	911.8612	R(50)	946.5378

00°1 - 02°0 Band

Transition	Wavenumber/cm^{-1}	Transition	Wavenumber/cm^{-1}
P(40)	980.8050	R(4)	1021.4592
P(38)	982.9125	R(6)	1022.9280
P(36)	984.9931	R(8)	1024.3677
P(34)	987.0466	R(10)	1025.7783
P(32)	989.0728	R(12)	1027.1597
P(30)	991.0715	R(14)	1028.5119
P(28)	993.0426	R(16)	1029.8351
P(26)	994.9859	R(18)	1031.1293
P(24)	996.9011	R(20)	1032.3945
P(22)	998.7883	R(22)	1033.6308
P(20)	1000.6473	R(24)	1034.8383
P(18)	1002.4778	R(26)	1036.0170
P(16)	1004.2799	R(28)	1037.1671
P(14)	1006.0533	R(30)	1038.2887
P(12)	1007.7981	R(32)	1039.3818
P(10)	1009.5140	R(34)	1040.4467
P(8)	1011.2011	R(36)	1041.4833
P(6)	1012.8592	R(38)	1042.4920

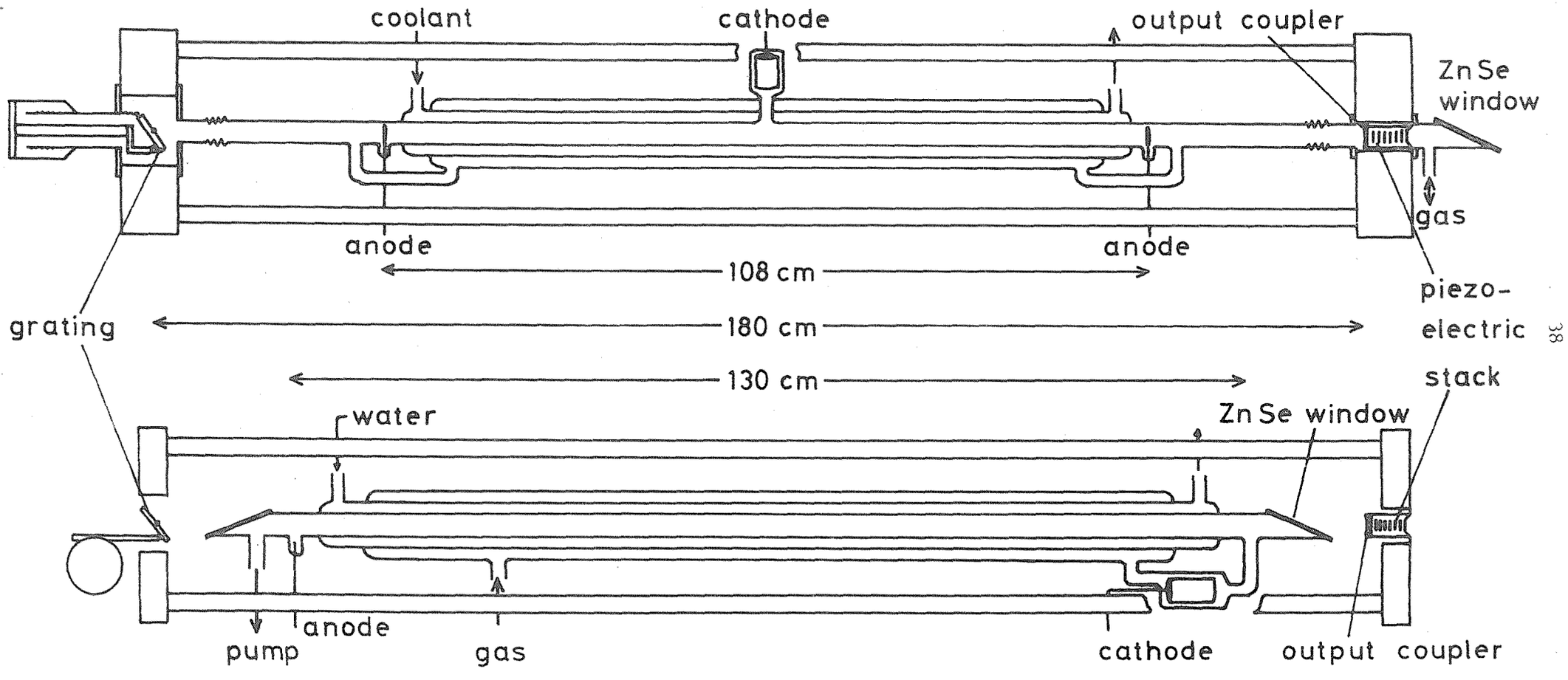

Figure 2.5

LASERS

a gimbal, allowing its angle to be adjusted by a very fine micrometer drive to select the laser frequency. Small adjustments to the cavity length (180 cm) are made using the piezoelectric stack on which the output coupler is mounted. A single longitudinal mode can then be chosen by centering it under the gain profile of the transition selected by the grating; adjacent modes are separated by about 80 MHz. The gas mixture for the PL3, 15.4% CO_2, 14.2% N_2, 4.0% Xe, 2.0% H_2 and 64.4% He, is excited by a double arm discharge between the central nickel cathode and the two nickel anodes. Typical discharge conditions are a total pressure of 22 mbar, current of 25 mA, and a cathode-anode potential difference of 11 kV; the total active length of the discharge is 108 cm. In normal operation the discharge is water cooled, and a 75% reflecting output coupler is used. The laser will then run on P(6) - P(42) and R(4) - R(40) for both bands of $^{12}CO_2$, the strongest lines, such as P(22) and R(20) of either band, give output powers in excess of 20 Watts. For $^{13}CO_2$ the performance on the (00°1) - (10°0) band is comparable to that for $^{12}CO_2$, but the higher frequency (00°1) - (02°0) band has a lower gain [108], and operation is restricted to P(12) - P(32) and R(10) - R(30), with maximum powers of about 10 Watts at the centres of these ranges. By replacing the 75% reflecting output coupler with one of 95% reflectivity, the operating range of the laser is extended to higher rotational transitions, at least as far as P(52) and R(50). The performance on the weak (00°1) - (02°0) band of $^{13}CO_2$ is also improved. To obtain laser action on the first few lines of each branch, R(0), R(2), P(2) and P(4), as well as using the high reflectivity output coupler, it is necessary to cool the discharge tube to -50°C. We have achieved this low temperature by flowing cold ethanol through the cooling jacket. The ethanol is cooled by passing it through a coil of copper tubing immersed in liquid nitrogen.

The PL4 laser normally operates with a constant flow of gas, 7% CO_2, 18% N_2 and 75% He, excited by a single arm discharge. The increased active length and flowing gas design give this laser a higher gain than the PL3, with a 75% reflective output coupler laser action can be obtained from P(4) to P(46) and R(2) to R(44) for $^{12}CO_2$, the strongest lines giving powers in excess of 50 Watts. The

discharge current can be chopped, resulting in a lower discharge temperature and improved gain on the weak lines at the limits of the branches. The cost of $^{13}CO_2$ precludes flowing gas operation, instead the laser is filled daily with the same gas mixture as used for the PL3, performance is slightly better than obtained from the PL3.

Laser lines are identified using a small monochromator (Optical Engineering), powers are measured using a thermoelectric power meter (Coherent). Limited variations in the laser power can be achieved by modifying the discharge conditions, but the use of a variable reflectivity germanium attenuator is preferred. Beam steering mirrors are made of molybdenum, lenses and windows are fabricated from zinc selenide and are antireflection coated. During alignment of the beams, their positions are monitored using heat sensitive papers or fluorescent screens.

The PL3 laser, with appropriate optics, can be made to lase on certain vibration-rotation transitions between excited vibrational levels of carbon monoxide. The CO is excited by electron impact, collisions between CO molecules spread the excitation over many vibrational levels. Although this may not produce vibrational population inversions, it can give inversion on P branch vibration-rotation transitions [107]. Using a 95% reflective output coupler we have observed laser action on a number of transitions over the range 1700 - 1950 cm^{-1}, see table 2.3. The laser wavenumbers are from the recent set of Dunham coefficients determined by Fourier transform spectroscopy on CO containing discharges [102]. By cooling the discharge tube to -50°C, using our ethanol cooling system, output powers of up to 4 Watts can be obtained from a gas mixture of 2.53% CO, 18.5% N_2, 3.37% Xe and 76.6% He. Lasing transitions may be identified with the aid of a grating monochromator. Transmissive optics made of calcium fluoride (lenses) or antireflection coated zinc selenide (windows) are used. Some CO laser lines are unfortunately strongly absorbed by atmospheric water vapour, so that our frequency coverage is not quite as good as might at first appear from table 2.3.

Table 2.3

Vacuum Wavenumbers for CO Infrared Lasers [102]

Transition v' P(J")	Wavenumber/cm^{-1}	Transition v' P(J")	Wavenumber/cm^{-1}
⋮			
16 P(15)	1700.3374	13 P(12)	1786.8579
15 P(21)	1701.5712	12 P(18)	1788.4012
16 P(14)	1704.1314	11 P(24)	1788.4413
15 P(20)	1705.5945	12 P(17)	1792.4332
16 P(13)	1707.8924	11 P(23)	1792.7002
15 P(19)	1709.5857	12 P(16)	1796.4327
16 P(12)	1711.6205	11 P(22)	1796.9274
15 P(18)	1713.5448	12 P(15)	1800.3996
14 P(24)	1713.9694	11 P(21)	1801.1229
15 P(17)	1717.4715	12 P(14)	1804.3338
14 P(23)	1718.1229	11 P(20)	1805.2866
15 P(16)	1721.3659	12 P(13)	1808.2350
14 P(22)	1722.2448	11 P(19)	1809.4181
15 P(15)	1725.2276	12 P(12)	1812.1032
14 P(21)	1726.3350	10 P(24)	1813.4273
15 P(14)	1729.0566	11 P(18)	1813.5175
14 P(20)	1730.3934	11 P(17)	1817.5846
15 P(13)	1732.8527	10 P(23)	1817.7213
14 P(19)	1734.4197	11 P(16)	1821.6192
15 P(12)	1736.6158	10 P(22)	1821.9837
14 P(18)	1738.4138	11 P(15)	1825.6212
13 P(24)	1738.7112	10 P(21)	1826.2143
14 P(17)	1742.3757	11 P(14)	1829.5904
13 P(23)	1742.8998	10 P(20)	1830.4130
14 P(16)	1746.3051	11 P(13)	1833.5267
13 P(22)	1747.0569	10 P(19)	1834.5797
14 P(15)	1750.2018	11 P(12)	1837.4299
13 P(21)	1751.1822	9 P(24)	1838.4923
14 P(14)	1754.0659	10 P(18)	1838.7142
13 P(20)	1755.2756	10 P(17)	1842.8163
14 P(13)	1757.8970	9 P(23)	1842.8214
13 P(19)	1759.3370	10 P(16)	1846.8860
14 P(12)	1761.6952	9 P(22)	1847.1188
13 P(18)	1763.3663	10 P(15)	1850.9230
12 P(24)	1763.5355	9 P(21)	1851.3845
13 P(17)	1767.3632	10 P(14)	1854.9273
12 P(23)	1767.7593	9 P(20)	1855.6184
13 P(16)	1771.3276	10 P(13)	1858.8986
12 P(22)	1771.9514	9 P(19)	1859.8201
13 P(15)	1775.2595	10 P(12)	1862.8369
12 P(21)	1776.1118	8 P(24)	1863.6347
13 P(14)	1779.1586	9 P(18)	1863.9897
12 P(20)	1780.2404	8 P(23)	1867.9989
13 P(13)	1783.0248	9 P(17)	1868.1269
12 P(19)	1784.3369	9 P(16)	1872.2316

Transition v' P(J")	Wavenumber/cm^{-1}	Transition v' P(J")	Wavenumber/cm^{-1}
8 P(22)	1872.3315	8 P(15)	1901.7619
9 P(15)	1876.3037	7 P(21)	1901.9560
8 P(21)	1876.6323	8 P(14)	1905.8363
9 P(14)	1880.3431	7 P(20)	1906.2600
8 P(20)	1880.9012	8 P(13)	1909.8778
9 P(13)	1884.3495	7 P(19)	1910.5319
8 P(19)	1885.1380	8 P(12)	1913.8862
9 P(12)	1888.3228	7 P(18)	1914.7716
7 P(24)	1888.8532	7 P(17)	1918.9790
8 P(18)	1889.3427	7 P(16)	1923.1538
7 P(23)	1893.2525	7 P(15)	1927.2961
8 P(17)	1893.5150	7 P(14)	1931.4055
7 P(22)	1897.6201	7 P(13)	1935.4820
8 P(16)	1897.6548	7 P(12)	1939.5254
		⋮	

Tabulation kindly made available by R. Blanckardt.

2.6 The Ion Beam Apparatus.

The remaining experimental requirements can all be met through the use of a fast beam of molecular ions. Figure 2.6 is a detailed diagram of the ion beam apparatus presently in use at Southampton. It is a specially modified reverse geometry double focusing mass spectrometer [109]. The basic components are an ion source and collimating optics, a magnetic analyser to select parent ions by momentum, a drift tube in which to interact the ions with a collinear laser beam, an electrostatic analyser (ESA) to separate the fragment ions by energy and off-axis electron multipliers with which to detect the ions.

The source chamber is pumped by a 6" diffstak, backed by two rotary pumps, achieving an ultimate vacuum of 3×10^{-8} mbar. In operation the pressure is typically 10^{-5} to 10^{-4} mbar, as monitored by an ion gauge immediately above the diffstak. The source chamber can be isolated from the rest of the apparatus and its diffstak, permitting rapid removal and replacement of ion sources requiring servicing. There is a high degree of differential pumping between the source and analyser regions, so that the analyser pressure is rarely above 2×10^{-7} mbar. The analyser is pumped by two 4" diffstaks, one immediately after the source earth slit. The other is situated beneath the drift tube, where the analyser pressure is monitored by an ion gauge. Vibrations due to the rotary pumps are a potential source of noise, as they will affect the precise geometry of the laser-ion beam interaction. They have been minimised by careful mounting of the pumps, any vibrations in the pumping lines are eliminated by rigidly attaching them to the laboratory floor.

Figure 2.6 also indicates the conventional axis system for ion beams, x is along the direction of propagation, and the ions are analysed by deflecting them in the xy plane with the magnetic and electrostatic sectors. Our instrument uses a 55° magnetic analyser of 30 cm radius and an 81.5° electrostatic sector with a radius of 38 cm. Both these devices focus the ion beam in the y direction, the design of the instrument ensures the optimum transmission of an ion

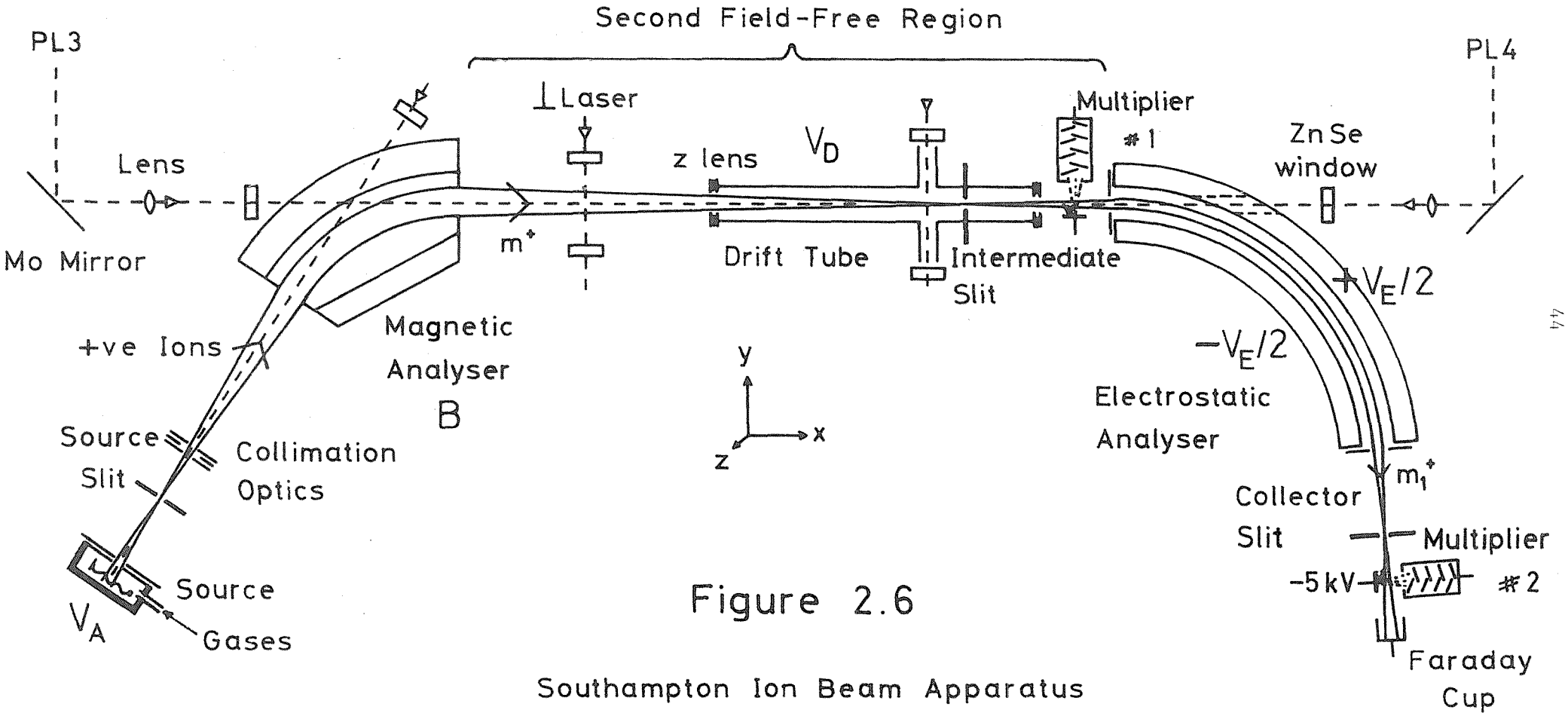

Figure 2.6

Southampton Ion Beam Apparatus

beam by matching their focusing characteristics. We have been able to produce beams of H_2^+ with currents in excess of 10^{-6} A, or a beam flux of greater than 6 x 10^{12} ions/sec. The parent beam is brought to a focus at the intermediate slit, where the estimated y dimension is about 0.3 mm. We use a y slit width rather greater than this to reduce beam flux instabilities due to slight drifts of the focus, for similar reasons we use a wide collector slit after the ESA. Reduction of the slit widths improves the resolution of the mass spectrometer, but only at the expense of beam current. The magnetic and electrostatic analysers have no effect on the motion of the ions in the z direction. Collimation of the beam in the z direction is achieved with electrostatic lenses mounted just after the source slit, and on the ends of the drift tube. The beam height at the intermediate slit is estimated to be about 4 mm.

The major modification to the commercial instrument was the provision of windows to allow interaction of the ion beam with lasers. Four windows have been provided along the second field-free region, to allow perpendicular interaction of the laser and ion beams for direct photodissociation experiments. Two windows are attached to the flight tube through the magnet, one to permit a laser to be directed along the ion beam into the source, the other to allow collinear interaction of the ion and laser beams in the second field-free region. By making a hole in the outer plate of the ESA and mounting a window in line with this hole, we have a clear line of sight through the second field-free region, allowing both parallel and antiparallel alignment of the laser and ion beams. The beams necessarily pass collinearly through the second field-free region, because the slits that define the path of the ion beam also limit the laser beams. The laser-ion beam interaction is further optimised by careful selection and positioning of the laser focusing optics. We attempt to match the shapes of the laser and ion beams by bringing the laser beams to a focus at the intermediate slit, with a spot size of about 0.5 mm. This arrangement also gives the maximum transmission of the laser beam through the instrument, about 30% of the input power of a CO_2 laser is usually lost during passage. For the sequential two photon photodissociation experiments, we can use two

counterpropagating laser beams. Disturbance of one laser by the other is eliminated by using beams which cross at a very small angle at the intermediate slit, the beams are then spatially separated. Mechanically stable mounting of the lasers and their associated optics is important if noise due to vibrations is to be minimised. We have accordingly insulated our lasers and optics from the tables on which they are mounted by judicious use of vibration absorbing materials, such as squash balls (Dunlop).

The ion beam current can be sampled in various places. A small proportion of the beam is collected by a monitor plate just after the source slit. Measurement of this total ion current can be useful in diagnosing faults within the ion source. The parent ion beam can be monitored by an off-axis electron multiplier situated just after the drift tube. The off-axis multipliers are used in tandem with a conversion dynode charged to -5kV. The multiplier amplifies the current of secondary electrons produced by impact of the positive ions on the electrode. After passing through the ESA the ions may be detected either by a second off-axis multiplier, or by a Faraday cup. The Faraday cup is basically a metal plate which collects all the ions, the current from the cup is used to calculate beam fluxes. The very small currents of fragment ions are amplified by the off-axis electron multiplier system, before being measured. The gain of the multiplier can be determined with the aid of the Faraday cup, so that multiplier signals can be converted to ion beam fluxes.

In the next few sections we describe the principle components of the instrument in greater detail, and how by scanning them we can obtain the desired spectroscopic data.

2.7 The Ion Source and The Magnetic Analyser.

Taken together the ion source and the magnetic analyser provide a mass-selected, mono-energetic beam of ions on which spectroscopic experiments can be performed. Figure 2.7 is a detailed diagram of the electron impact ionisation source used in the experiments described

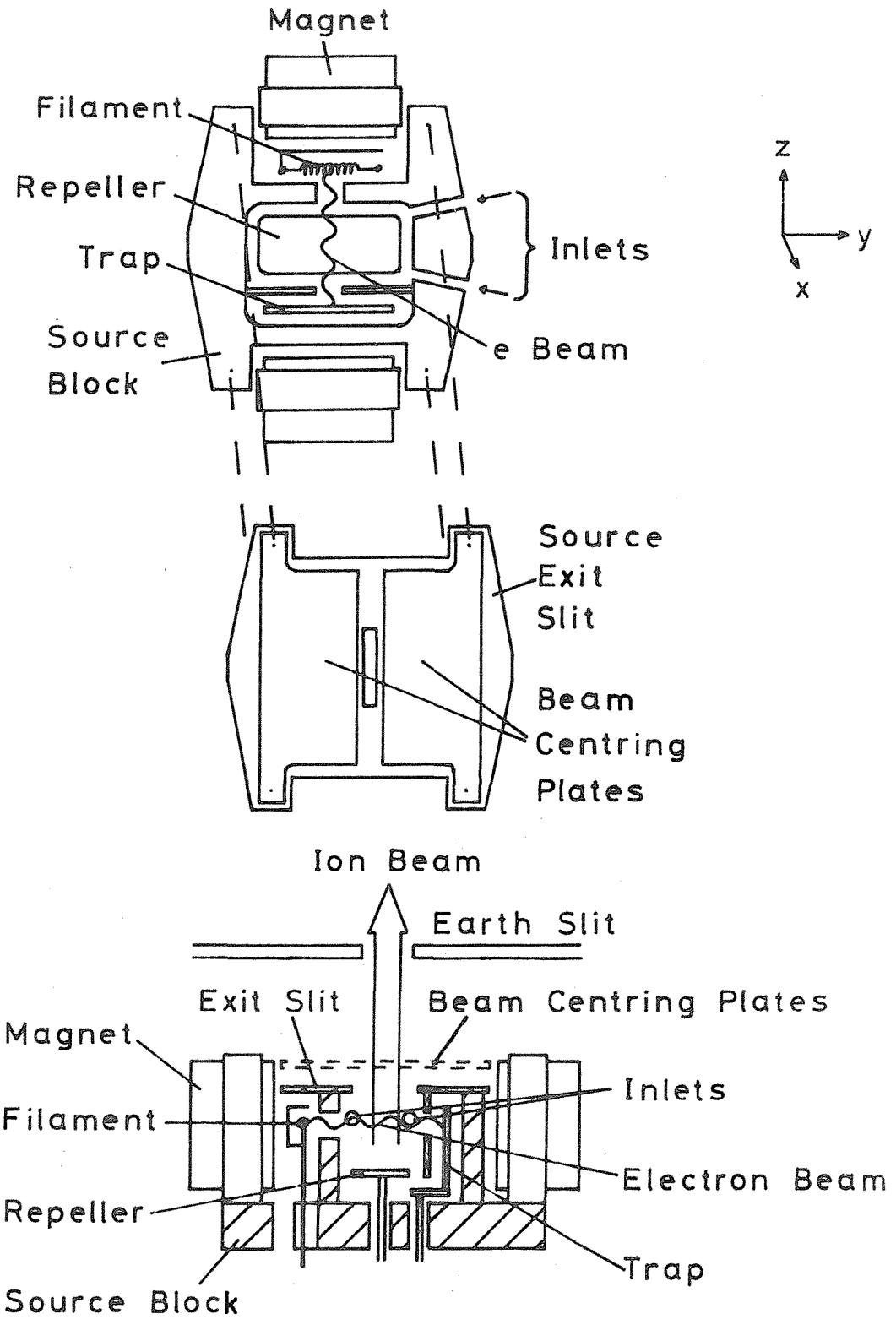

Figure 2.7

Ion Source

in this thesis. The various components of the source, filament, source block, repeller, electron trap and beam centering plates are isolated from one another and from earth by ceramic insulators. Electrons formed by thermionic emission from a coiled tungsten filament are accelerated into the source block by floating the filament at a potential below that of the block. The potential difference defines the electron energy, which can be varied continuously from 0 to 100 eV, or in steps of 50 eV from 50 to 500 eV; energies between 30 and 100 eV are usually used. The ionising electron beam is confined by a small magnetic field applied across the source, the electrons spiral about the field direction. Electron beam currents of up to 1 mA, as measured by the current between the filament and trap electrode, can be obtained, we usually use the maximum attainable current. The current is stabilised, either using the trap current, or the total emission to the source block and trap.

Gases are admitted to the source either through a glass capilliary, which is coupled to the source by a retractable metal cup, or through a thin metal tube, insulated from earth by incorporating a length of silicone rubber tubing into the line. Both inlet lines are connected to three gas reservoirs, via very fine needle valves. Gases escape relatively slowly from the source, consequently the pressure inside is much higher than measured by the source chamber gauge. Differential pressure ratios of about 10^2 are anticipated, so that with a typical external pressure of 3×10^{-5}mbar, the pressure inside is about 3×10^{-3} mbar. Higher differentials can be achieved by reducing the dimensions of the ion exit slit.

Once formed the ions are rapidly extracted by the small potential gradient inside the source caused by slight penetration of the earth electric field. The potential gradients within the source can be modified by floating the ion repeller relative to the source block, allowing the extraction efficiency to be optimised. The potential difference between the repeller and the source block is usually in the range 0 to +5V. As the ions leave the source they are deflected by the magnetic field used to confine the electron beam, this motion is corrected by applying a potential gradient between the

two beam centering plates.

At low pressures, source chamber ion gauge readings of less than 10^{-5} mbar, the ions are extracted before they undergo any collisions. This ensures that ions initially formed with high levels of internal excitation, rotational, vibrational and/or electronic, leave the source unrelaxed. Increasing the monitored pressure to about 10^{-4} mbar, allows some of the ions to react with molecules in the source before extraction, beams of HeH^+ and H_3^+ are formed in this manner. The number of collisions is still sufficiently low that the product ions experience little or no relaxation before extraction. As the ions are accelerated to the full ion beam energy, by the potential gradient between the source and the earth slit, some of them may undergo high energy collisions with the stream of unionised molecules leaking out of the source, and collisional excitation may ensue. Once through the earth slit the ions enter the essentially collision free environment of the analyser region, where the pressure is about 10^{-7} mbar.

The ion beam which emerges from the source chamber is deflected onto the desired path and collimated by a stack of electrostatic lenses and several defining slits. All the singly charged positive ions in the beam have approximately the same kinetic energy:

$$\frac{1}{2} mv^2 = eV_S \qquad (2.21)$$

where V_S is the potential at which the ions were formed. The deflection of the ions by a perpendicular magnetic field (along z) depends on their momenta:

$$mv = (2meV_S)^{\frac{1}{2}} \qquad (2.22)$$

within the field B the ions follow a circular path of radius:

$$r_m = \frac{mv}{e} \cdot \frac{1}{B} \qquad (2.23)$$

$$= \left(\frac{2mV_S}{e}\right)^{\frac{1}{2}} \cdot \frac{1}{B} \qquad (2.24)$$

The intermediate slit defines r_m to be 30 cm, and by varying B we select the parent ion mass according to (2.24). Sweeping either V_S or B and monitoring the ions with the first off-axis multiplier yields a mass spectrum of the ions formed in the source. Initial tuning of the source and optimisation of gas mixtures are usually performed with the instrument operating in this single focus mode. In practice a few of the parent ions fragment before reaching the magnetic analyser:

$$m^+ \rightarrow m_1^+ + m_2 \qquad (2.25)$$

the fragment ions m_1^+ appear at an effective mass of:

$$m_1^* = \frac{m_1^2}{m} \qquad (2.26)$$

The mass resolution is relatively low, with the intermediate slit wide open we are just able to separate D_3^+ from $^4HeD^+$; the mass difference is 6 parts in 1000.

The speed of the ions, required for Doppler shift calculations (2.13) or (2.14), is given by:

$$v = \left(\frac{2eV_S}{m}\right)^{\frac{1}{2}} \qquad (2.27)$$

values for e and m are taken from standard tabulations [105]. The problem is to determine V_S, the potential at which the ions are formed. We can measure the potential difference V_A between the source block and earth, but because of penetration the ions are actually extracted from a region of slightly lower potential than V_A. Carrington and Buttenshaw have described how this difference can be investigated by Doppler shift measurements [53]. Since $V_A > V_S$, Doppler shifts calculated using V_A are larger than actually occur. If the same transition is recorded using parallel and antiparallel alignments the V_A calculated shifts give:

$$\nu_{parallel} < \nu_{antiparallel} \qquad (2.28)$$

The differences between $\nu_{parallel}$ and $\nu_{antiparallel}$ for several transitions were fitted, and it was found that, for HD^+ formed in our source, penetration effects were accounted for by:

$$V_S = 0.9953 \times V_A \qquad (2.29)$$

This relationship is confirmed by the measurements on HD^+ and H_3^+ reported in this thesis. Constant usage causes a slow build up of contamination inside the source, further affecting V_S, and additional shifts in V_A of up to 20 V have been encountered. In general it is believed that the V_S values determined by (2.29) from experimentally measured V_A are accurate to better than 5V, so that transition frequencies can be determined to ± 0.001 cm^{-1}. Penetration is also responsible for the rather large (~1 eV) kinetic energy spread of the ions, corresponding to an effective translational temperature of ~12000 K, much higher than the source block temperature of ~200°C.

Estimation of the flight time of the ions from formation to the intermediate slit is hampered by uncertainty as to the source residence time [110]. We believe that the ions typically reach the intermediate slit within 4×10^{-6} sec (for mass = 3) of their formation, and take this value as the lower limit on the initial state lifetime.

2.8 The Second Field-Free Region.

The layout of this region of the apparatus is shown in figure 2.6. The drift tube is a 40 cm long metal tube to which a potential of up to ±500 V can be applied. Penetration of the earth field into the drift tube is minimised by guard electrodes at either end, the adjustable intermediate slit is at the same potential as the drift tube. The experiments described in this thesis have depended on the observation of fragmentation of molecular ions within the drift tube induced by laser beams propagating collinearly with the ion beam. The principle use of the drift tube in our experiments is to provide frequency modulation, and thereby discriminate the sharp transitions we are trying to observe from the often dominant, featureless direct

photodissociation. The principles are illustrated in figure 2.8, we irradiate the ions with a laser whose Doppler-shifted frequency is alternately:

$$\nu_+ = \nu_{ion} + \Delta f/2 \text{ and } \nu_- = \nu_{ion} - \Delta f/2 \qquad (2.30)$$

The fragment ion signals at these two frequencies are subtracted electronically using a lock-in amplifier. This procedure removes background photodissociation, and much of the noise and drift due to fluctuations in the laser power and/or the parent ion flux. This modulation scheme gives a pseudo first derivative lineshape, see figure 2.8. The technique is limited to narrow resonances, those with widths not much greater than the modulation amplitude Δf. Frequency modulation is actually achieved by superimposing a small square wave voltage of amplitude ΔV on the drift tube potential V_D, through the Doppler effect this gives:

$$\Delta f \simeq \nu \frac{\Delta V}{c} \left[\frac{e}{2m\ (V_S - V_D)} \right]^{\frac{1}{2}} \qquad (2.31)$$

ΔV is variable from 0 to 10 V, while the frequency of the square wave can be varied from 0 to 6 kHz. For the H_3^+ experiments described later in this thesis, we applied a 7 V modulation at about 730 Hz to the drift tube. At a beam potential of 8000 V and a laser wavenumber of 1000 cm^{-1}, this is equivalent to frequency modulation with an amplitude of 32 MHz.

We now consider the detailed kinematics of the following fragmentation:

$$m^{+*} \rightarrow m_1^+ + m_2 + \Delta \qquad (2.32)$$

The parent ion of mass m is prepared by the laser in a state with an energy Δ above a dissociation limit correlating to an ion of mass m_1 and a neutral of mass m_2. This fragmentation occurs within the drift tube, which is at a potential V_D relative to earth. The requirement that fragmentation occurs before the excited ion m^{+*} leaves the drift tube imposes an upper limit on the lifetime of the dissociated state of

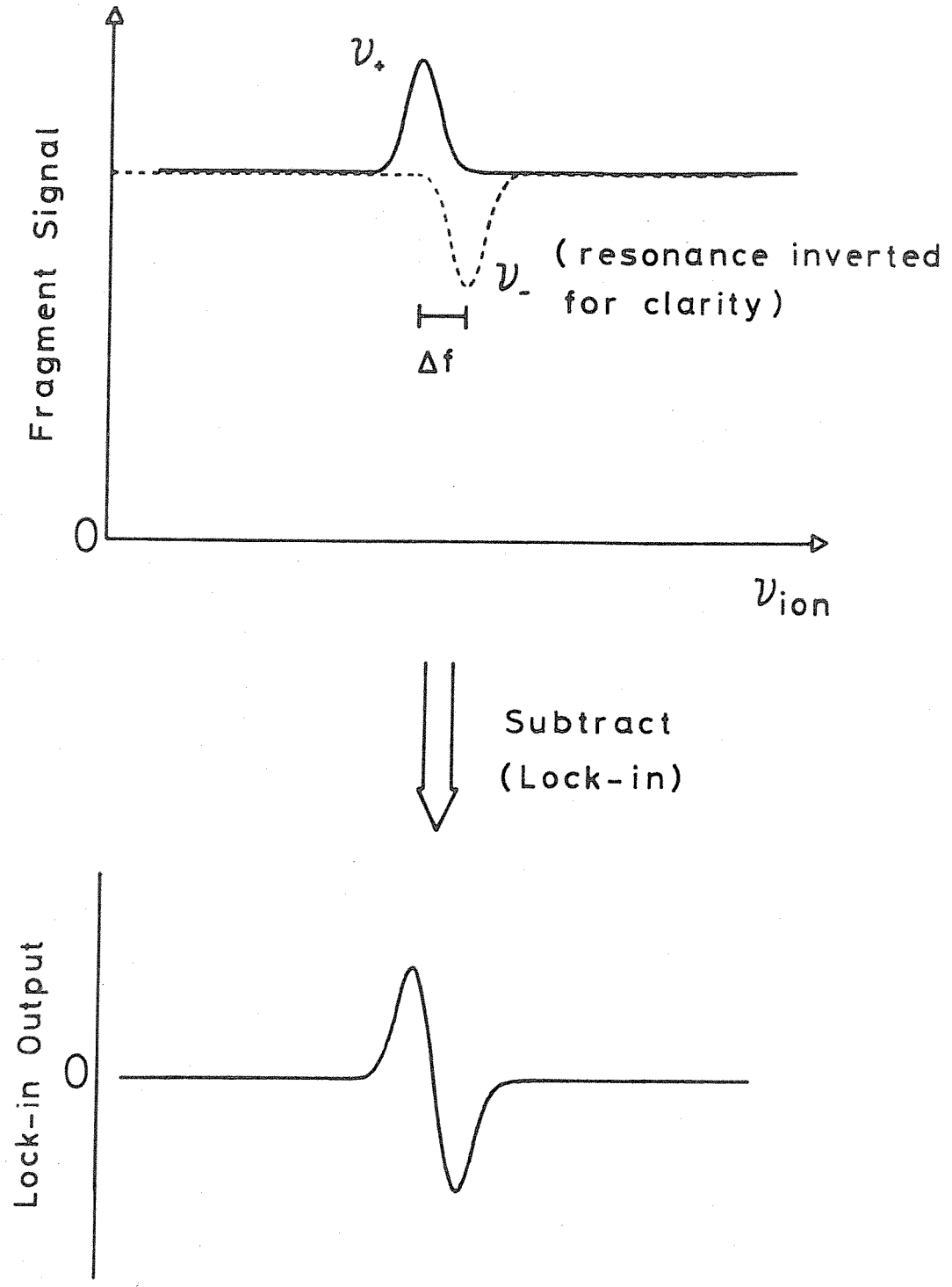

Figure 2.8

Frequency Modulation

typically about 10^{-6} secs. At earth potential the parent ions have a kinetic energy of:

$$\frac{1}{2} m v^2 = e V_S \tag{2.33}$$

within the drift tube this is shifted to:

$$\frac{1}{2} m v_D^2 = e (V_S - V_D) \tag{2.34}$$

Three conservation laws serve to define the fragmentation process, conservation of mass:

$$m = m_1 + m_2 \tag{2.35}$$

conservation of energy:

$$\Delta + \frac{1}{2} m v_D^2 = \frac{1}{2} m_1 v_{1D}^2 + \frac{1}{2} m_2 v_{2D}^2 \tag{2.36}$$

and conservation of momentum:

$$m \underline{v}_D = m_1 \underline{v}_{1D} + m_2 \underline{v}_{2D} \tag{2.37}$$

We simplify the discussion by assuming that fragmentation occurs along $\underline{v}_D$, the direction of propagation of the beam, so that (2.37) becomes:

$$m v_D = m_1 v_{1D} + m_2 v_{2D} \tag{2.38}$$

Manipulation of (2.35), (2.36) and (2.38) soon yields:

$$v_{1D} = v_D \pm \left(\frac{2\Delta m_2}{m_1 . m} \right)^{\frac{1}{2}} \tag{2.39}$$

We concentrate on determining the kinetic energies of the fragment ions, since the ESA separates them according to $m_1 v_{1x}^2$. Within the drift tube the kinetic energy of the fragment ion of mass m_1 is:

$$\frac{1}{2}\ m_1 v_{1D}^2 = \frac{m_1}{m}\ e\ (V_S - V_D) \pm \frac{2}{m}\ [e\ (V_S - V_D)\Delta m_1 m_2]^{\frac{1}{2}} + \frac{m_2}{m}\ \Delta \tag{2.40}$$

When these ions exit the drift tube and come to earth potential their kinetic energy is shifted to:

$$\frac{1}{2}\ m_1 v_1^2 = \frac{1}{2}\ m_1 v_{1D}^2 + e\ V_D \tag{2.41}$$

$$= \frac{m_1}{m}\ e\ V_S + \frac{m_2}{m}\ e\ V_D \pm \frac{2}{m}\ [e\ (V_S - V_D)\Delta m_1 m_2]^{\frac{1}{2}} + \frac{m_2}{m}\ \Delta \tag{2.42}$$

The leading terms in this expression show that fragment ions formed at earth potential have a kinetic energy:

$$\frac{1}{2}\ m_1 v_1^2 \simeq \frac{m_1}{m} \cdot \frac{1}{2}\ m\ v^2 \tag{2.43}$$

allowing them to be separated from the parent ions. We also see that the drift tube ions can be separated from the parent ions, and from the earth fragment ions. They are separated from the earth ions by:

$$\frac{m_2}{m}\ e\ V_D \tag{2.44}$$

$|V_D| \geq 250$ V is usually sufficient to achieve complete separation, the value required increases as (m_1/m) increases. At high beam potentials we usually employ a negative drift tube offset, this allows us to increase the maximum beam potential from 10 keV (V_S alone) to 10.5 keV (with $V_D = -500V$). At low beam energies the use of a large, positive drift tube potential ($V_D = +500$ V) has considerable advantages. Consider the fragmentation of H_3^+:

$$H_3^+ \rightarrow H^+ + H_2 \tag{2.45}$$

at a beam energy of 1500 eV. This could be achieved by $V_S = 1500$ V, $V_D = 0$, giving a proton kinetic energy of 500 eV, or with $V_S = 2000$ V, $V_D = 500$ V, in which case the H^+ energy is 1000 eV. The increased

kinetic energy obtained with V_D = 500 V greatly enhances the efficiency with which the protons are subsequently collected and detected.

The effect of a nonzero energy release Δ is to produce forward and backward scattered fragment ions, with kinetic energies differing by:

$$\frac{4}{m} [e (V_S - V_D) \Delta m_1 m_2]^{\frac{1}{2}} \qquad (2.46)$$

To discern the forward and backward ions we will require an energy resolution of better than:

$$\left(\frac{m_1 e V_S}{16 m_2 \Delta}\right)^{\frac{1}{2}} \qquad (V_S >> V_D) \qquad (2.47)$$

From which we see that it is easier to separate them if (m_1/m_2) is small, low beam potentials V_S will also assist. Unless Δ is very large the final term in (2.42) $(m_2/m)\ \Delta$ can be neglected, compared to the three preceding terms.

For the general case, when we do not constrain the fragmentation to occur solely along the x axis, we have:

$$\underline{v}_{1D} = \underline{v}_D + \underline{u}_\Delta \qquad (2.48)$$

where

$$|u_\Delta| = \left(\frac{2\Delta m_2}{m_1 \cdot m}\right)^{\frac{1}{2}} \qquad (2.49)$$

and $\underline{u}_\Delta$ may be in any direction. The kinetic energy of fragment ions formed within the drift tube can now take any value between the forward and backward limits of (2.42). The actual form of the kinetic energy distribution depends on the probability that $\underline{u}_\Delta$ is in a particular direction. For photofragmentation this is given by [84]:

$$I(\theta) = \frac{1}{4\pi} [1 + \beta P_2 (\cos\theta)] \qquad (2.50)$$

where θ is the angle between $\underline{u}_\Delta$ and the electric vector of the laser $\underline{E}$, and:

$$P_2(\cos\theta) = \frac{1}{2}(3\cos^2\theta - 1) \qquad (2.51)$$

β can take any value between 2, giving a $\cos^2\theta$ distribution, peaking along $\underline{E}$, and -1, giving a $\sin^2\theta$ distribution, peaking perpendicular to $\underline{E}$, $\beta = 0$ gives an isotropic distribution. The final kinetic energy distribution passed to the ESA is further complicated by the effects of the intermediate slit. Referring to the vector diagram, figure 2.9, ions formed a distance 1 upstream from the slit reach the slit after a time:

$$t = \frac{1}{v_D} \qquad (2.52)$$

If they have a transverse velocity of u_y, they will have moved a distance:

$$\begin{aligned} d &= t\, u_y \\ &= 1\, \frac{u_y}{v_D} \end{aligned} \qquad (2.53)$$

off the beam axis when they reach the slit. If the y slit width is w_y, the ions will pass through the slit only if:

$$d < \frac{w_y}{2} \quad \text{or} \quad \frac{u_y}{v_D} < \frac{w_y}{21} \qquad (2.54)$$

The slit tends to reject ions with transverse velocity, the extent of rejection depending on the dimensions of the slit, and the distance from the slit to the fragmentation point. The kinetic energy distribution passed by the slit will thus exhibit an exaggerated forward-backward peaking over that predicted using $I(\theta)$ alone. For experiments such as those we perform, using a collinear interaction geometry and slightly imperfect ion beams, the fragment ion kinetic energy distributions have to be calculated numerically by quasi-random trajectory simulations. The selection of trajectories is governed by $I(\theta)$, the shape of the ion beam, and the probability

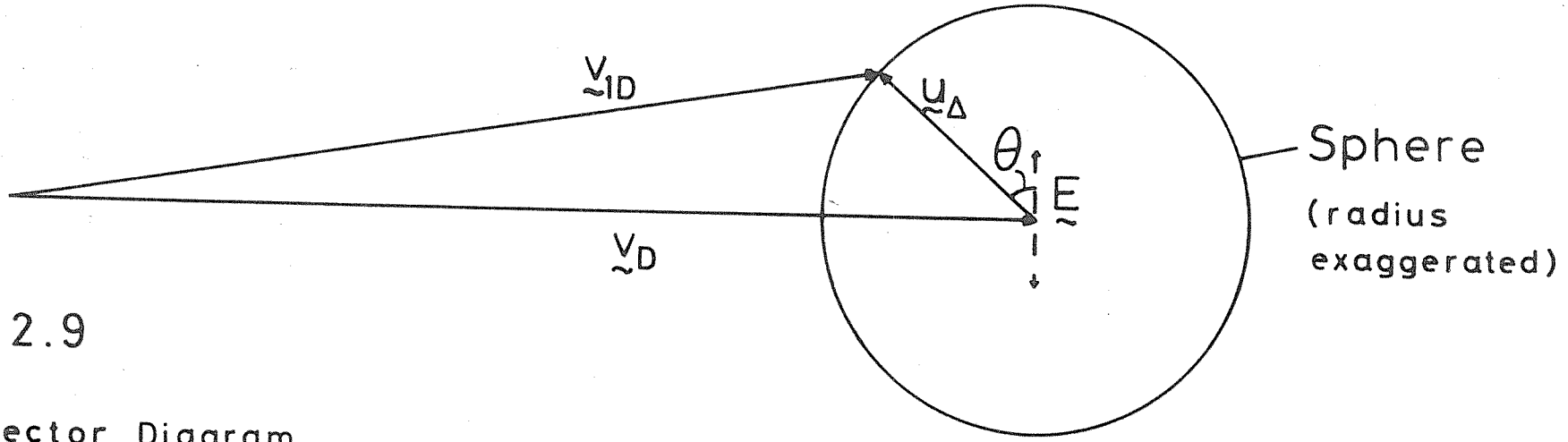

Figure 2.9

Velocity Vector Diagram

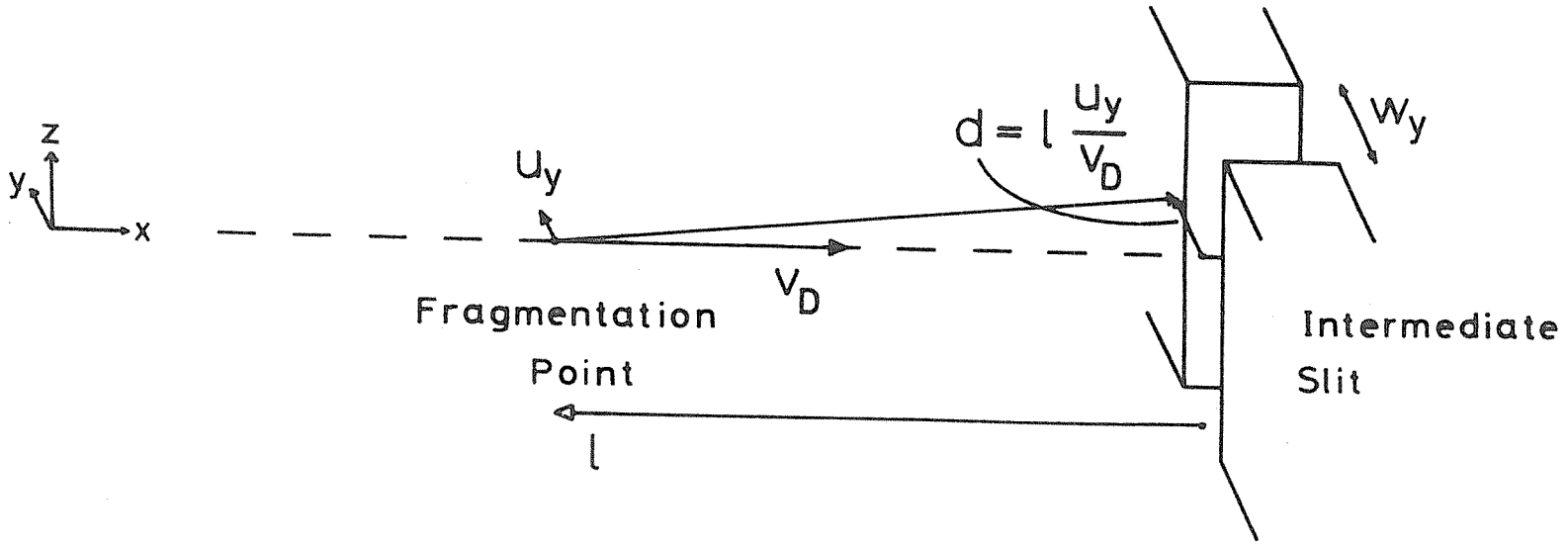

that fragmentation occurs at a particular point on the ion beam path. By using a sufficiently large number of trajectories, the experiment can be exactly reproduced by a Monte Carlo simulation. The kinetic energy distribution is obtained by counting the number of trajectories within a given kinetic energy range that are passed by the intermediate slit.

2.9 The Electrostatic Analyser (ESA).

The electrostatic analyser consists of two very smooth, exactly concentric cylindrical metal plates, held apart by precision ceramic spacers. The spacing s between the plates is nominally 2 cm, while the radius r of the central path between them, which the ions must follow if they are to pass through the defining slits is 38 cm. A radial electric field E is maintained by applying equal and opposite potentials ($V_E/2$) to the two plates:

$$E = \frac{V_E}{s} \tag{2.55}$$

The radius of the circular path of an ion through the radial field is:

$$r = \frac{mv_x^2}{eE} \quad (= 38 \text{ cm}) \tag{2.56}$$

and we immediately see that the ESA selects the ions according to their kinetic energy, or strictly $(m/e)\ v_x^2$. The kinetic energy of the ions can thus be determined by measuring V_E:

$$m\ v_x^2 = r'\ e\ V_E \tag{2.57}$$

where

$$r' = \frac{r}{s} = 19.0 \text{ (from nominal dimensions)} \tag{2.58}$$

In fact, by measuring V_E for ions of known kinetic energy, we have determined:

$$r' = 18.94\ (\pm\ 0.01) \tag{2.59}$$

Recalling the kinetic energy expression (2.42) given in the previous section, we see that:

$$V_E = \frac{2}{r'm} \left[m_1 V_S + m_2 V_D \pm 2 \left[(V_S - V_D) \frac{\Delta}{e} m_1 m_2 \right]^{\frac{1}{2}} + m_2 \frac{\Delta}{e} \right] \tag{2.60}$$

The ESA passes parent ions when:

$$V_{Ep} = \frac{2}{r'} V_S \tag{2.61}$$

fragment ions formed at earth potential with zero kinetic energy release when:

$$V_{Ee} = \frac{2}{r'} \frac{m_1}{m} V_S = \frac{m_1}{m} V_{Ep} \tag{2.62}$$

and drift tube fragment ions at:

$$V_{Ed} = \frac{2}{r'm} \left[m_1 V_S + m_2 V_D \right] \tag{2.63}$$

Unless otherwise stated the ESA differential voltage is set to satisfy (2.63) when we are recording Doppler-tuned spectra of molecular ions by monitoring ion fragmentation. All collinear photodissociations produce some fragment ions satisfying (2.63), although if Δ is large they may, as we have seen in the previous section, be rejected by the intermediate slit.

We can also use the ESA to determine the kinetic energy release Δ. Simulations of kinetic energy distributions, convoluted with an ESA resolution function, have shown that, reliable estimates of Δ are obtained by equating the full width at half maximum of the ESA spectrum with the kinetic energy difference between the limits of forward and backward scattering (2.46) [85]:

$$\Delta V_E = \frac{8}{er'm} \left[e (V_S - V_D) \Delta m_1 m_2 \right]^{\frac{1}{2}} \tag{2.64}$$

These Δ estimates can be improved by careful simulation, adjusting the values used for Δ and β to obtain the best match to the experimental

ESA spectrum. We have not yet developed a simulation program for our instrument, and our Δ estimates are based on the simple relationship (2.64).

The energy discrimination of the ESA can be employed to selectively detect transitions for which the kinetic energy release is greater than a threshold value Δ_{th} [78]. We offset the ESA differential voltage from the central value given by (2.63):

$$V_E = V_{Ed} + \delta V_{Eth} \tag{2.65}$$

The fragment ions must then be formed with a kinetic energy release:

$$\Delta \geq \Delta_{th} = \frac{e\ (r'm\ \delta V_{Eth})^2}{16\ (V_S - V_D)\ m_1 m_2} \tag{2.66}$$

if they are to be passed by the ESA. Two dimensional spectra (frequency, kinetic energy release) can be built up by recording a series of spectra with different offsets δV_{Eth}, see chapter five for an example.

An estimate of the ESA energy resolution can be formed from its dimensions. In travelling from the intermediate slit, through the 81.5° sector and then on to the collector slit, the ions cover a distance of 54.05 + 5 cm. Using wide slits (2 mm), the fractional deviation in the radius of the path of the ions:

$$\frac{\Delta r}{r} \leq \frac{2}{590} \tag{2.67}$$

if the ions are to pass through the collector slit. The energy resolution is then:

$$\frac{mv^2}{\Delta(mv^2)} = \frac{r}{\Delta r} = 295 \tag{2.68}$$

A value in agreement with simulations of ESA spectra recorded with our instrument, performed by Dr. P. G. Fournier. Recalling (2.47) and considering the fragmentation of H_3^+ (2.45) at V_S = 8000 V, we

see that we should be able to discern forward and backward scattering of protons for $\Delta > 20\ cm^{-1}$. The resolution can be increased by reducing the widths of the intermediate and collector slits, but only at the expense of a loss of signal. The sensitivity of the ESA to the kinetic energy release could be increased by retarding the fragment ions before they enter the analyser [111]. Our experiences in using the ESA indicate that its performance has not been adversely affected by the presence of the hole in its outer plate.

Finally we note that the functions of our ESA, selection of fragment ions and determination of kinetic energy releases, can also be accomplished by a magnetic, momentum analyser [112]. The ESA has the considerable advantage that its radial electric field responds instantaneously to changes in the potentials applied to its plates, while magnetic fields follow changes in the current through an electromagnet relatively slowly.

2.10 Computer Control.

Virtually all of our experiments require the use of a computer to provide the desired scan and to collect the data. The computer, a Digital MINC - 11/23, is able to program individually the source potential, the magnetic field, the drift tube potential and the ESA differential voltage using 0-5V control voltages. These control voltages are derived from 12 bit digital to analogue (0-5.12V) converters. The source potential can be increased from 0 to 10 keV by changing the control voltage from 0 to 5V. With one converter the minimum step size of 2.5eV is rather coarse. To provide the fine steps we require for our experiments, we electronically divide the output of one converter by 100 and add this to the unattenuated output of a second converter, giving a minimum source potential step size of 0.025 eV. The control signals for the magnetic field and the ESA are also derived by summing the outputs of two converters in this fashion. Adequate resolution of the drift tube potential, 0.125 eV, is obtained using a single 12 bit converter. The actual potentials applied to the source and the drift tube, as well as the ESA differential

voltage are continuously monitored using a digital voltmeter. Differences between the programmed requests and the actual values obtained have been minimised by careful optimisation of the software used to produce the control voltages.

The electronics of the ion beam apparatus provide an internal analogue linking of the ESA differential voltage V_E to the potentials applied to the source V_A and the drift tube V_D, according to the relationship:

$$V_E = \frac{2}{r'}\left[\frac{m_1}{m}(V_A - V_D) + V_D\right] \qquad (2.69)$$

where the fragment to parent ion mass ratio (m_1/m) is set using a potentiometer in the linking circuit. Recalling (2.63), we see that this linking ensures that the ESA remains on the centre of the fragment ion peak as V_A and/or V_D are varied. The fast response time of the ESA electric field allows it to exactly track rapid variations in V_D, such as the square wave voltage added to the drift tube potential to produce Doppler frequency modulation.

Various output voltages can be read into the computer's memory through 12 bit analogue to digital converters. The magnet control circuit uses analogue electronics to produce a voltage proportional to (B^2/V_A), by reading this output the computer can monitor the mass of the parent ion, see (2.24). The fragment ion current from the second off-axis electron multiplier is passed into a current pre-amplifier (Brookdeal 5002). This unit produces a DC voltage proportional to the total fragment ion current, it also separates off the AC component for subsequent processing by a lock-in amplifier (Brookdeal 9501). When the source potential V_A is being scanned, the computer controls the magnetic field to continuously optimise the transmission of the parent ion of interest. At the start of a scan the computer first sets the initial source potential, it then increases the magnetic field in relatively large steps, until the mass output voltage is just above that corresponding to the selected parent ion. The computer now switches its attention to the total fragment ion current signal from the preamplifier, which will be maximised when

the magnetic field satisfies (2.24); we use internal linking (2.69) of V_E to V_A, V_D in these scans. The magnetic field is decremented in small steps, after each decrease the field is allowed to settle for 10 ms, 64 readings of the fragment signal are then taken and averaged. Successive averages are compared, when three consecutive increases of greater than $\frac{1}{16}$ th have been detected the final peak location commences. The magnetic field is decremented until the increase in the fragment ion signal is less than $\frac{1}{64}$th. With the wide slits we use this algorithm easily and reproducibly locates the top of the parent ion peak. Readings of the lock-in amplifier output, which carry the information we are seeking, can now be taken. The lock-in is normally operated with a 1s time constant, the output is allowed to settle for 0.5s before four readings are taken at 0.1s intervals. The signal can be averaged for a predetermined number of seconds by repeating the reading procedure once a second. The final averaged signal is stored in the computer's memory. The scan is now incremented, a new source potential is set and, using the final stages of the peak locking algorithm described above, the computer makes minor adjustments to the magnetic field, searching bidirectionally for the peak top. Once the top has been located a further set of lock-in amplifier readings is averaged, and then stored. Scans of up to 2000 points, covering as wide a source potential range as 2000 eV are performed in this way. During the scan the recorded signals are displayed in real time on a video screen (Hewlett-Packard 1350S). The results of a scan can be stored on a hard disk for subsequent plotting (Hewlett-Packard 7225A) and measurement. Spectra are measured by hand and converted to Doppler-shifted frequencies using (2.34) and (2.13) or (2.14); these calculations are performed on a Hewlett-Packard 85 computer. Measurement of the spectra by the computer was considered, but as a unique line shape could not be defined this has never been implemented. Experiments in which the other elements of the instrument, the drift tube potential and/or the ESA are scanned are performed in a similar fashion, but with the magnetic field set manually to the top of the parent ion peak.

The software for the operating executive that performs these various functions is a set of FORTRAN and MACRO routines. MACRO is

a low level language, providing direct control of the components of the computer interface, such as the timing of digital to analogue and analogue to digital conversions. The basics of the operating system, the setting of control voltages, the tracking of the magnetic field, and the collection of signals, are performed by a MACRO routine. The user is interrogated about the scan details by a FORTRAN routine, which also calculates the control voltages required for each point of the desired scan. This information is passed to the MACRO routine, which sets the required voltages, collects the data, and then returns the averaged signal to the FORTRAN scan control routine. Other FORTRAN routines present this data on the video display system, control the storage and retrieval of completed scans, and drive the plotter. Figure 2.10 attempts to summarise the data gathering system.

2.11 Scanning Modes.

Our computer-controlled ion beam apparatus is capable of many different types of experiment. In order to perform the spectroscopic experiments outlined earlier:

1) investigation of the frequency dependence of the formation of a particular photofragment ion, and

2) determination of the kinetic energy distribution of the fragment ions formed by a state-selected photofragmentation,

we have developed a variety of scanning methods:

a) Beam Potential Scanning with Laser Amplitude Modulation.

The output power of our infrared lasers can be modulated by mechanically chopping the beam, or by rapidly switching the discharge current on and off (PL4 only). Irradiation of the ion beam with an amplitude modulated laser beam leads to synchronous modulation of the photofragment ion current, which can then be measured with a lock-in amplifier referenced to the chopping frequency. This photofragment

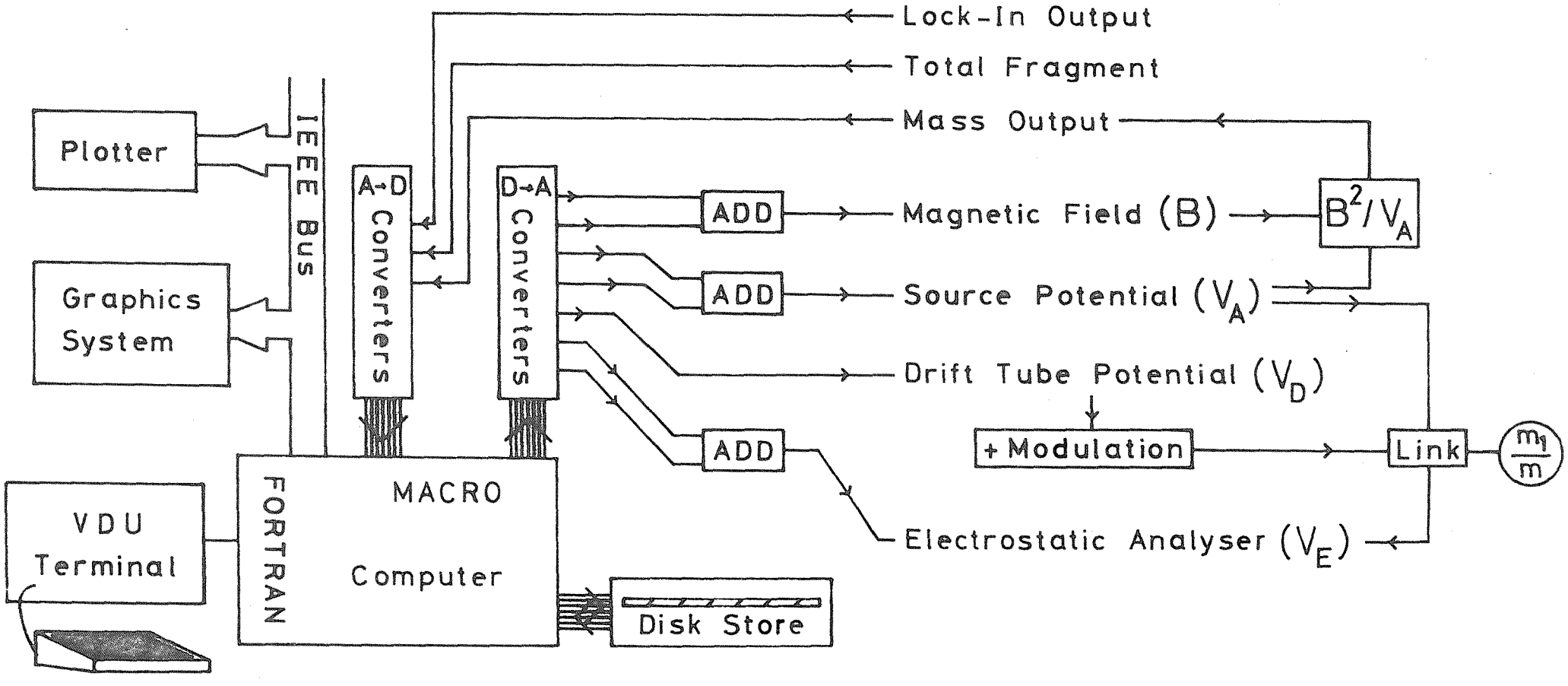

Figure 2.10

Data Gathering System

signal is recorded by the computer as the beam potential, Doppler-shifted laser frequency is swept by varying the source potential.

This method of recording transitions is most effective when the level of background photodissociation, due to direct excitation into the continuum, is low. Although it can be applied to two laser sequential two photon photodissociation experiments, by chopping the low power laser that pumps the vibration-rotation transition, it is generally only used for photopredissociation experiments. As the maximum scan width is about 0.2 cm^{-1}, lines with widths greater than 0.1 cm^{-1} cannot be recorded in their entirety on a single scan. For these very broad transitions we use a slightly different method:

b) Pointwise Frequency Scanning.

A suitable laser line is selected, the ion beam is manually tuned up at a series of widely spaced beam potentials, and the photofragment signal is measured at each point. These signals are then plotted against the Doppler-shifted laser frequency, to reveal the presence of any broad resonances. For very wide transitions it may be necessary to use several different laser lines, aligned either parallel or antiparallel, to cover the whole of the line profile. The reliability of lineshapes obtained by this method is uncertain, because the parent ion beam flux, the fragment detection efficiency and the laser-ion interaction time all vary with beam potential. Confirmation of the detection of a transition by this method can be obtained by comparing the photofragment signal recorded at the peak of the resonance with that measured using a different laser line, but otherwise identical conditions.

c) Beam Potential Scanning with Doppler Frequency Modulation.

The bound to bound transitions detected by sequential two photon photodissociation have very narrow, Doppler-limited linewidths. These transitions are best recorded by the frequency modulation method, see section 2.8. The internal linking of the ESA differential voltage to the drift tube potential ensures that V_E is modulated to exactly track

the kinetic energy of fragment ions formed in the drift tube:

$$V_{E\ mod} = \frac{2}{r'}\left(1 - \frac{m_1}{m}\right) V_{D\ mod} \qquad (2.70)$$

This causes a modulation of the earth fragment peak, the earth ions have a constant kinetic energy and are passed at a fixed differential voltage (2.62). The kinetic energy modulation of the earth fragment peak will swamp the frequency-modulated resonance signals from the drift tube ions. This problem is eliminated by separating the earth and drift tube fragment ions through the effect of a drift tube offset, (2.44) and (2.63).

This detection method can also be applied to transitions to predissociated states. It has the advantage of discriminating against background photodissociation, but it is limited to narrow resonances, those with widths of less than 100 MHz (mass = 3).

d) ESA Scanning with Laser Amplitude Modulation.

The ion beam potential is manually set to the centre of a transition pumped by a collinear, amplitude modulated laser, and the ESA differential voltage is scanned over the fragment ion peak. The recorded kinetic energy distribution of the photofragment ions corresponds to fragment ions from the state selected by the transition, plus ions formed by direct photodissociation. In favourable cases the spectrum is dominated by photofragment ions from the selected state, in other cases it may be necessary to subtract the background distribution recorded using an adjacent laser line, but otherwise identical conditions.

The same scanning technique can be used to investigate the kinetic energy spectrum of ions formed by direct photodissociation. A perpendicular laser-ion beam geometry is usually preferred for these experiments, so that the laser polarisation can be rotated relative to the direction of propagation of the ion beam. An alternative method for performing these direct photodissociation experiments is to scan the energy of the drift tube fragment ions using V_D, keeping

V_E fixed, see (2.60). An example of a kinetic energy spectrum recorded in this novel way can be found in [53].

e) ESA Scanning with Doppler Frequency Modulation.

We have devised a method for eliminating electronically the background signal from ESA scans by using frequency modulation. For sharp transitions the square wave frequency modulation obtained with the drift tube can be used to provide on/off modulation of a resonance, recall figure 2.8. The beam potential, including a drift tube offset, is tuned to produce the maximum frequency modulated signal, the average beam potential is then slightly to one side of the line centre potential. The ESA differential voltage is scanned over the drift tube fragment peak, superimposed on the scan is a modulation of amplitude given by (2.70), to match the kinetic energy modulation of the drift tube fragment ions. The modulated signal, due only to ions from the selected state, is demodulated using a lock-in amplifier referenced to the drift tube modulation frequency, and recorded by the computer. This method has been applied with great success to H_3^+, for which the change in photofragment yield on a resonance is much less than the background, due to direct photodissociation.

2.12 Advantages of Ion Beams for Laser Spectroscopy.

To conclude this chapter we collect together and review the various advantages of ion beams for spectroscopic experiments:

1) Identification of the Carrier of a Spectrum.

In conventional experiments the identification of the species responsible for an observed transition is frequently uncertain, and has to be based on the expected chemistry of the reaction mixture from which the spectrum is obtained, and a comparison of the observations with theoretical predictions. In an ion beam experiment we know the mass of the ion we are studying, and we can record its fragmentation pattern. This is normally more than sufficient information on which

to base an unambiguous identification.

2) Optimisation of the Formatiom of a Particular Ion.

The use of a mass spectrometer allows us to continuously and directly monitor the flux of a desired ion, as its formation is optimised by varying gas pressures, the electron energy and other source parameters. The ease with which this can be performed is to be contrasted with the usual situation, in which the presence of a species of interest can only be monitored through the intensity of a transition assigned to it. This can be particularly difficult if its spectrum has not been previously observed.

3) Spectroscopy in a Collision Free Environment.

The essentially collision free environment of an ion beam has many advantages, collision-induced dissociation, a potential source of noise in our experiments, is virtually eliminated as is the possibility of collisional broadening of transitions. The formation and equilibration of molecular ions is no longer controlled by ion-molecule collisions. We can form intense beams of ions such as H_2^+ which would be destroyed by its reaction with H_2 in a conventional, discharge experiment. The lack of collisions also ensures that the high levels of internal excitation, required for our experiments, created during ion formation are not lost through thermal equilibration. The combination of rapid ion extraction and subsequent selection by mass means that low levels of impurities are easily tolerated, and we use all gases as supplied, without tedious purification.

4) Precise Ion Beam Geometry.

Coupling the precise geometry of our apparatus with a knowledge of the speed of the ions allows us to place definite limits on the lifetimes of the states involved in the transitions we detect. The design of the instrument also ensures efficient interaction of the lasers with the ions, since in the collinear configuration the beams

are constrained to be exactly superimposed, if the laser beams are to exit cleanly. The use of fast, collimated beams greatly assists the efficient collection of mass selected fragment ions.

5) Doppler Tuning and Kinematic Compression.

Doppler tuning transitions of ions into resonance with fixed frequency lasers avoids many of the problems attendant to the use of tunable lasers. Fixed frequency lasers are easier to operate and more reliable than tunable lasers, they deliver higher powers and their frequencies are accurately known. The use of fast ion beams has the further advantage of inherently yielding spectra of extremely high resolution, due to the kinematic compression of the velocity distribution. Small hyperfine splittings may then be revealed, whose resolution would normally require some form of velocity selective saturation spectroscopy.

6) Ultra Sensitive Indirect Dectection Methods.

Traditional methods of infrared spectroscopy involve the direct detection of the absorption of radiation; the sensitivity is limited by the noise of the infrared source and detector. We achieve much higher sensitivity by monitoring the effects of the absorption of infrared radiation, detecting only the photons absorbed, rather than small changes in the total photon flux. Our indirect ion beam detection methods efficiently convert absorbed photons to fragment ions, which we have a high probability of detecting. There is a close analogy to the comparison of direct optical absorption measurements with laser induced fluorescence. Our sensitivity is limited by the noise Δn on the total fragment ion flux of n ions/sec, the ultimate limit is set by the counting statistics or shot noise:

$$\frac{\Delta n}{n} = \sqrt{n} \qquad (2.71)$$

Measurements of the noise on fragment ion peaks, performed with the help of Prof. W. H. Wing, indicate that our instrument is within a factor of three of this limit.

7) Determination of the Absolute Energies of States.

The measurement of transition frequencies only provides the relative energies of pairs of states. Their absolute energies may subsequently be obtained indirectly from an analysis of all the available spectroscopic data. Our ion beam experiments allow us to determine directly the absolute energy of a state, by measuring the kinetic energy distribution of fragment ions formed via a transition involving that state. This information can be invaluable in correctly assigning transitions, and in the determination of accurate dissociation energies. We can also use our kinetic energy discrimination to selectively detect transitions, according to the energy of the dissociated state above the dissociation limit (2.66).

To be balanced against these considerable advantages are the following disadvantages:

1) Very Slow Scanning Rate.

The unavoidable high resolution of Doppler-tuned ion beam spectroscopy using single frequency infrared lasers requires that scanning be performed very slowly. The maximum scanning rate is about 1 cm^{-1}/day, so that to search the entire CO_2 laser region from 875 to 1095 cm^{-1}, as we have done for the photopredissociation of H_3^+, takes about 1 year!

2) Incomplete Frequency Coverage.

The Doppler tuning range about a fixed laser frequency is limited by the minimum and maximum beam potentials, typically 2 keV and 10.5 keV, and is governed by the mass of the parent ion. For a light ion, such as H_3^+, we can achieve almost complete frequency coverage over the entire CO_2 laser region. For heavier ions the Doppler tuning range is reduced ($v \propto m^{-\frac{1}{2}}$), and complete coverage is impossible. We can then only record fragments of the spectrum which complicates the already difficult problem of assigning and analysing the spectra.

3) NonBoltzmann Population Distributions.

The initial assignment of spectra recorded from conventional sources is often assisted by noting characteristic intensity patterns, due to rotational populations being well described by a Boltzmann distribution. Although thermal rotational distributions of parent molecules appear to be preserved in electron impact ionisation, such as the formation of HD^+ from HD, they are destroyed by ion fragmentation and ion-molecule reactions. Since there are no collisions to thermally equilibrate the fragment ions, the rotational intensities no longer display recognisable patterns. High levels of vibrational excitation are vital to the experiments we perform, but coupled with a very broad rotational distribution they lead to extremely low populations of individual vibration-rotation states. Although we have been able to obtain spectra of several diatomic ions and of H_3^+ and its isotopic modifications, we suspect that for more complex polyatomic ions we may be defeated. There will not be enough ions in an individual state to produce a detectable change in the total fragment ion flux.

CHAPTER 3

SPECTROSCOPY OF HD^+ NEAR THE DISSOCIATION LIMIT MEASUREMENT OF THE v = 17 - 14 BAND

3.1 Introduction.

The simplicity of the hydrogen molecular ion H_2^+ has made it a favourite subject for theoretical studies. The absence of inter-electron interactions allows the wavefunction describing the motion of the electron about two fixed nuclei to be calculated exactly. Many properties of the hydrogen molecular ion have been calculated from this electronic wavefunction, but it is only recently that experimental results have been obtained which surpass the accuracy of the theory. The current state of the theory is considered in chapter six. At present the most accurate and comprehensive calculations on the vibration-rotation energy levels of the ground electronic state are due to Wolniewicz and Poll [48]. Their calculations, which started from the exact, fixed nuclei electronic wavefunctions, take account of corrections to the energy levels due to incomplete separation of the electronic and nuclear motions, and also radiative and relativistic corrections. It is these calculations that we set out to test by recording transitions in the v = 17 - 14 band of HD^+ [54].

Experimental data on the hydrogen molecular ion H_2^+ is limited, mainly because of the very rapid destruction of H_2^+ by its reaction with H_2:

$$H_2 + H_2^+ \rightarrow H_3^+ + H \qquad (3.1)$$

Electric discharges through hydrogen have yielded spectra of H_3^+ [30], but never of H_2^+. Spectroscopic studies are further hampered by the prediction [113] that the first transition from a bound excited

electronic state of H_2^+ will be at about 82200 cm^{-1}, a region of the electromagnetic spectrum which is not readily accessible. Some progress can be made by studying transitions to Rydberg states of the neutral molecules [114], the limits of the Rydberg series give the vibration-rotation energy levels of the molecular ion. Photoelectron spectra of the molecules with sufficiently high resolution to just reveal rotational structure have been reported [115, 116]. However these techniques do not produce data of sufficient precision to accurately test the best theoretical calculations that can be made on the molecular ions. To obtain spectroscopic data of higher resolution it has been necessary to create environments in which the hydrogen molecular ions are not destroyed by reactive collisions. The required collision free conditions can be obtained either by holding the ions at very low pressure in a quadrupole trap, or by extracting the ions from their source to form an ion beam before they can react. Radio-frequency spectroscopy on trapped H_2^+ ions has been described in chapter one.

A variety of experiments on H_2^+ and its isotopic modifications have been performed using fast ion beams. Dissociation energies for several vibration-rotation levels of the ground electron state, $1s\sigma_g$ $(^2\Sigma_g^+)$, have been obtained from the momenta of fragment ions formed by rotational (tunnelling) predissociation [117, 118], and by direct photodissociation $2p\sigma_u \leftarrow 1s\sigma_g$ [119]. These data are not very precise. The major breakthrough, to high resolution spectroscopy of the hydrogen molecular ion, was achieved by Wing et al in 1976 [46]. Although H_2^+ and D_2^+ do not have an electric dipole moment, the HD^+ ion has a mass asymmetry dipole moment, due to the separation of the centres of mass and charge in this molecule [120]. The HD^+ ion thus has an electric dipole allowed vibration-rotation spectrum, which can be predicted accurately from theoretical calculations of the energy levels. Transitions between low vibration-rotation levels ($v = 0 - 3$, $N = 0 - 2$) were observed, using the charge exchange detection method, by Doppler tuning an HD^+ ion beam into resonance with a CO laser. We use a radically different detection scheme, sequential two photon photodissociation, to detect vibration-rotation transitions between high vibrational levels. The method has been described in detail in

chapter two, and used by Carrington and Buttenshaw [53] to detect nine rotational components of the v = 18 - 16 band of HD^+, Doppler tuned into resonance with lines from a CO_2 laser. The transition frequencies were determined to ±0.001 cm^{-1}, and for the higher rotational components they deviate significantly from the theoretical predictions [48]. Partially resolved hyperfine structure was interpreted as being mainly due to a difference in the proton Fermi contact interaction between the lower and upper states. The same technique has now been applied to measure seven rotational components of the v = 17 - 14 band, Doppler tuned into resonance with a line tunable carbon monoxide laser [54]. This chapter describes the measurements and discusses the results obtained.

3.2 Experimental Methods.

The apparatus has been described in detail in chapter two. HD^+ ions were formed by electron impact ionisation of HD, with electron energies in the range 60 to 100 eV. HD gas was obtained by passing a mixture with an original composition of 50% H_2 and 50% D_2 (BOC Prochem) over a heated palladium catalyst. The gas entering the source is a statistical mixture of 25% H_2, 50% HD and 25% D_2. HD^+ beam currents of up to 10^{-6} A were obtained, corresponding to beam fluxes of 6×10^{12} ions/sec. The populations of the various vibrational levels of HD^+ are determined by the Franck-Condon factors for ionisation of HD. Fractional populations have been calculated [121] using *ab initio* potentials for HD and HD^+, see figure 3.1 and table 3.1. Although most of the ions are formed in low vibrational levels, the higher levels are occupied, 0.50% of the HD^+ ions are in v = 14 and 0.19% in v = 17. Ionisation of HD occurs with little or no rotational excitation, so the rotational distribution within each vibrational level is that of the neutral HD molecules in the source, since the HD^+ ions exit the source before they experience any rotationally inelastic collisions. The population distribution of HD^+, calculated using the HD rotational constants given in [122] and a source temperature of 500 K, are given in table 3.1.

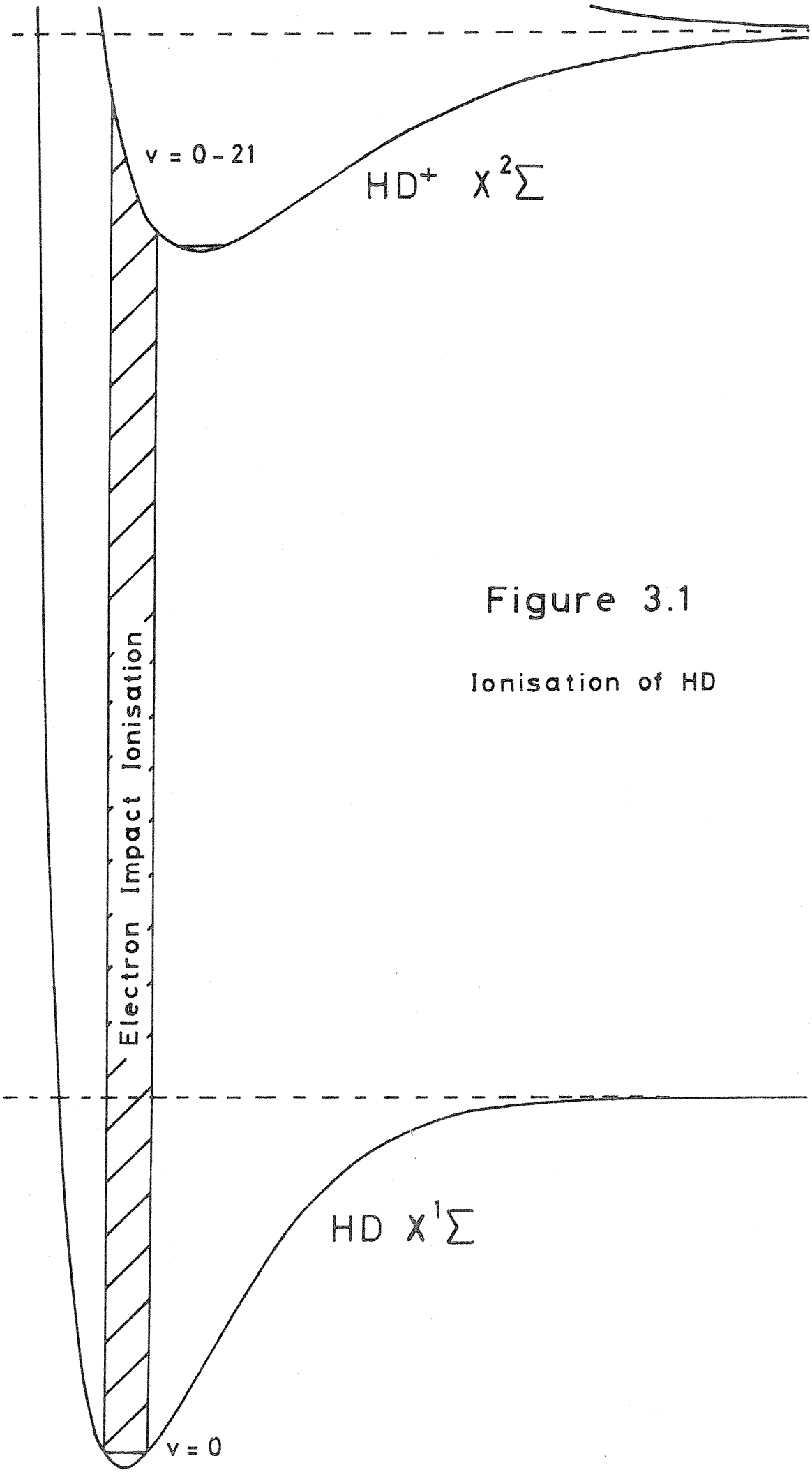

Figure 3.1

Ionisation of HD

Table 3.1

Fractional Populations for HD^+ Formed by Electron Impact Ionisation of HD at 500K

a) Vibrational Populations [121], from HD (0,2).

v	Population	v	Population
0	0.06308	11	0.01371
1	0.12841	12	0.00976
2	0.15713	13	0.00699
3	0.15174	14	0.00503
4	0.12841	15	0.00364
5	0.10042	16	0.00262
6	0.07485	17	0.00187
7	0.05422	18	0.00129
8	0.03866	19	0.00083
9	0.02736	20	0.00043
10	0.01934	21	0.00011

b) Rotational Populations of HD at 500K.
(Using $B_0 = 44.6656\ cm^{-1}$ [122]).

N	Population	N	Population
0	0.12312	4	0.08476
1	0.28562	5	0.02865
2	0.28469	6	0.00724
3	0.18432	7	0.00138

c) Vibration-Rotation Populations for HD^+ in v = 17 and 14.

(v, N)	Population($x10^4$)	(v, N)	Population($x10^4$)
(17,0)	2.30	(14,0)	6.19
(17,1)	5.34	(14,1)	14.37
(17,2)	5.32	(14,2)	14.32
(17,3)	3.45	(14,3)	9.27
(17,4)	1.58	(14,4)	4.26
(17,5)	0.54	(14,5)	1.44
(17,6)	0.14	(14,6)	0.36
(17,7)	0.03	(14,7)	0.07

Electronic excitation from the bound ground electronic state $1s\sigma$, $^2\Sigma^+$ to the first excited state $2p\sigma$, $^2\Sigma^+$, which is repulsive, leads to photodissociation, see figure 3.2. Note that there are two dissociation limits, $H^+ + D$ and $D^+ + H$, separated by about 30 cm^{-1}. The high velocity with which the fragments fly apart after photodissociation ensures that H^+ and D^+ fragment ions are formed with essentially equal probability. Qualitative radial wavefunction overlap arguments suggest that, with a CO_2 laser operating at about 1000 cm^{-1}, v = 18 should have the largest photodissociation cross-section. This expectation is confirmed, both by experiment [53] and by calculations [123]. Similar arguments suggest that with a CO laser at about 1800 cm^{-1}, v = 17 should have the highest cross-section. A number of rotational components of the v = 17 - 14 band of HD^+ are predicted [48] to lie within the range of our CO laser (1700 - 1950 cm^{-1}). We use the same CO laser to pump the transition and drive the photodissociation; the rate of photodissociation increases on resonance.

Scanning of the spectrum was achieved by sweeping the source potential. The transitions were detected through Doppler frequency modulation, using a square wave voltage of 1V amplitude at about 600 Hz applied to the drift tube. The ESA was set to transmit D^+ ions. Full details of the scanning and recording methods can be found in chapter two. Initial searches for the transitions, using wide and rapid scans, were guided by the nonadiabatic calculations of Wolniewicz and Poll [48]. Once located the lines were recorded with narrow scans of 40V width, at a scan rate of 0.02V/sec. Each resonance was recorded using as many different laser lines as possible, aligned either parallel or antiparallel to the ion beam.

3.3 Results.

Seven rotational components of the v = 17 - 14 band of HD^+ have been observed. The results are presented in table 3.2, together with the predictions from the energy levels calculated by Wolniewicz and Poll [48]. Laser wavenumbers are from the most recent set of Dunham coefficients for CO [102]. The HD^+ transition wavenumbers were calculated

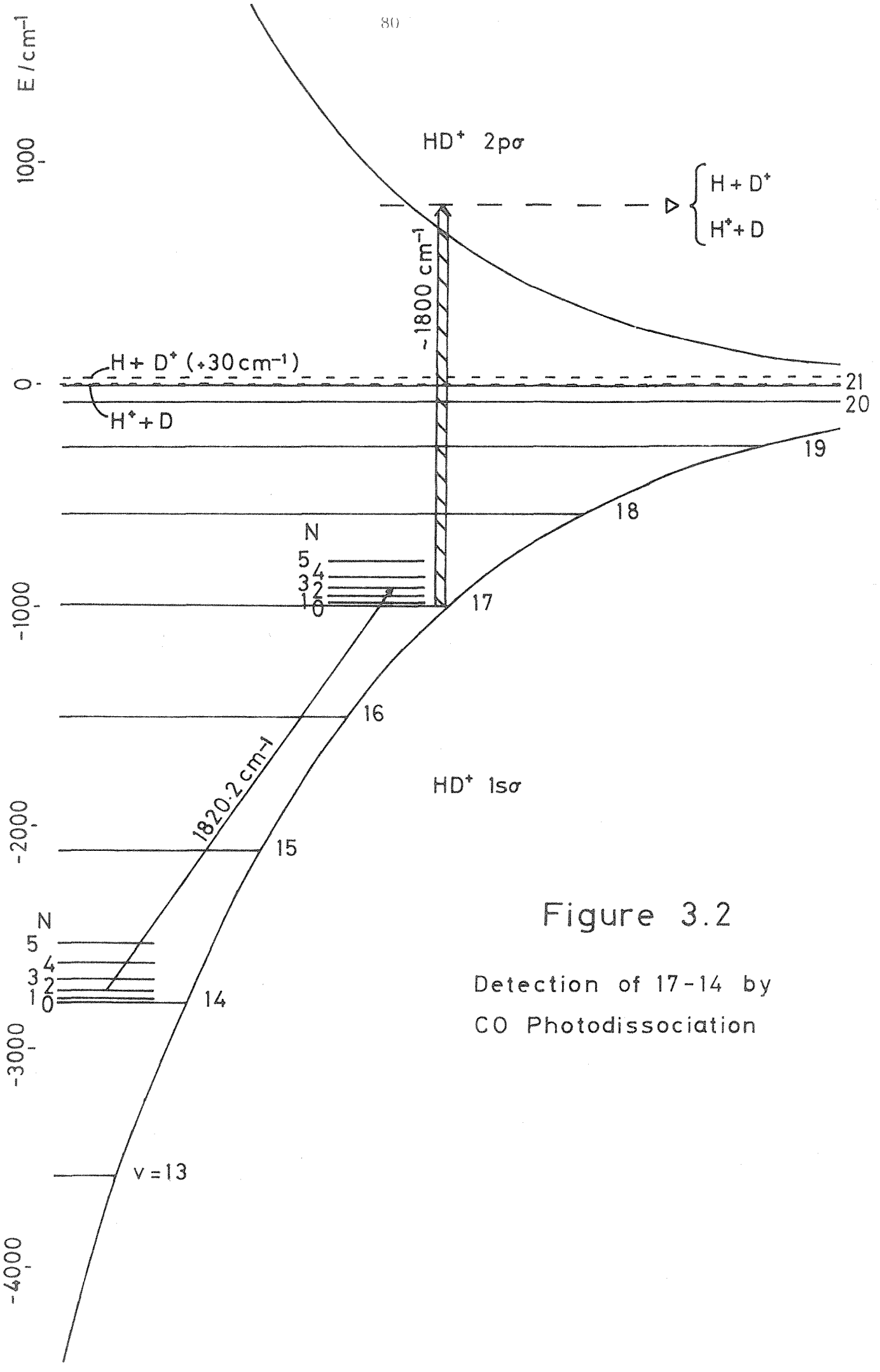

Figure 3.2

Detection of 17-14 by CO Photodissociation

TABLE 3.2

Experimental and Theoretical Wavenumbers for the v = 17 - 14 Band of HD^+

Transition v', N'	v'', N''	Laser line v' P(J'')	Laser wavenumber/ cm^{-1}	Alignment	Beam Potential (V_A-V_D)/ Volts	Experimental wavenumber/ cm^{-1}	Final wavenumber/ cm^{-1}	Theoretical wavenumber/ cm^{-1}	Experiment -Theory/ cm^{-1}
17,1	14,0	10 P(23)	1817.7213	P	6416.0	1813.853			
		11 P(17)	1817.5846	P	5972.0	1813.852			
		11 P(19)	1809.4181	A	8472.0	1813.853	1813.853	1813.852	0.001
17,2	14,1	10 P(22)	1821.9837	P	1341.5	1820.210			
		11 P(16)	1821.6192	P	846.0	1820.210			
		10 P(23)	1817.7213	A	2642.5	1820.208			
		11 P(17)	1817.5846	A	2943.0	1820.209	1820.209	1820.201	0.008
17,3	14,2	10 P(22)	1821.9837	P	1354.5	1820.201			
		11 P(16)	1821.6192	P	856.5	1820.202			
		10 P(23)	1817.7213	A	2623.5	1820.199			
		11 P(17)	1817.5846	A	2923.0	1820.200	1820.201	1820.187	0.014
17,4	14,3	10 P(23)	1817.7213	P	7128.5	1813.644			
		11 P(17)	1817.5846	P	6652.0	1813.646			
		11 P(19)	1809.4181	A	7694.0	1813.644	1813.645	1813.627	0.018
17,5	14,4	11 P(20)	1805.2866	P	10560.5	1800.359			
		12 P(14)	1804.3338	P	6873.5	1800.359			
		11 P(22)	1796.9274	A	5145.0	1800.359			
		12 P(16)	1796.4327	A	6733.5	1800.358	1800.359	1800.333	0.026
17,6	14,5	12 P(19)	1784.3369	P	7819.0	1780.145	1780.145	1780.115*	0.030*
17,0	14,1	12 P(19)	1784.3369	P	1087.0	1782.773	1782.773	1782.776	-0.003

P denotes parallel alignment of the laser and ion beams, A antiparallel.

* Theoretical wavenumbers are derived from the energy levels calculated by Wolniewicz and Poll [48], extrapolated to (17,6) using B, D and H given in table 3.3.

from the laser wavenumber value and the observed beam potential, according to (2.29), (2.34) and (2.13) or (2.14). The internal consistency of our results is satisfactory, and we believe our final transition wavenumbers are accurate to ±0.001 cm^{-1}. Figure 3.3 shows recordings of the two strongest transitions (17,2) - (14,1) and (17,3) - (14,2), using two different CO laser lines. The figure provides a dramatic illustration of the spectroscopic consequences of kinematic compression of the velocity distribution.

HD^+ has a $^2\Sigma^+$ electronic ground state. A normally characteristic feature of the term values for a $^2\Sigma$ state is the spin-rotation doubling of the rotational levels [124]. The hydrogen molecular ion is unusual, the spin-rotation coupling has been investigated theoretically [9, 10] and shown to be very weak. In analysing the transition wavenumbers we have obtained it can be neglected. The vibration-rotation term values are then given by:

$$E(v, N) = E(v, 0) + B_v N(N + 1) - D_v N^2(N + 1)^2 + H_v N^3(N + 1)^3 + \ldots\ldots \qquad (3.2)$$

where B_v, D_v and H_v are the usual rotational and centrifugal distortion constants. The observed transitions must obey the electric dipole selection rule on the rotational quantum number N, for a $\Sigma - \Sigma$ transition this is $\Delta N = N' - N'' = \pm 1$; the double prime denotes the lower level, single prime the upper. We then obtain the standard $^1\Sigma$ expression for the vibration-rotation transition wavenumbers [124]:

$$\nu = \nu_0 + (B_{17} + B_{14})m + (B_{17} - B_{14} - D_{17} + D_{14})m^2 - (2D_{17} + 2D_{14} - H_{17} - H_{14})m^3 - (D_{17} - D_{14} - 3H_{17} + 3H_{14})m^4 + (3H_{17} + 3H_{14})m^5 + (H_{17} - H_{14})m^6 \qquad (3.3)$$

where $m = N'' + 1$ for the R branch ($\Delta N = +1$), $m = -N''$ for the P branch ($\Delta N = -1$), and $\nu_0 = E(17, 0) - E(14, 0)$ is the vibrational energy separation between v = 17 and 14. Our seven observed transition wavenumbers were fitted to this expression, with H_{17} and H_{14} constrained

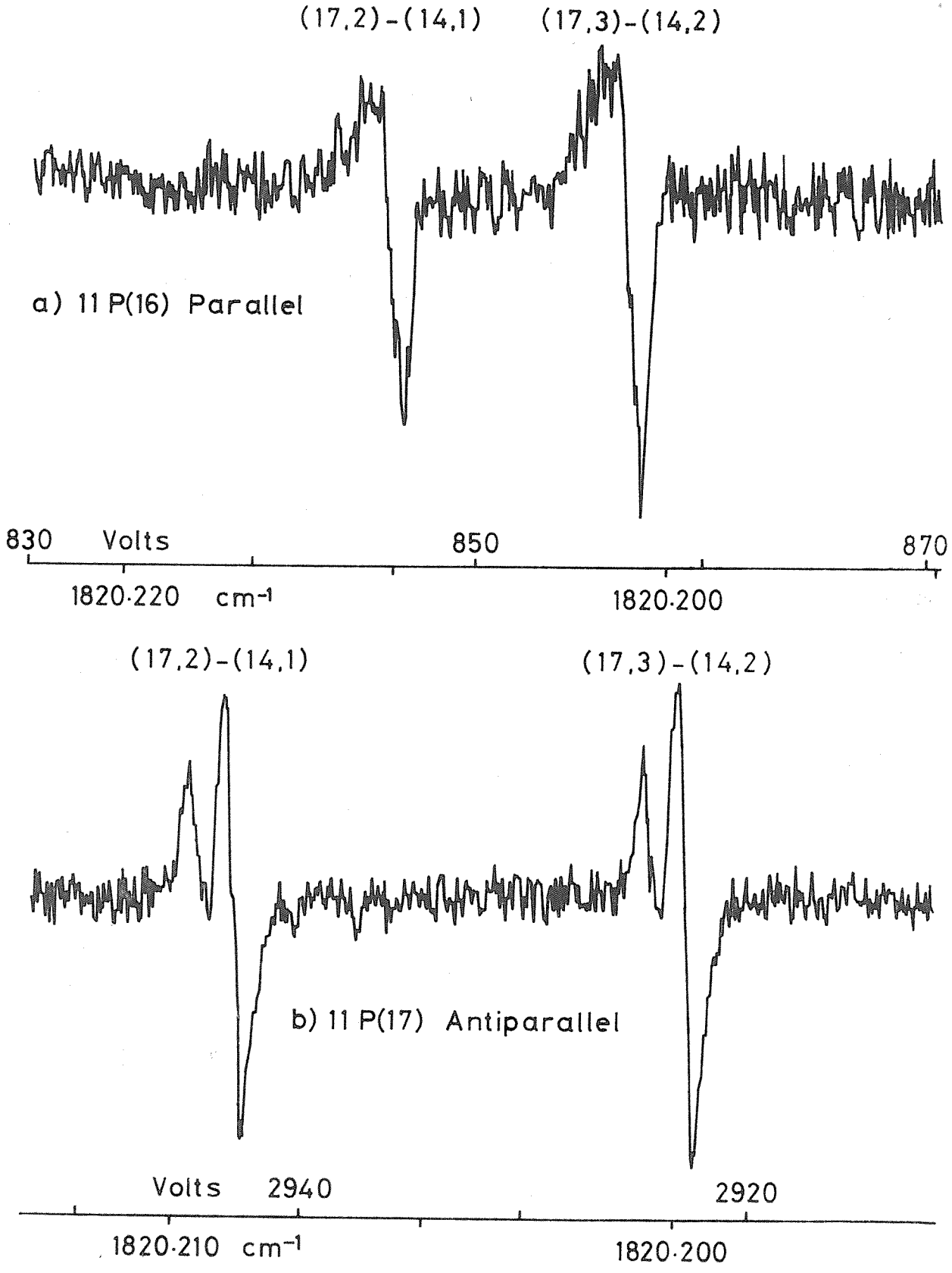

Figure 3.3

Recordings of (17,2)-(14,1) and (17,3)-(14,2) of HD^+

Note the effects of kinematic compression.

to be zero. The results of this fit appear in table 3.3, together with values for B_v, D_v and H_v obtained by fitting the calculated energy levels [48] to (3.2). Our assignment of the transitions (17,3) - (14,2) and (17,2) - (14,1) is based mainly on the fact that it leads to the best fit. Also, the larger population difference on the (17,3) - (14,2) transition compared to (17,2) - (14,1), see table 3.1, leads us to expect, see figure 2.2, that the former transition should be slightly stronger, in accord with the experimental recordings (figure 3.3). The experimental molecular constants given in table 3.3 reproduce the observed transition wavenumbers to within the estimated experimental error of ±0.001 cm^{-1}.

Doublet splittings of about 20 MHz were observed for all the transitions, see figure 3.3, the splitting increasing slightly with increasing N along the R branch. This splitting is due to the proton Fermi contact interaction, as discussed in the next section. The relatively low power available from the CO laser ensured that this small splitting was not obscured by power broadening.

3.4 Hyperfine Interactions.

The hyperfine splittings observed in the infrared spectrum of HD^+ can be interpreted in terms of the following effective nuclear hyperfine and spin-rotation Hamiltonian:

$$\mathcal{H} = b_1 \underset{\sim}{I}_1 \cdot \underset{\sim}{S} + b_2 \underset{\sim}{I}_2 \cdot \underset{\sim}{S} + c_1 I_{1z} S_z + c_2 I_{2z} S_z + \gamma \underset{\sim}{S} \cdot \underset{\sim}{N} \qquad (3.4)$$

$\underset{\sim}{I}_1$ and $\underset{\sim}{I}_2$ are the nuclear spins of the proton and deuteron respectively, $\underset{\sim}{S}$ is the electron spin, and z is along the internuclear vector $\underset{\sim}{R}$. A derivation of this Hamiltonian from the Dirac equation for the electron has been presented [125]. The hyperfine parameters appearing in (3.4) are averages over the nuclear radial wavefunction $F_{vN}(R)$ of the electronic matrix elements:

Table 3.3

Molecular Constants (in cm^{-1}) for v = 14 and 17 of HD^+

	E(17,0) - E(14,0)	B_{14}	$D_{14} \times 10^3$	$H_{14} \times 10^6$	B_{17}	$D_{17} \times 10^3$	$H_{17} \times 10^6$
Experiment	1801.316	9.2860	7.22	0.0	6.2835	7.37	0.0
	±0.002	±0.0008	±0.13	-	±0.0006	±0.09	-
Theory	1801.316	9.28441	7.259	3.65	6.28192	7.426	2.10
		±0.00012	±0.010	±0.23	±0.00014	±0.012	±0.26

Experimental values are from a least squares analysis of the data in table 3.2. Theoretical values are from a least squares analysis of the energy levels given by Wolniewicz and Poll [48].

Error limits are one standard deviation.

$$b_1(R) = g_e\, g_H\, \mu_B\, \mu_N \left\langle \frac{8\pi}{3}\, \delta(\underset{\sim}{r}_1) + \frac{x_1^2 - z_1^2}{r_1^5} \right\rangle \qquad (3.5)$$

$$c_1(R) = -3\, g_e\, g_H\, \mu_B\, \mu_N \left\langle \frac{x_1^2 - z_1^2}{r_1^5} \right\rangle \qquad (3.6)$$

where the fundamental constants g_e, g_H, μ_B and μ_N [105] have their usual meanings. r_1 is the distance from the proton to the electron. If it is assumed that the electronic wavefunction is symmetrical about the geometric centre of the nuclei, the hyperfine constants for the deuteron will be given by:

$$b_2 = \frac{g_D}{g_H}\, b_1 \text{ and } c_2 = \frac{g_D}{g_H}\, c_1 \; ; \; \frac{g_D}{g_H} = 0.15351 \qquad (3.7)$$

This is expected to be an excellent approximation, except for vibrational levels very close to the dissociation limit, where the electron must start to follow the deuteron. The first term in the expression (3.5) for b represents the Fermi contact interaction, $\delta(\underset{\sim}{r})$ is the Dirac delta function,

$$\langle \delta(\underset{\sim}{r}_1) \rangle = |\psi_e(R;\, 0_1)|^2 \qquad (3.8)$$

The other contribution and the parameter c arise from the dipolar interaction between the nuclear and electron magnetic moments. Frosch and Foley [126] give the electronic matrix elements in terms of a slightly different co-ordinate system, describing the position of the electron by means of the angle χ_1 between $\underset{\sim}{r}_1$ and $\underset{\sim}{R}$. Careful consideration of the evaluation of the electronic matrix element, in particular averaging over the azimuthal co-ordinate, shows that:

$$\left\langle \frac{x_1^2 - z_1^2}{r_1^5} \right\rangle = -\frac{1}{2} \left\langle \frac{3\cos^2\chi_1 - 1}{r_1^3} \right\rangle \qquad (3.9)$$

Note that because we have averaged the Dirac equation over the electronic wavefunction, the effective Hamiltonian (3.4) neglects hyperfine couplings between different electronic states. Electric quadrupole terms for the deuteron have also been neglected.

The electron spin-nuclear rotation interaction, described by the

term $\gamma \underset{\sim}{S} \cdot \underset{\sim}{N}$ in (3.4), has two sources. A direct, magnetic interaction between the electron spin and the nuclear rotation, which gives a contribution to γ of:

$$\gamma'(R) = 4\, g_e\, \mu_B\, \mu_N \left(\frac{\mu_{H_2^+}}{\mu_{HD^+}}\right) \left\langle \frac{z_1^2}{R r_1^3} \right\rangle \qquad (3.10)$$

where μ_{HD^+} is the reduced nuclear mass of HD^+:

$$\mu_{HD^+} = \frac{m_{H^+} \cdot m_{D^+}}{m_{H^+} + m_{D^+}} \qquad (3.11)$$

Rotation of the HD^+ molecule mixes states of Π symmetry into the ground Σ state. This mixing causes small, nonadiabatic shifts of the vibration-rotation energy levels, and introduces a second order contribution to the spin-rotation splitting. It has been shown [125] that this contribution to γ can be represented by:

$$\gamma''(R) = \frac{-g_e}{R^2\, \mu_{HD^+}} \sum_n{}' \frac{\langle \psi_0 | a' L_x - 2b' p_y | \psi_n \rangle \langle \psi_n | L_x | \psi_0 \rangle}{E_0 - E_n} \qquad (3.12)$$

$$\text{where } a' = 2\mu_B^2 \left(\frac{1}{r_1^3} + \frac{1}{r_2^3}\right) \text{ and } b' = \frac{\mu_B^2 R}{r_1^3} \qquad (3.13)$$

For most molecules the dominant contribution to γ is γ'', but for the hydrogen molecular ion $\gamma' > \gamma''$, and the spin-rotation coupling is very weak.

A tabulation of all the above electronic matrix elements has been published for H_2^+ [10], together with vibrational averages for $v = 0 - 8$, $N = 0 - 2$; $v = 8$ is predicted [127] to be about 7220 cm^{-1} below the dissociation limit for H_2^+. Unfortunately the tabulated values do not extend to sufficiently large R to permit averages over the radial nuclear wavefunctions to be calculated for the high vibrational levels of HD^+ we have studied. However we can still use the H_2^+ vibrational averages to make reasonable guesses at the parameters for $v = 14$ and 17 of HD^+. The parameters for H_2^+ all decrease with increasing v, tending towards the separated nuclei limits of $c = 0$, $\gamma = 0$ and $b \simeq \frac{1420}{2} = 710$ MHz (the electron is equally shared

by the two protons); at v = 8 with N = 0 the values are c = 71.9 MHz, γ = 24.2 MHz and b = 752.3 MHz. For HD^+ we accordingly choose (values in MHz):

$$\left.\begin{aligned} b_1 &= 741.0,\ c_1 = 15.0,\ \gamma = 8.0 \\ b_2 &= 113.8,\ c_2 = 2.3\ (\text{using } g_D/g_H) \end{aligned}\right\} \quad \text{for } v = 14$$

and:

$$\left.\begin{aligned} b_1 &= 725.0,\ c_1 = 9.0,\ \gamma = 4.0 \\ b_2 &= 111.3,\ c_2 = 1.4\ (\text{using } g_D/g_H) \end{aligned}\right\} \quad \text{for } v = 17$$

It is immediately obvious that the dominant terms in (3.4) are b_1 $\underset{\sim}{I}_1 \cdot \underset{\sim}{S}$ and b_2 $\underset{\sim}{I}_2 \cdot \underset{\sim}{S}$, which couple the electron spin to the two nuclear spins. An appropriate angular momentum coupling scheme is then the following:

$$\begin{array}{llllll} \underset{\sim}{S} + \underset{\sim}{I}_1 = \underset{\sim}{G}_1 & & G_1 = & 1 & & 0 \\ \underset{\sim}{G}_1 + \underset{\sim}{I}_2 = \underset{\sim}{G}_2 & G_2 = & 2 & 1 & 0 & 1 \\ \underset{\sim}{G}_2 + \underset{\sim}{N} = \underset{\sim}{F} & F = & N+2, \ldots, & N+1,\ N, & N & N+1,\ N, \\ & & |N-2| & |N-1| & & |N-1| \end{array} \qquad (3.14)$$

Before proceeding to set up a representation of the Hamiltonian (3.4) in this coupling scheme, it is convenient to express it in terms of a slightly different set of parameters. Defining a dipolar matrix element:

$$t_1(R) = -g_e\ g_H\ \mu_B\ \mu_N \left\langle \frac{x_1^2 - z_1^2}{r_1^5} \right\rangle \qquad (3.15)$$

we have:

$$b_1 = b_{1F} - t_1 \text{ and } c_1 = 3t_1, \qquad (3.16)$$

where b_{1F} is the Fermi contact term:

$$b_{1F}(R) = g_e\, g_H\, \mu_B\, \mu_N \left\langle \frac{8\pi}{3} \quad \delta(\underset{\sim}{r}_1) \right\rangle \tag{3.17}$$

The effective Hamiltonian (3.4) is then written as:

$$H = b_{1F}\, \underset{\sim}{I}_1 \cdot \underset{\sim}{S} + t_1\, (2I_{1z}\, S_z - I_{1x}\, S_x - I_{1y}\, S_y) + b_{2F}\, \underset{\sim}{I}_2 \cdot \underset{\sim}{S} + t_2\, (2I_{2z}\, S_z - I_{2x}\, S_x - I_{2y}\, S_y) + \gamma\, \underset{\sim}{S} \cdot \underset{\sim}{N} \tag{3.18}$$

The angular momentum algebra involved in obtaining the matrix elements of this Hamiltonian can readily be performed using standard methods [128]. The results have previously been given by Roberts [129], but his expressions contain a few minor errors. All the matrix elements of H are diagonal in the quantum numbers F and M_F. The representation is also diagonal in N, if we neglect dipolar interactions between basis functions differing in N. This is a reasonable assumption for HD^+, the rotational spacings are large and the dipolar coupling, described by the parameters t, is very weak. Denoting the basis functions by $|G_1 G_2 F\rangle$, the representation of H obtained for a particular N is:

F = N + 2 block

	$\lvert 12F\rangle$
$\lvert 12F\rangle$	$\frac{b_{1F}}{4} + \frac{b_{2F}}{2} + \frac{\gamma N}{2}$ $- \frac{t_1 N}{2(2N+3)} - \frac{t_2 N}{(2N+3)}$

(3.19)

F = N + 1 block

	|12F⟩	|11F⟩	|01F⟩
|12F⟩	$\frac{b_{1F}}{4} + \frac{b_{2F}}{2} + \frac{\gamma}{4}(N-2)$ $\frac{+t_1(N+6)}{4(2N+3)} \quad \frac{+t_2(N+6)}{2(2N+3)}$	$\frac{-\gamma[N(N+2)]^{\frac{1}{2}}}{4}$ $\frac{+3t_1[N(N+2)]^{\frac{1}{2}}}{4(2N+3)}$	$\frac{-\gamma[N(N+2)]^{\frac{1}{2}}}{2\sqrt{2}}$ $\frac{+3t_2[N(N+2)]^{\frac{1}{2}}}{2\sqrt{2}\ (2N+3)}$
|11F⟩		$\frac{b_{1F}}{4} - \frac{b_{2F}}{2} + \frac{\gamma N}{4}$ $\frac{+t_1N}{4(2N+3)} - \frac{t_2N}{2(2N+3)}$	$\frac{-b_{2F}}{\sqrt{2}} - \frac{\gamma N}{2\sqrt{2}}$ $- \frac{t_2N}{2\sqrt{2}(2N+3)}$
|01F⟩			$\frac{-3b_{1F}}{4}$

(3.20)

F = N block.

	|12F⟩	|11F⟩	|10F⟩	|01F⟩
|12F⟩	$\frac{b_{1F}}{4} + \frac{b_{2F}}{2} - \frac{3\gamma}{4}$ $\frac{+t_1(2N-3)(2N+5)}{4(2N-1)(2N+3)}$ $\frac{+t_2(2N-3)(2N+5)}{2(2N-1)(2N+3)}$	$\frac{-\gamma[(2N-1)(2N+3)]^{\frac{1}{2}}}{4\sqrt{3}}$ $- \frac{3\sqrt{3}t_1}{4[(2N-1)(2N+3)]^{\frac{1}{2}}}$	$\frac{-t_1}{\sqrt{2}}\left[\frac{N(N+1)}{(2N-1)(2N+3)}\right]^{\frac{1}{2}}$ $\frac{+t_2}{\sqrt{2}}\left[\frac{N(N+1)}{(2N-1)(2N+3)}\right]^{\frac{1}{2}}$	$\frac{-\gamma[(2N-1)(2N+3)]^{\frac{1}{2}}}{2\sqrt{6}}$ $- \frac{3\sqrt{3}t_2}{2\sqrt{2}[(2N-1)(2N+3)]^{\frac{1}{2}}}$
|11F⟩		$\frac{b_{1F}}{4} - \frac{b_{2F}}{2} - \frac{\gamma}{4} - \frac{t_1}{4}$ $\frac{+t_2}{2}$	$\frac{-\gamma[N(N+1)]^{\frac{1}{2}}}{\sqrt{6}}$	$\frac{-b_{2F}}{\sqrt{2}} + \frac{\gamma}{2\sqrt{2}} + \frac{t_2}{2\sqrt{2}}$
|10F⟩			$\frac{b_{1F}}{4} - b_{2F}$	$\frac{\gamma[N(N+1)]^{\frac{1}{2}}}{2\sqrt{3}}$
|01F⟩				$\frac{-3b_{1F}}{4}$

(3.21)

F = N - 1 block.

	$\|12F\rangle$	$\|11F\rangle$	$\|01F\rangle$
$\|12F\rangle$	$\frac{b_{1F}}{4} + \frac{b_{2F}}{2} - \frac{\gamma(N+3)}{4}$ $\frac{+t_1(N-5)}{4(2N-1)} + \frac{t_2(N-5)}{2(2N-1)}$	$\frac{-\gamma[(N-1)(N+1)]^{\frac{1}{2}}}{4}$ $\frac{-3t_1[(N-1)(N+1)]^{\frac{1}{2}}}{4(2N-1)}$	$\frac{-\gamma[(N-1)(N+1)]^{\frac{1}{2}}}{2\sqrt{2}}$ $\frac{-3t_2[(N-1)(N+1)]^{\frac{1}{2}}}{2\sqrt{2}(2N-1)}$
$\|11F\rangle$		$\frac{b_{1F}}{4} - \frac{b_{2F}}{2} - \frac{\gamma(N+1)}{4}$ $\frac{+t_1(N+1)}{4(2N-1)} \quad \frac{-t_2(N+1)}{2(2N-1)}$	$\frac{-b_{2F}}{\sqrt{2}} + \frac{\gamma(N+1)}{2\sqrt{2}}$ $\frac{-t_2(N+1)}{2\sqrt{2}(2N-1)}$
$\|01F\rangle$			$\frac{-3b_{1F}}{4}$

(3.22)

F = N - 2 block.

	$\|12F\rangle$
$\|12F\rangle$	$\frac{b_{1F}}{4} + \frac{b_{2F}}{2} - \frac{\gamma(N+1)}{2}$ $\frac{-t_1(N+1)}{2(2N-1)} - \frac{t_2(N+1)}{(2N-1)}$

(3.23)

The minimum value of F that can be constructed from $\underset{\sim}{G}_2$ and $\underset{\sim}{N}$ is given by:

$$F = |N - G_2| \tag{3.24}$$

so that for N = 1, the basis function $|12N-1\rangle$ is missing from the F = N - 1 block, and $|12N-2\rangle$ is also forbidden. The only surviving basis functions for N = 0 are $|12N+2\rangle$, $|11N+1\rangle$, $|01N+1\rangle$ and $|10N\rangle$.

A computer program has been written to set up the above matrices, and diagonalise them to obtain the hyperfine energy levels of HD^+. The results for (14,2) are shown in figure 3.4, using b_{1F} = 746.0 MHz (b_{2F} = 114.50 MHz), t_1 = 5.00 MHz (t_2 = 0.77 MHz) and γ = 8.0 MHz. The b_{1F} and t parameters are calculated from the estimates given earlier for b_1 and c_1:

$$t_1 = \frac{c_1}{3} \text{ and } b_{1F} = b_1 + t_1 \qquad (3.25)$$

The effects of the different terms in the effective Hamiltonian on the hyperfine energy levels are clearly evident in figure 3.4. As the mixing of the basis functions is small, we label the eigenstates obtained by diagonalisation according to the dominant basis function $|G_1G_2F\rangle$.

The relative probabilities of the electric dipole allowed transitions between the various hyperfine components of the lower and upper levels can also be calculated with the aid of angular momentum theory. The matrix elements of the electric dipole transition operator:

$$H_L = \underset{\sim}{\mu}\cdot\underset{\sim}{E} \qquad (3.26)$$

have been derived in the $|G_1G_2F\rangle$ basis. $\underset{\sim}{E}$ is the electric vector of the laser, which we take to be along the space fixed z axis, and $\underset{\sim}{\mu}$ is the dipole moment operator. For transitions within the ground state of HD^+ the only nonzero component of $\underset{\sim}{\mu}$ is along the internuclear axis. The following selection rules on the angular momentum quantum numbers are found:

$$\Delta M_F = 0;\ \Delta F = 0(F\neq 0), \pm 1;\ \Delta N = \pm 1;\ \Delta G_2 = 0;\ \Delta G_1 = 0 \qquad (3.27)$$

The full matrix of H_L, summed over M_F, for an R branch transition (ΔN = +1) is given in table 3.4. We have suppressed the dependence on the transition dipole moment $\mu_{v'v''}$, and on the magnitude of $\underset{\sim}{E}$, as they do not affect the relative intensities. The P branch matrix is obtained by replacing N by N - 1, and then transposing the matrix.

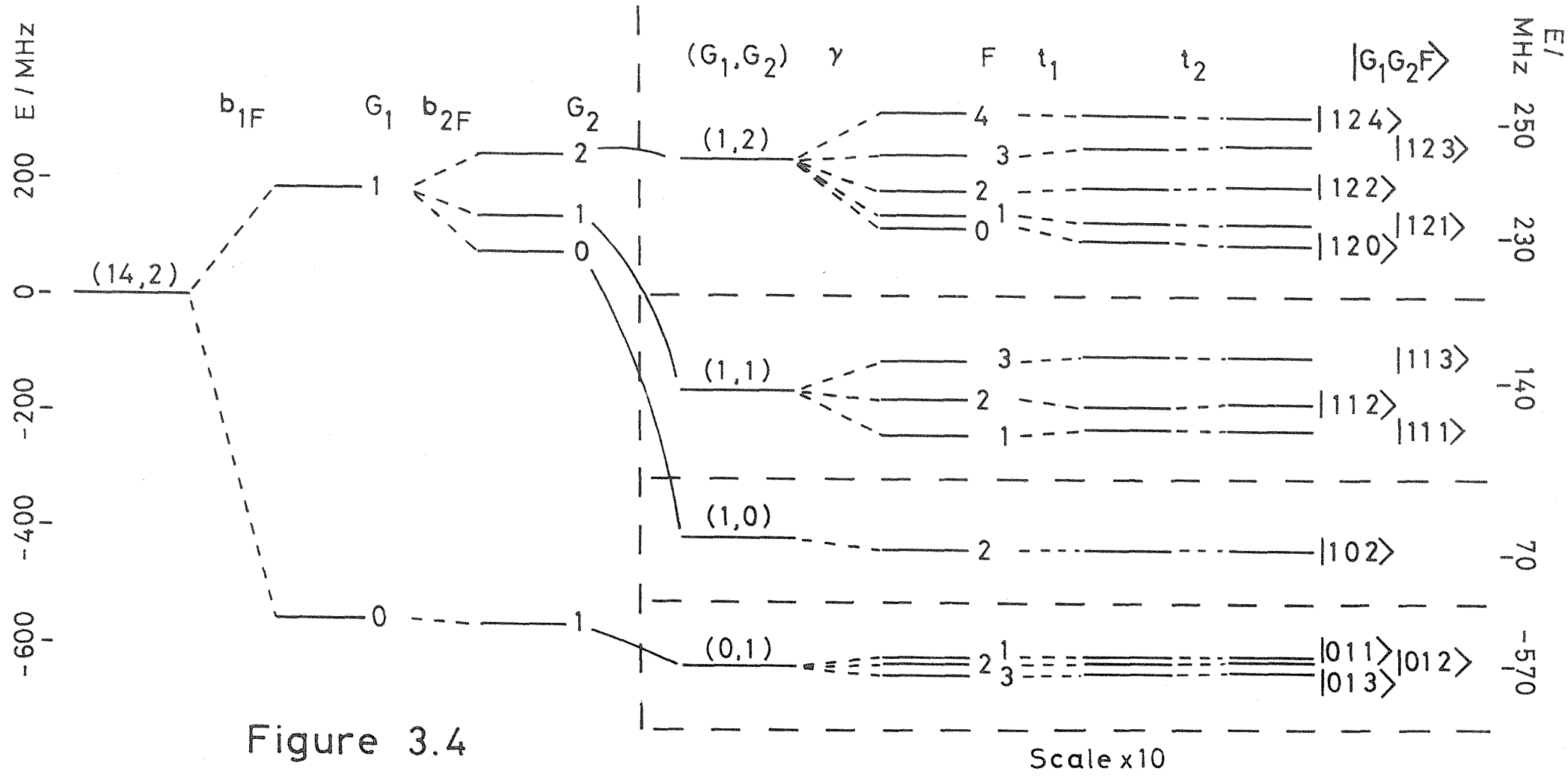

Figure 3.4

Hyperfine Interactions for (14,2)

Upper State

Lower State F		N+3	N+2			N+1				N			N-1
		$\|12N+3\rangle$	$\|12N+2\rangle$	$\|11N+2\rangle$	$\|01N+2\rangle$	$\|12N+1\rangle$	$\|11N+1\rangle$	$\|10N+1\rangle$	$\|01N+1\rangle$	$\|12N\rangle$	$\|11N\rangle$	$\|10N\rangle$	$\|12N-1\rangle$
N+2	$\|12N+2\rangle$	$\left[\frac{(2N+7)(N+1)}{(2N+3)}\right]^{\frac{1}{2}}$	$\left[\frac{2(2N+5)}{(N+2)(2N+3)}\right]^{\frac{1}{2}}$	0	0	$-\left[\frac{6}{(N+2)(2N+1)(2N+3)}\right]^{\frac{1}{2}}$	0	0	0	0	0	0	0
N+1	$\|12N+1\rangle$	0	$\left[\frac{(2N+5)(N+3)N}{(N+2)(2N+3)}\right]^{\frac{1}{2}}$	0	0	$\left[\frac{3N(2N+5)}{(N+1)(N+2)(2N+1)}\right]^{\frac{1}{2}}$	0	0	0	$-\left[\frac{9}{(N+1)(2N+1)(2N+3)}\right]^{\frac{1}{2}}$	0	0	0
	$\|11N+1\rangle$	0	0	$\left[\frac{(2N+5)(N+1)}{(2N+3)}\right]^{\frac{1}{2}}$	0	0	$\left[\frac{1}{(N+1)}\right]^{\frac{1}{2}}$	0	0	0	$-\left[\frac{1}{(N+1)(2N+1)(2N+3)}\right]^{\frac{1}{2}}$	0	0
	$\|01N+1\rangle$	0	0	0	$\left[\frac{(2N+5)(N+1)}{(2N+3)}\right]^{\frac{1}{2}}$	0	0	0	$\left[\frac{1}{(N+1)}\right]^{\frac{1}{2}}$	0	0	$-\left[\frac{1}{(N+1)(2N+1)(2N+3)}\right]^{\frac{1}{2}}$	0
N	$\|12N\rangle$	0	0	0	0	$\left[\frac{(N+2)(2N+5)(2N-1)N}{(N+1)(2N+1)(2N+3)}\right]^{\frac{1}{2}}$	0	0	0	$\left[\frac{3(N+2)(2N-1)}{N(N+1)(2N+3)}\right]^{\frac{1}{2}}$	0	0	$-\left[\frac{6}{N(2N+1)(2N+3)}\right]^{\frac{1}{2}}$
	$\|11N\rangle$	0	0	0	0	0	$\left[\frac{N(N+2)}{(N+1)}\right]^{\frac{1}{2}}$	0	0	0	$\left[\frac{1}{(N+1)}\right]^{\frac{1}{2}}$	0	0
	$\|10N\rangle$	0	0	0	0	0	0	$[(N+1)]^{\frac{1}{2}}$	0	0	0	0	0
	$\|01N\rangle$	0	0	0	0	0	0	0	$\left[\frac{N(N+2)}{(N+1)}\right]^{\frac{1}{2}}$	0	0	$\left[\frac{1}{(N+1)}\right]^{\frac{1}{2}}$	0
N-1	$\|12N-1\rangle$	0	0	0	0	0	0	0	0	$\left[\frac{(N+2)(N-1)(2N-1)}{N(2N+1)}\right]^{\frac{1}{2}}$	0	0	$\left[\frac{2(2N-1)}{N(2N+1)}\right]^{\frac{1}{2}}$
	$\|11N-1\rangle$	0	0	0	0	0	0	0	0	0	$\left[\frac{(N+1)(2N-1)}{(2N+1)}\right]^{\frac{1}{2}}$	0	0
	$\|01N-1\rangle$	0	0	0	0	0	0	0	0	0	0	$\left[\frac{(N+1)(2N-1)}{(2N+1)}\right]^{\frac{1}{2}}$	0
N-2	$\|12N-2\rangle$	0	0	0	0	0	0	0	0	0	0	0	$\left[\frac{(2N-3)(N+1)}{(2N+1)}\right]^{\frac{1}{2}}$

TABLE 3.4

MATRIX ELEMENTS OF H_L

The relative probabilities of the transitions between the hyperfine eigenstates are given by the squares of the elements of the matrix:

$$\underline{\underline{V}}_l^T \; \underline{\underline{H}}_L \; \underline{\underline{V}}_u \qquad (3.28)$$

where $\underline{\underline{V}}_u$ is the columnwise matrix of the coefficients of the basis functions for the upper level eigenstates, and $\underline{\underline{V}}_l^T$ is the transpose of the corresponding matrix for the lower level.

The calculated relative line positions and probabilities for (17,3) - (14,2) are shown in figure 3.5. To obtain a lineshape for comparison with the experimental data, we convolute each of these lines with a Gaussian of 5.5 MHz full width at half maximum, and then calculate the effect of square wave frequency modulation with an amplitude of 13 MHz. These values were chosen to closely correspond to the experimental conditions of figure 3.3(b). The theoretical calculation successfully reproduces the observed lineshape. After convolution we see that there are essentially two partially resolved peaks, the stronger peak is due to the $G_1 = 1$ eigenstates, the weaker peak at slightly higher frequency to $G_1 = 0$. Their integrated relative intensities are in the ratio 3:1, matching the ratio of the total populations in the $G_1 = 1$ to $G_1 = 0$ states, so that the same intensity pattern is expected if the transitions are saturated. The separation between the two peaks is largely determined by the difference in the proton Fermi contact parameter b_{1F} between the lower and upper vibration-rotation levels. The proportionately reduced difference in the deuteron parameter b_{2F} causes the $G_1 = 1$ peak to be noticeably broader than the $G_1 = 0$ peak. The dipolar terms and the small spin-rotation coupling cause further broadening of both peaks.

In view of the complexity of the predicted pattern of lines, very greatly increased experimental resolution will be required to separate the individual transitions. Although we cannot extract values for the ten hyperfine parameters, our results do confirm the theoretical guesses made earlier. The proton Fermi contact interaction is dominant, and b_{1F} for $v = 17$ is slightly smaller than for $v = 14$. The deuteron Fermi contact term is much smaller than for the proton, probably

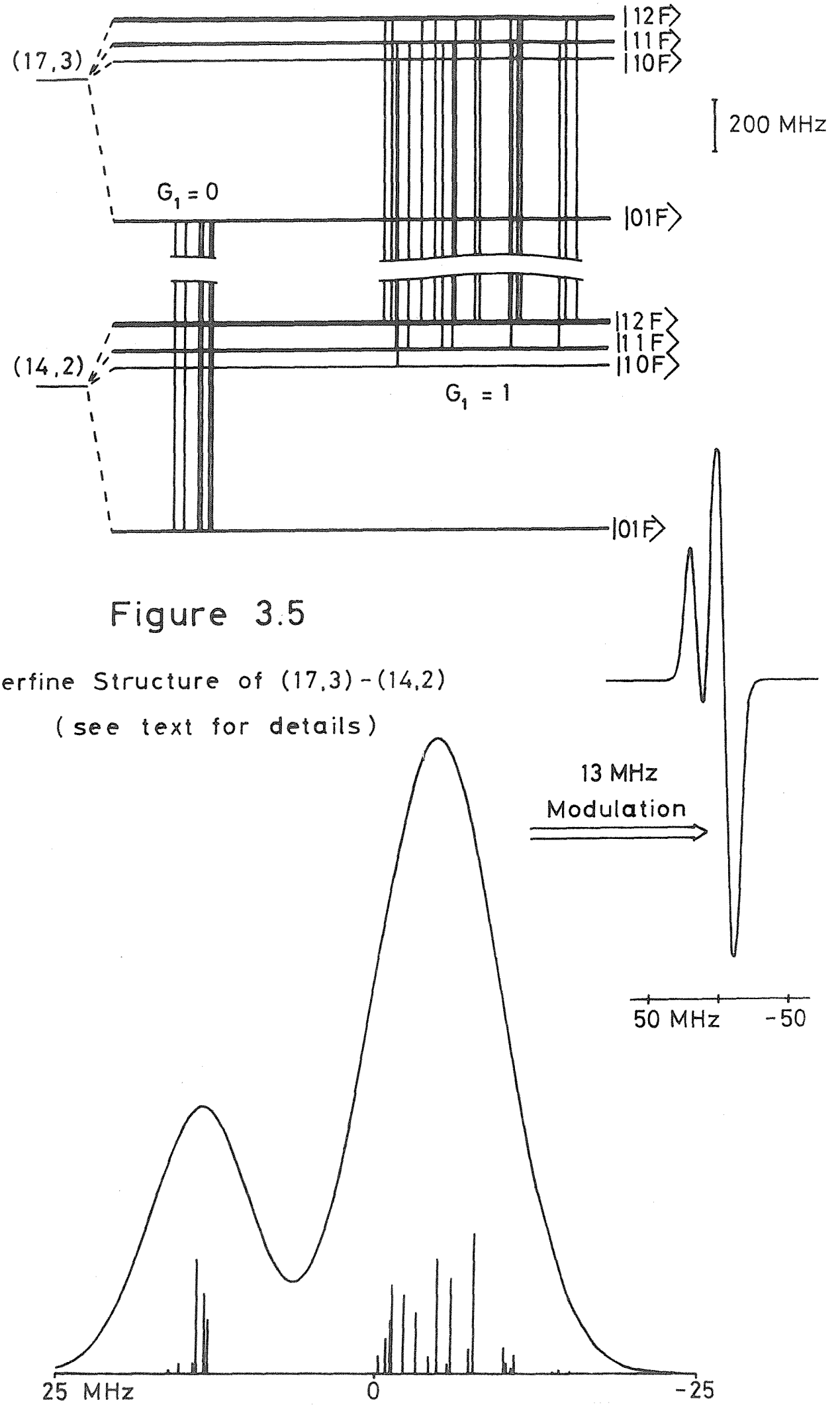

Figure 3.5

Hyperfine Structure of (17,3) - (14,2)

(see text for details)

satisfying $(b_{2F}/b_{1F}) = 0.15351$, which would indicate a symmetrical electronic distribution over the two nuclei. The weakness of the spin-rotation and dipolar interactions is also substantiated. The calculated proton Fermi contact parameters for H_2^+ [10] and HD^+ [9] decrease with N, approximately as:

$$b_{1F}(v, N) = b_{1F}(v, 0) - b_{1FD}(v)\, N(N + 1) \qquad (3.29)$$

so that the b_{1F} difference for an R branch transition will increase with N":

$$b_{1F}(v'', N'') - b_{1F}(v', N'' + 1) = b_{1F}(v'', 0) - b_{1F}(v', 0) + [b_{1FD}(v'') + b_{1FD}(v')]\,(N'' + 1) + [b_{1FD}(v') - b_{1FD}(v'')]\,(N'' + 1)^2 \qquad (3.30)$$

This will cause a small increase in the splitting between the $G_1 = 1$ and $G_1 = 0$ peaks as N" increases along the R branch, providing a plausible explanation for the observed increase.

The observation of transitions for which formally $\Delta G_1 \neq 0$ and/or $\Delta G_2 \neq 0$ would allow considerably more information on the hyperfine interactions to be extracted. Unfortunately our calculations predict these transitions to have probabilities of less than 10^{-3}, compared to the central transitions we have observed. These transitions gain their intensity through the mixing of the basis functions by coupling of the spins to the internuclear axis, via the spin-rotation and dipolar interactions, which are very weak for the hydrogen molecular ion. The use of greatly increased laser powers, obtained by pulsed operation, might permit their observation, but they could then be masked by the much stronger $\Delta G_1 = 0$, $\Delta G_2 = 0$ transitions, which are known to be easily power broadened [53].

3.5 Discussion and Conclusions.

Our experimentally measured transition frequencies show significant deviations, of up to 0.03 cm^{-1}, from the best available

theoretical predictions, those of Wolniewicz and Poll [48]. The discrepancies increase with increasing rotational quantum number. The results of the fits, presented in table 3.3, show that, while the vibrational energy separation between v = 17 and 14 has been successfully predicted, there are differences between the rotational constants determined experimentally and those derived from the theoretical calculations. This strongly suggests that the effects of rotation of the nuclear framework have not been adequately accounted for in the calculations of the energy levels. Indeed Wolniewicz and Poll state that their calculations of the nonadiabatic energy corrections neglect the effects of vibration-rotation interactions (centrifugal distortion). An alternative explanation is that the nonadiabatic shifts due to Π states, which are proportional to $N(N + 1)$, are slightly in error. Finally the possibility of inaccuracies in the adiabatic calculations, which are the starting point of Wolniewicz and Poll's treatment, must not be excluded. The earlier results on the v = 18 - 16 band [53] showed the same type of discrepancy from the theoretical predictions. Until the cause of these differences can be definitely identified, and then removed, questions must remain as to our ability to completely describe the simplest possible molecule.

The technique of sequential two photon photodissociation has so far been used to observe nine transitions in the v = 18 - 16 band, seven in the 17 - 14 band, and also one line in the 17 - 15 band of HD^+. We are confident that many more transitions of HD^+ can be detected. We particularly hope to measure transitions in the v = 20 - 17 and 21 - 17 bands; v = 21 is predicted [48] to be the highest bound vibrational level of the ground state of HD^+. The intention is to monitor the population in v = 17 using a CO laser, as in the experiments reported above, while vibration-rotation transitions in the 20 - 17 and 21 - 17 bands are Doppler tuned into resonance with a CO_2 laser. The probabilities of photodissociation from v = 20 and 21 by CO and CO_2 lasers are expected to be small. The nonadiabatic calculations of Wolniewicz and Poll [48] predict the origins of the 20 - 17 and 21 - 17 bands to be at 913.483 cm^{-1} and 1004.156 cm^{-1}, respectively. However, we believe that these estimates may be considerably in error, because of the very strong mixing between the ground and

first excited states of HD^+, that occurs near the dissociation limit. It appears to be likely that their second order perturbation treatment of the nonadiabatic energy corrections will underestimate the effects of this coupling for the highest vibrational levels, see chapter six. The mixing of the two states will have a dramatic effect on the hyperfine structure. It causes the electron to localise about the deuteron in the ground electronic state, so that $b_{1F}(R) \to 0$ and $b_{2F}(R) \to 218$ MHz as the dissociation limit ($R \to \infty$), $H^+ + D$, is approached. We thus aim to directly observe the effects of nonadiabatic coupling on the electronic structure of HD^+, and further test the adequacy of Wolniewicz and Poll's treatment of this fundamental molecule.

Many other experiments can be contemplated, using the very high powers available from pulsed CO_2 lasers it might be possible to pump two or more photon vibration-rotation transitions in HD^+. Higher frequency lasers would allow us to monitor the populations in lower vibrational levels, and considerably extend the spectroscopic data on HD^+. Although H_2^+ and D_2^+ do not have an electric dipole moment, they do have an electric quadrupole moment, and the use of very high laser powers might permit the observation of electric quadrupole transitions in these ions [130, 131]. It should also be possible to find other molecular ions to which this sensitive technique can be applied, $^3He^4He^+$ is an obvious candidate.

CHAPTER 4

BOUND TO QUASIBOUND VIBRATION-ROTATION SPECTRUM OF HeH^+ AND ITS ISOTOPES

4.1 Introduction.

We have two main objectives in our studies of the helium hydride ions, HeH^+ and its isotopic modifications. The first is to test the reliability of recent ab initio calculations of the $X\ ^1\Sigma^+$, ground state potential energy curve [52, 132, 133], and in particular the isotope dependent adiabatic corrections [52]. This is achieved by determining vibration-rotation transition frequencies, which are then compared with predictions using adiabatic potentials for the ions. The transitions we detect are from bound vibration-rotation states to quasibound states, which predissociate by tunnelling through the centrifugal potential barrier, associated with rotation of the nuclear framework (see figure 2.3(a)). The second objective is to study this process of rotational predissociation. Ion beam experiments allow one to obtain an unprecedented amount of information about quasibound states. We can determine, with high precision, not only the frequencies of transitions to predissociated states, but also the predissociation lifetimes, from linewidths. The energies of quasibound states above the dissociation limit can be estimated by recording fragment ion kinetic energy distributions. This wealth of data may then be compared with theoretical predictions, testing current methods for calculating the positions and widths of quasibound states [134].

HeH^+ is the simplest closed shell heteronuclear molecule. Like H_2^+, the simplest molecule, it has been subjected to intense theoretical scrutiny [135], but only recently has this been complemented by high resolution spectroscopic data [33, 49, 55, 56]. The experimental problems are similar to those encountered in spectroscopic

studies of H_2^+. In discharges the ion is destroyed by the exothermic reaction:

$$HeH^+ + H_2 \rightarrow He + H_3^+ \qquad (4.1)$$

which can be suppressed by using only a trace of hydrogen. Nine transitions in the fundamental band of HeH^+ have been detected in absorption from a discharge using a difference frequency laser [33]. Electronic spectroscopy does not appear to be feasible, since the first excited electronic states ($A^1\Sigma^+$, $a^3\Sigma^+$) are only weakly bound, and lie about 100 000 cm^{-1} above the ground state [132]. The ground state dissociates to ^4He (1^1S) + H^+, while the excited states correlate with $^4He^+$ (1^2S) + H (1^2S), these limits are separated by 88632 cm^{-1}.

Several experimental studies of HeH^+ ions have been made using ion beams; the collision free environment eliminates the destruction of HeH^+ by ion-molecule reactions. The kinetic energies and momenta of H^+ fragment ions from five relatively long lived rotationally quasi-bound states of $^4HeH^+$ have been measured by translational spectroscopy [136, 137]. These experiments give the positions of the quasibound states with respect to the dissociation limit, together with rough estimates of the lifetimes of the states. The isotopic modifications $^4HeD^+$, $^3HeH^+$ and $^3HeD^+$ have also been studied by translational spectroscopy [138]. Five P branch transitions in the v = 1 - 0 and 2 - 1 bands of $^4HeH^+$ have been Doppler tuned into resonance with a CO laser, and detected by the charge exchange attenuation method [49]. Our approach has been to study vibration-rotation levels of $^4HeH^+$ [55], $^4HeD^+$, $^3HeH^+$ and $^3HeD^+$ [56] near the dissociation limit by infrared predissociation spectroscopy. This chapter reports the observation of two transitions in $^4HeH^+$, six in $^4HeD^+$, one in $^3HeH^+$ and two in $^3HeD^+$, Doppler tuned into resonance with a line tunable CO_2 laser. The results are compared with adiabatic calculations, performed by Dr. P. G. Fournier.

4.2 Experimental.

The most direct way of recording predissociation spectra is by

monitoring the production of photofragments as a function of frequency. This type of experiment can readily be performed for molecular ions, such as HeH^+, using the ion beam methods described in chapter two.

HeH^+ ions were formed in the electron impact source from a mixture of H_2 (or D_2) and ^4He (or ^3He); the composition of the mixture was not found to be critical. The ^3He was kindly provided by Dr. P. G. Fournier. The HeH^+ ions are believed to be formed by the reaction [139]:

$$He + H_2^+ \rightarrow HeH^+ + H \qquad (4.2)$$

which is known to produce internally excited ions. Bound to quasibound transitions of the mass selected ions were Doppler tuned into resonance with $^{12}CO_2$ or $^{13}CO_2$ line tunable lasers (coverage 875-1095 cm^{-1}). The transitions were detected by monitoring the flux of H^+ (or D^+) photofragments, selected by the ESA, as the beam potential was scanned:

$$HeH^+ + h\nu \rightarrow (HeH^+)^* \rightarrow He + H^+ + \Delta \qquad (4.3)$$

For each resonance, the kinetic energy distribution of the fragment ions from the predissociated state populated by the laser was also recorded, allowing Δ to be estimated.

There are a number of experimental constraints on the transitions which may be observed. The initial state must have a lifetime of longer than 5×10^{-6}s, so that it will still be populated when the HeH^+ ions reach the drift tube. All the transitions we have detected are from bound levels, so only their radiative lifetimes need be considered. Roberge and Dalgarno [140] have calculated radiative lifetimes for many of the vibration-rotation states of $^4HeH^+$, obtaining values in the range 4×10^{-4}s to 10^{-3}s. The behaviour of the isotopic modifications will be similar, and we can be confident that the initial states will not be significantly depleted before we probe the ions. For the upper, predissociated states we can define a lifetime window. If the parent HeH^+ ions are to predissociate before leaving the drift tube, the lifetime of the quasibound state must be shorter than 10^{-6}s, corresponding to a width of greater than 5×10^{-6} cm^{-1}. The maximum width of a

single scan is about 0.2 cm^{-1}, so that the linewidth must be less than 0.1 cm^{-1} for a reasonably complete recording to be made on a single scan. This gives a lower lifetime limit of 5×10^{-11}s. Transitions to states with much shorter lifetimes must be recorded pointwise, as described in chapter two.

4.3 Theory.

The theoretical calculations on the vibration-rotation energy levels of $^4HeH^+$, $^4HeD^+$, $^3HeH^+$ and $^3HeD^+$, from which we predicted transition frequencies and widths, were performed by Dr. P. G. Fournier.

Kołos and Peek [132, 133] have reported accurate ab initio calculations of the ground state energy of the HeH^+ ion within the Born-Oppenheimer approximation. The calculations used an 83 term variational wavefunction, expressed in elliptic co-ordinates, and energies were calculated at 36 internuclear separations, R (0.9 - 9.0 Bohrs). Subsequently Bishop and Cheung [52] repeated the calculations at 6 internuclear separations using a 255 term wavefunction, and obtained energies lower by up to about 5.5 cm^{-1} than those given by Kołos and Peek. They commented on the difficulties of achieving convergence in these calculations. Bishop and Cheung also calculated the adiabatic corrections to the Born-Oppenheimer potential:

$$-\hbar^2 \left[\frac{\langle (\nabla_{\sim 1} + \nabla_{\sim 2})^2 \rangle}{8\mu} + \frac{\langle \nabla^2_R \rangle}{2\mu} + \frac{\langle \nabla_R \cdot (\nabla_{\sim 1} + \nabla_{\sim 2}) \rangle}{2\mu_a} \right] \qquad (4.4)$$

where μ is the reduced nuclear mass:

$$\mu = \frac{m_{H^+}\, m_{He^{2+}}}{m_{H^+} + m_{He^{2+}}} \qquad (4.5)$$

$$\text{and } \mu_a = \frac{m_{H^+}\, m_{He^{2+}}}{m_{He^{2+}} - m_{H^+}} \qquad (4.6)$$

∇_i^2 is the Laplacian operator for electron i relative to the geometric centre of the nuclei, and ∇_R^2 is the Laplacian for one nucleus relative to the other. Some discussion of the adiabatic approximation can be

found in chapter six. Figure 4.1 shows the isotope independent Born-Oppenheimer potential, and also the total adiabatic correction (4.4) for each of the isotopic modifications of HeH^+. The corrections were evaluated from the electronic matrix elements $\langle(\underset{\sim}{\nabla}_1 + \underset{\sim}{\nabla}_2)^2\rangle$, $\langle\nabla_R{}^2\rangle$ and $\langle\underset{\sim}{\nabla}_R \cdot (\underset{\sim}{\nabla}_1 + \underset{\sim}{\nabla}_2)\rangle$ given by Bishop and Cheung, nuclear masses were taken from [105], except for $^3He^{2+}$, its mass was derived from the atomic mass. The total correction has been adjusted to zero at infinite internuclear separation.

The vibration-rotation levels were obtained by numerically solving the radial Schrödinger equation:

$$\left\{\frac{-\hbar^2}{2\mu}\nabla_R{}^2 + U^{AD}(R) + \frac{\hbar^2 J(J+1)}{2\mu R^2}\right\} F_{vJ}(R) = E_{vJ} F_{vJ}(R) \tag{4.7}$$

or

$$\left\{\frac{d^2}{dR^2} + \frac{2\mu}{\hbar^2}\left[E_{vJ} - U^{AD}(R)\right] - \frac{J(J+1)}{R^2}\right\} \chi_{vJ}(R) = 0 \tag{4.8}$$

where $\chi_{vJ}(R) = \frac{1}{R} F_{vJ}(R)$ (4.9)

is usually referred to as the radial wavefunction; v and J are the vibrational and rotational quantum numbers. The first step was to generate the adiabatic potential $U^{AD}(R)$ on a very fine grid of equally spaced R points over the range R_{min} to R_{max}. The limits of the grid are selected so that the energy levels E_{vJ} are insensitive to decreases in R_{min} and increases in R_{max}. Fournier paid particular attention to the interpolation and extrapolation methods used to generate $U^{AD}(R)$ on the required fine grid from the limited number of calculated points. The 6 Born-Oppenheimer energy improvements of Bishop and Cheung were interpolated by a cubic spline method, and added to the 36 points of Kołos and Peek yielding the best Born-Oppenheimer potential. The adiabatic corrections were also interpolated by a cubic spline, and added to the Born-Oppenheimer energies to produce an adiabatic potential defined at 36 points from 0.9 to 9.0 Bohrs. The final $U^{AD}(R)$ used for numerical solution of (4.8) was generated by 4 point Lagrangian

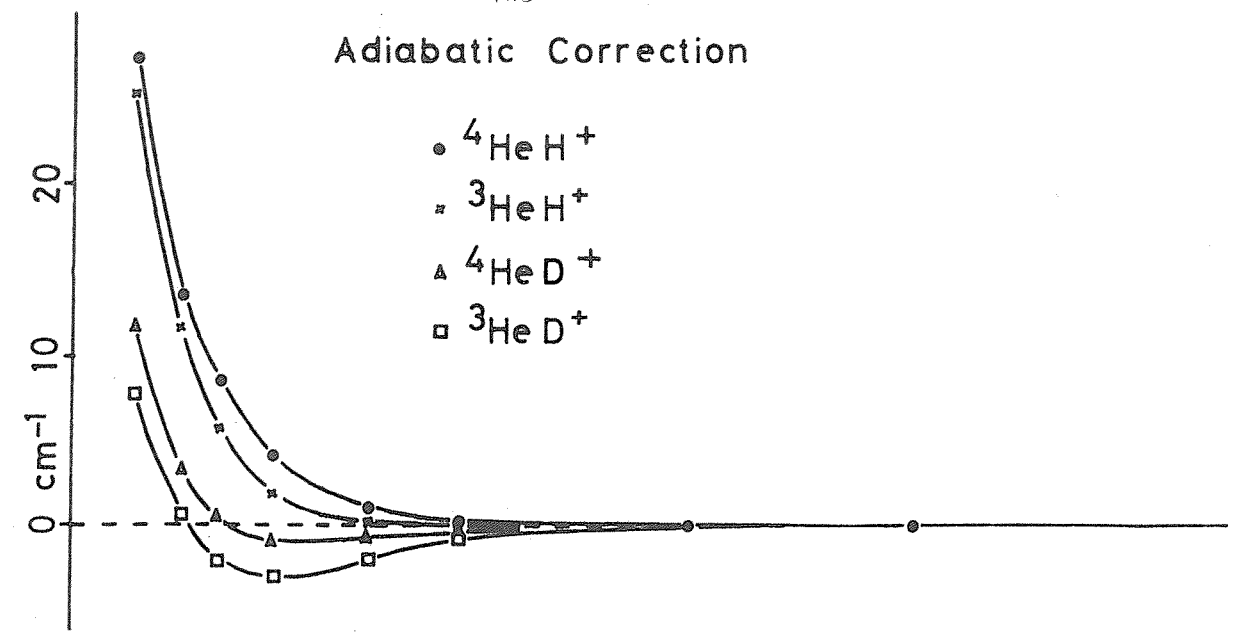
Adiabatic Correction
^{4}He H$^+$
^{3}He H$^+$
^{4}He D$^+$
^{3}He D$^+$
20
10
0 cm^{-1}

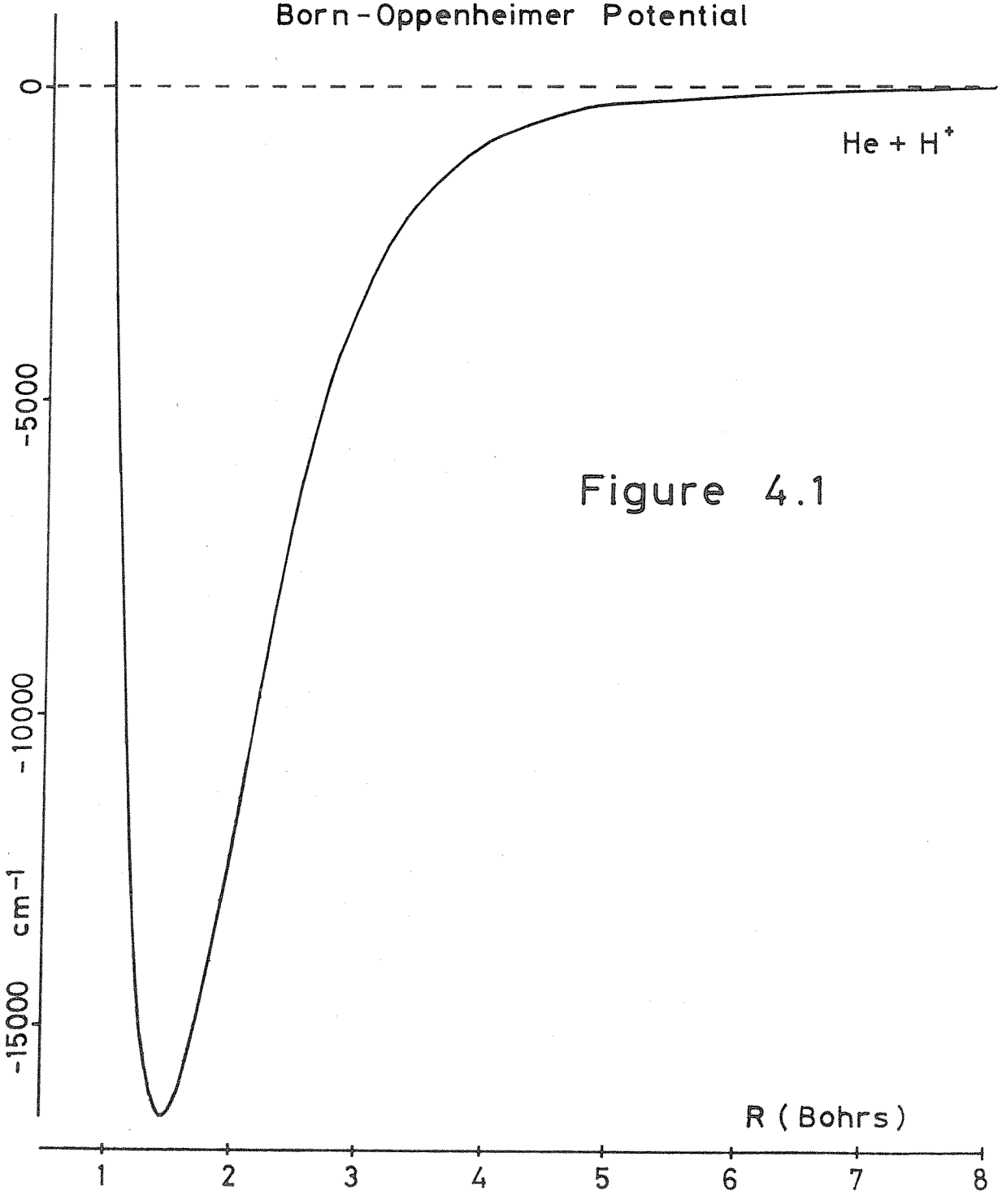
Born-Oppenheimer Potential
0
He + H$^+$
-5000
-10000
-15000 cm^{-1}
R (Bohrs)
1
2
3
4
5
6
7
8

Figure 4.1

interpolation of $R^2\ U^{AD}(R)$ over the range 0.9 to 9.0 Bohrs, extended below 0.9 Bohr by an exponentially repulsive form:

$$U^{AD}(R) = A \exp(-\beta R) + B \qquad (4.10)$$

and extrapolated beyond 9.0 Bohrs using:

$$U^{AD}(R) = C_6/R^6 - C_8/R^8 \qquad (4.11)$$

(Strictly the leading term at large R should be $-C_4/R^4$, charge-induced dipole). The energy levels derived from $U^{AD}(R)$ obtained in this way gave the best agreement with the available spectroscopic data on $^4HeH^+$ [33, 49, 55]. Calculations using potentials generated by other interpolation and extrapolation schemes produced energy levels typically differing by about 1 cm^{-1}, while the widths of quasibound states were changed by a few percent.

The equation (4.8) was solved for all the bound and quasibound levels of $^4HeH^+$, $^4HeD^+$, $^3HeH^+$ and $^3HeD^+$ using a program due to Le Roy [134, 141]. Solution for bound levels is straightforward, application of the two boundary conditions:

$$\chi_{vJ}(R) \to 0 \quad \text{as } R \to 0 \quad \text{and as } R \to \infty \qquad (4.12)$$

yields a one dimensional eigenvalue problem. The program uses the predictor-corrector algorithm due to Cooley [142], which rapidly converges to the eigenvalue nearest the initial guess at E_{vJ}. For the quasibound levels we still have:

$$\chi_{vJ}(R) \to 0 \quad \text{as } R \to 0 \qquad (4.13)$$

but an outer boundary condition cannot immediately be written down.

The quasibound levels lie above the dissociation limit, they are supported by the potential maximum due to the addition of the centrifugal term $\hbar^2 J(J+1)/2\mu R^2$ to the potential $U^{AD}(R)$. There are a number of quantum mechanical methods which define the energies and widths of

predissociated states, in terms of the behaviour of the radial wavefunction $\chi_{EJ}(R)$ as a function of the energy E above the dissociation limit. The $\chi_{EJ}(R)$ are obtained by outward integration, according to (4.8). Figure 4.2 shows $\chi_{EJ}(R)$ at energies just below, at and just above the energy E_{QB} of a quasibound state [143]. Two characteristics are immediately apparent, a much larger amplitude of $\chi_{EJ}(R)$ over the well region when $E = E_{QB}$, and a change in the phase by π at large R as the energy passes through E_{QB}. A third feature is that the collisional time delay function, the difference between the time required for an actual collision and that for a collision at the same energy if the interaction potential ($U^{AD}(R)$) is everywhere zero, passes through a maximum at $E = E_{QB}$. The energy widths, lifetimes of the quasibound states may be determined from the breadth of the energy range over which these characteristic features are observed to occur. One approach to the determination of the positions and widths of levels which predissociate by tunnelling is then to obtain $\chi_{EJ}(R)$ at a series of energies for a selected value of J, compute one or more of the properties mentioned above at each energy, and locate the quasibound levels from their energy dependent behaviour. The analogy to a spectroscopic search for a transition should be apparent. The method is tedious and computationally expensive, also very fine energy grids are required if narrow levels are to be found. It is thus not surprising that approximate outer boundary conditions have been sought, for the problem of locating the quasibound levels then reduces to a one dimensional eigenvalue problem. The outer boundary condition for a quasibound state employed in the Le Roy program is to require that the radial wavefunction satisfies:

$$\chi_{E_{QB}J}(R) \propto Bi[(c - R)F^{\frac{1}{3}}] \text{ for } R \simeq c \qquad (4.14)$$

where c is the third classical turning point (see figure 4.2),

$$F = \left| \frac{d}{dR} \left[\frac{2\mu}{\hbar^2} U^{AD}(R) + \frac{J\,(J+1)}{R^2} \right] \right|_{R = c} \qquad (4.15)$$

and Bi is an Airy function of the second kind [144]. The use of this Airy function boundary condition was suggested [145] by the excellent agreement it gave with quasibound energies determined by the exact

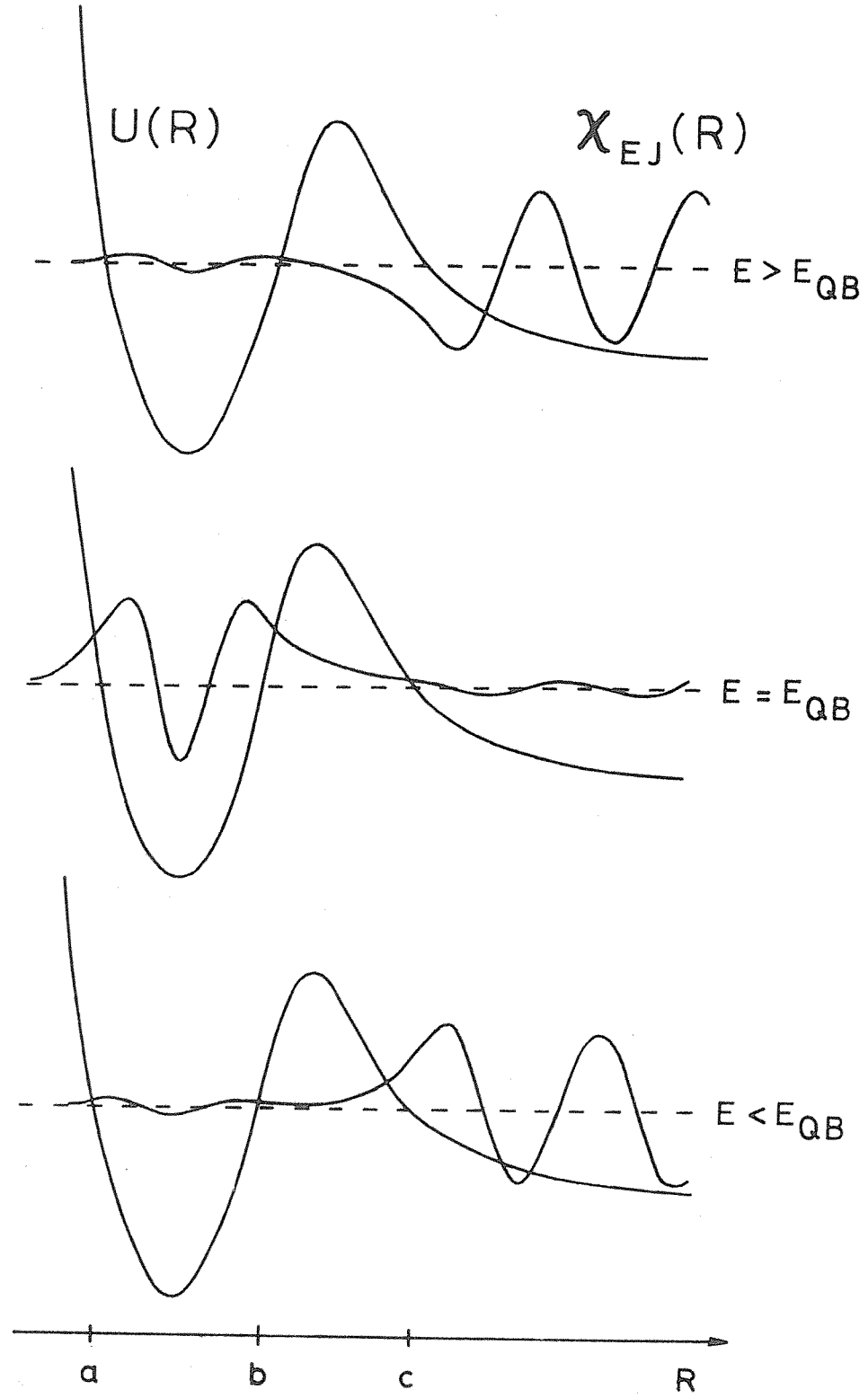

Figure 4.2

Predissociation by Tunnelling

methods outlined above. It has subsequently been justified by Le Roy and Liu [134] using semiclassical arguments, involving a consideration of how the radial wavefunction for a quasibound state over the well region ($a < R << c$) must connect with the continuum ($R >> b$) wavefunction beneath the potential maximum ($b << R << c$). The justification relies on the three classical turning points being well separated. The boundary condition (4.14) is not expected to give good results for predissociated states with energies close to the barrier maximum, for then $b \sim c$. Semiclassical methods [134, 146] are also used to estimate the widths of the quasibound states, so that the need to study the behaviour of $\chi_{EJ}(R)$ as a function of E is completely avoided.

Energy level calculations on the helium hydride ions have been performed by other authors. Dabrowski and Herzberg [147] have calculated the energy levels, and where appropriate the widths, for $^4HeH^+$ from the Born-Oppenheimer potential of Kołos and Peek. Using their improvements to this potential and their adiabatic corrections, Bishop and Cheung [52] have computed energies for the first few rotational levels in v = 0, 1 and 2 of $^4HeH^+$. Calculations on the quasibound levels of $^4HeH^+$ and $^3HeH^+$ have been reported by Kołos and Peek [133], similar calculations on all the isotopic modifications have been performed by Price [148], using approximate adiabatic potentials.

4.4 Results.

From the results of the adiabatic calculations described above, we predicted the positions of a number of transitions from bound to quasibound levels which would lie within the wavenumber range of our carbon dioxide lasers (875 - 1095 cm^{-1}). On the basis of these predictions we searched for those lines with widths in our experimental range (10^{-5} - 0.1 cm^{-1}). We have located one resonance in $^4HeH^+$, five in $^4HeD^+$, one in $^3HeH^+$ and two in $^3HeD^+$. We have also used the pointwise recording method to find two very broad resonances, one in $^4HeH^+$ and one (tentatively) in $^4HeD^+$. No attempt has yet been made to search for the other predicted wide transitions. As examples of the experimental spectra, we show in figure 4.3 recordings of (v = 7, J = 19) - (5, 20)

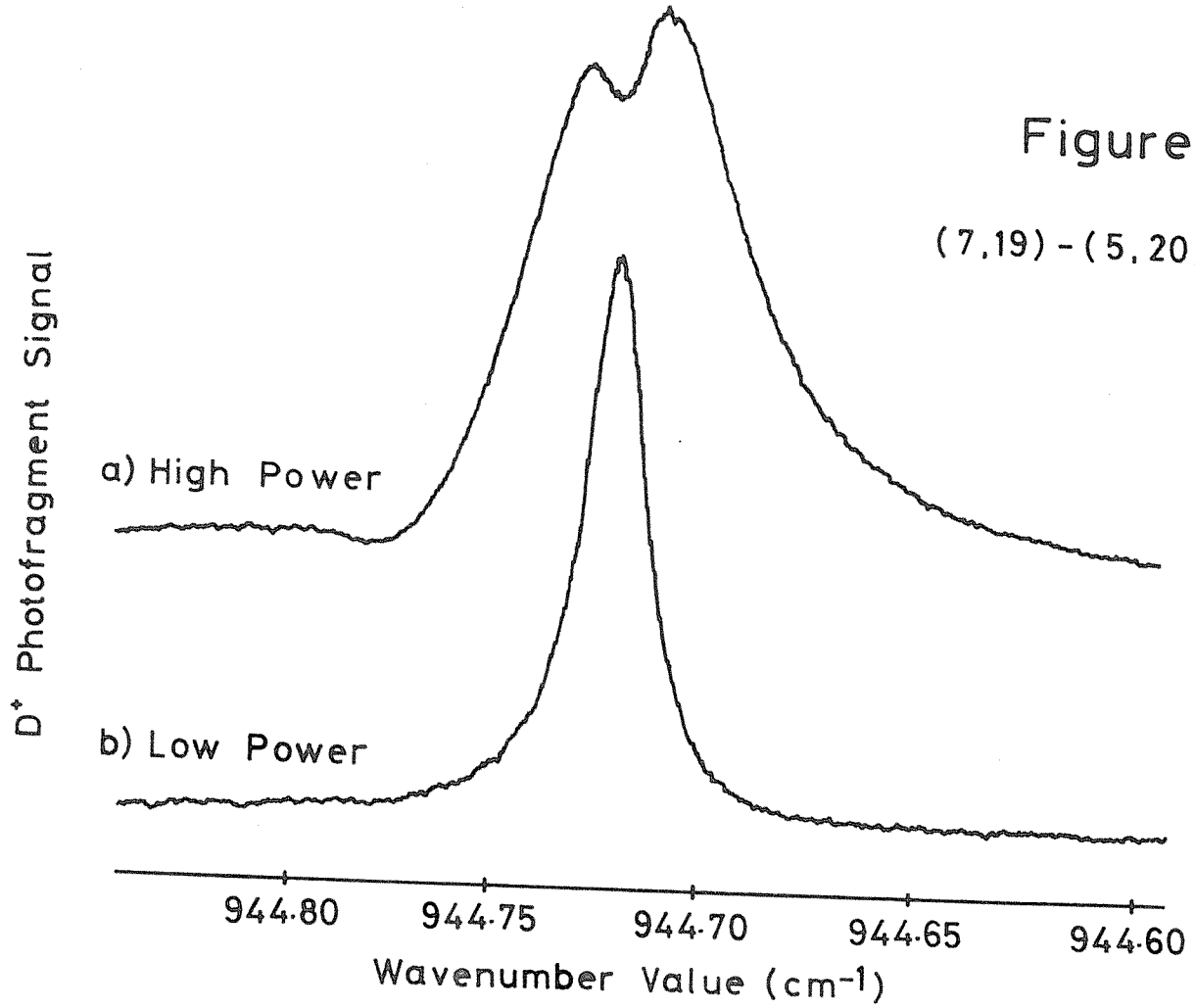

Figure 4.3

(7,19) - (5,20) of $^4HeD^+$

of $^4HeD^+$ at high and low laser powers, and in figure 4.4 (6, 19) - (5, 18) of $^3HeD^+$ at low laser power. The theoretical results and the experimental results are presented in tables 4.1 and 4.2. Table 4.1 contains all the available high resolution spectroscopic data on bound to bound transitions for $^4HeH^+$. Table 4.2 presents the results of our experiments. Transition wavenumbers were calculated from the laser wavenumbers [103] and the measured beam potentials ($V_A - V_D$) as described in chapter two. The beam potentials were corrected for earth field penetration into the source, using the factor of 0.9953 obtained from measurements on HD^+ [53]. Introduction of this correction changes the transition wavenumbers by about 0.003 cm^{-1}, which otherwise we believe are accurate to ±0.001 cm^{-1} for the sharp lines. The centres of the two very broad transitions recorded pointwise are less well determined, the tables contain estimates of the error limits.

Most of the sharp transitions could readily be saturated and showed considerable power broadening at high laser powers. Experimental predissociation linewidths (full width at half maximum) were obtained from spectra recorded with the minimum possible laser power. In a few cases it is conceivable that there was some residual power broadening. This is believed to be the explanation as to why (6, 21) - (5, 20) of $^4HeD^+$ is apparently broader than (6, 21) - (4, 22), although they have the same upper, predissociated state. The lowest power at which (6, 21) - (5, 20) was studied was about five times that used for (6, 21) - (4, 22). For the sharpest line observed, (6, 19) - (5, 18) of $^3HeD^+$, the residual Doppler width ($\sim 10^{-4}$ cm^{-1}), will make a significant contribution to the linewidth, in addition to any residual power broadening. We expect that for this transition the experimental linewidth will be considerably greater than the natural, predissociation linewidth.

The assignment of the transition at 911.705 cm^{-1} for $^4HeD^+$ to (13, 5) - (9, 6) rather than (12, 7) - (9, 6) is based on the fact that the measured width of this resonance was identical to that of (13, 5) - (9, 4), which has the same predissociated upper state. Using the differences between our experimental results and the theoretical predictions, we expect (12, 7) - (9, 6) to be at about 911.0 cm^{-1}. This is unfortunately just outside the limit of our experimental coverage

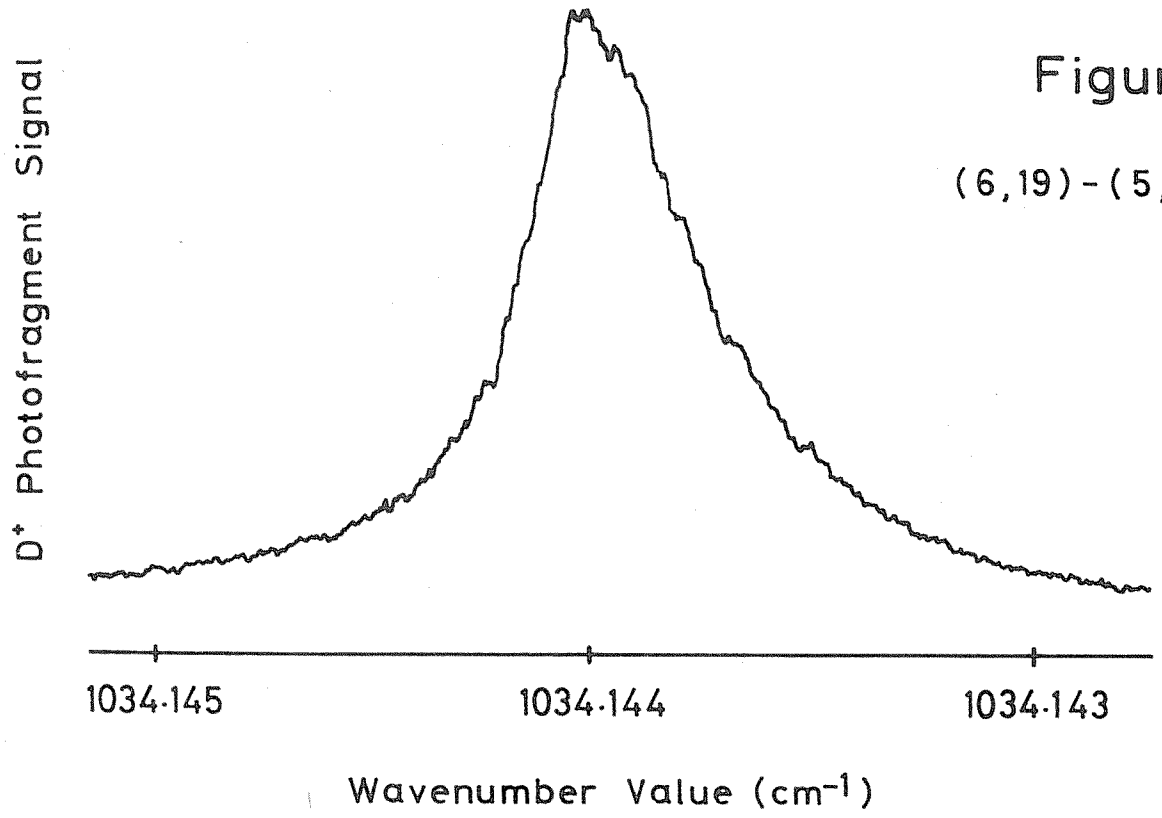

Figure 4.4

(6,19) - (5,18) of $^{3}HeD^{+}$

Table 4.1

High Resolution Spectroscopic Data for Bound to Bound Transitions of $^4HeH^+$

Transition v',J'	v",J"	Position (cm^{-1}) Experiment	Adiabatic Theory	Theory-Expt.
1,5	0,4	3157.2967[a]	3157.58	0.28
1,4	0,3	3121.0765[a]	3121.36	0.28
1,3	0,2	3077.9919[a]	3078.28	0.29
1,2	0,1	3028.3750[a]	3028.66	0.29
1,1	0,0	2972.5732[a]	2972.86	0.29
1,0	0,1	2843.9035[a]	2844.19	0.29
1,1	0,2	2771.8059[a]	2772.09	0.28
1,2	0,3	2695.0500[a]	2695.32	0.27
1,3	0,4	2614.0295[a]	2614.30	0.27
1,11	0,12	1855.905[b]	1856.12	0.22
1,12	0,13	1751.971[b]	1752.17	0.20
2,8	1,9	1896.992[b]	1897.10	0.11
2,9	1,10	1802.349[b]	1802.44	0.09
2,10	1,11	1705.543[b]	1705.62	0.08

a From ref. [33]

b From ref. [49]

TABLE 4.2

Experimental Observations and Theoretical Predictions of Bound to Rotationally Quasibound Vibration-Rotation Transitions in the Range 875-1095 cm^{-1} for $^4HeH^+$, $^4HeD^+$, $^3HeH^+$ and $^3HeD^+$.

Quasibound State v', J'	Bound State v'', J''	Laser Isot.	Laser Line/cm^{-1}	Laser Align.	Ion Beam Potential (V_A-V_D)/eV	Experiment Position/cm^{-1}	Experiment FWHM/cm^{-1}	Adiabatic Theory Position/cm^{-1}	Adiabatic Theory Theory-Expt./cm^{-1}	Adiabatic Theory Width/cm^{-1}
$^4HeH^+$										
6,13	5,12	12	978.4723	A	5037.0	979.904	0.103	980.16	0.26	0.109
7,11	5,12					938.2±0.3	4.1±0.3	938.04	-0.16	3.87
$^4HeD^+$										
7,19	5,20	12	945.9802	P	5000.0	944.720	1.8×10^{-2}	945.02	0.30	1.6×10^{-2}
6,21	5,20	13	1004.2799	P	2525.3	1003.329	1.0×10^{-3}	1003.53	0.20	0.43×10^{-3}
6,21	4,22	12	1086.8698	A	5375.7	1088.373	0.81×10^{-3}	1088.65	0.28	0.43×10^{-3}
13,5	9,4	12	1071.8838	A	6195.9	1073.475	2.7×10^{-2}	1074.19	0.71	8.6×10^{-2}
13,5	9,6	13	910.2779	A	6908.5	911.705	2.7×10^{-2}	912.37	0.67	8.6×10^{-2}
11,10	8,11					897.5±0.3	2.2±0.2	897.04	-0.46	2.3
12,7	9,6	outside available tuning range						911.57		5.3×10^{-4}
10,12	8,11							913.62		0.11
6,22	5,21							886.58		3.5
6,22	4,23							905.80		3.5
5,24	4,23	wide						1052.25		0.73
5,24	3,25							1030.96		0.73
4,27	3,26							1052.84		23.
$^3HeH^+$										
6,12	5,11	12	979.7054	A	5118.7	981.322	2.9×10^{-2}	981.46	0.14	3.2×10^{-2}
7,10	5,11	wide						953.48		2.7
$^3HeD^+$										
6,19	5,18	13	1036.0170	P	7707.6	1034.144	4.5×10^{-4}	1034.26	0.12	0.39×10^{-4}
7,17	5,18	13	996.9011	P	5235.7	995.415	0.56×10^{-2}	995.61	0.19	0.43×10^{-2}
8,14	6,15	predissociation lifetime too long						959.64		1.3×10^{-14}
6,20	5,19							915.12		2.4
6,20	4,21	wide						970.76		2.4
9,13	7,12							1061.77		5.8
4,25	2,26							1001.45		18.

in this region; we were able to scan down from 912.04 cm^{-1} only as far as 911.17 cm^{-1}. The (10, 12) - (8, 11) transition of $^4HeD^+$ is also predicted to lie in a gap of our frequency coverage, at the origin of the 00°1 - 10°0 band of $^{13}CO_2$. Table 4.2 contains one predicted transition, (8, 14) - (6, 15) of $^3HeD^+$, for which the predissociation lifetime of (8, 14) is about 400 s, much too long to allow detection by any predissociation method.

To give some indication of the sensitivity of this experiment, we note that when we recorded one of the strongest lines, (7, 19) - (5, 20) of $^4HeD^+$, the total $^4HeD^+$ beam flux was 12 x 10^9 ions/sec. The change in the D^+ fragment signal on resonance corresponded to 5 x 10^5 ions/sec when the transition was saturated. The fractional population of the bound state (5, 20) in the $^4HeD^+$ beam may thus be estimated to have been of the order of 4 x 10^{-5}. The exceptional sensitivity is due to the very high efficiency with which we are able to detect the D^+ fragment ions, and the fact that the background D^+ signal, due to unimolecular and collisional dissociation, and weak direct photodissociation, was more than an order of magnitude smaller than the photopredissociation signal.

We have also recorded the laboratory frame kinetic energy distributions of the fragment ions from each of the predissociated states found. An example is shown in figure 4.5 for D^+ ions from (7, 19) of $^4HeD^+$, populated by pumping the transition (7, 19) - (5, 20). The shape and width of the distribution are in accord with the predicted position of (7, 19) above the dissociation limit (259.17 cm^{-1}), as shown by the Monte Carlo simulation, performed by Dr. P. G. Fournier. Note in particular that a good estimate of the energy of the state is provided by the width of the distribution at half maximum. The resolution of our instrument is sufficient to allow us to determine the energy of a quasibound state with respect to the dissociation limit to about ten percent of this energy. Thus we can obtain, not only the relative energies of states, from transition wavenumbers, but also their absolute energies, from these kinetic energy experiments. For two of the transitions observed, (13, 5) - (9, 6) and (13, 5) - (9, 4) of $^4HeD^+$, the predissociated state (13, 5) lies extremely close to the

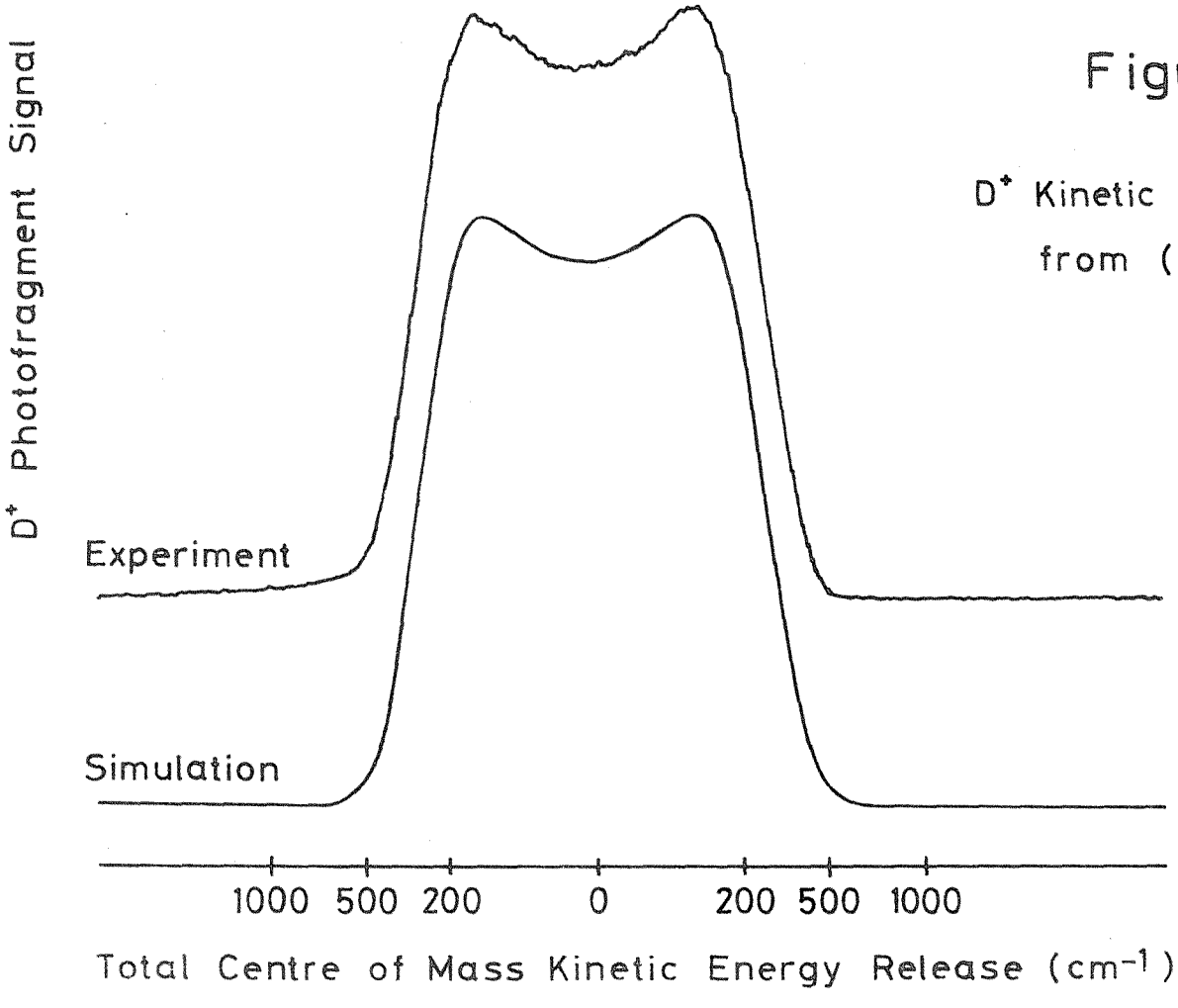

Figure 4.5

D^+ Kinetic Energy Spectrum from (7,19) of $^4He\,D^+$

dissociation limit. This allows us to determine the dissociation energies of the states involved in these transitions with considerable precision. Experimentally we have found that (13, 5) can be no more than 6 cm^{-1} above the dissociation limit; the theoretical value is 3.21 cm^{-1}. Using the measured transition wavenumbers for (13, 5) - (9, 4) and (13, 5) - (9, 6), we conclude that (9, 4) and (9, 6) are situated at 1070.5 (±3.0) cm^{-1} and 908.7 (±3.0) cm^{-1} respectively below the dissociation limit. For comparison the theoretical values are 1070.98 cm^{-1} for (9, 4) and 909.16 cm^{-1} for (9, 6).

4.5 Discussion.

Tables 4.1 and 4.2 reveal excellent agreement between the adiabatic predictions and the experimental results. For the transition wavenumbers the theoretical predictions are consistently higher than the experimental results, the differences being generally less than 0.3 cm^{-1}. Predicted energies with respect to the dissociation limit were found to lie well within the experimental error limits, as shown in the previous section. The comparison between the theoretical widths, and the experimentally measured full width at half maximum of the resonances is also very satisfying. The agreement for the linewidths of the sharper lines is poorer than for the broader lines, suggesting that these transitions may still be power broadened, even at the very low laser powers employed. The two transitions (13, 5) - (9, 4) and (13, 5) - (9, 6) of $^4HeD^+$ show a much larger discrepancy in their widths and wavenumbers from the theoretical predictions than for the other lines observed. This was not unexpected, since the predissociated state (13, 5) lies very close to the barrier maximum in the centrifugally adjusted potential for J = 5, a situation in which the semiclassical theory behind the calculations is no longer reliable [134].

The close agreement between experiment and theory for all the isotopic modifications confirms the accuracy of the isotope dependent adiabatic potentials, and justifies the methods used to calculate the positions and widths of the energy levels. To further test the adiabatic predictions more points on the potentials must be directly calculated

by ab initio methods, so that the uncertainties introduced by interpolation and extrapolation can be reduced. To obtain complete agreement between experiment and theory, it will be necessary to consider the small corrections due to nonadiabatic, radiative and relativistic effects. Calculations of the energy level shifts due to these effects for HD^+ [48] show that, for this ion, they typically change transition wavenumbers by 0.2 cm^{-1} from the adiabatic values. No estimates of the effects are yet available for the helium hydride ions, but our results are certainly of sufficient precision to test calculations of these corrections.

A number of the resonances showed an unusual lineshape at high laser power; an example is shown in figure 4.3(a). At first, as the power is increased, the line broadens as might be expected. However at higher powers a "hole" appears in the centre of the line profile. We have developed a very simple kinetic model which successfully accounts for the "hole", and leads to some other interesting conclusions. We describe the photopredissociation experiment by the coupled rate equations method outlined in section 2.2; k_{bX} is to be identified as the predissociation rate of state b. We consider the state (7, 19) of $^4HeD^+$, for which $k_{bX} = 3 \times 10^9\ s^{-1}$. In figure 4.6(a) we show the rate of production of D^+ fragment ions as a function of time, or equivalently distance from the intermediate slit (beam velocity = $4 \times 10^5\ ms^{-1}$), for $k_{ab} = 1 \times 10^6\ s^{-1}$ (moderate transition probability) and $k_{ab} = 5 \times 10^6\ s^{-1}$ (approaching saturation). The D^+ ions have a velocity of $1.4 \times 10^3\ ms^{-1}$ in the centre of mass frame. Since the ESA is set to collect fragment ions with a nominal Δ value of zero, we take this velocity to be along y, perpendicular to the ion beam. Fragment ions formed more than 28 cm away from the 2 mm wide intermediate slit will be stopped (2.54), and see figure 2.9. We only collect those D^+ ions which are formed within 28 cm of the intermediate slit; our recorded signals correspond to the shaded areas in figure 4.6(a). The dependence of the signal on k_{ab} is shown in figure 4.6(b). Initially the signal increases, but eventually it decreases as more of the ions are formed further from the slit. To investigate the effect of this dependence on the lineshape we take k_{ab} to have a Lorentzian dependence on the wavenumber value ν:

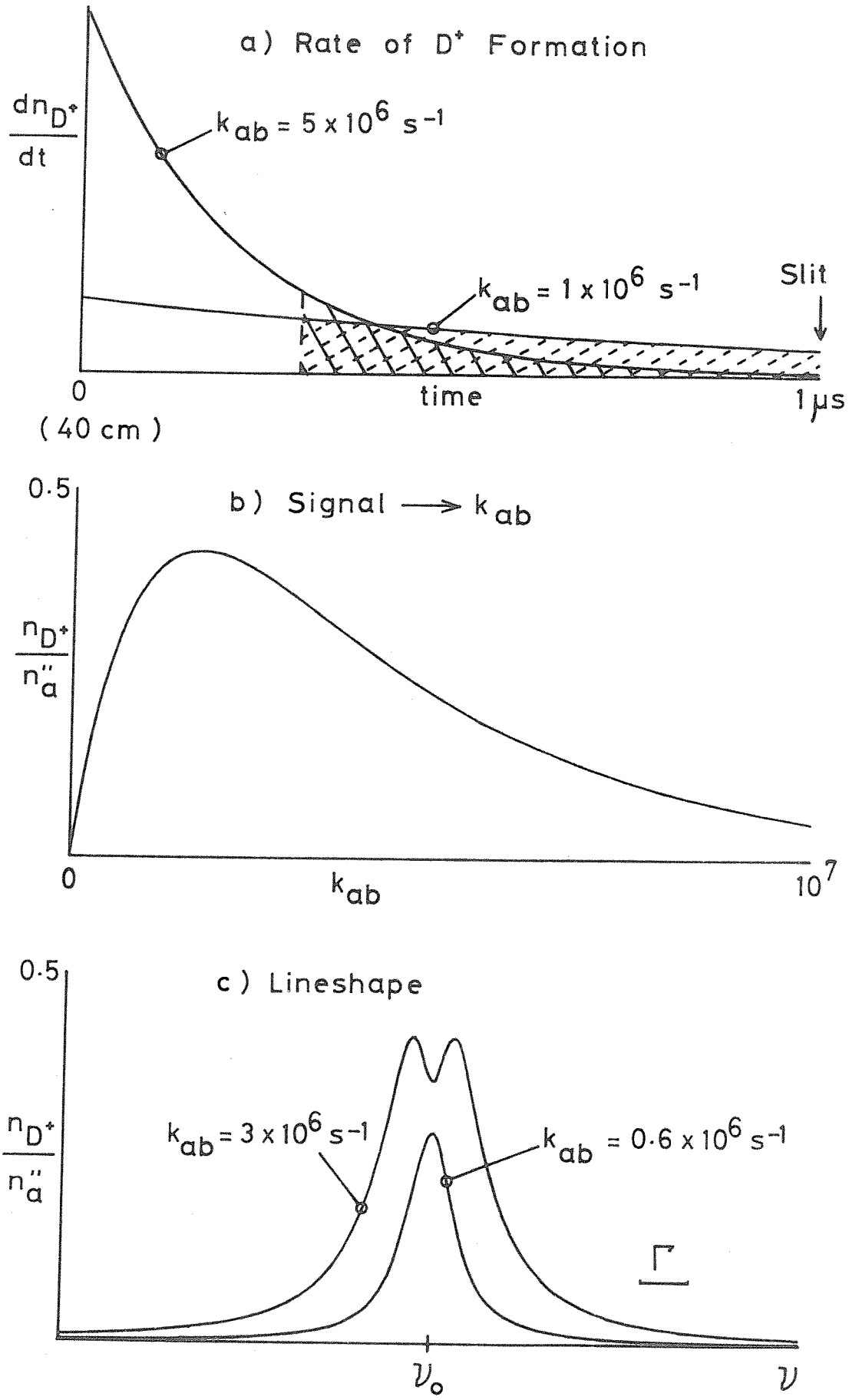

Figure 4.6

"Hole" Simulation

$$k_{ab}(\nu) = \frac{\Gamma^2 k_{max}}{4(\nu - \nu_0)^2 + \Gamma^2} \qquad (4.16)$$

where Γ is the full width at half maximum, and ν_0 is the line centre wavenumber. The results of this calculation for $k_{max} = 3 \times 10^6\ s^{-1}$ and $k_{max} = 0.6 \times 10^6\ s^{-1}$ are displayed in figure 4.6(c). At low k_{max}, low laser power, we obtain an approximately Lorentzian lineshape, but at high powers a "hole" does indeed appear at the line centre. Other features worthy of note are that:

a) the number of fragment ions detected at the centre of a line can be considerably less than the number of parent ions in the initial state, n_a". Any population estimates we make must thus be regarded as lower limits.

b) the FWHM of the simulated high power lineshape is much greater than Γ, due to the loss of intensity from the peak of the resonance signal. We conclude that some of the power broadening we noted may be more apparent than real.

c) since the lineshape depends on k_{max}, it might be possible to extract an estimate for the transition probability. In recent experiments on CH^+ [57] we have also observed the appearance of "holes", but only for lines which can be detected using very low laser powers, indicating a high transition probability.

The high power lineshape shown in figure 4.3(a) displays a marked asymmetry, there even appears to be a small dip in the profile on the high frequency side. These initially curious observations can also be explained by a careful consideration of potential instrumental effects. Referring to figure 2.6, we see that the ions interact with the laser for a distance of about 40 cm before they enter the drift tube. If a predissociated transition is pumped in this region, significant depopulation of the initial state can occur before the ions enter the drift tube. This leads to a decrease in the resonance signal detected by monitoring fragment ions formed in the drift tube. For the recordings of (7, 19) - (5, 20) of $^4HeD^+$ shown in figure 4.3 a drift tube offset of +450 V was used, to enhance the D^+ collection efficiency. The

maximum depopulation is expected at a total potential, for ions in the drift tube, lower by 450 eV than at the peak of the resonance; this is equivalent to a wavenumber difference of -0.056 cm^{-1}. We thus predict that there will be a decreased D^+ photofragment flux on the high frequency side of the resonance, causing the asymmetry we observed at high laser powers. This explanation is supported by the lineshape simulation shown in figure 4.7, which allows for the beam potential dependent depopulation of the initial state.

Other methods for investigating the quasibound states of HeH^+, supported by a centrifugal maximum in the potential, namely translational spectroscopy [136, 137, 138], and most recently low energy proton-helium scattering experiments [149] are of much lower resolution than our results. It is also very easy to interpret our spectra, and extract transition wavenumbers and linewidths, which can be directly compared with theoretical predictions. The interpretation and inversion of the results from scattering experiments requires great expertise, and the energy resolution is at best 100 cm^{-1}, compared to our limit of 10^{-4} cm^{-1}. However the scattering experiments are complementary, since they are especially sensitive to the very broad orbiting resonances near and above the top of the centrifugal barrier, which are far too wide to be observed in high resolution spectroscopic experiments.

Translational spectroscopy principally yields the positions of fairly long lived (10^{-7} to 10^{-5} sec) predissociated states, relative to the dissociation limit. Generally a number of states contribute to the observed fragment ion momentum or kinetic energy spectrum, and careful simulation is required to obtain the best data on the predissociated states. Our experiments allow us to probe the full details of the predissociation of a single quasibound state, selectively populated by a laser. In particular we are able to obtain directly absolute lifetimes from the widths of the resonances observed. The complementary nature of the two techniques must however be recognised. The translational spectroscopy experiments are sensitive to states with significantly longer lifetimes than we can observe with our present instrument. Translational spectroscopy is also able to probe states not accessible to spectroscopic experiments using carbon dioxide lasers, although many

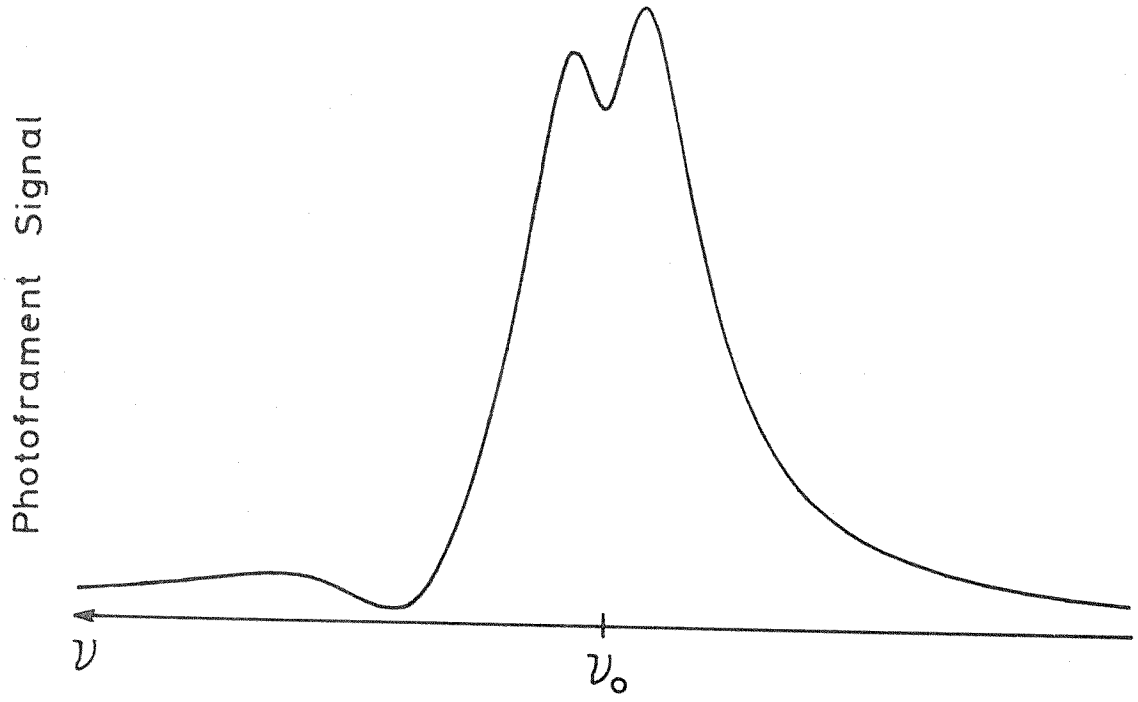

Figure 4.7

Lineshape Simulation with Asymmetry

(See text for details)

of these states could be reached by using other infrared lasers.

4.6 Conclusions.

The results presented above have confirmed the accuracy of the adiabatic description of HeH^+, and vindicated the methods used to compute energy levels and widths from the potentials. These conclusions are particularly significant in the light of current interest concerning the formation and destruction of HeH^+ in astrophysical plasmas [140]. One of the main formation mechanisms is expected to be radiative association, the reverse of the process of photopredissociation which we have studied. The hope is that HeH^+ may be detected in a gaseous nebula by observing its infrared emission spectrum.

The experiments on HeH^+ amply demonstrate the power of our instrument, applied to the study of transitions to predissociated states. We plan to extend the measurements on the HeH^+ systems to the wavenumber range covered by a carbon monoxide laser (1700-1950 cm^{-1}) where several resonances are predicted to lie. We are confident that the methods we have applied to HeH^+ will yield infrared predissociation spectra of similar quality for many more diatomic molecular ions; spectra of CH^+ [57] and $HeNe^+$ have already been obtained.

CHAPTER 5

INFRARED PREDISSOCIATION SPECTRUM OF THE H_3^+ ION

5.1 Introduction.

The dynamics of simple diatomic molecules are now fairly well understood. The excellent agreement between the predictions of ab initio theory and the experimental results presented in the two previous chapters supports this assertion. The same cannot be said for polyatomic molecules, especially if they are highly vibrationally excited. We therefore felt that it would be most instructive to study, by high resolution infrared spectroscopy, the behaviour of the simplest polyatomic molecule H_3^+ near its dissociation limits.

The H_3^+ molecular ion was discovered by J. J. Thomson in 1911 [150], and since then it has been the subject of numerous experimental and theoretical investigations. It is an efficient protonating agent for many simple molecules [151], and as such it plays a central role in models of interstellar chemistry [152]. Several theoretical investigations of the potential surface for the ground electronic state of H_3^+ have been reported, for a brief review see Porter [153]. They are unanimous in predicting an equilateral triangle equilibrium geometry, which has been substantiated by Coulomb explosion experiments [154]. The most accurate calculations to date for the minimum of the H_3^+ potential are those of Dykstra et al [155], who give r_e = 1.6504 Bohr (= 0.8734 Å). A good characterisation of all regions of the H_3^+ surface has been provided by Schinke et al [156]. Figure 5.1 shows the energetics of H_3^+, the D_e value for H_3^+ ($\rightarrow H_2 + H^+$) is from [155], the zero point energy is given in [157]. Building up from D_e are shown the energies of the dissociation products, the different vibration-rotation energy levels of the ground state of H_2 [158]. The only excited electronic state of H_3^+ which supports any bound vibrational levels is a

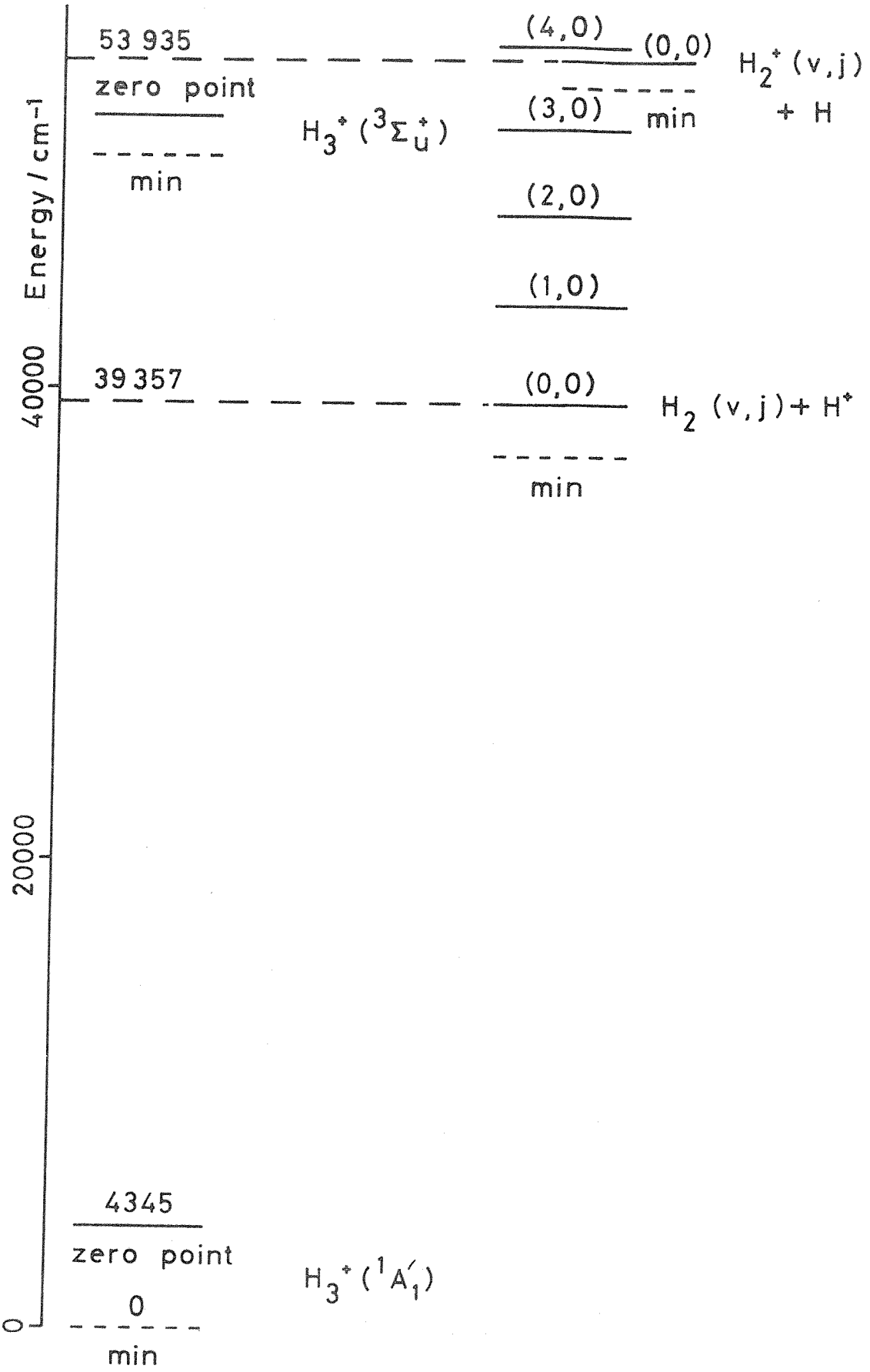

Figure 5.1

Energetics of H_3^+

shallow triplet state, with a linear equilibrium geometry [159]. The accuracy of the energies given in figure 5.1 is uncertain, errors of more than 100 cm^{-1} are possible.

Consideration of the theoretical data on the electronic states of H_3^+ leads to the conclusion that H_3^+ will not have a discrete electronic spectrum. Transitions between different vibration-rotation levels of the ground electronic state can be detected. In particular the degenerate bending fundamental band is electric dipole allowed, and predictions of the transition frequencies can be made [157]. Encouraged by these predictions, Oka [30] initiated a project to observe the infrared absorption spectrum of H_3^+ using the widely tunable infrared radiation from a difference frequency laser. To date [31] thirty transitions have been reported, producing constants in excellent agreement with the final set of theoretical predictions [32]. A few transitions in the ν_2 band of D_3^+ have been observed by Wing et al [50]. The ions were Doppler tuned into resonance with a carbon monoxide laser, transitions were detected by the charge exchange attenuation method. Wing et al [51] have also reported the observation of transitions in H_2D^+, but they are so far unassigned.

The spectroscopic investigations of H_3^+ and D_3^+ outlined above demonstrate the essential correctness of theoretical descriptions of the simplest polyatomic molecule in its lowest vibration-rotation energy levels. In this chapter we give a detailed description of the remarkable infrared predissociation spectrum of H_3^+; preliminary observations were reported by Carrington, Buttenshaw and Kennedy [58]. The results, which comprise more than 26000 transitions spanning only 222 cm^{-1} of the infrared region, suggest that in levels near the dissociation limits H_3^+ is best regarded as a proton - H_2 collision complex. A total assignment of the spectrum may never be possible, but we will show that its general features are at least qualitatively accounted for by our collision complex model.

Each infrared transition we have observed is detected by monitoring the protons formed through photopredissociation:

$$H_3^+ \xrightarrow{h\nu} (H_3^+)^* \rightarrow H_2(v, j) + H^+ \qquad (5.1)$$

It follows that at least the upper level of each transition must lie above the lowest dissociation limit, $H_2(0, 0) + H^+$. Our results lead us to believe that many of the lower levels are also located above the lowest dissociation limit. Our experiments are related to studies of low energy collisions of protons on molecular hydrogen, for reviews see [160, 161]. We probe a similar energy range, and the predissociation process can be regarded as half an inelastic collision between H_2 and H^+.

Trajectory and statistical calculations, corroborated by scattering experiments [161, 162, 163] have suggested the existence of H_3^+ collision complexes with lifetimes of longer than 10^{-13} s, at energies of up to 25000 cm^{-1} above the lowest dissociation limit. The spectroscopic experiments we have performed, which offer very much higher energy resolution than scattering experiments, provide clear evidence for the existence of many metastable states, with lifetimes in the range 10^{-6} to 10^{-9} s, probably with energies of at least up to 13300 cm^{-1} above the lowest dissociation limit. The weakly bound $^3\Sigma_u^+$ state of H_3^+ lies within this energy range, but we have no evidence to indicate that it plays a part in the spectrum we have observed.

5.2 Experimental Methods.

A full description of the apparatus and the recording methods can be found in chapter two. The H_3^+ ions were formed from molecular hydrogen in the electron impact source, using electron energies in the range 35 to 70 eV. Formation of H_3^+ ions was encouraged by running the source at a relatively high pressure. At a source potential of 8 keV the H_3^+ beam current was typically 1.3×10^{-7} A (8×10^{11} ions/sec). H_2^+ and H^+ ions were also formed, their measured currents were 10^{-6} A and 2×10^{-8} A, respectively.

In the absence of laser irradiation, a scan of the ESA differential voltage shows that H_3^+ fragments to form H^+ and H_2^+. These fragment ions arise almost entirely from collisional dissociation [164] in the second

field-free region, where the pressure was about 2 x 10^{-7} mbar. Our ESA spectrum is shown in figure 5.2(a). Irradiating the parent ions with an amplitude modulated CO_2 laser beam, and processing the fragment ion signal with a lock-in amplifier, allows us to ascertain whether fragment ions can also be produced by photodissociation. The resulting ESA scan appears in figure 5.2(b), the predominant mode of photodissociation is:

$$H_3^+ \xrightarrow{h\nu} H_2 + H^+ \qquad (5.2)$$

The yield of H^+ ions increasing linearly with laser power. The doubling of each peak is caused by the drift tube potential of 250 eV. The apparent production of H_2^+ photofragment ions has been identified as being due to D^+ photoproduct ions from HD^+ present in natural abundance. HD^+ ions are not separated from H_3^+ by the magnetic analyser, and HD^+ is known to exhibit strong infrared photodissociation [53]. As we show later D_3^+ photodissociates to produce D^+ ions; there is no evidence for photofragment D_2^+ ions.

Observation of infrared photodissociation of H_3^+ indicates that levels close to the dissociation limit must be populated, and that a predissociation spectrum may be observable. Predissociation resonances in the infrared spectrum of H_3^+ were searched for by the Doppler frequency modulation method, using a square wave voltage of 7 V amplitude at about 730 Hz, applied to the drift tube. For ion beam potentials in the range 4 to 10.5 keV the spectrum was recorded in 1 keV segments; at lower potentials smaller scan widths were used. In most cases the lowest beam potential required to achieve overlap with a scan at higher potential from an adjacent laser line was 3 keV; the minimum beam potential used was 1.2 keV. Both parallel and antiparallel alignments of the laser and ion beams were used. The positions and signal to noise ratios of all the observed resonances were measured by hand. Comparison of recordings of the same transition at different beam potentials, using different laser lines, revealed that signal to noise ratios were approximately constant. We have accordingly used signal to noise ratios as an estimate of the relative intensities of the transitions.

Figure 5.2

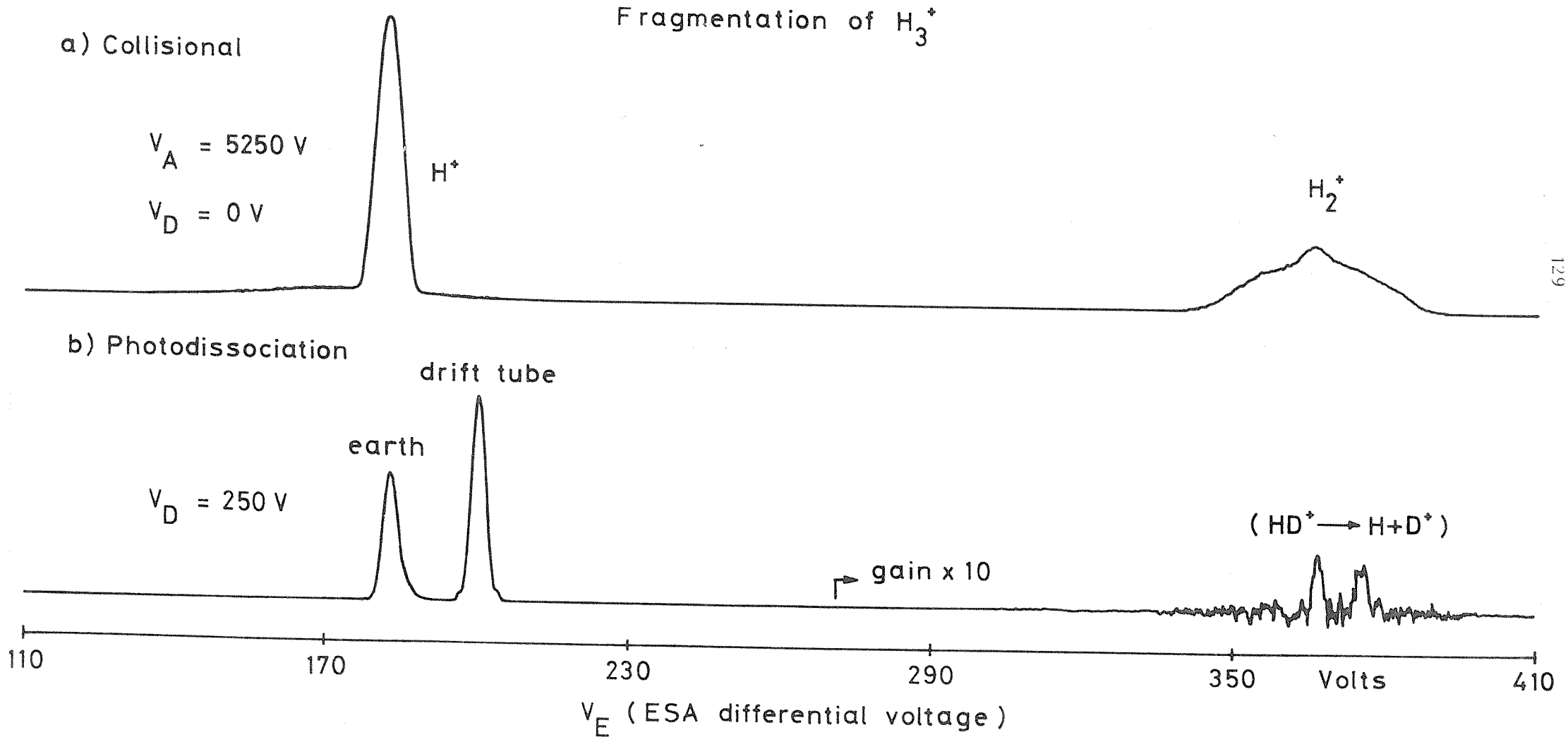
Fragmentation of H_3^+
a) Collisional
V_A = 5250 V
V_D = 0 V
H^+
H_2^+
b) Photodissociation
drift tube
earth
V_D = 250 V
($HD^+ \longrightarrow H+D^+$)
gain x 10
110
170
230
290
350
Volts
410
V_E (ESA differential voltage)

5.3 The Observed Spectrum.

After our initial discovery of the remarkable predissociation spectrum of H_3^+ [58], it was clear that measurement and analysis presented a formidable task. Although the very high resolution afforded by ion beam spectroscopy should ultimately be advantageous, our inability to obtain an overview of the entire spectrum seemed a considerable handicap. We therefore decided that, as a first priority, we should record the complete spectrum under a set of standard conditions, and use computer convolution techniques to construct spectra of lower resolution.

Unfortunately it is impossible to achieve a truly standard set of conditions under which to record the spectrum. Transitions are detected by scanning the beam potential, but the H_3^+ beam intensity decreases as the potential is lowered; this is to some extent balanced by the longer time the ions spend within the drift tube. The laser power available varies according to the CO_2 transition selected. The modulation amplitude should, ideally, be optimised for each transition according to its width. Finally the efficiency with which the H^+ fragment ions from a given transition are detected depends on their velocity in the H_3^+ centre of mass frame. In our survey of the spectrum we have naturally been forced to compromise. We have measured the positions (in cm^{-1}) and signal to noise ratios of the transitions by detecting protons with a nominal Δ value of zero, at a laser power of 7 ± 3 Watts, scanning the beam potential at a rate of 0.5 eV/sec. Under these conditions we have been able to record the spectrum from 872.120 cm^{-1} to 1094.006 cm^{-1}, but with the following small gaps:

873.593 to 874.094, 1015.723 to 1016.133 and 1017.920 to 1018.278 cm^{-1}

These gaps arose because we were unable to obtain adequate power from laser lines of $^{12}CO_2$ or $^{13}CO_2$ which would have filled these ranges. The average scanning rate was about 0.1 cm^{-1}/hr, so that a single recording of the complete spectrum takes about 2500 hrs! We have measured a total of 26514 lines, with signal to noise ratios up to a maximum of 30:1. A representative section of the spectrum is shown in

figure 5.3. Note in particular the obvious variations in linewidths, widths (FWHM) of 3 to 60 MHz have been observed. These widths are principally determined by the lifetimes of the predissociated states; kinematic compression reduces the Doppler width to about 3 MHz at 1000 cm^{-1}. Lines with widths in excess of 60 MHz are heavily discriminated against by the frequency modulation detection scheme, and there are probably many resonances which are too wide to be detected under the present set of conditions. Preliminary experiments using a detection scheme based on laser amplitude modulation have revealed the presence of broad lines.

In table 5.1 (microfiche in back cover), we list the wavenumbers and intensities (signal to noise ratios) of all the observed resonances. Experimental tests of the consistency of the transition wavenumbers, from measurements using different laser lines, indicate that they are accurate to ±0.002 cm^{-1}. The reliability of the intensities is rather harder to quantify. They are reproducible to about 10%, provided that the original recording conditions are duplicated.

The energy levels involved in the predissociated transitions are occupied by only a very small fraction of the H_3^+ ions in the beam. For the strongest transition observed, at 929.853 cm^{-1} (beam potential = 3461 eV), we have determined the following beam fluxes, using a laser power ($^{13}CO_2$ R(24) parallel at 931.3092 cm^{-1}) of 8.5 Watts:

H_3^+	parent beam	3×10^{11} ions/sec
H^+	from collision-induced dissociation	1.5×10^{7} ions/sec
H^+	from direct, background photodissociation	0.7×10^{7} ions/sec
H^+	from photopredissociation	1.0×10^{5} ions/sec

For this transition the fractional H_3^+ population in the lower level may be estimated to have been about 3×10^{-7}; for the majority of the lines the population factors were an order of magnitude smaller.

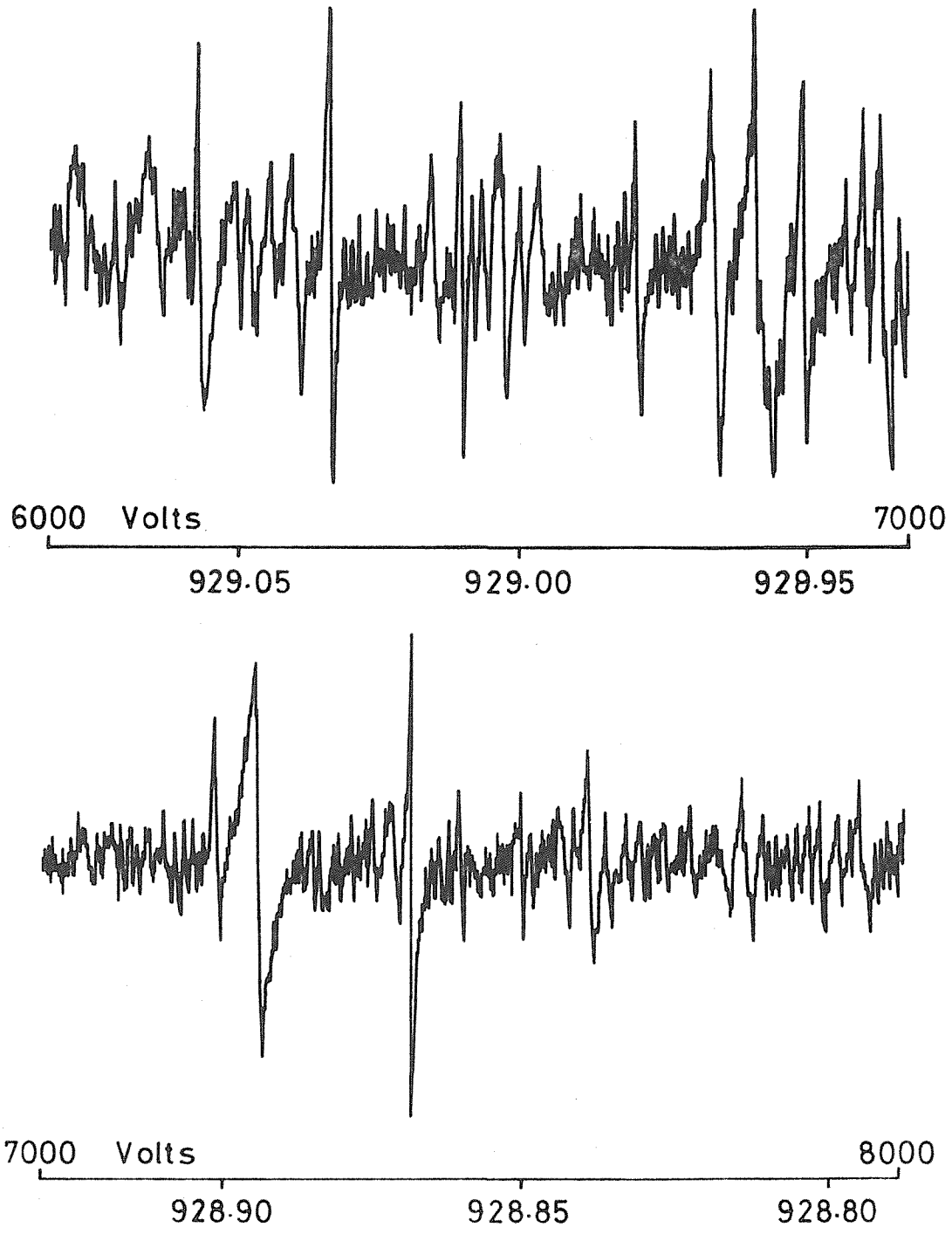

Figure 5.3

Section of the H_3^+ Predissociation Spectrum

Laser Line : $^{12}CO_2$ P(34) 931·0014 cm^{-1}, Parallel

5.4 Lifetimes.

It is possible, using the velocity of the H_3^+ ions, calculated from the beam potential, and the dimensions of the instrument, to establish certain limits on the lifetimes of the levels involved in the infrared predissociation spectrum we have observed. At a beam potential of 5 keV the H_3^+ ions have a speed of 5.64×10^5 ms^{-1}. The distance from the source exit slit to the entrance to the drift tube is 1.20 m, which is traversed by the ions in 2×10^{-6} s. We estimate that the time taken for the ions to be extracted from the source is probably about 2×10^{-6} s. The initial energy level in an observed transition must have a lifetime of 4×10^{-6} s or greater, if it is still to be appreciably populated when the ions reach the drift tube. The length of the drift tube is 40 cm, so that the final state must have a predissociation lifetime of 0.7×10^{-6} s or less, for a significant number of H^+ ions to be formed before the H_3^+ ions leave the drift tube; the ESA only collects protons formed within the drift tube. Our frequency modulation detection scheme imposes an upper limit of about 60 MHz on the linewidth, so that the predissociation lifetime of the final level must be 2×10^{-9} s or longer.

These lifetime criteria are the only fundamental experimental limitations on the energy levels we can probe. As we stressed in chapter two, there is no requirement that the initial level must lie below the final level. Our experiments will be just as successful if the initial level is above the predissociated final level, provided that the lifetimes fall within the limits:

$$\begin{aligned} \tau_{initial} &\geqslant 4 \times 10^{-6} \text{ s} \\ 0.7 \times 10^{-6} \text{ s} \geqslant \tau_{final} &\geqslant 2 \times 10^{-9} \text{ s} \end{aligned} \qquad (5.3)$$

5.5 Proton Kinetic Energies.

The primary purpose of the ESA in our investigations of H_3^+ has been to separate the fragment H^+ ions from the parent H_3^+ ions.

However the energy resolution of the ESA (about 300) is sufficient to allow us to determine the centre of mass kinetic energy of the proton fragments from each transition to a predissociated level. This energy immediately gives us the difference in energy, Δ, between the quasi-bound state and its H_2 (v,j) + H^+ dissociation channel. The theory behind these experiments has been presented in chapter two. For the specific case of the fragmentation of H_3^+ the difference in ESA differential voltage between the forward and backward scattered protons (2.64) is:

$$\Delta V_E = \frac{8}{3r'} \left[2 \frac{\Delta}{e} (V_S - V_D)\right]^{\frac{1}{2}} \qquad (5.4)$$

We have devised two different types of experiment to obtain ΔV_E, and hence Δ. In the first, we perform frequency scans in the usual manner, by sweeping the source potential, but with the ESA differential voltage offset by δV_{Eth} from the centre of the proton fragment peak. Recalling (2.66), this excludes protons formed by processes with:

$$\Delta < \Delta_{th} = \frac{e}{2(V_S - V_D)} \left(\frac{3r'}{4} \delta V_{Eth}\right)^2 \qquad (5.5)$$

Frequency scans are performed for a series of δV_{Eth} values, and the resulting spectra are assembled by a computer program to produce a two dimensional spectrum. An example is shown in figure 5.4. The Doppler-shifted wavenumber was scanned from 981.176 to 981.201 cm^{-1}, while the ESA offsets covered Δ_{th} of 0 to 3000 cm^{-1}. Three features of figure 5.4 are particularly worthy of consideration. First, we notice lines with ESA widths which indicate kinetic energy releases of 50 to 100 cm^{-1}. Second, we observe the characteristic splitting into forward ($\delta V_{Eth} > 0$), and backward scattered peaks when $\Delta > 500$ cm^{-1}. Third, and most important, we note the appearance of peaks with kinetic energy releases of about 3000 cm^{-1}.

In the second, rather more sophisticated, type of experiment, we employ the Doppler-switching technique described in chapter two. This method labels the protons associated with a selected transition, and by scanning the ESA differential voltage we can then obtain Δ. The technique is much more efficient than the two dimensional method, since we directly record spectra along the energy release axis. Figure 5.5 shows

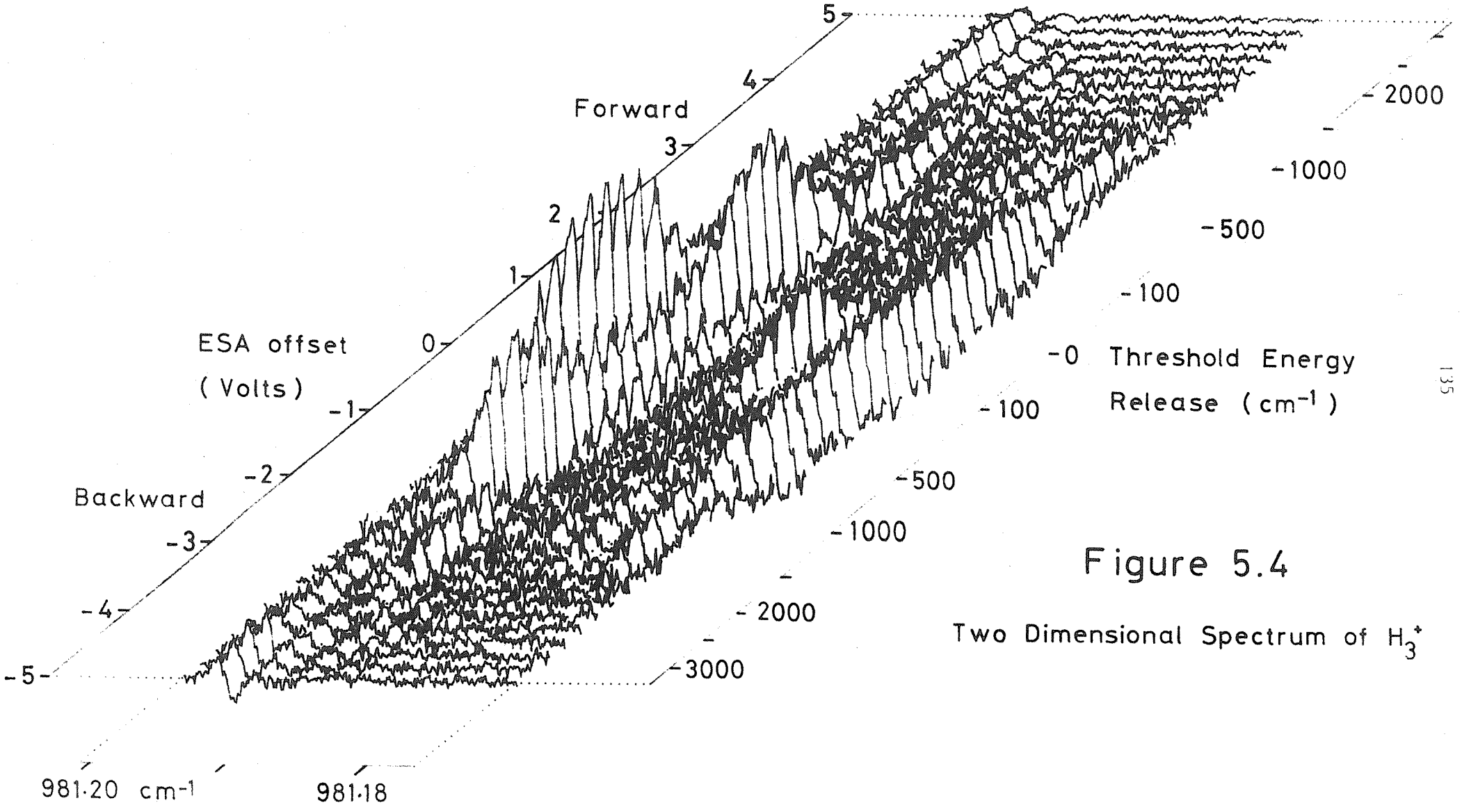

Figure 5.4

Two Dimensional Spectrum of H_3^+

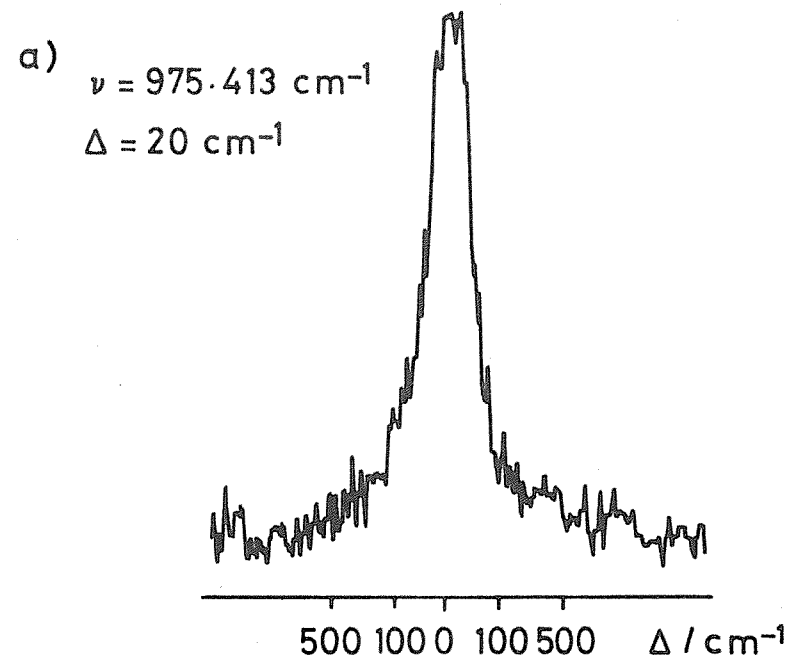

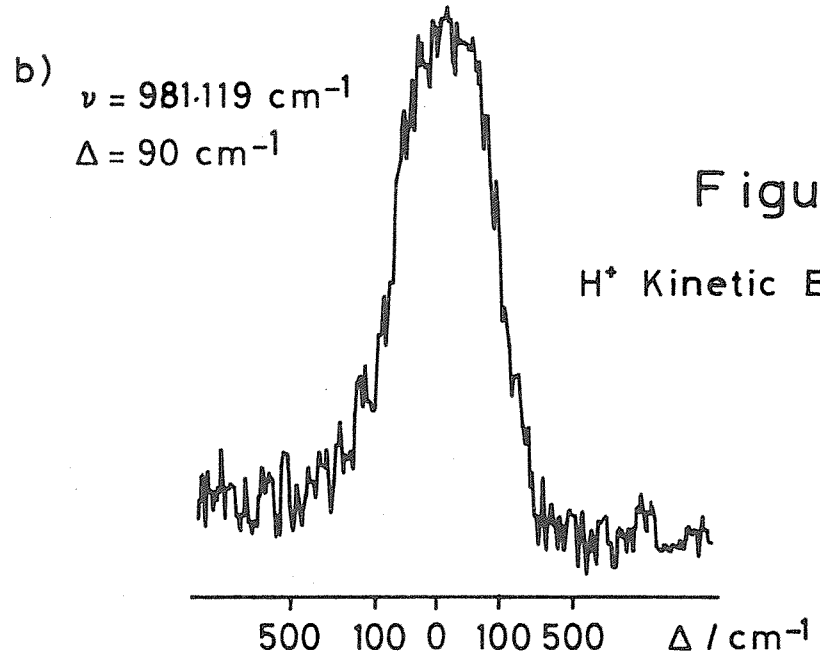

Figure 5.5

H^+ Kinetic Energy Spectra

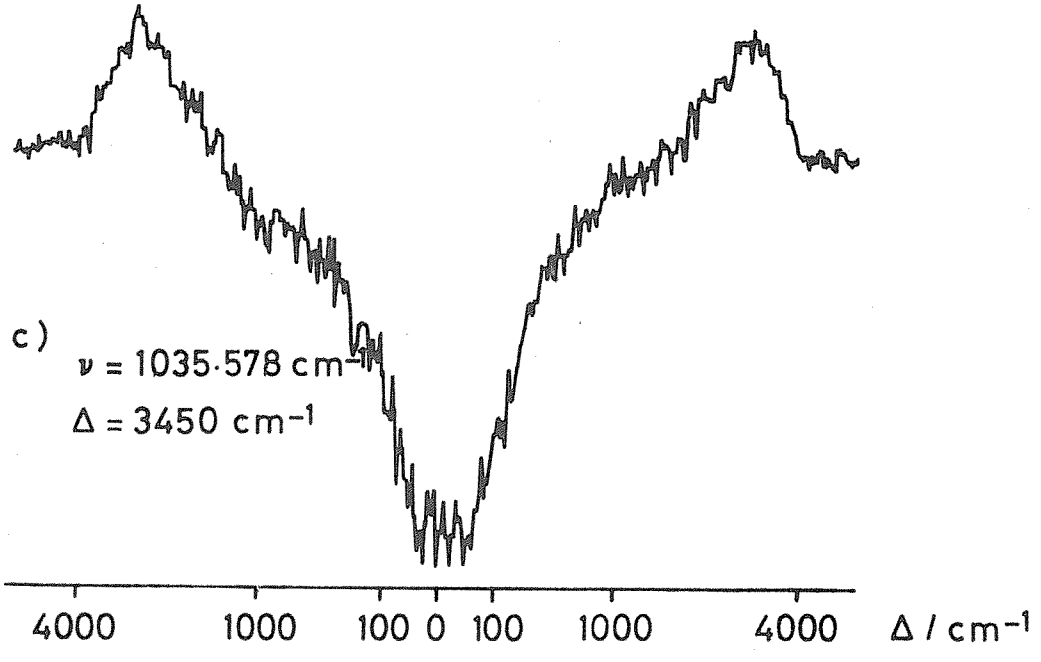

recordings for three transitions with differing values of Δ. Locating transitions with releases in excess of 1000 cm^{-1} presents a problem, since they do not appear in our usual ($\Delta_{th} = 0$) frequency scans. The difficulty is resolved by offsetting the ESA so that $\Delta_{th} \sim 3000$ cm^{-1}, and then recording a frequency spectrum, see figure 5.4. We typically find about 10 lines/cm^{-1} with $\Delta \geqslant 3000$ cm^{-1}; this is a preliminary value based on a few random searches. Except for the lines we deliberately searched for with releases of greater than 3000 cm^{-1}, most of the lines we have investigated were found to have Δ values of less than 250 cm^{-1}. All of the kinetic energy spectra exhibiting releases of $\geqslant 3000$ cm^{-1} show additional features, corresponding to smaller values of Δ, see figure 5.5(c). These features can be ascribed to transitions in the very dense spectrum observed with $\Delta_{th} = 0$, we do not believe that they are directly associated with the transitions responsible for the large releases. The negative signal seen at small Δ in figure 5.5(c) arises from the negative lobe of a transition with a slightly different resonant frequency from that producing the positive signal with $\Delta = 3450$ cm^{-1}.

The most startling and exciting result of these experiments is the observation of kinetic energy releases in excess of 3000 cm^{-1}, or more than three times the energy of a CO_2 laser photon. We believe that this proves conclusively that many of the resonances in the infrared predissociation spectrum must arise from transitions in which both the upper and lower energy levels lie well above the lowest dissociation limit, $H_2(v = 0, j = 0) + H^+$. The corollary to this assertion is that there must be many metastable levels of H_3^+ with lifetimes in excess of 4×10^{-6} s.

5.6 Pseudo Low Resolution Spectra by Convolution.

The complexity of the H_3^+ predissociation spectrum we have recorded is staggering, and traditional methods of spectroscopic analysis and assignment cannot immediately be applied. We felt that a low resolution view of the spectrum might reveal structure, which could then suggest a model for H_3^+ near and above its lowest dissociation limit.

Unfortunately we cannot obtain a low resolution spectrum by direct experiment, we have instead used a computer to generate low resolution spectra from our high resolution data. The positions ν_n (in cm^{-1}) and intensities I_n of all the lines are stored on two floppy disks, and a FORTRAN program enables us to interrogate and manipulate the data. A subroutine convolutes the data with a Gaussian of FWHM $\Gamma(< 5\ cm^{-1})$. The pseudo low resolution spectrum is calculated as the sum over all the data:

$$I(\nu) = \sum_{n=1}^{n_{dat}} I_n \exp\left[\frac{-(\ln 16)(\nu_n - \nu)^2}{\Gamma^2}\right] \qquad (5.6)$$

After rescaling $I(\nu)$ is plotted as a function of ν over the wavenumber range of interest. The program allows the convolution to be restricted to those lines whose intensities fall within a range specified by the user. $I(\nu)$ is not a genuine low resolution spectrum, our method of recording the high resolution spectrum using frequency modulation discriminates against the broader lines, which would contribute to a genuine low resolution spectrum.

Figure 5.6 shows convolutions obtained with $\Gamma = 4.0\ cm^{-1}$. Spectrum (a) includes all of the recorded lines, it appears to show some structure. This structure is greatly enhanced by restricting the convolution to the strongest lines, those with intensities (signal to noise ratios) of five or greater, see convolution (b). These strong lines constitute only 7.3% of the total number of measured transitions, their summed intensity is 17.8% of the total. A convolution of the remaining 92.7% of the data shows little recognisable structure, see spectrum (c).

The four prominent peaks in convolution (b) occur at wavenumbers (cm^{-1}) of:

1033.62 978.45 928.02 875.65

with an uncertainty of about 0.5 cm^{-1}. The position of the peak at

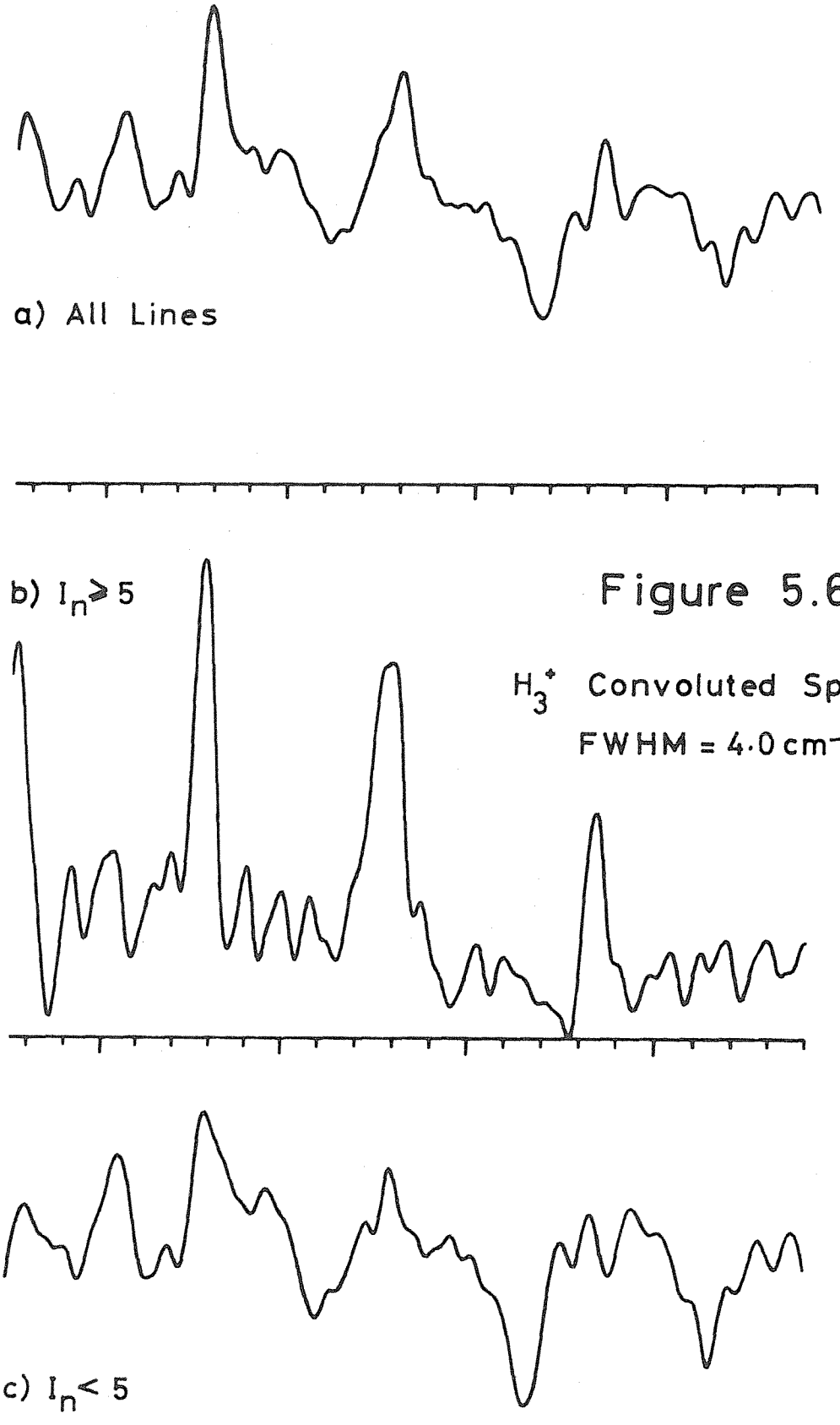

Figure 5.6

H_3^+ Convoluted Spectra

FWHM = 4·0 cm^{-1}

875.65 cm^{-1} is subject to greater error, since strictly we do not have enough data to extend the convolution below about 880 cm^{-1}.

Near its dissociation limits we expected that H_3^+ would take on the character of its dissociation products, behaving as an $H_2(v, j)....H^+$ complex. We accordingly sought to relate the peaks to transitions of the H_2 molecule. We find that they show an excellent correlation with the j = 5-3 transitions for v = 0, 1, 2, 3 in the ground electronic state of H_2 [158]:

v =	0	1	2	3
j = 5-3	1034.67	982.54	931.45	881.13

The above correlation could be coincidental, but that seems unlikely. We believe it is highly significant, and strongly supports our suggestion that H_3^+ in the levels giving rise to the observed predissociation spectrum can be regarded as an $H_2(v, j)....H^+$ collision complex, in which the H_2 partner is approximately described by the free diatom quantum numbers (v, j). In section 5.8 we consider qualitatively some of the consequences of this model, but first we justify our implicit assumption that the spectrum we have recorded is due to predissociation.

5.7 Evidence for Predissociation.

We have assumed that the spectrum we have obtained arises from the absorption (or stimulated emission) of a single infrared photon, followed by predissociation:

$$H_3^+ \xrightarrow{h\nu} (H_3^+)^* \xrightarrow{\text{pred.}} H_2 + H^+ \qquad (5.7)$$

We have made a few measurements of the power dependence of selected sections of the spectrum, these confirm a single photon process, with saturation of some lines occurring at high powers (> 15 Watts). The linewidths appeared to be approximately independent of the laser power. Two other mechanisms could lead to the detection of vibration-rotation transitions of H_3^+ by monitoring the frequency dependence of H^+ fragment formation. They are sequential two photon photodissociation, analogous

to our HD^+ experiments [53]:

$$H_3^+ \xrightarrow{h\nu} (H_3^+)' \xrightarrow{h\nu} H_2 + H^+ \qquad (5.8)$$

and collision induced dissociation:

$$H_3^+ \xrightarrow{h\nu} (H_3^+)' + M \rightarrow (H_3^+)^* \rightarrow H_2 + H^+ \qquad (5.9)$$

We consider first the suggestion of sequential two photon photodissociation. Our measurements of the number of H^+ fragment ions formed by direct photodissociation of H_3^+ reveal this process to be about fifty times less efficient than for HD^+. This could in part be due to a possibly lower fractional population of H_3^+ accessible to single photon photodissociation, but we believe it is primarily a reflection of the relative photodissociation probabilities. In HD^+ photodissociation occurs through the allowed electronic transition from the ground electronic state to the first excited, repulsive state. For H_3^+ we are attempting to pump molecules directly into the vibrational continuum of the ground electronic state, which must have a much smaller cross-section. The sensitivity for detection of a single transition in H_3^+ will be further degraded by the fact that the H_3^+ ions near the dissociation limit are spread over many more energy levels than for HD^+. As a very rough estimate, the overall sensitivity must be decreased by a factor of at least 5000 relative to HD^+, and we should not then expect to be able to detect a spectrum.

The other crucial observation is that the transitions have widely differing widths, see figure 5.3. This is totally inconsistent with the sequential two photon mechanism, by which we would detect bound to bound transitions. The widths of such transitions should all be approximately the same, being determined by the residual velocity spread of the ion beam, and possibly power broadening. We can thus reject the sequential two photon photodissociation mechanism.

We now turn to the possibility of detection through changes in the production of H^+ fragment ions by collision induced dissociation. The arguments concerning the observed variations in the widths of the transitions again apply, and repudiate this proposal. Several other

reasons can be advanced for the rejection of the collision induced dissociation mechanism. Our ESA scan, figure 5.1(a), shows that both H^+ and H_2^+ fragment ions are formed by collisional fragmentation of H_3^+. Despite several attempts, we have never succeeded in detecting transitions via the H_2^+ channel:

$$H_3^+ \xrightarrow{h\nu} (H_3^+)' + M \rightarrow (H_3^+)^* \rightarrow H_2^+ + H \qquad (5.10)$$

which should be feasible, if the collisional mechanism is valid. We usually only collect fragment protons from $(H_3^+)^*$ ions with energies of less than 1000 cm^{-1} above a dissociation limit. Collision induced dissociation of H_3^+ can produce fragments with energy releases in excess of 4000 cm^{-1}. Hence the collisional mechanism implies that we should be able to observe transitions which cause a decrease in the number of fragment protons with low Δ, but all the transitions we have recorded lead to an increase in the number of protons collected. Finally, consideration of the likely sensitivity of the collisional mechanism also leads to its rejection. Our measurements, section 5.3, show that only 5×10^{-5} of the H_3^+ ions formed H^+ fragments during their passage through the drift tube. The efficiency for detecting a transition will be even lower, since it depends on the difference in rates with which the initial and final states produce protons in collisions; a value of 10^{-7} does not seem unreasonable. We can use this figure to estimate the fraction of H_3^+ ions involved in each of the transitions we have recorded. The change in H^+ fragment signal for a typical resonance was 10^{-8} of the parent H_3^+ current, so that each transition would have to involve about 10% of the total number of H_3^+ ions, which is clearly ridiculous. The much higher, approximately unit efficiency for detection by predissociation gives a reasonable fractional population estimate of about 10^{-8} for a typical transition. The conclusive test of a collisional mechanism, the effect of changing the pressure in the second field-free region is not presently possible. We shall shortly have an extra pump attached to the instrument, to achieve a lower analyser pressure. We do not expect to lose our spectrum, we hope that reduction of the production of H^+ ions by collisional dissociation will improve our signal to noise.

It is our contention that the only mechanism consistent with all our observations is predissociation. The final corroboration will be provided by a successful prediction of levels of H_3^+ with predissociation lifetimes satisfying the criteria (5.3). Dr. J. M. Hutson is currently working on this problem.

5.8 A Model for H_3^+ Near Its Dissociation Limits.

Any model for H_3^+ in the levels involved in the transitions we have detected must be able to account for three crucial observations we have made:

a) There are a very large number of H_3^+ energy levels above the lowest dissociation limit, with predissociation lifetimes in the range 10^{-9} to 10^{-6} s.

b) The observation of protons from predissociated levels of H_3^+ lying further above a dissociation limit than the photon energy implies that there must be levels of H_3^+ with predissociation lifetimes of longer than 4×10^{-6} s.

c) The pseudo low resolution spectrum shows that the intensity distribution of the lines displays marked peaking close to the j = 5-3 transitions of H_2 in different vibrational levels.

The spectra produced by convolution suggest that a promising approach is to consider the interaction of a proton with a hydrogen molecule in its different vibration-rotation states. This view is encouraged by recognising that the transitions are detected through the slow predissociation of H_3^+ to form H_2 and H^+. It seems reasonable to suppose that near the dissociation limits the parent molecule should possess many of the attributes of the dissociation fragments. The integrity of the H_2 and H^+ partners will be lost at lower energies, where H_3^+ is best treated as a triatomic molecule with three equivalent nuclei [157].

The model we are proposing is closely related to those encountered in describing atom-diatom van der Waals molecules, such as H_2....Ar [165]. The obvious difference is that the dissociation energy of H_3^+ is very much greater than for any van der Waals molecule. Three co-ordinates are sufficient to specify the geometry of an atom-diatom complex, they are shown in figure 5.7. R is the distance from the centre of mass of the diatom to the atom, r is the length of the diatom bond, and θ is the angle between the vectors $\underset{\sim}{r}$ and $\underset{\sim}{R}$. The interaction potential between the partners may be expressed as an expansion in Legendre polynomials [144]:

$$V(r, R, \theta) = \sum_{\lambda=0}^{\infty} V_\lambda (r, R) P_\lambda (\cos\theta) \qquad (5.11)$$

For the special case of a homonuclear diatomic fragment, such as H_2, symmetry restricts the expansion to even values of λ.

The general features of the model can best be appreciated by making some rather severe approximations. First, we neglect all couplings between the motion of the H_2 molecule and the proton partner. We can then separate the wavefunction for motion about the centre of mass of the complex according to:

$$\Psi (\underset{\sim}{r}, \underset{\sim}{R}) = \psi_{vj} (\underset{\sim}{r}) \phi (\underset{\sim}{R}) \qquad (5.12)$$

where $\psi_{vj} (\underset{\sim}{r})$ is the wavefunction for a free H_2 molecule in the vibration-rotation state (v, j). This separation is related to the Born-Oppenheimer separation of electronic and nuclear motions. The motion of the proton relative to the H_2 molecule, described by $\phi(\underset{\sim}{R})$, is then governed by an effective potential, obtained by averaging $V(r, R, \theta)$ over the radial wavefunction of the H_2 molecule. This yields a set of potential surfaces $V'_{vj} (R, \theta)$, one for each vibration-rotation state of the H_2 molecule, just like the different potential curves for the various electronic states of a diatomic molecule. Neglecting the effects of anisotropy of the potential, so that:

$$V'_{vj} (R, \theta) = V'_{vj} (R) \quad \text{for all } \theta \qquad (5.13)$$

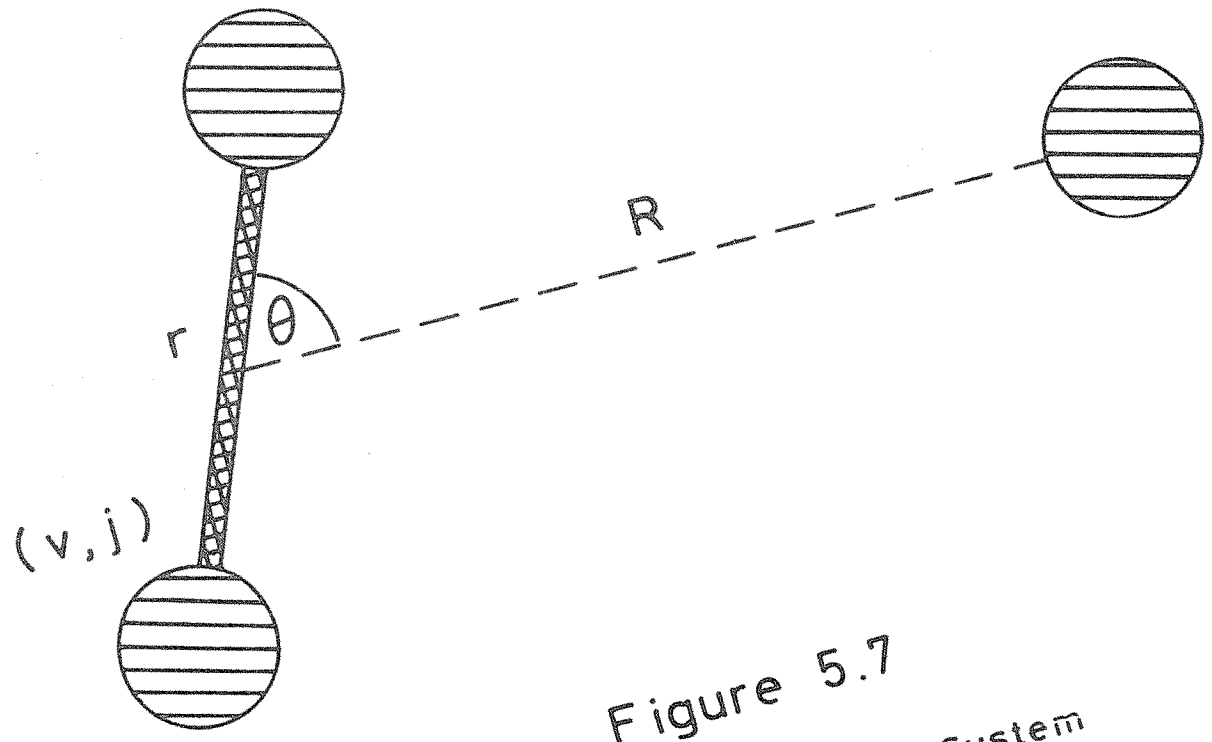

Figure 5.7

Atom-Diatom Coordinate System

reduces the motion of the proton relative to the H_2 molecule to a pseudo-diatomic problem. Figure 5.8 shows schematically the energy levels that arise from this simplified model, for clarity rotation of the complex as a whole is not included. This diagram forms the basis for our qualitative discussion of the implications of the model.

The first question we tackle is that of the predissociation mechanism. Three modes of predissociation can be envisaged:

i) Tunnelling through a centrifugal barrier. Rotation of the R vector creates a centrifugal maximum in the pseudo-diatomic potential curve. For the interaction of H_2 (v = 2, j = 5) with H^+ there may be quasibound states lying above the H_2 (2, 5) + H^+ dissociation limit, which predissociate by tunnelling through the centrifugal barrier. States of this type are known as shape or orbiting resonances in the language of scattering theory.

ii) Rotational predissociation. Predissociation can occur through the conversion of H_2 rotational energy into translational energy of the fragments. Consider an H_3^+ level derived from the H_2 (2, 5) + H^+ interaction, which lies above the H_2 (2, 3) + H^+ dissociation channel. There is a weak coupling between the bound level and the continuum associated with the H_2 (2, 3) + H^+ dissociation limit, induced by the anisotropy of the full interaction potential. The couplings are subject to a selection rule:

$$\Delta j = 0, \pm 2, \pm 4, \ldots . \qquad (5.14)$$

due to the symmetry of the interaction potential, it only contains even Legendre polynomials. This is in accord with our expectation that the interconversion of ortho and para H_2 is forbidden. Specifically the V_2 term in the interaction potential directly couples levels associated with H_2 (2, 5) + H^+ to the continuum of H_2 (2, 3) + H^+. Assuming that the direct V_2 coupling dominates the predissociation, we would anticipate energy releases in the range 0 to 900 cm^{-1}, and indeed most of the transitions we have detected must have Δ values within this range. Model calculations on this predissociation mechanism have recently been performed for H_2 (1, 2)....Ar [166], energy widths of the order of

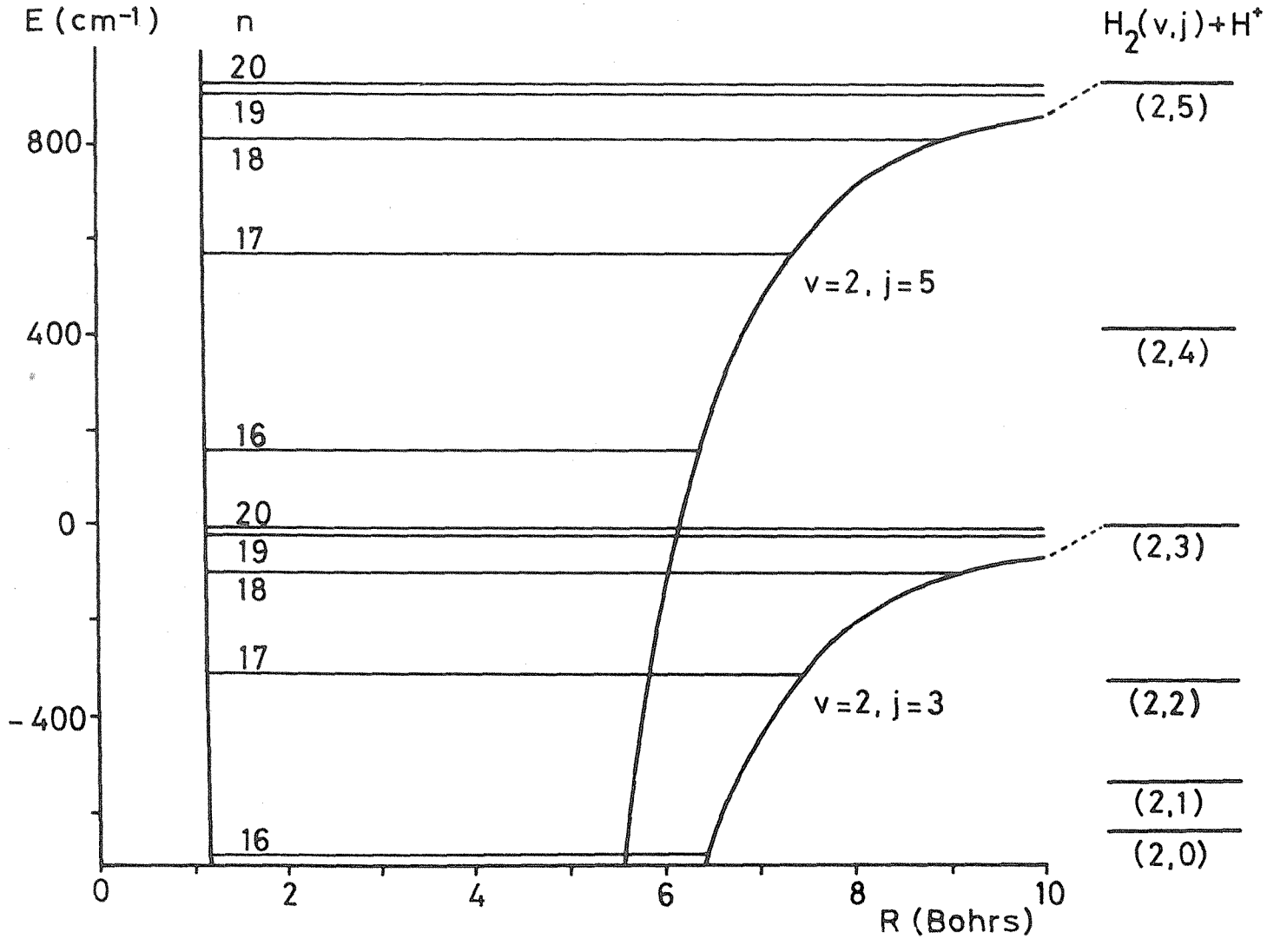

Figure 5.8

Pseudodiatomic Model

600 MHz were obtained. This is rather larger than our H_3^+ linewidths, but since the widths are very sensitive to the details of the system, widths of 60 MHz or less for some levels of H_3^+ may be reasonable. In scattering theory quasibound states of this type are known as compound state or Feshbach resonances.

iii) Vibrational predissociation. Predissociation can also occur by the conversion of H_2 vibrational energy into translational energy of the fragments. Consider an H_3^+ level arising from the H_2 (2, 5) + H^+ interaction, which lies below the H_2 (2, 3) + H^+ limit. Rotational predissociation is impossible, if we assume that it is limited to direct V_2 coupling. However there are couplings between this bound level, and the continua associated with lower vibration-rotation energy levels of the H_2 molecule, subject to the selection rule (5.14). These couplings will induce vibrational predissociation of H_3^+. Kinetic energy releases of up to about 4000 cm^{-1} would then be expected ($\Delta v = -1$), and when we have looked for resonances with $\Delta_{th} \sim 3000$ cm^{-1} we have regularly found transitions. Model calculations on the vibrational predissociation of H_2 (1, 0)....Ar [167] produced extremely narrow widths, very much less than 30 kHz. We hope that rather shorter lifetimes will pertain for some levels of H_3^+. These calculations are encouraging, since they imply that there should be many levels of H_3^+ above the lowest dissociation limit with vibrational predissociation lifetimes >> 4×10^{-6} s, our lower limit for the initial state lifetime. Two recent experiments have provided evidence for metastable van der Waals molecules with long vibrational predissociation lifetimes. Laser induced fluorescence assigned to metastable Cl_2 (v'' = 1)....Ne has been observed in a pulsed molecular beam experiment [168], the lifetime of the complex must be at least 10^{-5} s. Infrared spectroscopy of $(HF)_2$ reveals the presence of many quasibound levels with lifetimes of longer than 10^{-8} s [169].

At this stage our conclusions regarding the predissociation of H_3^+ are necessarily very tentative. We favour rotational predissociation as being the mechanism most likely to produce a large number of levels with lifetimes in the range 10^{-9} to 10^{-6} s. Dr. J. M. Hutson is presently attempting to perform calculations on H_3^+ similar to those for H_2....Ar [166, 167], to test our suggestions. At a qualitative

level the model successfully accounts for the observed proton kinetic energy spectra. A very large number of metastable levels are fully consistent with the model. There are more than 120 vibration-rotation levels of H_2 lying within 25000 cm^{-1} of H_2 (0, 0) [158]. When the effects of coupling between the proton and H_2 motions, as well as the anisotropy of the potential, are taken into account it should be easily possible to find sufficient levels to account for the density of our spectrum.

We now attempt to explain why the pseudo low resolution spectrum should show peaks, whose positions correlate with the j = 5-3 transitions of H_2. The question is difficult to answer conclusively, since several factors influence the appearance of the convoluted spectrum:

i) the relative positions of energy levels with the correct lifetimes.

ii) the populations of these energy levels.

iii)the selection rules and transition probabilities governing transitions between these energy levels.

We offer the following plausible explanation. We assume that the strongest transitions are between levels associated with different H_2 (v, j) + H^+ dissociation limits. At large R the dipole moment induced in the H_2 partner by the interaction of the point proton charge with the anisotropic, r dependent polarisability of the H_2 molecule gives an electric dipole selection rule on j of $\Delta j = 0, \pm 2$ [170]. At smaller R the chemical bonding will modify this simple view of the transition moment, but within our model, which assumes a distinguishable proton, conservation of nuclear spin symmetry in the H_2 unit requires that Δj be even. In table 5.2 we list all the H_2 transitions satisfying $\Delta j = 0, \pm 2$, which lie in the range 870 to 1100 cm^{-1}, based upon the compilation of Dabrowski [158]. Transitions involving H_2 levels lying more than 25000 cm^{-1} above the lowest H_2 (0, 0) level are arbitrarily excluded. The j = 5-3 transitions in v = 0, 1, 2 and 3 are seen to require the least excitation of the H_2 partner. We also note that the energy levels responsible for these four transitions all lie below the H_2^+ (0, 0) + H limit, which is 14740 cm^{-1} above H_2 (0, 0) + H^+. It seems reasonable to expect that H_3^+ levels associated with these H_2

Table 5.2

H_2 Transitions in the Range 870-1100 cm^{-1}
(with E (upper) < 25000 cm^{-1}) [158]

$\Delta v = 0$

v	j'	j''	ν/cm^{-1}	E(lower)/cm^{-1}
0	5	3	1034.67	705.54
1	5	3	982.54	4831.41
2	5	3	931.45	8722.70
3	5	3	881.13	12384.14
3	6	4	1060.40	12778.78
4	6	4	999.70	16190.66
5	6	4	938.78	19375.99
5	7	5	1087.91	19807.03
6	6	4	876.92	22332.85
6	7	5	1015.34	22735.61

$\Delta v = 1$

v'	j'	v''	j''	ν/cm^{-1}	E(lower)/cm^{-1}
1	13	0	15	1067.40	12123.66
1	14	0	16	920.01	13479.07
2	13	1	15	982.52	15649.58
3	12	2	14	1045.05	17771.73
3	13	2	15	896.81	18950.27
4	12	3	14	951.23	20918.25
5	11	4	13	997.07	22834.61

states will be more highly populated than those from higher H_2 (v, j) + H^+ limits. A further point in their favour is that the H_2 unit has j odd, and they will be preferrentially populated over levels with j even due to nuclear spin statistics. To go beyond these broad statements we will require a very detailed understanding of the mechanism by which we form H_3^+ in these highly excited levels.

Our final assumption is that the interaction potential, averaged over r, is relatively insensitive to the vibration-rotation state of the H_2 unit. This leads to an approximate selection rule on n, the vibrational quantum number for motion of H^+ relative to H_2, of $\Delta n = 0$, from vibrational overlap integrals. The strongest bands will then all have their origins close to the free H_2 transition frequencies, and intensity will tend to build up at these points, in accord with our pseudo low resolution spectrum. Lifetimes in the correct ranges are easily conceived for the j = 5-3 transitions. Levels associated with H_2 (v, 3) + H^+ lying below the H_2 (v, 1) + H^+ limit will have long, vibrational predissociation lifetimes ($> 4 \times 10^{-6}$ s). These initial levels can give transitions to levels of H_2 (v, 5)....H^+, lying above the H_2 (v, 3) + H^+ limit, which will have shorter, rotational predissociation lifetimes ($< 10^{-6}$ s).

Prof. A. Carrington is presently attempting to put the qualitative model outlined above on a more quantitative basis. Preliminary results of his calculations lend support to the assumptions made above, and in particular peaking in the convoluted spectrum close to the H_2 j = 5-3 transitions can be obtained.

5.9 Formation of Excited H_3^+.

The most important reaction leading to the formation of H_3^+ is:

$$H_2 + H_2^+ \rightarrow H_3^+ + H \qquad (5.15)$$

With H_2 and H_2^+ both in the lowest vibration-rotation levels of their respective ground states, D_0^0 (H_2) = 36118 cm^{-1} and D_0^0 (H_2^+) = 21379 cm^{-1},

the reaction is exothermic by 17978 cm^{-1}, using a theoretical value for D_0^0 ($H_3^+ \rightarrow H_2 + H^+$) [155, 157]. This reaction will produce H_3^+ ions with a considerable amount of internal energy, but levels close to and above the lowest dissociation limit cannot be reached. Additional energy can be provided by reacting H_2 with vibrationally excited H_2^+, produced by electron impact ionisation [171]. With H_2^+ in its highest bound vibrational level the lowest dissociation limit of H_3^+ is almost reached. To access levels above the lowest dissociation limit other mechanisms must be considered. The capture of a proton by an H_2 molecule, inverse predissociation, is an obvious possibility. However, the most likely explanation is that the kinetic energy of the reactants is converted into internal energy of H_3^+. There is experimental evidence for this process from merged beams studies of reaction (5.15) [172]. Ions are accelerated within the source by the field gradient due to earth field penetration. The pressure within the source is quite low, as evidenced by the high proportion of H_2^+ in the ion beam exiting the source; reaction (5.15) has a large cross-section [172]. Thus some of the H_2^+ ions will have acquired a considerable amount of kinetic energy before they react with H_2 to form H_3^+, and beams containing H_3^+ in levels above the lowest dissociation limit may be generated. Some support for this hypothesis comes from our observation that the strength of the predissociation spectrum depends on the source conditions. In particular, if we use a source with a narrower exit slit, so that the pressure within the source is much higher, we obtain a beam containing a greatly increased proportion of H_3^+, $n(H_3^+)/\ n(H_2^+) \simeq 10$, rather than 0.1. However we have been unable to observe a predissociation spectrum from the H_3^+ ions produced by this source. This is presumably because the H_2^+ ions are unable to acquire sufficient kinetic energy to reach the H_3^+ dissociation limit before they react.

We would naturally like to simplify our spectrum by selectively reducing the number of H_3^+ levels populated by reaction (5.15). Two methods are being considered. Firstly, cooling the source would reduce the population in higher rotational levels of H_2 and H_2^+, and this should influence the H_3^+ population distribution. The detailed effects cannot be predicted, as our knowledge of the state selective dynamics of reaction (5.15) is very limited [173]. The second possibility is that we could

restrict H_2 and H_2^+ to j even levels by using pure para - H_2; this requires that ortho-para conversion does not occur before reaction. Nuclear spin statistics lead to detailed symmetry selection rules on the rovibronic states of H_3^+ which can be formed by (5.15) [174].

5.10 Preliminary Investigations of D_3^+, D_2H^+ and H_2D^+.

One of the advantages of using a mass spectrometer in spectroscopic experiments is the ease with which isotope studies can be undertaken. The admission of suitable mixtures of H_2 and D_2 into the electron impact source produces beams containing D_2H^+ and H_2D^+, while pure D_2 gives a D_3^+ beam. The magnetic analyser allows the selection of the desired isotopic modification of H_3^+, and we have performed preliminary experiments on D_3^+ ($\rightarrow D^+ + D_2$), H_2D^+ ($\rightarrow H^+ + HD$) and D_2H^+ ($\rightarrow H^+ + D_2$ and $D^+ + HD$).

ESA scans of the fragment ions are shown in figure 5.9 ($V_D = 0$). They reveal that collisional dissociation produces all possible atomic and diatomic fragment ions. In contrast only atomic fragment ions are produced by infrared photodissociation, D_2H^+ definitely yielding both H^+ and D^+ photofragment ions. The results for H_2D^+ are confused, since our mass resolution is insufficient to separate H_2D^+ from D_2^+. The D^+ peaks appearing in the H_2D^+ ESA scans are dominated by the fragmentation of D_2^+ ions.

We have observed an infrared predissociation spectrum of D_3^+, by monitoring the D^+ fragment ion intensity as the frequency is Doppler scanned. A small segment of this spectrum is shown in figure 5.10(a). The density of lines is even higher than in our H_3^+ spectrum, but the intensities are rather lower; repetition of the scan confirms the existence of many weak lines. D_3^+ is heavier than H_3^+, and the lower intensity is presumably a reflection of the higher density of D_3^+ energy levels, over which a similar number of parent ions must be distributed.

For D_2H^+ we have been able to search for predissociation resonances by monitoring the production of either H^+ or D^+ fragment ions. Figure 5.10(b)

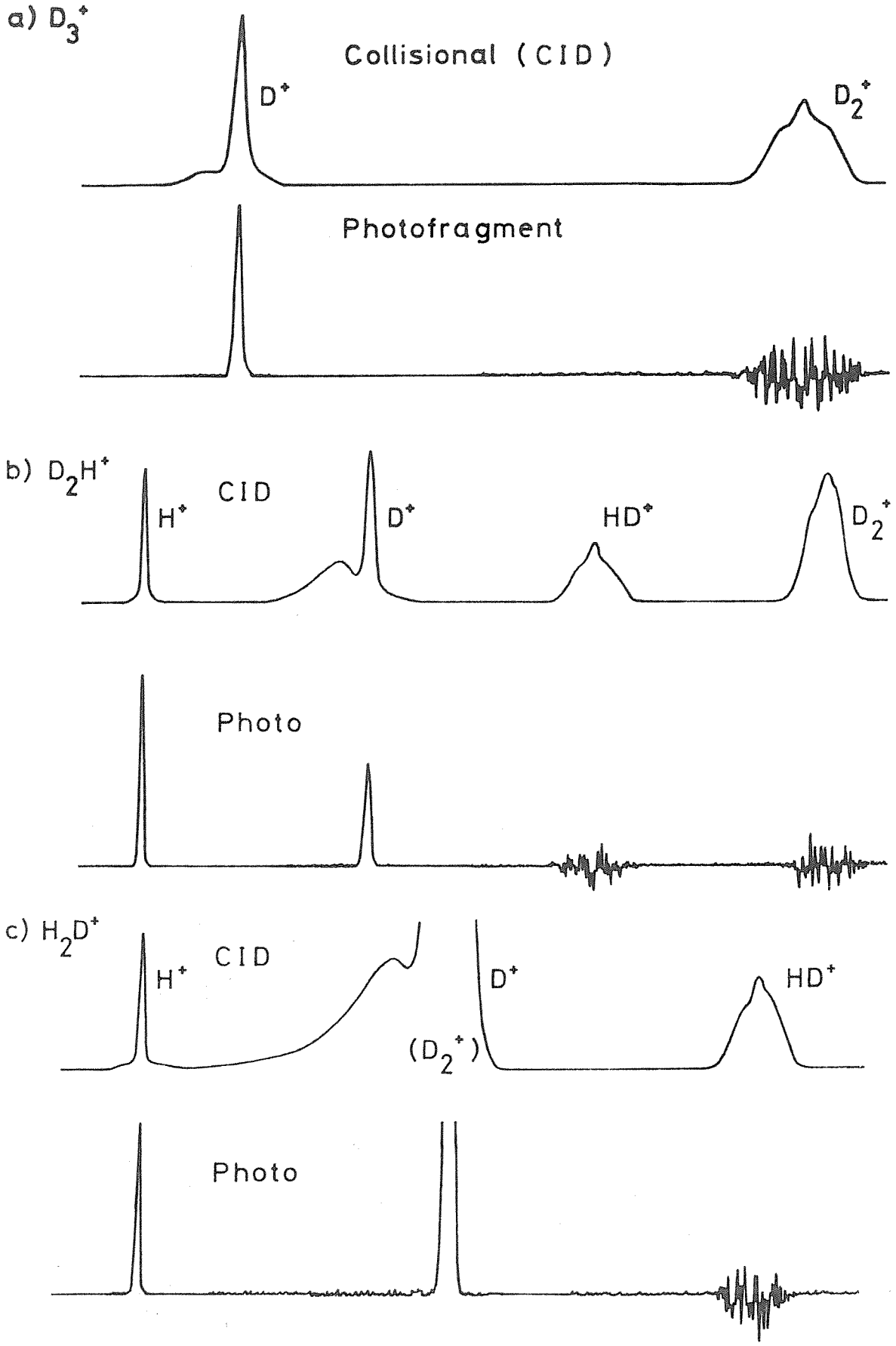

Figure 5.9

Fragmentation of H_3^+ Isotopes

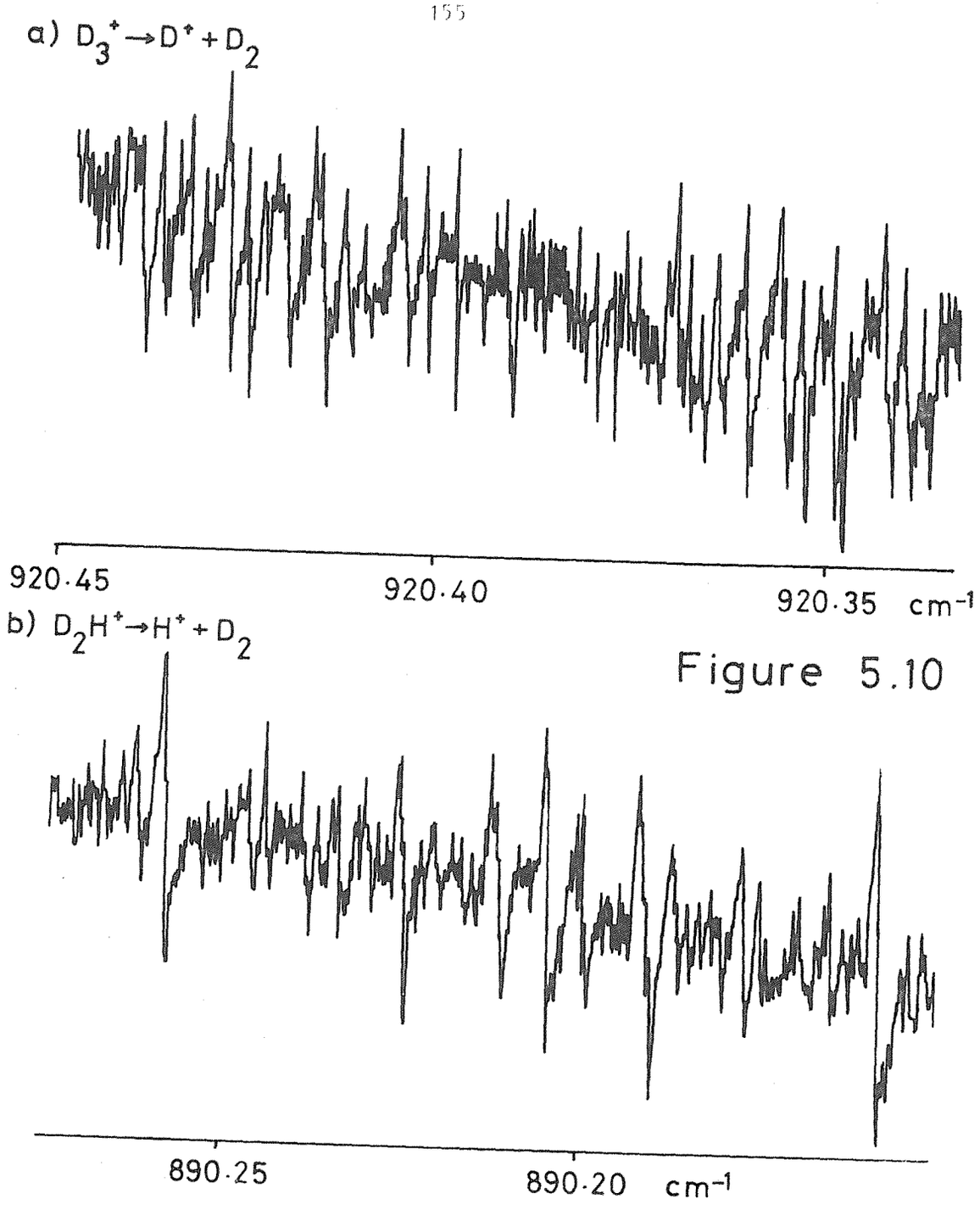
a) $D_3^+ \rightarrow D^+ + D_2$
920·45
920·40
920·35 cm⁻¹
b) $D_2H^+ \rightarrow H^+ + D_2$
890·25
890·20 cm⁻¹
c) $H_2D^+ \rightarrow H^+ + HD$
890·10
890·05
890·00 cm⁻¹

Figure 5.10

shows a portion of the extensive spectrum obtained from the proton fragments. Identical scans have been performed with the ESA set to transmit D^+ fragment ions, no resonances could be detected. These preliminary results indicate that if there are resonances to be observed via the D^+ + HD channel, they are either much sparser than from the H^+ + D_2 channel, or they are at least an order of magnitude weaker. Our studies of the H_2D^+ ion were unfortunately necessarily limited to the H^+ + HD dissociation mode, and here again a rich spectrum was observed, see figure 5.10(c).

We cannot yet provide a satisfactory explanation for our failure to observe resonances in the D_2H^+ predissociation spectrum, via the D^+ + HD channel. A tempting reason, in terms of our qualitative model for H_3^+, is that HD....D^+ complexes predissociate very much more rapidly than D_2....H^+ complexes, giving lines which are too broad for us to detect. There are many more allowed dissociation channels for HD....D^+. The interaction potential for HD....D^+, referred to the centre of mass of the complex, contains odd as well as even Legendre polynomials, so there is no selection rule on Δj(HD). However, this argument leads one to anticipate that HD....H^+ should also not give a detectable spectrum, but we have observed many sharp resonances via the protons from H_2D^+. We hope that detailed calculations on the predissociation mechanisms may be able to account for this perplexing isotope effect.

5.11 Conclusions.

We started this project with the aim of investigating the behaviour of the simplest polyatomic molecule near its dissociation limits. In the process, we have discovered that in H_3^+ there are many metastable levels which lie well above the lowest dissociation limit. To account for the results of our experiments, and in particular the correlation of the peaks in a pseudo low resolution spectrum with transitions in the free H_2 molecule, we have proposed a simple model for H_3^+. We regard H_3^+ as a complex between a proton and a hydrogen molecule. A qualitative investigation of the implications of this model suggests that it provides a useful approach to the interpretation of

our results. It is vital that this model be put on a rigorous basis, and thoroughly tested quantitatively. Calculations on the predissociation mechanisms are urgently required, since our arguments hinge on the existence of many energy levels with lifetimes in the range 10^{-6} to 10^{-9} s, and the occurrence of many others with lifetimes of 4×10^{-6} s or longer.

Further experiments on H_3^+ are being planned. We intend to carry out a careful investigation of the linewidths, and attempt to ascertain if they show any correlation with the kinetic energy releases. Reduction of the collisional background, by lowering the analyser pressure, will improve our signal to noise. This will allow us to reduce the ESA slit widths, and so increase the resolution of our kinetic energy experiments. Predissociation of H_3^+ need not occur through a unique H_2 (v, j) + H^+ channel, indeed calculations on the vibrational predissociation of H_2....Ar [167] predict the production of H_2 in a range of rotational states. High resolution proton kinetic energy spectra could reveal the formation of different H_2 (v, j) states from a single predissociated state of H_3^+. The ultimate experiment would be to determine the vibration-rotation state of the H_2 fragment, as well as the associated kinetic energy release. This would completely define the energetics of the predissociation products, and allow absolute energies for the upper and lower levels to be obtained. Unfortunately the sensitivities of the extremely sophisticated methods recently devised for the state selective detection of H_2 [175, 176, 177] are inadequate for our purposes, and the final H_2 state(s) must regrettably remain unknown. We hope that extensive recordings of the spectra of D_3^+, D_2H^+ and H_2D^+ will reveal correlations similar to those found for H_3^+. However the massive investment in time required to obtain the data makes this a very long term aim.

The results presented here potentially add greatly to our understanding of H_3^+ near its dissociation limits, a region of its potential surface previously only probed by scattering experiments. Statistical, collision complex models have provided an adequate explanation of many of the features of low energy H^+/H_2 scattering experiments [161]. We have interpreted our results using a collision complex model, but the

much greater detail revealed by spectroscopic experiments demands an exact quantum mechanical treatment of their dynamics. We have expressed our model in terms of the conventional time independent description of bound states of molecules. An alternative approach is to adopt a time dependent, wave packet description, the quantum mechanical analogue of classical trajectory calculations. Very recently some initial calculations on low energy H^+/H_2, D^+/HD and D^+/H_2 collisions using this type of method have been presented [178].

One of the most important conclusions from our work is that near dissociation the molecule H_3^+ takes on many of the characteristics of its dissociation products. We believe that this must be a general phenomenon, and we intend to search for predissociation resonances in the infrared spectra of other simple triatomic molecular ions to test this idea.

CHAPTER 6

THEORY OF THE HYDROGEN MOLECULAR ION

6.1 Introduction.

The hydrogen molecular ion H_2^+ and its isotopic modifications have occupied a central position in the development of molecular quantum mechanics, since the foundations were laid some sixty years ago. Our recent experimental investigations of the spectroscopy of HD^+ in levels close to its dissociation limit [53,54] have prompted us to critically investigate the current state of the theory for this model system. A number of excellent reviews [135,179] have appeared in recent years. The absence of interelectron interactions greatly simplifies the quantum mechanics of this fundamental molecule, permitting extremely accurate ab initio calculations of its properties. Our specific aim in this chapter is to address the problems encountered in treating the very highest vibrational levels of the ground state of HD^+. To this end, we present preliminary results of calculations on the behaviour of HD^+ near its lowest dissociation limits. We begin by reviewing the present state of the theory.

6.2 The Complete Nonrelativistic Hamiltonian.

For a system of point charges interacting electrostatically and moving through field free space, the complete nonrelativistic Hamiltonian can be written in the form:

$$\mathcal{H} = \sum_i -\frac{\hbar^2 \nabla_i^2}{2m_i} + \sum_i \sum_{j>i} \frac{z_i z_j e^2}{4\pi\varepsilon_0 r_{ij}} \qquad (6.1)$$

where all the symbols have their usual meanings. We separate out the translational motion of the three particles making up a hydrogen molecular

ion by applying the transformation:

$$\begin{pmatrix} \underset{\sim}{r}_g \\ \underset{\sim}{R} \\ \underset{\sim}{R}_{CM} \end{pmatrix} = \begin{pmatrix} -\frac{1}{2} & -\frac{1}{2} & 1 \\ -1 & 1 & 0 \\ m_{1/M} & m_{2/M} & m_{e/M} \end{pmatrix} \begin{pmatrix} \underset{\sim}{r}_1 \\ \underset{\sim}{r}_2 \\ \underset{\sim}{r}_e \end{pmatrix} \qquad (6.2)$$

where $M = m_1 + m_2 + m_e$. The coordinate systems are illustrated in figure 6.1. $\underset{\sim}{r}_1$, $\underset{\sim}{r}_2$ and $\underset{\sim}{r}_e$ are the position vectors of the three particles relative to an arbitrary space-fixed origin. The new basis vectors are the internuclear vector $\underset{\sim}{R}(= \underset{\sim}{r}_2 - \underset{\sim}{r}_1)$, $\underset{\sim}{R}_{CM}$ the position of the centre of mass of the system relative to the space-fixed origin, and $\underset{\sim}{r}_g$ the position of the electron relative to the geometric centre of the nuclei. $\underset{\sim}{r}_g$ is the natural choice for the position vector of the electron, since its motion is governed by a potential which is symmetric about the centre of the internuclear vector. Applying the transformation (6.2) to the kinetic energy operators in the Hamiltonian (6.1) we obtain:

$$-\hbar^2 \sum_i \frac{\nabla_i^2}{2m_i} = -\hbar^2 \left(\frac{\nabla_g^2}{2m_e} + \frac{\nabla_R^2}{2\mu} + \frac{\nabla_g^2}{8\mu} + \frac{\underset{\sim}{\nabla}_g \cdot \underset{\sim}{\nabla}_R}{2\mu_a} + \frac{\nabla_{CM}^2}{2M} \right) \qquad (6.3)$$

where $\frac{1}{\mu} = \frac{1}{m_1} + \frac{1}{m_2}$ and $\frac{1}{\mu_a} = \frac{1}{m_1} - \frac{1}{m_2}$ (6.4)

Note that for the homonuclear case, such as H_2^+, $m_1 = m_2$ and $(1/\mu_a) = 0$. The electrostatic potential V is unchanged by the transformation:

$$V = \frac{e^2}{4\pi\varepsilon_0} \left(\frac{1}{R} - \frac{1}{r_{1e}} - \frac{1}{r_{2e}} \right) \qquad (6.5)$$

because it depends only on the relative positions of the particles. The translational motion is immediately separated out of the Schrödinger equation:

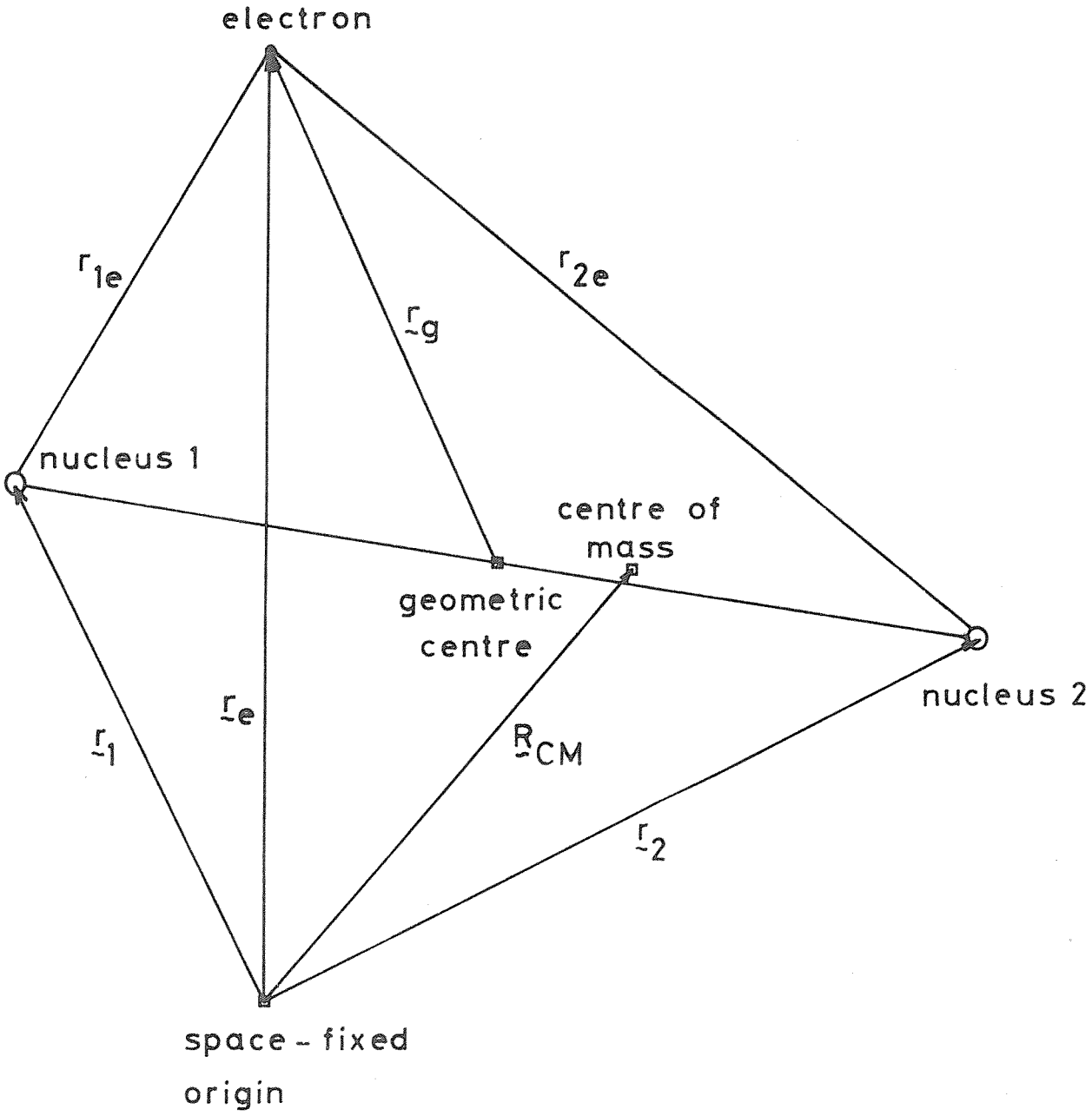

Figure 6.1

Coordinate Systems

$$\left[-\hbar^2 \left(\frac{\nabla_g^2}{2m_e} + \frac{\nabla_R^2}{2\mu} + \frac{\nabla_g^2}{8\mu} + \frac{\nabla_{\underset{\sim}{g}} \cdot \nabla_{\underset{\sim}{R}}}{2\mu_a} + \frac{\nabla_{CM}^2}{2M} \right) + V \right] \Psi_{tot} = E_{tot} \Psi_{tot} \qquad (6.6)$$

by writing:

$$\Psi_{tot}(\underset{\sim}{R}_{CM}, \underset{\sim}{R}, \underset{\sim}{r}_g) = A_{CM}(\underset{\sim}{R}_{CM}) \psi_{mol}(\underset{\sim}{R}, \underset{\sim}{r}_g) \qquad (6.7)$$

giving:

$$\left[-\hbar^2 \left(\frac{\nabla_g^2}{2m_e} + \frac{\nabla_R^2}{2\mu} + \frac{\nabla_g^2}{8\mu} + \frac{\nabla_{\underset{\sim}{g}} \cdot \nabla_{\underset{\sim}{R}}}{2\mu_a} \right) + V \right] \psi_{mol} = E_{int} \psi_{mol} \qquad (6.8)$$

and

$$-\hbar^2 \frac{\nabla_{CM}^2}{2M} A_{CM} = (E_{tot} - E_{int}) A_{CM} \qquad (6.9)$$

Equation (6.9) is simply the time independent Schrödinger equation for a body of mass M freely translating through space with kinetic energy $(E_{tot} - E_{int})$.

In summary, the nonrelativistic Hamiltonian, in atomic units, for the internal motion of the hydrogen molecular ion is:

$$\mathcal{H}_{int} = -\frac{\nabla_g^2}{2} - \frac{\nabla_R^2}{2\mu} - \frac{\nabla_g^2}{8\mu} - \frac{\nabla_{\underset{\sim}{g}} \cdot \nabla_{\underset{\sim}{R}}}{2\mu_a} + \frac{1}{R} - \frac{1}{r_{1e}} - \frac{1}{r_{2e}} \qquad (6.10)$$

6.3 Solution of the Schrödinger Equation.

The nonrelativistic Hamiltonian (6.10) contains terms which couple the electronic and nuclear motions. This makes it impossible to obtain exact solutions. However, by making certain approximations it is possible to reduce the problem to one which can be solved exactly. We follow the method suggested by Born [180], and expand the complete molecular wave function as the series :

$$\psi_{mol}(\underset{\sim}{R}, \underset{\sim}{r}_g) = \sum_t F_t(\underset{\sim}{R}) \phi_t(\underset{\sim}{R}, \underset{\sim}{r}_g) \qquad (6.11)$$

where the $\phi_t(R,\underset{\sim}{r}_g)$ are the exact solutions of what we will call the electronic Born-Oppenheimer equation for the hydrogen molecular ion:

$$\left(-\frac{\nabla_g^2}{2}-\frac{1}{r_{1e}}-\frac{1}{r_{2e}}+\frac{1}{R}\right)\phi_t(R,\underset{\sim}{r}_g) = E_t(R)\phi_t(R,\underset{\sim}{r}_g) \qquad (6.12)$$

Substituting the Born expansion (6.11) into the complete nonrelativistic Schrödinger equation (6.8), we obtain a set of coupled differential equations for the functions $F_t(\underset{\sim}{R})$:

$$\mathcal{H}_{int}\sum_t F_t(\underset{\sim}{R})\phi_t(R,\underset{\sim}{r}_g) = E_{int}\sum_t F_t(\underset{\sim}{R})\phi_t(R,\underset{\sim}{r}_g) \qquad (6.13)$$

The equation is simplified by premultiplying by $\phi_s^*(R,\underset{\sim}{r}_g)$, and integrating over the electronic coordinates $\underset{\sim}{r}_g$, to obtain:

$$\left\{E_s(R)-\frac{\nabla_R^2}{2\mu}-\int\phi_s^*(R,\underset{\sim}{r}_g)\left[\frac{\nabla_g^2}{8\mu}+\frac{\nabla_R^2}{2\mu}\right]\phi_s(R,\underset{\sim}{r}_g)d\underset{\sim}{r}_g\right\}F_s(\underset{\sim}{R}) +$$

$$+\sum_{t\neq s}\left\{\int\phi_s^*(R,\underset{\sim}{r}_g)\left[-\frac{\nabla_R^2}{2\mu}-\frac{\nabla_g^2}{8\mu}-\frac{\underset{\sim}{\nabla}_g\cdot\underset{\sim}{\nabla}_R}{2\mu_a}\right]\phi_t(R,\underset{\sim}{r}_g)d\underset{\sim}{r}_g +\right.$$

$$\left.+\int\phi_s^*(R,\underset{\sim}{r}_g)\left[-\frac{\underset{\sim}{\nabla}_R}{\mu}-\frac{\underset{\sim}{\nabla}_g}{2\mu_a}\right]\phi_t(R,\underset{\sim}{r}_g)d\underset{\sim}{r}_g\cdot\underset{\sim}{\nabla}_R\right\}F_t(\underset{\sim}{R}) = E_{int}F_s(\underset{\sim}{R}) \qquad (6.14)$$

where we have made use of the implicit symmetry properties of the functions $\phi_t(R,\underset{\sim}{r}_g)$. An exact solution of these coupled differential equations is not feasible, since the couplings between the infinite set of functions $F_t(\underset{\sim}{R})\phi_t(R,\underset{\sim}{r}_g)$ would have to be considered. The problem can be made tractable by neglecting some of the couplings, alternatively a different approach to the solution of (6.8) may be sought.

6.4 The Electronic Born-Oppenheimer Equation.

Before proceeding to describe the methods that have been used to obtain approximate solutions to equation (6.8), we return to the electronic Born-Oppenheimer equation (6.12). The problem is to solve for the motion of a single electron about two fixed nuclear charge

centres. The equation is most readily solved in a prolate spheroidal coordinate system, because the three dimensional equation (6.12) then separates into three one dimensional equations. Figure 6.2 shows the cartesian coordinate system; the prolate spherical coordinates are:

$$\xi = \frac{(r_{1e} + r_{2e})}{R} \quad [1 \leq \xi < \infty], \quad \eta = \frac{(r_{1e} - r_{2e})}{R} \quad [-1 \leq \eta \leq 1] \tag{6.15}$$

and χ, rotation of $\underset{\sim}{r}_g$ about the z axis $[0 \leq \chi < 2\pi]$. In this coordinate system we have:

$$\underset{\sim}{\nabla}_g = \frac{\partial}{\partial x}\underset{\sim}{i} + \frac{\partial}{\partial y}\underset{\sim}{j} + \frac{\partial}{\partial z}\underset{\sim}{k} = \frac{2\left[(\xi^2-1)(1-\eta^2)\right]^{\frac{1}{2}}}{R(\xi^2-\eta^2)} \left\{ \left[\xi \cos\chi \frac{\partial}{\partial \xi} - \eta \cos\chi \frac{\partial}{\partial \eta} \right.\right.$$

$$\left. - \frac{\sin\chi(\xi^2-\eta^2)}{(\xi^2-1)(1-\eta^2)} \frac{\partial}{\partial \chi} \right] \underset{\sim}{i} + \left[\xi \sin\chi \frac{\partial}{\partial \xi} - \eta \sin\chi \frac{\partial}{\partial \eta} + \frac{\cos\chi(\xi^2-\eta^2)}{(\xi^2-1)(1-\eta^2)} \frac{\partial}{\partial \chi} \right] \underset{\sim}{j}$$

$$\left. + \left[\frac{\eta(\xi^2-1)^{\frac{1}{2}}}{(1-\eta^2)^{\frac{1}{2}}} \frac{\partial}{\partial \xi} + \frac{\xi(1-\eta^2)^{\frac{1}{2}}}{(\xi^2-1)^{\frac{1}{2}}} \frac{\partial}{\partial \eta} \right] \underset{\sim}{k} \right\} \tag{6.16}$$

The Laplacian operator in the prolate spherical coordinate system is:

$$\nabla_g^2 = \frac{4}{R^2(\xi^2-\eta^2)} \left[\frac{\partial}{\partial \xi}(\xi^2 - 1) \frac{\partial}{\partial \xi} + \frac{\partial}{\partial \eta}(1 - \eta^2) \frac{\partial}{\partial \eta} + \frac{(\xi^2-\eta^2)}{(\xi^2-1)(1-\eta^2)} \frac{\partial^2}{\partial \chi^2} \right]$$

(6.17)

and the volume element is:

$$d\underset{\sim}{r}_g = \frac{R^3}{8}(\xi^2 - \eta^2)\, d\xi\, d\eta\, d\chi \tag{6.18}$$

The electron-nuclear electrostatic attraction operator becomes:

$$-\frac{1}{r_{1e}} - \frac{1}{r_{2e}} = -\frac{4\xi}{R(\xi^2-\eta^2)} \tag{6.19}$$

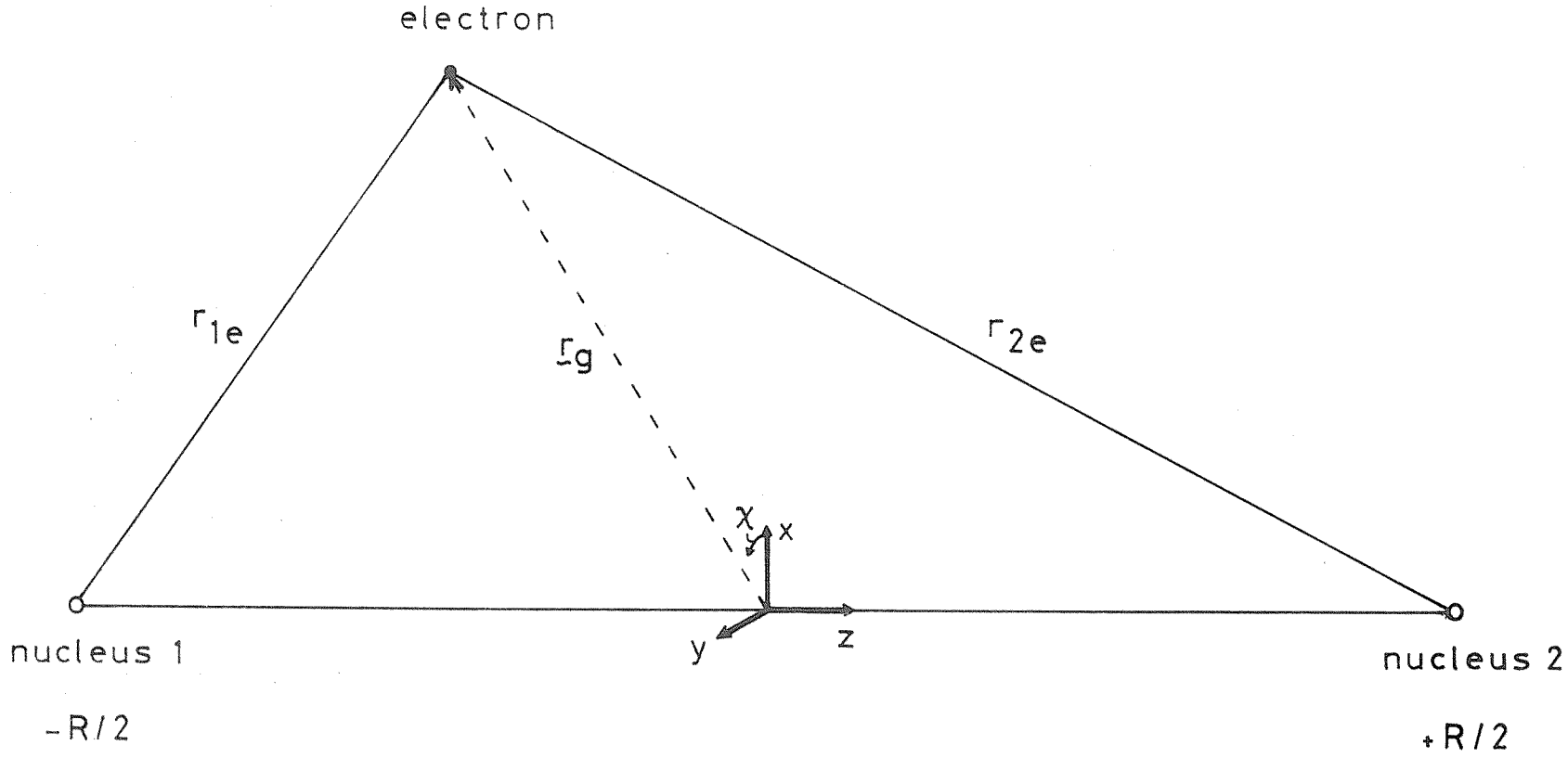

Figure 6.2

Cartesian Coordinates

Defining:

$$p^2 = -\frac{R^2}{2}\left[E_t(R) - \frac{1}{R}\right] \tag{6.20}$$

we see that the electronic Born-Oppenheimer equation (6.12) can be written as:

$$\left\{\frac{\partial}{\partial\xi}(\xi^2-1)\frac{\partial}{\partial\xi} + \frac{\partial}{\partial\eta}(1-\eta^2)\frac{\partial}{\partial\eta} + \left[\frac{1}{(\xi^2-1)} + \frac{1}{(1-\eta^2)}\right]\frac{\partial^2}{\partial\chi^2} + 2R\xi - p^2(\xi^2-\eta^2)\right\}\phi_t(R,\xi,\eta,\chi) = 0 \tag{6.21}$$

The separation into three one dimensional equations is achieved by making the substitution:

$$\phi_t(R,\xi,\eta,\chi) = L(R,\xi)M(R,\eta)N(\chi) \tag{6.22}$$

We then obtain the three separated equations:

$$\left[\frac{d^2}{d\chi^2} + \Lambda^2\right]N = 0 \tag{6.23}$$

$$\left[\frac{d}{d\xi}(\xi^2-1)\frac{d}{d\xi} + A - \frac{\Lambda^2}{(\xi^2-1)} + 2R\xi - p^2\xi^2\right]L = 0 \tag{6.24}$$

$$\left[\frac{d}{d\eta}(1-\eta^2)\frac{d}{d\eta} - A - \frac{\Lambda^2}{(1-\eta^2)} + p^2\eta^2\right]M = 0 \tag{6.25}$$

where Λ^2 and A are the separation constants. The χ equation (6.23) can be solved analytically with the result:

$$N(\chi) = \frac{1}{(2\pi)^{\frac{1}{2}}}\exp(i\Lambda\chi) \qquad \text{where} \quad \Lambda = 0,\pm1,\pm2,..... \tag{6.26}$$

The ξ and η equations have to be solved numerically by series expansion methods. Expansions over orthogonal polynomials offer advantages for the evaluation of integrals over the coordinates ξ and η. The ξ equation can be solved using an expansion over associated Laguerre polynomials,

due originally to Hylleraas [181]:

$$L(R,\xi) = (\xi^2-1)^{\Lambda/2}\exp[-p(\xi-1)]\left\{\sum_{n=0}^{\infty} g_n(R)L_n^{\Lambda}[2p(\xi-1)]\right\} \tag{6.27}$$

Substitution of this expansion into (6.24) and application of the properties of the Laguerre functions [144] leads to a set of recursion relations between the coefficients $g_n(R)$. They are conveniently expressed as a matrix eigenvalue equation, when the series is truncated at n = N.

$$\underline{\underline{G}}\,\underline{g} = -A\,\underline{g} \tag{6.28}$$

where

$$\underline{g} = \begin{pmatrix} g_o \\ g_1 \\ \vdots \\ g_N \end{pmatrix} \tag{6.29}$$

The non-zero elements of the tridiagonal matrix $\underline{\underline{G}}$ are:

$$\left.\begin{aligned} G_{n,n-1} &= -(\sigma - n + 1)n \\ G_{n,n} &= (\Lambda+1)(\Lambda+\sigma) - p^2 + 2p\sigma + 2n(\sigma - 2p) - 2n^2 \\ G_{n,n+1} &= (n + \Lambda + 1)(n - \Lambda - \sigma) \end{aligned}\right\} \tag{6.30}$$

where $\sigma = \left(\frac{R}{p}\right) - \Lambda - 1$ (6.31)

An alternative expansion due to Jaffé [182] has also been widely used:

$$L(R,\xi) = (\xi^2-1)^{\Lambda/2}(\xi+1)^{\sigma}\exp(-p\xi)\left\{\sum_{n=0}^{\infty} g_n(R)\left(\frac{\xi-1}{\xi+1}\right)^n\right\} \tag{6.32}$$

The coefficients are again given by a matrix eigenvalue equation [183].

The η equation may be solved using an expansion over associated Legendre functions:

$$M(R,\eta) = \sum_{s=0}^{\infty} f_s(R) P_{\Lambda+s}^{\Lambda}(\eta) \tag{6.33}$$

The symmetry of the η equation (6.25) restricts the expansion for a given state to terms with only even or only odd values of s. Substitution of (6.33) into (6.25) and use of the properties of the functions $p_{\Lambda+s}^{\Lambda}(\eta)$ [144], gives a matrix eigenvalue equation for the coefficients $f_s(R)$:

$$\underline{\underline{F}}\ \underline{f} = A\ \underline{f} \tag{6.34}$$

where

$$\underline{f} = \begin{pmatrix} f_0 \\ f_2 \\ \vdots \\ f_{2S} \end{pmatrix} \quad \text{or} \quad \underline{f} = \begin{pmatrix} f_1 \\ f_3 \\ \vdots \\ f_{2S+1} \end{pmatrix} \tag{6.35}$$

The non-zero elements of the tridiagonal matrix $\underline{\underline{F}}$ are:

$$\left.\begin{aligned} F_{s,s-2} &= \frac{p^2(s-1)s}{(2\Lambda + 2s-3)(2\Lambda + 2s-1)} \\ F_{s,s} &= -(\Lambda + s)(\Lambda + s + 1) + \frac{p^2}{(2\Lambda+2s+1)}\left[\frac{(2\Lambda+s)s}{(2\Lambda+2s-1)} + \frac{(2\Lambda+s+1)(s+1)}{(2\Lambda+2s+3)}\right] \\ F_{s,s+2} &= \frac{p^2(2\Lambda+s+1)(2\Lambda+s+2)}{(2\Lambda+2s+3)(2\Lambda+2s+5)} \end{aligned}\right\} \tag{6.36}$$

The solution of the electronic Born-Oppenheimer equation (6.12), determining $\underline{f}(R)$, $\underline{g}(R)$ and $E_t(R)$ for state t, is achieved by requiring that A simultaneously satisfies (6.28) and (6.34). Numerical methods have been outlined by Hunter and Pritchard [183].

6.5 Levels of Approximation.

(a) The Born-Oppenheimer Approximation

At this level of approximation all terms coupling the electronic and nuclear motions are neglected. Equation (6.14) then reduces to the Born-Oppenheimer equation for nuclear motion:

$$\left\{E_s(R) - \frac{\nabla_R^2}{2\mu}\right\} F_s^{BO}(\underset{\sim}{R}) = E_{int}^{BO} \; F_s^{BO}(\underset{\sim}{R}) \qquad (6.37)$$

The advantage of this approximation is the great simplification we have achieved over (6.14). However, this simplification is achieved at the expense of a considerable loss of accuracy in the results of any calculations.

(b) The Adiabatic Approximation

In this approximation we retain the terms coupling the electronic and nuclear motions which are diagonal in the electronic state. Equation (6.14) then reduces to:

$$\left\{E_s(R) - \int \phi_s^*(R,\underset{\sim}{r}_g) \frac{\nabla_g^2}{8\mu} \phi_s(R,\underset{\sim}{r}_g) d\underset{\sim}{r}_g - \int \phi_s^*(R,\underset{\sim}{r}_g) \frac{\nabla_R^2}{2\mu} \phi_s(R,\underset{\sim}{r}_g) d\underset{\sim}{r}_g - \frac{\nabla_R^2}{2\mu}\right\} F_s^{AD}(\underset{\sim}{R})$$

$$= E_{int}^{AD} \; F_s^{AD}(\underset{\sim}{R}) \qquad (6.38)$$

The effect of the approximation is that the nuclear motion is now governed by an effective potential:

$$U_s^{AD}(R) = E_s(R) - \int \phi_s^*(R,\underset{\sim}{r}_g) \frac{\nabla_g^2}{8\mu} \phi_s(R,\underset{\sim}{r}_g) d\underset{\sim}{r}_g$$

$$- \int \phi_s^*(R,\underset{\sim}{r}_g) \frac{\nabla_R^2}{2\mu} \phi_s(R,\underset{\sim}{r}_g) d\underset{\sim}{r}_g \qquad (6.39)$$

obtained by averaging the complete Hamiltonian (6.10) over the Born-Oppenheimer electronic wave function $\phi_s(R,\underset{\sim}{r}_g)$. The averaging can readily be performed numerically [184,185]. The adiabatic corrections take account of the finite masses of the nuclei. The nuclei must move in response to the instantaneous position of the electron to maintain the uniformity of the motion of the centre of mass of the system.

Working at this level of approximation, we retain the basic simplicity of the Born-Oppenheimer equation (6.37), since the electronic and nuclear motions are effectively separated. Calculations performed within the adiabatic approximation will be considerably more accurate, because we have included the diagonal corrections in the potential. The adiabatic approximation will provide a good description, so long as there are no close lying states directly coupled to the state of interest. Because of the convenient separation it allows of the electronic and nuclear motions, the approximation is widely used in the evaluation of properties of the hydrogen molecular ion. The calculations reduce to the averaging of electronic matrix elements, obtained from $\phi_s(R,\underset{\sim}{r}_g)$, over the adiabatic vibration-rotation wave function $F_s^{AD}(\underset{\sim}{R})$. A typical example is the evaluation of nuclear hyperfine parameters [9,10].

(c) Nonadiabatic Calculations

The exact solution of the nonadiabatic problem, as expressed by (6.14), is impossible, as it requires the solution of an infinite set of coupled differential equations. Following the approximations described above we could reduce the problem by considering the coupling with only a limited number of other states, and hope that the Born expansion (6.11) converges rapidly. This approach has been investigated by Hunter and Pritchard [186]. The initial convergence for low vibrational levels of the ground state was found to be rapid, but to obtain high accuracy in the calculations and to extend them to higher vibrational levels will require excessively long Born expansions. To perform efficient and accurate nonadiabatic calculations, alternative formulations of the problem are desirable. Two approaches have been successfully applied to the ground electronic state of the hydrogen molecular ion.

i) Variational approach

In this method, investigated by Bishop [187] and by Bishop and Cheung [47], the eigenenergies of the complete Hamiltonian (6.10) are sought by variational adjustment of a trial wavefunction. Bishop and Cheung used a wavefunction of the form:

$$\psi_{mol} = \sum_{i=0}^{I} \sum_{j=0,2}^{J} \sum_{k=0}^{K} c_{ijk}\, \phi_{ijk}\,(\xi,\eta,R)$$

$$+ \sum_{i=0}^{I'} \sum_{j=1,3}^{J'} \sum_{k=0}^{K'} c_{ijk}\, \phi_{ijk}\,(\xi,\eta,R) \qquad (6.40)$$

where the basis functions of the expansion were:

$$\phi_{ijk} = \exp(-\alpha\xi)\cosh(\beta\eta)\xi^{i}\eta^{j}R^{-3/2}\exp\left[-x^2/2\right]H_k(x) \qquad (6.41)$$

The $H_k(x)$ are Hermite polynomials [144], $x = \gamma(R-\delta)$, and α,β,γ and δ are adjustable parameters chosen to minimise the energy. Even and odd states, defined by the η symmetry, are only mixed by the $(-\nabla_g.\nabla_R/2\mu_a)$ term in the Hamiltonian (6.10), so that the second triple summation only appears for heteronuclear systems, such as HD^+. The final results for the lowest nonrotating vibrational levels of the ground electronic state of HD^+, obtained with an expansion of up to 515 terms, are claimed to be accurate to $\pm$ 0.001 cm^{-1}, after the inclusion of radiative and relativistic corrections [47]. Energies for rotating states were calculated using an approximate formula for the rotational nonadiabatic shift [188]. The results compare very favourably with the available experimental data on HD^+ [46].

ii) Variation-perturbation approach

The variational approach avoids the problem of having to consider explicitly the couplings between the adiabatic states. This method makes no use of the exact adiabatic energies and wavefunctions which can readily be obtained for the hydrogen molecular ion. The adiabatic approximation is usually quite accurate, so that a method which uses the adiabatic solutions as a starting point for nonadiabatic calculations would appear to offer greater efficiency and elegance than the fully variational approach.

Wolniewicz and Poll [48,185] have developed such an alternative formulation of the problem, in which the nonadiabatic effects are treated as a perturbation to the adiabatic approximation. They define an adiabatic

Hamiltonian $\mathcal{H}^{AD}$ by the equation:

$$\mathcal{H}^{AD} = \sum_n E_n^{AD} \, |\psi_n^{AD}\rangle\langle\psi_n^{AD}| \tag{6.42}$$

such that its eigenvalues are the adiabatic molecular energy levels E_n^{AD}, and its eigenfunctions are the adiabatic states of the molecule:

$$\psi_n^{AD} = \phi_n^{BO}(R, \underset{\sim}{r}_g) F_n^{AD}(\underset{\sim}{R}) \tag{6.43}$$

which can be obtained exactly from (6.12) and (6.38). This abstract definition allows the Hamiltonian (6.10) to be decomposed into an adiabatic part, and a nonadiabatic term:

$$\mathcal{H}_{int} = \mathcal{H}^{AD} + \mathcal{H}^{'N.AD} \tag{6.44}$$

The methods of perturbation theory are used to calculate the nonadiabatic energy corrections.

$$\mathcal{H}_{int}|\psi_n^{AD}\rangle = E_n^{AD}|\psi_n^{AD}\rangle + \mathcal{H}^{'N.AD}|\psi_n^{AD}\rangle \tag{6.45}$$

since from (6.38) we have:

$$\langle\psi_n^{AD}|\mathcal{H}_{int}|\psi_n^{AD}\rangle = E_n^{AD} \tag{6.46}$$

the first order nonadiabatic energy correction is zero:

$$\langle\psi_n^{AD}|\mathcal{H}^{'N.AD}|\psi_n^{AD}\rangle = 0 \tag{6.47}$$

The variation-perturbation method of Wolniewicz and Poll is to evaluate the second order nonadiabatic energy corrections from the first order correction to the wavefunction:

$$\psi_n = \psi_n^{AD} + \psi_n' \tag{6.48}$$

The first order correction ψ_n' satisfies:

$$(\mathcal{H}^{AD} - E_n^{AD})\psi_n' = -\mathcal{H}'^{N.AD}\,\psi_n^{AD} \tag{6.49}$$

where we have used (6.47). The nonadiabatic energy correction to second order in perturbation theory is then:

$$E'' = \langle\psi_n'|\mathcal{H}'^{N.AD}|\psi_n^{AD}\rangle \tag{6.50}$$

Equation (6.49) from which the ψ_n' are to be obtained can be simplified by separating out those parts of the wavefunctions which describe their angular momenta [189]:

$$\left.\begin{aligned} \psi_n^{AD} &= u_n^{AD}\,\Omega^J_{M_J\Lambda_0} \\ \text{and}\quad \psi_n' &= \sum_\Lambda u_{n\Lambda}\,\Omega^J_{M_J\Lambda} \end{aligned}\right\} \tag{6.51}$$

The $\Omega^J_{M_J\Lambda}$ are the angular momentum eigenfunctions of a symmetric top. J is the total angular momentum, M_J its projection along a space-fixed axis and Λ its component along the internuclear axis. Λ is of course the electronic orbital angular momentum. After premultiplying by $\Omega^{J\,*}_{M_J\Lambda}$, and integrating over the angular variables, equation (6.49) becomes:

$$\begin{aligned} &(\langle J\ M_J\ \Lambda|\mathcal{H}^{AD}|J\ M_J\ \Lambda\rangle - E_n^{AD})u_{n\Lambda} \\ &\qquad = -\langle J\ M_J\ \Lambda|\mathcal{H}'^{N.AD}|J\ M_J\ \Lambda_0\rangle\, u_n^{AD} \end{aligned} \tag{6.52}$$

Appropriate differential forms for the operators $\mathcal{H}^{AD}$ and $\mathcal{H}'^{N.AD}$ are obtained as follows. From equation (6.45) we have:

$$\mathcal{H}'^{N.AD} = \mathcal{H}_{int} - E_n^{AD} \tag{6.53}$$

while, as indicated in the Born development of the theory, the adiabatic Hamiltonian:

$$\mathcal{H}^{AD} = -\frac{\nabla_g^2}{2} + \frac{1}{R} - \frac{1}{r_{1e}} - \frac{1}{r_{2e}} - \frac{\nabla_R^2}{2\mu} - \frac{\nabla_g^2}{8\mu} \qquad (6.54)$$

contains all the nonzero diagonal terms. These forms are acceptable for calculating the first order correction ψ_n'. Equation (6.49) finally becomes:

$$(\langle JM_J\Lambda|\mathcal{H}^{AD}|JM_J\Lambda\rangle - E_n^{AD})u_{n\Lambda}$$

$$= -\langle JM_J\Lambda|\mathcal{H}_{int} - E_n^{AD}|JM_J\Lambda_0\rangle\, u_n^{AD} \qquad (6.55)$$

Explicit forms for the operators appearing in (6.55) are given later. It will be shown that the only nonzero matrix elements of the complete Hamiltonian $\mathcal{H}_{int}$ are between states which satisfy:

$$\Lambda = \Lambda_0, \quad \Lambda_0 \pm 1 \qquad (6.56)$$

and for homonuclear systems there is a further symmetry rule:

$$u \longleftrightarrow u, \quad g \longleftrightarrow g, \quad \text{but } u \not\longleftrightarrow g \qquad (6.57)$$

For the ground electronic state of $HD^+ {}^1\Sigma_g$ (the g subscript is retained to label the symmetry of the Born-Oppenheimer electronic wavefunction under nuclear permutation), on which Wolniewicz & Poll have performed their most detailed calculations [48], only states of symmetry $\Sigma_g(\Lambda=0)$, $\Sigma_u(\Lambda=0)$, $\Pi_g(\Lambda = \pm 1)$ and $\Pi_u(\Lambda = \pm 1)$ are directly coupled. Qualitatively the corrections can be interpreted as arising from the inability of the electron to exactly follow the motion of the nuclei. For nuclear motion along the internuclear vector, vibrations, the lagging behind of the electron can be described by mixing states of Σ_g and Σ_u symmetry into the ground state. Both g and u corrections appear, because vibrational motion is not symmetric about the geometric centre of the nuclei. Σ_u corrections must be introduced to allow for the larger amplitude of motion of the proton compared to the heavier deuteron. When the molecule rotates Π corrections appear, to account for the slippage of the electron about the axis of rotation, and again, because of the unequal nuclear masses, both g and u corrections are required. Each of these types of state is coupled in by a separate term in $\mathcal{H}_{int}$,

so that the total second order energy correction may be written as a sum:

$$E'' = E''_{0,g} + E''_{0,u} + 2E''_{1,g} + 2E''_{1,u} \tag{6.58}$$

where we have used the fact that:

$$E''_{+1,g} = E''_{-1,g} \quad \text{and} \quad E''_{+1,u} = E''_{-1,u} \tag{6.59}$$

Since the symmetries of the states which are mixed into the ground state are known, appropriate trial forms for $u_{n\Lambda}$ are easily written down. Wolniewicz & Poll [48] use:

$$u_{n\Lambda} = R^{-5/2} \sum_{i,j} g_{ij}(\xi,\eta)\chi_{ij}(R) \tag{6.60}$$

referring to (6.32) and (6.33), for Σ_g (j even) and Σ_u (j odd) we have:

$$g_{ij}(\xi,\eta) = \exp(-\gamma\xi)(\xi+1)^{\beta}\left(\frac{\xi-1}{\xi+1}\right)^{i} P_j^{0}(\eta) \tag{6.61}$$

while for Π_g(j odd) and Π_u (j even):

$$g_{ij}(\xi,\eta) = (\xi^2-1)^{\frac{1}{2}} \exp(-\gamma\xi)(\xi+1)^{\beta}\left(\frac{\xi-1}{\xi+1}\right)^{i} P_j^{1}(\eta) \tag{6.62}$$

β and γ are adjustable parameters, determined variationally.

The approach provides an approximate method for directly performing the infinite summations appearing in equation (6.14) to second order in perturbation theory. The numerical implementation of this technique has been described fully by Wolniewicz & Poll [48,185]. For HD^+ [48], they present nonadiabatic calculations for all the bound vibration-rotation levels (v = 0 to 21) with J = 0 to 5, with an estimated accuracy of the order of 0.001 cm^{-1}. Relativistic and radiative corrections were included in these calculations. The results agree well with the available experimental data [46,53,54] see table 6.1, but there do appear to be significant deviations at higher rotational quantum numbers. We have discussed the possible origins of these discrepancies in chapter three.

TABLE 6.1

Comparison of Experimental Transition Wavenumbers for HD^+ with Nonadiabatic Calculations

Transition (v',J')-(v",J")	Experiment (cm^{-1})	Nonadiabatic[e] (cm^{-1})	Exp.-Nonad. (cm^{-1})
(1,0)-(0,1)	1869.134[a]	1869.135	-0.001
(1,1)-(0,2)	1823.533[a]	1823.533	0.000
(1,2)-(0,3)	1776.459[b]	1776.461	-0.002
(2,1)-(1,0)	1856.778[a]	1856.779	-0.001
(3,1)-(2,0)	1761.616[a]	1761.616	0.000
(3,2)-(2,1)	1797.522[a]	1797.519	0.003
(3,3)-(2,2)	1831.083[b]	1831.078	0.005
(3,1)-(2,2)	1642.108[a]	1642.111	-0.003
(17,1)-(14,0)	1813.853[c]	1813.852	0.001
(17,2)-(14,1)	1820.209[c]	1820.201	0.008
(17,3)-(14,2)	1820.201[c]	1820.187	0.014
(17,4)-(14,3)	1813.645[c]	1813.627	0.018
(17,5)-(14,4)	1800.359[c]	1800.333	0.026
(17,6)-(14,5)	1780.145[c]	1780.115[f]	0.030
(17,0)-(14,1)	1782.773[c]	1782.776	-0.003
(18,1)-(16,0)	926.4895[d]	926.490	0.000
(18,2)-(16,1)	932.2237[d]	932.220	0.004
(18,3)-(16,2)	933.2129[d]	933.207	0.006
(18,4)-(16,3)	929.2471[d]	929.238	0.009
(18,5)-(16,4)	920.1001[d]	920.089	0.011
(18,6)-(16,5)	905.5191[d]	905.512[f]	0.007
(18,7)-(16,6)	885.2183[d]	885.229[f]	-0.011
(18,0)-(16,1)	901.5648[d]	901.571	-0.006
(18,1)-(16,2)	882.7312[d]	882.743	-0.012
(17,8)-(15,7)	1078.8532[d]	1078.907[f]	-0.054

a) from reference [46]

b) from J.J.Spezeski, Ph.D. Thesis, University of Yale

c) from chapter four

d) from reference [53]

e) from reference [48]

f) extrapolated, using B, D and H from a fit to the data of [48].

More fundamentally, we question the accuracy of their approach for treating the Σ_u corrections for the highest vibrational levels of the Σ_g ground state. A second order perturbation treatment starting from the adiabatic approximation must be inadequate, since the adiabatic potentials for the ground state Σ_g and first excited state (Σ_u) become identical at very large internuclear separations. This degeneracy is lifted by the $(-\nabla_{\sim g}\cdot\nabla_{\sim R}/2\mu_a)$ term in the complete Hamiltonian (6.10), which couples together states of Σ_g and Σ_u symmetry. In reality the dissociation limits are $H^+ + D(1s)$ and $H(1s) + D^+$, which are separated by 29.8 cm^{-1}. Mixing of the Σ_u electronic wavefunction into the ground state Σ_g wave function allows the electron to follow the deuteron, as the dissociation limit of the ground state is approached. Our calculations, described later in this chapter, have addressed this problem. They lead us to believe that the results of Wolniewicz & Poll's calculations may be seriously in error for v = 21 of HD^+.

d) Relativistic and radiative corrections

A detailed treatment of the origin and calculation of these small corrections lies beyond the scope of this chapter [190-195]. The corrections are significant, and must be included to obtain accurate energy levels. The important corrections only involve the motion of the electron, and they are diagonal in the adiabatic electronic states. They may be introduced as additional terms:

$$\Delta E^r(R) = \langle \phi^{BO} | \mathcal{H}^r(R, r_{\sim g}) | \phi^{BO} \rangle \qquad (6.63)$$

to be added to the adiabatic potential (6.39). The corrections to the adiabatic energy levels are found by obtaining the vibration-rotation eigenvalues of this modified potential [47,48,195]. As we seek to perform still more accurate calculations, it may be necessary to consider some other small corrections, such as the effects of finite nuclear size. The values for some of the fundamental constants may ultimately require re-examination [196].

6.6 Matrix Elements of the Hamiltonian

In order to apply the formal Hamiltonian (6.10) to the hydrogen molecular ion, we require explicit forms for the operators in terms

of the internal coordinates of the system. We follow the treatment of Kołos & Wolniewicz [189], in their pioneering nonadiabatic calculations on the hydrogen molecule. The angular motion of the nuclei is separated out first, and the resulting matrix elements are developed in the (R,ξ,η,χ) coordinate system.

We separate off the angular motion of the nuclei by transforming from the space-fixed axis system (X,Y,Z) to a set of rotating molecule-fixed axes (x,y,z). The transformation is defined by two Euler rotations:

i) ϕ about the initial Z axis $(0 \leq \phi < 2\pi)$

ii) θ about the resultant y axis $(0 \leq \theta < \pi)$

Following the usual right handed convention:

$$\begin{pmatrix} x \\ y \\ z \end{pmatrix} = \begin{pmatrix} \cos\phi\ \cos\theta & \sin\phi\ \cos\theta & -\sin\theta \\ \sin\phi & \cos\phi & 0 \\ \cos\phi\ \sin\theta & \sin\phi\ \sin\theta & \cos\theta \end{pmatrix} \begin{pmatrix} X \\ Y \\ Z \end{pmatrix} \tag{6.64}$$

The coordinates (R,θ,ϕ) are sufficient to describe the motion of the nuclear framework. Applying the transformation (6.64), the operator ∇_R becomes:

$$\begin{aligned} \nabla_R = & \left[\cos\phi\ \sin\theta \left(\frac{\partial}{\partial R}\right)_s + \frac{\cos\phi\ \cos\theta}{R}\left(\frac{\partial}{\partial\theta}\right)_s - \frac{\sin\phi}{R\ \sin\theta}\left(\frac{\partial}{\partial\phi}\right)_s\right]\underset{\sim}{i} \\ & + \left[\sin\phi\ \sin\theta \left(\frac{\partial}{\partial R}\right)_s + \frac{\sin\phi\ \cos\theta}{R}\left(\frac{\partial}{\partial\theta}\right)_s + \frac{\cos\phi}{R\ \sin\theta}\left(\frac{\partial}{\partial\phi}\right)_s\right]\underset{\sim}{j} \\ & + \left[\cos\theta \left(\frac{\partial}{\partial R}\right)_s - \frac{\sin\theta}{R}\left(\frac{\partial}{\partial\theta}\right)_s\right]\underset{\sim}{k} \end{aligned} \tag{6.65}$$

where $\underset{\sim}{i}$, $\underset{\sim}{j}$, $\underset{\sim}{k}$ are unit vectors along the space-fixed axes (X,Y,Z). The partial differentials in the above operator are to be performed with the coordinates of the electron in the space-fixed axis system held constant, denoted by the subscript s. The Laplacian operator ∇_R^2 becomes:

$$\nabla_R^2 = \frac{1}{R^2}\frac{\partial}{\partial R}\Big)_s \left\{R^2 \frac{\partial}{\partial R}\Big)_s\right\} + \frac{1}{R^2}\left\{\frac{1}{\sin\theta}\frac{\partial}{\partial\theta}\Big)_s\left[\sin\theta\,\frac{\partial}{\partial\theta}\Big)_s\right] + \frac{1}{\sin^2\theta}\frac{\partial^2}{\partial\phi^2}\Big)_s\right\} \qquad (6.66)$$

Use of this form for ∇_R^2 in (6.37) and (6.38) allows the rotational motion to be separated, the equations can then be solved numerically, see for example [142]. Since the motion of the electron is governed by a molecule-fixed potential, $(-1/r_{1e} - 1/r_{2e})$, it is physically more reasonable to transform the operators to a molecule-fixed electron coordinate system. Partial differentials in this coordinate system are denoted by the subscript m.

$$\frac{\partial}{\partial\phi}\Big)_s = \frac{\partial}{\partial\phi}\Big)_m + \frac{\partial x}{\partial\phi}\Big)_s \frac{\partial}{\partial x}\Big)_m + \frac{\partial y}{\partial\phi}\Big)_s \frac{\partial}{\partial y}\Big)_m + \frac{\partial z}{\partial\phi}\Big)_s \frac{\partial}{\partial z}\Big)_m \qquad (6.67)$$

$$= \frac{\partial}{\partial\phi}\Big)_m - i\cos\theta\, L_z + i\sin\theta\, L_x \qquad (6.68)$$

$$\frac{\partial}{\partial\theta}\Big)_s = \frac{\partial}{\partial\theta}\Big)_m - i\, L_y \qquad (6.69)$$

$$\frac{\partial}{\partial R}\Big)_s = \frac{\partial}{\partial R}\Big)_m \qquad (6.70)$$

The ∇_R^2 operator may now be written as:

$$\nabla_R^2 = \frac{\partial^2}{\partial R^2}\Big)_m + \frac{2}{R}\frac{\partial}{\partial R}\Big)_m + \frac{1}{R^2}\left[\frac{\partial^2}{\partial\theta^2}\Big)_m + \cot\theta\,\frac{\partial}{\partial\theta}\Big)_m + \frac{1}{\sin^2\theta}\frac{\partial^2}{\partial\phi^2}\Big)_m\right]$$

$$+ \frac{1}{R^2}\left[L_Z - L^+L^- - \cot^2\theta\, L_z^2 - 2i\,\frac{\cot\theta}{\sin\theta} L_z \frac{\partial}{\partial\phi}\Big)_m\right]$$

$$+ \frac{L^+}{R^2}\left[-\frac{\partial}{\partial\theta}\Big)_m + \frac{i}{\sin\theta}\frac{\partial}{\partial\phi}\Big)_m + \cot\theta\, L_z\right] + \frac{L^-}{R^2}\left[\frac{\partial}{\partial\theta}\Big)_m + \frac{i}{\sin\theta}\frac{\partial}{\partial\phi}\Big)_m + \cot\theta\, L_z\right] \qquad (6.71)$$

where $L^{\pm} = L_x \pm i\, L_y$, and L_x, L_y and L_z are the components of the electronic orbital angular momentum in the rotating coordinate system. The operator $\underset{\sim}{\nabla}_g.\underset{\sim}{\nabla}_R$ is treated similarly, and we obtain:

$$\underset{\sim}{\nabla}_g \cdot \underset{\sim}{\nabla}_R = i\, P_z \left.\frac{\partial}{\partial R}\right]_m + \frac{i}{2R}\,(P^+ L^- - P^- L^+) + \frac{iP^+}{2R}\left[\left.\frac{\partial}{\partial\theta}\right]_m - \frac{i}{\sin\theta}\left.\frac{\partial}{\partial\phi}\right]_m - \cot\theta\, L_z\right]$$

$$+ \frac{iP^-}{2R}\left[\left.\frac{\partial}{\partial\theta}\right]_m + \frac{i}{\sin\theta}\left.\frac{\partial}{\partial\phi}\right]_m + \cot\theta\, L_z\right] \qquad (6.72)$$

where $P^{\pm} = P_x \pm iP_y$, and P_x, P_y and P_z are the components of the electron's impulse operator $\underset{\sim}{P} = -i\underset{\sim}{\nabla}_g$ in the molecule-fixed coordinate system. The remaining operators:

$$\nabla_g^2 = \left.\frac{\partial^2}{\partial x^2}\right]_m + \left.\frac{\partial^2}{\partial y^2}\right]_m + \left.\frac{\partial^2}{\partial z^2}\right]_m \qquad (6.73)$$

and $$V = \frac{1}{R} - \frac{1}{r_{1e}} - \frac{1}{r_{2e}} \qquad (6.74)$$

are independent of the Euler angles ϕ and θ.

We now expand the total molecular wavefunction as:

$$\psi_{mol} = \sum_{\Lambda} \Omega^J_{M_J\Lambda}(\theta,\phi,\chi)\, u_{\Lambda}(\xi,\eta,R) \qquad (6.75)$$

where the functions u_{Λ} depend only on the relative positions of the particles. The $\Omega^J_{M_J\Lambda}$ are the normalised symmetric top eigenfunctions:

$$\Omega^J_{M_J\Lambda} = \frac{1}{2\pi}\exp(iM_J\phi)\exp(i\Lambda\chi)\, d^J_{M_J\Lambda}(\theta) \qquad (6.76)$$

$\underset{\sim}{J}$ is the total angular momentum in the space-fixed frame, M_J is its component along the space-fixed Z axis, and Λ its component along the internuclear axis, z. The motion of the electron about the z axis is described by the angle χ.

$$L_z = -i\frac{\partial}{\partial\chi} \qquad (6.77)$$

The functions $d^J_{M_J\Lambda}(0)$ satisfy the following relations [189]:

$$\left[\frac{d^2}{d\theta^2} + \cot\theta \frac{d}{d\theta} + 2M_J\Lambda \frac{\cot\theta}{\sin\theta} - \frac{M_J^2+\Lambda^2}{\sin^2\theta} + J(J+1)\right] d^J_{M_J\Lambda} = 0 \tag{6.78}$$

$$\left[\frac{d}{d\theta} - \Lambda \cot\theta + \frac{M_J}{\sin\theta}\right] d^J_{M_J\Lambda} = \left[(J+\Lambda+1)(J-\Lambda)\right]^{\frac{1}{2}} d^J_{M_J\Lambda+1} \tag{6.79}$$

$$\left[-\frac{d}{d\theta} - \Lambda \cot\theta + \frac{M_J}{\sin\theta}\right] d^J_{M_J\Lambda} = \left[(J+\Lambda)(J-\Lambda+1)\right]^{\frac{1}{2}} d^J_{M_J\Lambda-1} \tag{6.80}$$

Substituting the above form for ψ_{mol} into the Schrödinger equation (6.8) premultiplying by $(\Omega^J_{M_J\Lambda'})^*$, and integrating over the angular coordinates, leads to the immediate elimination of the Euler angles θ and ϕ and eventually χ also. The Hamiltonian (6.10) is diagonal in J and M_J, we accordingly adopt the following notation for its matrix elements:

$$< J\ M_J\ \Lambda' |\mathcal{H}_{int}|\ J\ M_J\ \Lambda > = < \Lambda' |\mathcal{H}_{int}|\ \Lambda > \tag{6.81}$$

$$= -\frac{1}{2} < \Lambda' |\ \nabla_g^2\ |\ \Lambda > + < \Lambda' |V|\ \Lambda > - \frac{1}{8\mu} < \Lambda' |\ \nabla_g^2\ |\ \Lambda >$$

$$-\frac{1}{2\mu} < \Lambda' |\ \nabla_R^2\ |\ \Lambda > - \frac{1}{2\mu_a} < \Lambda' |\ \underset{\sim}{\nabla}_g . \underset{\sim}{\nabla}_R\ |\ \Lambda > \tag{6.82}$$

From the expressions given in (6.71), (6.72), (6.73) and (6.74) for the operators in the Hamiltonian, it is apparent that the only non-zero matrix elements of $\mathcal{H}_{int}$ are those which satisfy:

$$\Lambda' = \Lambda,\ \Lambda \pm 1 \tag{6.83}$$

Specifically, the nonvanishing matrix elements are as follows:

$$< \Lambda |\nabla_R^2| \Lambda > = \frac{\partial^2}{\partial R^2} + \frac{2}{R}\frac{\partial}{\partial R} - \frac{1}{R^2}\left[J(J+1) - \Lambda(\Lambda+1)\right] - \frac{1}{R^2} < \Lambda |L^+L^-| \Lambda > \tag{6.84}$$

$$< \Lambda-1 |\nabla_R^2| \Lambda > = -\frac{1}{R^2}\left[(J+\Lambda)(J-\Lambda+1)\right]^{\frac{1}{2}} < \Lambda-1 |L^-| \Lambda > \tag{6.85}$$

$$< \Lambda+1 |\nabla_R^2| \Lambda > = -\frac{1}{R^2}\left[(J+\Lambda+1)(J-\Lambda)\right]^{\frac{1}{2}} < \Lambda+1 |L^+| \Lambda > \tag{6.86}$$

$$< \Lambda |\underset{\sim}{\nabla}_g . \underset{\sim}{\nabla}_R| \Lambda > = i\left[P_z \frac{\partial}{\partial R} + \frac{1}{2R} < \Lambda |P^+L^- - P^-L^+| \Lambda > \right] \tag{6.87}$$

$$< \Lambda-1 | \underset{\sim}{\nabla}_g . \underset{\sim}{\nabla}_R | \Lambda > = - \frac{i}{2R} \left[(J+\Lambda)(J-\Lambda+1) \right]^{\frac{1}{2}} < \Lambda-1 | P^- | \Lambda > \tag{6.88}$$

$$< \Lambda+1 | \underset{\sim}{\nabla}_g . \underset{\sim}{\nabla}_R | \Lambda > = \frac{i}{2R} \left[(J+\Lambda+1)(J-\Lambda) \right]^{\frac{1}{2}} < \Lambda+1 | P^+ | \Lambda > \tag{6.89}$$

$$< \Lambda' | \nabla_g^2 | \Lambda > = 0 \qquad \text{unless} \quad \Lambda' = \Lambda \tag{6.90}$$

$$< \Lambda' | \nabla | \Lambda > = 0 \qquad \text{unless} \quad \Lambda' = \Lambda \tag{6.91}$$

so that we obtain the results:

$$\begin{aligned} < \Lambda | \mathcal{H}_{int} | \Lambda > = & - \frac{1}{2} < \Lambda | \nabla_g^2 | \Lambda > + V - \frac{1}{8\mu} < \Lambda | \nabla_g^2 | \Lambda > \\ & - \frac{1}{2\mu} \left\{ \frac{\partial^2}{\partial R^2} + \frac{2}{R} \frac{\partial}{\partial R} - \frac{1}{R^2} \left[J(J+1) - \Lambda(\Lambda+1) + < \Lambda | L^+ L^- | \Lambda > \right] \right\} \\ & - \frac{i}{2\mu_a} \left\{ P_z \frac{\partial}{\partial R} + \frac{1}{2R} < \Lambda | P^+ L^- - P^- L^+ | \Lambda > \right\} \end{aligned} \tag{6.92}$$

$$\begin{aligned} < \Lambda-1 | \mathcal{H}_{int} | \Lambda > = & \left[(J+\Lambda)(J-\Lambda+1) \right]^{\frac{1}{2}} \left\{ \frac{1}{2\mu R^2} < \Lambda-1 | L^- | \Lambda > \right. \\ & \left. + \frac{i}{4\mu_a R} < \Lambda-1 | P^- | \Lambda > \right\} \end{aligned} \tag{6.93}$$

$$\begin{aligned} < \Lambda+1 | \mathcal{H}_{int} | \Lambda > = & \left[(J+\Lambda+1)(J-\Lambda) \right]^{\frac{1}{2}} \left\{ \frac{1}{2\mu R^2} < \Lambda+1 | L^+ | \Lambda > \right. \\ & \left. - \frac{i}{4\mu_a R} < \Lambda+1 | P^+ | \Lambda > \right\} \end{aligned} \tag{6.94}$$

all differentials are to be performed within the molecule-fixed coordinate system, so the subsrcipt m has been dropped. Expressions for the above matrix elements can be developed in terms of the internal coordinates (R, ξ, η, χ) of the system. We first define some useful operator abbreviations:

$$X_\Lambda = \frac{1}{(\xi^2-\eta^2)} \left[\frac{\partial}{\partial \xi} (\xi^2-1) \frac{\partial}{\partial \xi} + \frac{\partial}{\partial \eta} (1-\eta^2) \frac{\partial}{\partial \eta} \right] - \frac{\Lambda^2}{(\xi^2-1)(1-\eta^2)} \tag{6.95}$$

$$Y = \frac{1}{(\xi^2-\eta^2)} \left[\xi(\xi^2-1) \frac{\partial}{\partial \xi} + \eta(1-\eta^2) \frac{\partial}{\partial \eta} \right] \tag{6.96}$$

$$Z = \frac{1}{(\xi^2-\eta^2)} \left[\eta(\xi^2-1) \frac{\partial}{\partial \xi} + \xi(1-\eta^2) \frac{\partial}{\partial \eta} \right] \tag{6.97}$$

$$A = \frac{\left[(\xi^2-1)(1-\eta^2)\right]^{\frac{1}{2}}}{(\xi^2-\eta^2)} \left[\xi \frac{\partial}{\partial \xi} - \eta \frac{\partial}{\partial \eta} \right] \tag{6.98}$$

$$B = \frac{\left[(\xi^2-1)(1-\eta^2)\right]^{\frac{1}{2}}}{(\xi^2-\eta^2)} \left[\eta \frac{\partial}{\partial \xi} - \xi \frac{\partial}{\partial \eta} \right] \tag{6.99}$$

The partial derivatives with respect to R appearing in the expressions (6.84), (6.87) and (6.92) are to be performed with the molecule-fixed cartesian coordinates (x,y,z) held constant. With the more useful set of coordinates (ξ,η,χ) held constant we obtain:

$$\left.\frac{\partial}{\partial R}\right)_{xyz} = \left.\frac{\partial}{\partial R}\right)_{\xi\eta\chi} - \frac{Y}{R} \tag{6.100}$$

Using the results given in the treatment of the electronic Born-Oppenheimer equation, namely (6.16), (6.17), and (6.19), we can obtain the results:

$$\langle \Lambda | \nabla_g^2 | \Lambda \rangle = \frac{4}{R^2} X_\Lambda \tag{6.101}$$

$$V = \frac{1}{R} - \frac{4\xi}{R(\xi^2-\eta^2)} \tag{6.102}$$

$$L^+ = \exp(i\chi) \left\{ B + \frac{i\xi\eta}{\left[(\xi^2-1)(1-\eta^2)\right]^{\frac{1}{2}}} \frac{\partial}{\partial \chi} \right\} \tag{6.103}$$

$$\langle \Lambda+1 | L^+ | \Lambda \rangle = B - \frac{\xi\eta\Lambda}{\left[(\xi^2-1)(1-\eta^2)\right]^{\frac{1}{2}}} \tag{6.104}$$

$$L^- = \exp(-i\chi) \left\{ -B + \frac{i\xi\eta}{\left[(\xi^2-1)(1-\eta^2)\right]^{\frac{1}{2}}} \frac{\partial}{\partial \chi} \right\} \tag{6.105}$$

$$< \Lambda-1|L^-|\Lambda > = -B - \frac{\xi\eta\Lambda}{[(\xi^2-1)(1-\eta^2)]^{\frac{1}{2}}} \tag{6.106}$$

$$P^+ = \frac{2\exp(i\chi)}{R} \left\{-iA + \frac{1}{[(\xi^2-1)(1-\eta^2)]^{\frac{1}{2}}} \frac{\partial}{\partial\chi}\right\} \tag{6.107}$$

$$< \Lambda+1|P^+|\Lambda > = \frac{2i}{R} \left\{-A + \frac{\Lambda}{[(\xi^2-1)(1-\eta^2)]^{\frac{1}{2}}}\right\} \tag{6.108}$$

$$P^- = \frac{2\exp(-i\chi)}{R} \left\{-iA - \frac{1}{[(\xi^2-1)(1-\eta^2)]^{\frac{1}{2}}} \frac{\partial}{\partial\chi}\right\} \tag{6.109}$$

$$< \Lambda-1|P^-|\Lambda > = \frac{2i}{R} \left\{-A - \frac{\Lambda}{[(\xi^2-1)(1-\eta^2)|^{\frac{1}{2}}}\right\} \tag{6.110}$$

$$P_z = -\frac{2i}{R} Z \tag{6.111}$$

With these results we can obtain the matrix elements of the operators appearing in the Hamiltonian (6.10). They are as follows:

$$< \Lambda|-\frac{\nabla_g^2}{2} + V | \Lambda > = -\frac{2X_\Lambda}{R^2} + \frac{1}{R}\left[1 - \frac{4}{(\xi^2-\eta^2)}\right] \tag{6.112}$$

$$< \Lambda|-\frac{\nabla_g^2}{8\mu} | \Lambda > = -\frac{X_\Lambda}{2\mu R^2} \tag{6.113}$$

$$< \Lambda|-\frac{\nabla_R^2}{2\mu}| \Lambda > = -\frac{1}{2\mu}\left[\frac{1}{R^2}\frac{\partial}{\partial R}\left(R^2\frac{\partial}{\partial R}\right) - \frac{2}{R^2} Y \frac{\partial}{\partial R} R\right.$$

$$\left. + \frac{(\xi^2+\eta^2-1)}{R^2} X_\Lambda - \frac{J(J+1)}{R^2} + \frac{2\Lambda^2}{R^2}\right] \tag{6.114}$$

$$< \Lambda | - \frac{\underset{\sim}{\nabla}_g \cdot \underset{\sim}{\nabla}_R}{2\mu_a} | \Lambda > = - \frac{1}{\mu_a R^2} \left[Z \frac{\partial}{\partial R} R - \xi\eta X_\Lambda \right] \qquad (6.115)$$

The elements off diagonal in Λ are:

$$< \Lambda-1 | - \frac{\nabla_R^2}{2\mu} | \Lambda > = \frac{\left[(J+\Lambda)(J-\Lambda+1)\right]^{\frac{1}{2}}}{2\mu R^2} \left\{ - B - \frac{\xi\eta\Lambda}{\left[(\xi^2-1)(1-\eta^2)\right]^{\frac{1}{2}}} \right\} \qquad (6.116)$$

$$< \Lambda+1 | - \frac{\nabla_R^2}{2\mu} | \Lambda > = \frac{\left[(J+\Lambda+1)(J-\Lambda)\right]^{\frac{1}{2}}}{2\mu R^2} \left\{ B - \frac{\xi\eta\Lambda}{\left[(\xi^2-1)(1-\eta^2)\right]^{\frac{1}{2}}} \right\} \qquad (6.117)$$

$$< \Lambda-1 | - \frac{\underset{\sim}{\nabla}_g \cdot \underset{\sim}{\nabla}_R}{2\mu_a} | \Lambda > = \frac{\left[(J+\Lambda)(J-\Lambda+1)\right]^{\frac{1}{2}}}{2\mu_a R^2} \left\{ A + \frac{\Lambda}{\left[(\xi^2-1)(1-\eta^2)\right]^{\frac{1}{2}}} \right\} \qquad (6.118)$$

$$< \Lambda+1 | - \frac{\underset{\sim}{\nabla}_g \cdot \underset{\sim}{\nabla}_R}{2\mu_a} | \Lambda > = \frac{\left[(J+\Lambda+1)(J-\Lambda)\right]^{\frac{1}{2}}}{2\mu_a R^2} \left\{ - A + \frac{\Lambda}{\left[(\xi^2-1)(1-\eta^2)\right]^{\frac{1}{2}}} \right\} \qquad (6.119)$$

There are symmetry selection rules on the electronic matrix elements of the above operators. We define the symmetries of the electronic wavefunctions $\phi^{BO}(\xi,\eta)$ with respect to inversion through the centre of charge of the molecule, the midpoint of the internuclear vector. This operation is equivalent to $\eta \longrightarrow -\eta$. Since the $\phi^{BO}(\xi,\eta)$ are obtained from the Born-Oppenheimer electronic equation, which treats the nuclei as fixed point charges, the $g[\phi^{BO}(\xi,\eta) = \phi^{BO}(\xi,-\eta)]$ or $u[\phi^{BO}(\xi,\eta) = -\phi^{BO}(\xi,-\eta)]$ symmetry label applies for HD^+ as well as H_2^+. The operators (6.112), (6.113) and (6.114) are diagonal in Λ, and even in η, so there is the rule:

$$g \longleftrightarrow g \ , \ u \longleftrightarrow u \ , \quad \text{but} \quad u \not\longleftrightarrow g \qquad (6.120)$$

for the odd operator (6.115), which does not appear for H_2^+ ($1/\mu_a = 0$), the selection rule is:

$$g \not\longleftrightarrow g \ , \ u \not\longleftrightarrow u \ , \quad \text{but} \quad u \longleftrightarrow g \qquad (6.121)$$

For the operators off-diagonal in Λ , the matrix elements of the even operators (6.118) and (6.119) (heteronuclear case only) satisfy (6.121), while those of the odd operators (6.116) and (6.117) obey (6.120). Considering the specific case of the ground (Σ_g) state of the hydrogen molecular ion, the adiabatic Hamiltonian, defined by (6.54) is given by:

$$< 0_g|\mathcal{H}^{AD}|0_g > = -\frac{2X_0}{R^2} + \frac{1}{R}\left[1 - \frac{4}{(\xi^2-\eta^2)}\right]$$

$$- \frac{1}{2\mu R^2}\left[\frac{\partial}{\partial R}\left(R^2\frac{\partial}{\partial R}\right) - 2Y\frac{\partial}{\partial R}R + (\xi^2+\eta^2)X_0 - J(J+1)\right] \qquad (6.122)$$

Finally the matrix elements of the complete Hamiltonian (6.10) are as follows:

$$< 0_g'|\mathcal{H}_{int}|0_g > = < 0_g'|\mathcal{H}^{AD}|0_g > \qquad (6.123)$$

$$< 0_u|\mathcal{H}_{int}|0_g > = < 0_u| -\frac{\nabla_g\cdot\nabla_R}{2\mu_a}|0_g > \qquad (6.124)$$

$$= -\frac{1}{\mu_a R^2}\left[Z\frac{\partial}{\partial R}R - \xi\eta X_0\right] \qquad (6.125)$$

$$< \pm 1_g|\mathcal{H}_{int}|0_g > = < \pm 1_g|-\frac{\nabla_R^2}{2\mu}|0_g > \qquad (6.126)$$

$$= \pm\frac{[J(J+1)]^{\frac{1}{2}}B}{2\mu R^2} \qquad (6.127)$$

$$< \pm 1_u|\mathcal{H}_{int}|0_g > = < \pm 1_u|-\frac{\nabla_g\cdot\nabla_R}{2\mu_a}|0_g > \qquad (6.128)$$

$$= \mp\frac{[J(J+1)]^{\frac{1}{2}}}{2\mu_a R^2}A \qquad (6.129)$$

Matrix elements (6.122) to (6.129) are the operators required for performing nonadiabatic calculations, such as those described by Wolniewicz & Poll [48]. Notice in particular that the $\Sigma - \Sigma$ coupling operators are J independent, while those for $\Pi - \Sigma$ are proportional to $[J(J+1)]^{\frac{1}{2}}$, and so will give second order energy corrections proportional to $J(J+1)$.

6.7 Numerical Calculations.

In the next few sections, we describe preliminary results from some numerical calculations on the hydrogen molecular ion. Commencing with the solutions to the electronic Born-Oppenheimer equation (6.12), we have obtained the Born-Oppenheimer potentials for the ground state ($1s\sigma_g, {}^2\Sigma_g^+$) and first excited state ($2p\sigma_u, {}^2\Sigma_u^+$) of the hydrogen molecular ion. The adiabatic corrections to these potentials, see (6.39), have been calculated, and also the electronic transition moment between the states. We have investigated the effect of the $(-\underset{\sim}{\nabla}_g.\underset{\sim}{\nabla}_R/2\mu_a)$ term in the complete Hamiltonian (6.10) for HD^+, which couples together the $1s\sigma_g$ and $2p\sigma_u$ states (6.125). New effective potentials are proposed, and the influence of the coupling on the electronic wave functions is calculated. Evaluation of the electronic transition moment between the coupled electronic wave functions provides a dramatic illustration of the effects of this nonadiabatic mixing on the properties of the HD^+ molecular ion. Vibration-rotation energy levels have been calculated at all three stages, they can be compared with the available experimental spectroscopic data and also the nonadiabatic calculations of Wolniewicz & Poll [48].

6.8 Calculation of the Born-Oppenheimer Potential.

The methods for solving the electronic Born-Oppenheimer equation (6.12) in the (R,ξ,η,χ) coordinate system have already been outlined, see section 6.4. We have solved the equation using both the Hylleraas (6.27) and Jaffé (6.32) expansions. Using an estimate for $E_t(R)$, the matrices $\underline{\underline{G}}$ and $\underline{\underline{F}}$ are set up for a given R and Λ. The Rayleigh quotient inverse iteration algorithm [197] is used to solve the matrix eigenvalue equations (6.28) and (6.34), starting from reasonable guesses at the

eigenvectors $\underline{f}$ and $\underline{g}$, and the eigenvalue A. The solution of the matrix equations involved is particularly simple, because both $\underline{\underline{F}}$ and $\underline{\underline{G}}$ are tridiagonal, so that Gauss elimination [197] can immediately be used. Finally $E_t(R)$ is adjusted until A simultaneously satisfies (6.28) and (6.34).

The required reasonable guesses at $E_t(R)$, A, $\underline{f}$ and $\underline{g}$ are obtained in the following manner. At the first R value, consideration of the united atom limit gives an initial guess at the separation constant of:

$$A = -\ell(\ell+1) \tag{6.130}$$

$$\text{and } E_t(R) = -\frac{2}{n^2} + \frac{1}{R} \tag{6.131}$$

For the ground state of the hydrogen molecular ion, the united atom limit is $He^+(1s)$, giving A = 0 and $[E_t(R) - 1/R] = -2.0$, while for the first excited state the limit is $He^+(2p)$, and we have A = -2.0, $[E_t(R) - 1/R] = -0.5$. The first guesses at the eigenvectors are:

$$\underline{g} = \begin{pmatrix} 1 \\ 0 \\ \vdots \\ 0 \end{pmatrix} \quad \text{and} \quad \underline{f} = \begin{pmatrix} 1 \\ 0 \\ \vdots \\ 0 \end{pmatrix} \tag{6.132}$$

Note that the η expansion for the $1s\sigma_g$ ground state is restricted to even Legendre polynomials ($f_{2s+1} = 0$), while that for the $2p\sigma_u$ state contains only odd terms ($f_{2s} = 0$). For subsequent values of R the solutions are propagated, the initial guesses at A, $E_t(R)$, $\underline{f}$ and $\underline{g}$ are the final results of the calculation at the preceeding R value. The series are truncated when the coefficients of two successive terms are less than 10^{-13} of the first. Iterative adjustment of $E_t(R)$ is discontinued when the A values given by (6.28) and (6.34) agree to better than one part in 10^{13}. The results of the calculations are found to be insensitive to a change by a factor of 10 in these convergence criteria. They agree with those previously reported by others, notably Peek [198].

The electronic wavefunctions are normalised according to:

$$\underset{\sim}{f}.\underset{\sim}{f} = 1 \tag{6.133}$$

$$\text{and} \quad \int L^2(R,\xi)M^2(R,\eta)\,\frac{R^3}{8}\,(\xi^2-\eta^2)d\xi d\eta = 1 \tag{6.134}$$

The integrals appearing in (6.134) are evaluated analytically, by using the properties of the orthogonal polynomials $L_n^{\Lambda}[2p(\xi-1)]$ and $P_{\Lambda+s}^{\Lambda}(\eta)$ [144]. For the Jaffé expansion (6.32) the ξ integrals are obtained numerically, by Gauss-Laguerre quadrature [197]. The use of the Jaffé expansion provides a valuable test of the results we obtain from the Hylleraas expansion. Table 6.2 lists the potentials obtained, they are plotted in figure 6.3. Note that there is a small minimum in the $2p\sigma_u$ potential at about 12.5 Bohrs.

6.9 Calculation of the Electronic Transition Moment.

We define the electronic transition moment as:

$$\underset{\sim}{Q}(R) = \int \phi_f^*(R,\underset{\sim}{r}_g)\underset{\sim}{r}_g\,\phi_i(R,\underset{\sim}{r}_g)d\underset{\sim}{r}_g \tag{6.135}$$

For a parallel transition, such as $2p\sigma_u \leftarrow 1s\sigma_g$, only the molecule-fixed z component of $\underset{\sim}{Q}$ is non-zero. In the (R,ξ,η,χ) coordinate system.

$$Q_z(R) = \frac{R^4}{16}\int \phi_f^*(R,\xi,\eta,\chi)\xi\eta\,\phi_i(R,\xi,\eta,\chi)(\xi^2-\eta^2)d\xi\,d\eta\,d\chi \tag{6.136}$$

Integration over χ gives the selection rule $\Delta\Lambda = 0$ expected for a parallel transition. The transition moment operator is proportional to η, giving the further symmetry selection rules:

$$g \not\longleftrightarrow g\ ,\ u \not\longleftrightarrow u\ ,\ \text{but}\ u \longleftrightarrow g \tag{6.137}$$

The integral in (6.136) is separable, and using the Hylleraas expansion the ξ and η integrals are readily evaluated analytically. A check on the calculations is provided by comparing the results with those obtained from the Jaffé expansion. Selected values of the $2p\sigma_u \leftarrow 1s\sigma_g$ transition moment are presented in table 6.2, and $Q_z(R)$ is plotted in figure 6.4. It is this large transition moment which is responsible for the strong

TABLE 6.2

Born-Oppenheimer Potentials and Parallel Transition Moment for the $1s\sigma_g$ and $2p\sigma_u$ States of the Hydrogen Molecular Ion.

R	$E_{1s\sigma_g}(R)$	$E_{2p\sigma_u}(R)$	$Q_z(R)$
(Bohrs)	(Hartress)	(Hartrees)	(electron charge.Bohr)
1.0	-0.4517863134	0.4351863749	0.6748985439
2.0	-0.6026342145	-0.1675343922	1.049942577
3.0	-0.5775628640	-0.3680850000	1.432686784
4.0	-0.5460848837	-0.4455506394	1.870909773
5.0	-0.5244202952	-0.4772916132	2.360694818
6.0	-0.5119690485	-0.4906438924	2.879085039
7.0	-0.5055940042	-0.4962717125	3.404325927
8.0	-0.5025703886	-0.4986060156	3.925941423
9.0	-0.5011954529	-0.4995438295	4.441978213
10.0	-0.5005787289	-0.4999010686	4.953507721
11.0	-0.5002992294	-0.5000244219	5.461905650
12.0	-0.5001683070	-0.5000578946	5.968185014
13.0	-0.5001034957	-0.5000594682	6.473006392
14.0	-0.5000689508	-0.5000515049	6.976794709
15.0	-0.5000489385	-0.5000420624	7.479829521
16.0	-0.5000363755	-0.5000336777	7.982300624
17.0	-0.5000279358	-0.5000268817	8.484340846
18.0	-0.5000219639	-0.5000215534	8.986045645
19.0	-0.5000175749	-0.5000174155	9.487485196
20.0	-0.5000142593	-0.5000141977	9.988712102
30.0	-0.5000027907	-0.5000027907	14.99499526
∞	-0.5	-0.5	∞

1 Bohr = 0.52917706 Å

1 Hartree = 219474.6354 cm^{-1}

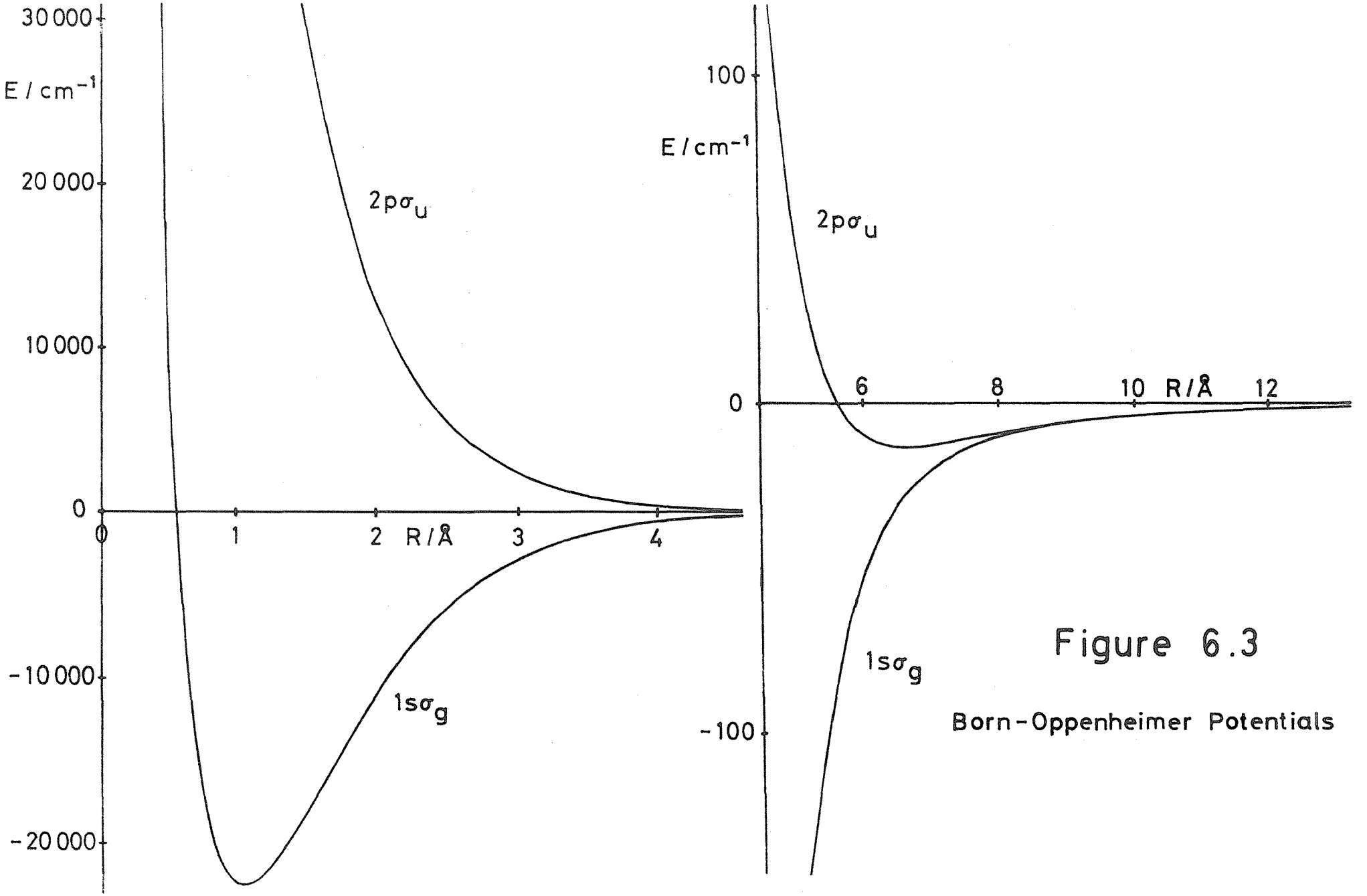

Figure 6.3

Born-Oppenheimer Potentials

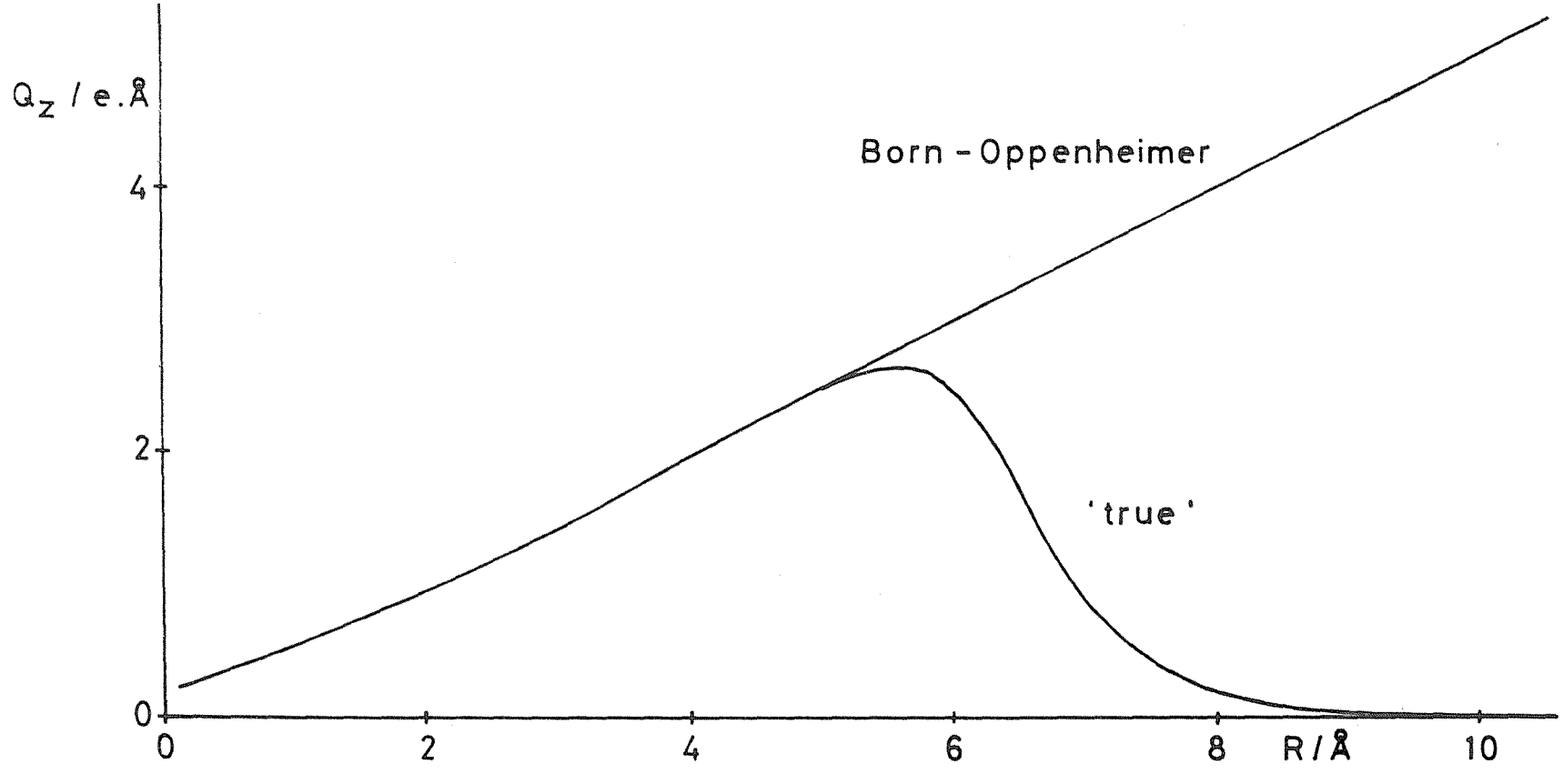

Figure 6.4

$2p\sigma_u - 1s\sigma_g$ Transition Moment

infrared photodissociation of HD^+ [53], which makes feasible our spectroscopic studies of this ion. At large R we see that:

$$Q_z(R) \simeq \frac{R}{2} \tag{6.138}$$

This proportionality to R is a characteristic feature of charge transfer transitions [199]. At very large R, when the molecule has dissociated it is physically unrealistic, for the transition moment must then be zero. We will see that when the two states are coupled, the correct behaviour is obtained.

6.10 Calculation of the Adiabatic Corrections.

The adiabatic corrections are:

$$\int \phi_s^* < \Lambda \mid -\frac{\nabla_g^2}{8\mu} \mid \Lambda > \phi_s \, d\underset{\sim}{r}_g \tag{6.139}$$

$$\text{and} \quad \int \phi_s^* < \Lambda \mid -\frac{\nabla_R^2}{2\mu} \mid \Lambda > \phi_s \, d\underset{\sim}{r}_g \tag{6.140}$$

where for HD^+ $\mu = 1223.8984$, in atomic units, using the values of the fundamental constants given by Cohen & Taylor [105]. Explicit forms for the operators can be found in section 6.6. We consider first the evaluation of the ∇_g^2 correction. Noting that the Born-Oppenheimer electronic wavefunctions satisfy (6.12), we see that:

$$\int \phi_s^* < \Lambda \mid -\frac{\nabla_g^2}{8\mu} \mid \Lambda > \phi_s \, d\underset{\sim}{r}_g = \frac{E_s(R)}{4\mu} - \frac{1}{4\mu R}$$

$$+ \frac{1}{\mu} \int \phi_s^* \, \frac{\xi}{R(\xi^2-\eta^2)} \, \phi_s \, \frac{R^3}{8} (\xi^2-\eta^2) d\xi \, d\eta \tag{6.141}$$

The problem of obtaining the ∇_g^2 correction then reduces to the evaluation of:

$$\int L^2(\xi)\, M^2(\eta)\, \xi\, d\xi\, d\eta \tag{6.142}$$

This integral is separable, and is then readily evaluated analytically, by utilisation of the properties of the orthogonal polynomials in the expansions for L and M [144]. The ∇_R^2 correction is more difficult:

$$\int \phi_s^* < \Lambda \mid -\frac{\nabla_R^2}{2\mu} \mid \Lambda > \phi_s \, d\underset{\sim}{r}_g = -\frac{1}{2\mu}\left[\int \phi_s^* \frac{\partial^2}{\partial R^2} \phi_s \, d\underset{\sim}{r}_g \right.$$

$$+ \frac{2}{R}\int \phi_s^* \frac{\partial}{\partial R} \phi_s \, d\underset{\sim}{r}_g - \frac{2}{R}\int \phi_s^* Y \frac{d}{dR} \phi_s \, d\underset{\sim}{r}_g$$

$$- \frac{2}{R^2}\int \phi_s^* Y \phi_s \, d\underset{\sim}{r}_g + \frac{1}{R^2}\int \phi_s^* (\xi^2+\eta^2) X_\Lambda \phi_s \, d\underset{\sim}{r}_g$$

$$\left. - \int \phi_s^* \frac{\nabla_g^2}{4} \phi_s \, d\underset{\sim}{r}_g - \frac{J(J+1)}{R^2} + \frac{2\Lambda^2}{R^2} \right] \tag{6.143}$$

and requires the determination of the effects of the operators $\partial/\partial R$ and $\partial^2/\partial R^2$ on the electronic wavefunctions. It fortunately transpires that all the integrals prove to be separable, and can be evaluated analytically using results given in [144].

The wavefunctions depend on R through the variation of the coefficients $\underline{f}$ and $\underline{g}$ with R. They also depend parametrically on R due to the appearance of p in the Hylleraas expansion, see (6.20); for the Jaffé expansion the R dependence of σ must also be considered. We follow the analytical method proposed by Wolniewicz & Poll [185]. We first require $dE_s(R)/dR$, from which we may then obtain dp/dR and $d\sigma/dR$. We apply the virial theorem [200] in the form:

$$\frac{dE_s(R)}{dR} = -\frac{1}{R}\left[2E_s(R) - {}^1/_R + \int \phi_s^* V \phi_s \, d\underset{\sim}{r}_g\right] \tag{6.144}$$

We obtain the vectors $d\underline{f}/dR$ and $d\underline{g}/dR$ in the following manner. Defining $\hat{\underline{f}}$ as the lefthand eigenvector of $\underline{\underline{F}}$, it satisfies:

$$\underline{\underline{F}}^T \, \underline{\hat{f}} = A \, \underline{\hat{f}} \tag{6.145}$$

where $\underline{\underline{F}}^T$ is the transpose of $\underline{\underline{F}}$. The equation (6.145) is readily solved by matrix methods, subject to the constraint:

$$\underline{\hat{f}} . \underline{f} = 1 \tag{6.146}$$

Using dp/dR, $d\underline{\underline{F}}/dR$ is set up, and dA/dR obtained from:

$$\frac{dA}{dR} = \underline{\hat{f}} \, \frac{d\underline{\underline{F}}}{dR} \, \underline{f} \tag{6.147}$$

With $\frac{dA}{dR}$ determined, we solve:

$$(\underline{\underline{F}} - A) \, \frac{d\underline{f}'}{dR} = - \left(\frac{d\underline{\underline{F}}}{dR} - \frac{dA}{dR} \right) \underline{f} \tag{6.148}$$

But since A is an eigenvalue of $\underline{\underline{F}}$ (6.148) does not have a unique solution, for if $d\underline{f}'/dR$ is a solution, then so also is:

$$\frac{d\underline{f}}{dR} = \frac{d\underline{f}'}{dR} + c\underline{f} \tag{6.149}$$

c is determined by recalling (6.133), this provides the constraint:

$$\frac{d\underline{f}}{dR} . \underline{f} = 0 \tag{6.150}$$

$$\text{giving} \quad c = - \frac{d\underline{f}'}{dR} . \underline{f} \tag{6.151}$$

In practice equation (6.148) is solved with the first element of $d\underline{f}'/dR$ fixed at the value obtained from the previous point; for the first point we use $df_0'/dR = 0$ $(1s\sigma_g)$ or $df_1'/dR = 0$ $(2p\sigma_u)$.

$d\underline{g}/dR$ is similarly given by:

$$(\underline{\underline{G}} + A) \, \frac{d\underline{g}'}{dR} = - \left(\frac{d\underline{\underline{G}}}{dR} + \frac{dA}{dR} \right) \underline{g} \tag{6.152}$$

in this case the required additional constraint is provided by:

$$\frac{d}{dR}\left[\int L^2(\xi)M^2(\eta)\,\frac{R^3}{8}\,(\xi^2-\eta^2)d\xi\,d\eta\right] = 0 \qquad (6.153)$$

and at the first point we use $dg_0'/dR = 1$. The effects of $\partial^2/\partial R^2$ are ascertained in a similar fashion.

An additional point of note concerns the evaluation of the integral:

$$\int \phi_s^*(\xi^2+\eta^2)X_\Lambda\phi_s\,d\underset{\sim}{r}_g \qquad (6.154)$$

The calculation is greatly simplified by using (6.24) and (6.25).

Two of the integrals appearing in (6.143) can be evaluated analytically, without recourse to a specific form for the wavefunction:

$$\int \phi_s^*\,\frac{\partial}{\partial R}\,\phi_s\,d\underset{\sim}{r}_g = -\frac{3}{2R}\text{ , from (6.153),} \qquad (6.155)$$

and from integration by parts:

$$\int \phi_s^*\,Y\,\phi_s\,d\underset{\sim}{r}_g = -\frac{3}{2} \qquad (6.156)$$

We see that in (6.143) these two integrals will cancel.

Checks on the calculations are provided by these last two results, and also by approximate numerical calculations of the derivatives with respect to R of $E_s(R)$, p, σ, A, $\underline{f}$ and $\underline{g}$. As a final test the entire calculation has been repeated using the Jaffé expansion, no discrepancies are found. The results are presented in table 6.3, and in figure 6.5. For the ground state the values obtained agree with those published by Bishop and Wetmore [184] for H_2^+, after rescaling to allow for the change in reduced mass, μ. Adiabatic corrections to the $2p\sigma_u$ potential do not appear to have previously been reported. The adiabatic corrections are positive, the absolute energies (relative to separated nuclei and electron) are decreased. The corrections are slightly smaller at the minimum of the potential than at the dissociation limit, so that the adiabatic dissociation energy D_e^{AD} is slightly larger than the depth of the Born-Oppenheimer well. The increase is about 2.2 cm^{-1} for the ground state of HD^+. Within the adiabatic approximation the absolute

TABLE 6.3

Adiabatic Corrections to the Born-Oppenheimer Potentials for HD^+

a) for the $1s\sigma_g$ state

R (Bohrs)	Adiabatic Corrections $-\nabla_g^2/2\mu$ ($\times 10^{-3}$ Hartrees)	$-\nabla_R^2/2\mu$ ($\times 10^{-3}$ Hartrees)
1.0	0.1986987846	0.0742949852
2.0	0.1229796234	0.0714065948
3.0	0.0970025620	0.0748965465
4.0	0.0894917944	0.0826353371
5.0	0.0901835833	0.0907434727
6.0	0.0936927755	0.0964912937
7.0	0.0970834475	0.0995750632
8.0	0.0993968868	0.1009988356
9.0	0.1007284235	0.1016018580
10.0	0.1014275801	0.1018697639
11.0	0.1017771851	0.1019910073
12.0	0.1019482303	0.1020489759
13.0	0.1020318423	0.1020787478
14.0	0.1020735031	0.1020953611
15.0	0.1020951040	0.1021054447
16.0	0.1021069870	0.1021120374
17.0	0.1021140153	0.1021166091
18.0	0.1021184961	0.1021199199
19.0	0.1021215510	0.1021223939
20.0	0.1021237481	0.1021242853
30.0	0.1021309446	0.1021309813
∞	0.1021326570	0.1021326570

TABLE 6.3 continued

b) for the $2p\sigma_u$ state

R (Bohrs)	Adiabatic Corrections $-\nabla_g^2/2\mu$ ($\times 10^{-3}$ Hartrees)	$-\nabla_R^2/2\mu$ ($\times 10^{-3}$ Hartrees)
1.0	0.1391457660	0.8417990748
2.0	0.1642026659	0.2361073802
3.0	0.1478602597	0.1468243929
4.0	0.1299620817	0.1209029552
5.0	0.1178388090	0.1104109693
6.0	0.1105369159	0.1057109967
7.0	0.1064101206	0.1035937781
8.0	0.1041996424	0.1026729774
9.0	0.1030749993	0.1022946939
10.0	0.1025310910	0.1021514938
11.0	0.1022814347	0.1021045858
12.0	0.1021735487	0.1020944322
13.0	0.1021307288	0.1020968255
14.0	0.1021162637	0.1021025109
15.0	0.1021133659	0.1021082589
16.0	0.1021147039	0.1021131404
17.0	0.1021172464	0.1021170397
18.0	0.1021198382	0.1021200875
19.0	0.1021221045	0.1021224589
20.0	0.1021239749	0.1021243105
30.0	0.1021309446	0.1021309813
∞	0.1021326570	0.1021326570

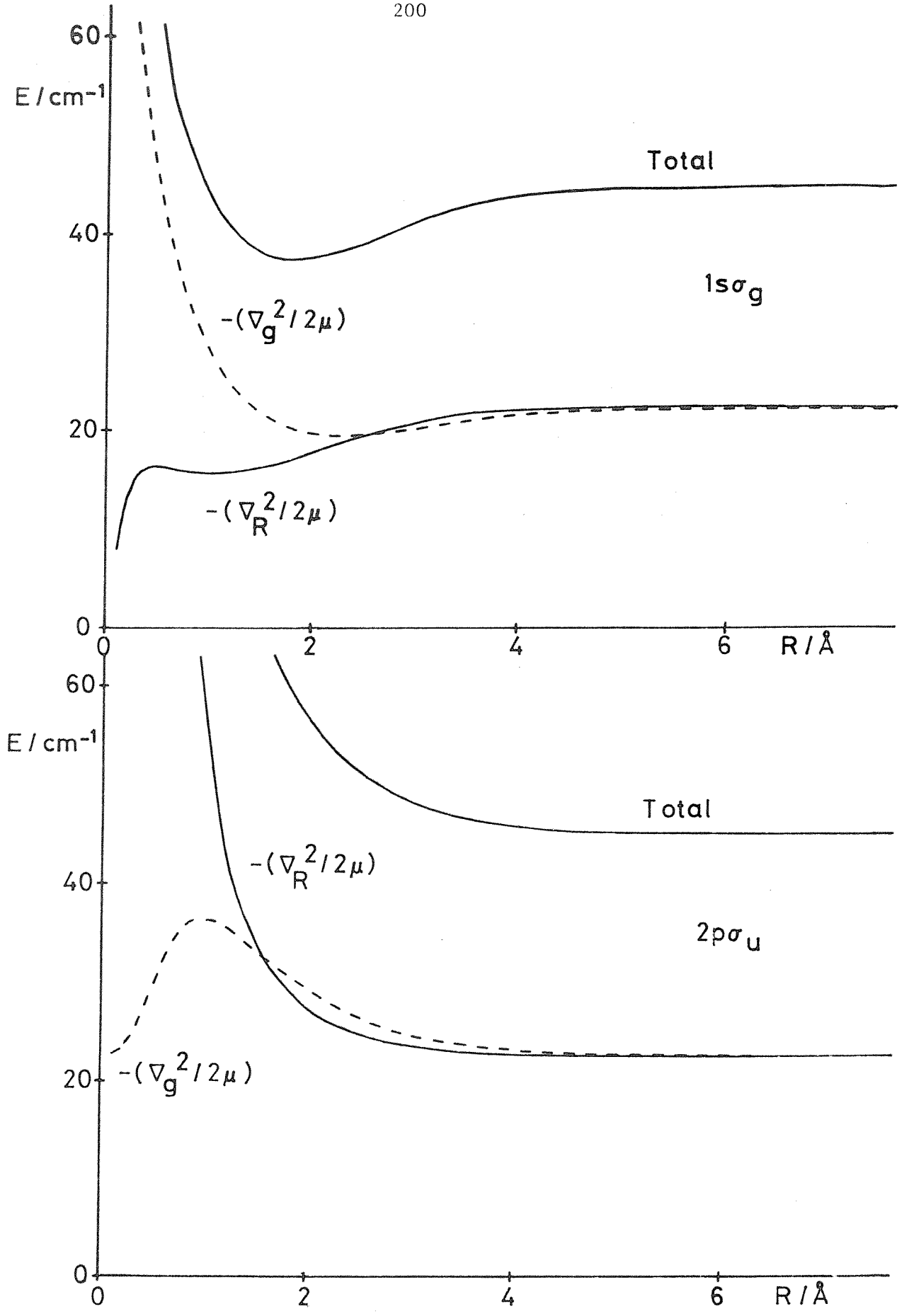

Figure 6.5

Adiabatic Corrections for HD^+

energies of the dissociation products of the ground state ($1s\sigma_g$), and first excited state ($2p\sigma_u$) of HD^+ are identical, -0.499795735 Hartrees. This value is the average of the energies of the true dissociation limits of $H^+ + D$ (-0.499863778) and $H + D^+$ (-0.499727691). This false degeneracy is removed by considering the coupling between the ground and first excited states of HD^+.

6.11 The Coupling between $1s\sigma_g$ and $2p\sigma_u$.

In the HD^+ molecular ion, the $1s\sigma_g$ and $2p\sigma_u$ adiabatic states are coupled together by the $(-\underset{\sim}{\nabla}_g.\underset{\sim}{\nabla}_R/2\mu_a)$ term in the complete Hamiltonian (6.10). This coupling has a marked effect on the behaviour of HD^+ near the dissociation limit. It breaks down the g/u symmetry of the electronic wavefunction, allowing the electron to follow one of the nuclei as the molecule dissociates. The physically unrealistic behaviour of the transition moment at very large R is removed, and the correct dissociation limits are obtained. The coupling term operates on both the electronic and nuclear parts of the molecular wavefunction, so that in a full treatment of its effects the concept of a potential curve for nuclear motion will be lost. As we have indicated previously this concept is valuable, both for visualising the physical aspects of the problem and for calculating properties of the molecule. We have evaluated the electronic matrix element of $(-\underset{\sim}{\nabla}_g.\underset{\sim}{\nabla}_R/2\mu_a)$ between the states, and used the results to construct effective potential curves for the ground and first excited states of HD^+. The extent of mixing of the electronic wavefunctions has also been calculated, as well as the residual vibronic coupling terms.

We require:

$$\int \phi^*_{1s\sigma_g} < O_g \mid -\frac{\underset{\sim}{\nabla}_g.\underset{\sim}{\nabla}_R}{2\mu_a} \mid O_u > \phi_{2p\sigma_u}\, d\underset{\sim}{r}_g$$

$$= -\frac{1}{\mu_a R^2}\left\{ \int \phi^*_{1s\sigma_g} \left[Z + RZ\,\frac{\partial}{\partial R} - \xi\eta\, X_O \right] \phi_{2p\sigma_u}\, d\underset{\sim}{r}_g \right.$$

$$\left. + R \int \phi^*_{1s\sigma_g}\, Z\, \phi_{2p\sigma_u}\, d\underset{\sim}{r}_g\, \frac{\partial}{\partial R} \right\} \qquad (6.157)$$

and $\int \phi^*_{2p\sigma_u} < O_u \mid -\frac{\nabla_g \cdot \nabla_R}{2\mu_a} \mid O_g > \phi_{1s\sigma_g} \, d\underset{\sim}{r}_g$

where in atomic units $\mu_a = 3674.1273$ [105], taking the internuclear vector $\underset{\sim}{R} = \underset{\sim}{r}_D - \underset{\sim}{r}_H$. The explicit forms for the operators X_O and Z appear in (6.95) and (6.97), respectively, and we can use them to show that:

$$\int \phi^*_{2p\sigma_u} Z \, \phi_{1s\sigma_g} \, d\underset{\sim}{r}_g = - \int \phi^*_{1s\sigma_g} Z \, \phi_{2p\sigma_u} \, d\underset{\sim}{r}_g \tag{6.158}$$

$$\int \phi^*_{2p\sigma_u} \xi\eta \, X_O \, \phi_{1s\sigma_g} d\underset{\sim}{r}_g = 2 \int \phi^*_{1s\sigma_g} Z \, \phi_{2p\sigma_u} \, d\underset{\sim}{r}_g + \int \phi^*_{1s\sigma_g} \xi\eta \, X_O \, \phi_{2p\sigma_u} \, d\underset{\sim}{r}_g \tag{6.159}$$

$$\int \phi^*_{2p\sigma_u} Z \frac{\partial}{\partial R} \phi_{1s\sigma_g} \, d\underset{\sim}{r}_g = \int \phi^*_{1s\sigma_g} Z \frac{\partial}{\partial R} \phi_{2p\sigma_u} \, d\underset{\sim}{r}_g - \frac{d}{dR} \int \phi^*_{1s\sigma_g} Z \, \phi_{2p\sigma_u} \, d\underset{\sim}{r}_g \tag{6.160}$$

The perhaps at first sight surprising result that the electronic matrix element is non-Hermitian:

$$\int \phi^*_{1s\sigma_g} < O_g \mid -\frac{\nabla_g \cdot \nabla_R}{2\mu_a} \mid O_u > \phi_{2p\sigma_u} \, d\underset{\sim}{r}_g \neq \int \phi^*_{2p\sigma_u} < O_u \mid -\frac{\nabla_g \cdot \nabla_R}{2\mu_a} \mid O_g > \phi_{1s\sigma_g} \, d\underset{\sim}{r}_g \tag{6.161}$$

is consistent with the necessary Hermiticity of $(-\nabla_g \cdot \nabla_R / 2\mu_a)$. Its effects on both the electronic and nuclear motions must be taken into account.

The electronic matrix elements of Z, $Z\partial/\partial R$ and $\xi\eta X_O$ are calculated analytically from the wavefunction expansions (6.27) and (6.33) [144].

Derivatives with respect to R are obtained from the adiabatic treatment, see previous section. With these results we can set up a matrix of the complete Hamiltonian (6.8) at each value of R, describing the electronic coupling between the $1s\sigma_g$ and $2p\sigma_u$ states:

$$\begin{pmatrix} \int \phi^*_{1s\sigma_g} \langle O_g|\mathcal{H}_{int}|O_g\rangle \phi_{1s\sigma_g} d\underset{\sim}{r}_g & \int \phi^*_{1s\sigma_g} \langle O_g|\mathcal{H}_{int}|O_u\rangle \phi_{2p\sigma_u} d\underset{\sim}{r}_g \\ \int \phi^*_{2p\sigma_u} \langle O_u|\mathcal{H}_{int}|O_g\rangle \phi_{1s\sigma_g} d\underset{\sim}{r}_g & \int \phi^*_{2p\sigma_u} \langle O_u|\mathcal{H}_{int}|O_u\rangle \phi_{2p\sigma_u} d\underset{\sim}{r}_g \end{pmatrix}$$

$$= \begin{pmatrix} U^{AD}_{1s\sigma_g} & \int \phi^*_{1s\sigma_g} \langle O_g|-\frac{\underset{\sim}{\nabla}_g \cdot \underset{\sim}{\nabla}_R}{2\mu_a}|O_u\rangle \phi_{2p\sigma_u} d\underset{\sim}{r}_g \\ \int \phi^*_{2p\sigma_u} \langle O_u|-\frac{\underset{\sim}{\nabla}_g \cdot \underset{\sim}{\nabla}_R}{2\mu_a}|O_g\rangle \phi_{1s\sigma_g} d\underset{\sim}{r}_g & U^{AD}_{2p\sigma_u} \end{pmatrix} \qquad (6.162)$$

where U^{AD}_s is the adiabatic potential for state s, given by (6.39). This matrix can be decomposed into a Hermitian part and an anti-Hermitian component:

$$\begin{pmatrix} U^{AD}_{1s\sigma_g} & H \\ H & U^{AD}_{2p\sigma_u} \end{pmatrix} + \begin{pmatrix} 0 & A \\ -A & 0 \end{pmatrix} \qquad (6.163)$$

where:

$$H = \frac{1}{2}\left[\int \phi^*_{1s\sigma_g} \langle O_g|-\frac{\underset{\sim}{\nabla}_g \cdot \underset{\sim}{\nabla}_R}{2\mu_a}|O_u\rangle \phi_{2p\sigma_u} d\underset{\sim}{r}_g + \int \phi^*_{2p\sigma_u} \langle O_u|-\frac{\underset{\sim}{\nabla}_g \cdot \underset{\sim}{\nabla}_R}{2\mu_a}|O_g\rangle \phi_{1s\sigma_g} d\underset{\sim}{r}_g\right] \qquad (6.164)$$

$$\text{and} \quad A = \frac{1}{2} \left[\int \phi^*_{1s\sigma_g} < O_g | - \frac{\nabla_{\tilde{g}} \cdot \nabla_{\tilde{R}}}{2\mu_a} | O_u > \phi_{2p\sigma_u} d\tilde{r}_g \right.$$

$$\left. - \int \phi^*_{2p\sigma_u} < O_u | - \frac{\nabla_{\tilde{g}} \cdot \nabla_{\tilde{R}}}{2\mu_a} | O_g > \phi_{1s\sigma_g} d\tilde{r}_g \right] \qquad (6.165)$$

We diagonalise the Hermitian matrix, to obtain the mixed orthonormal electronic wavefunctions:

$$\phi_A = a\phi_{1s\sigma_g} + b\phi_{2p\sigma_u} \quad \text{and} \quad \phi_B = b\phi_{1s\sigma_g} - a\phi_{2p\sigma_u} \qquad (6.166)$$

where (a,b) are given by:

$$\begin{pmatrix} U^{AD}_{1s\sigma_g} - \lambda & H \\ H & U^{AD}_{2p\sigma_u} - \lambda \end{pmatrix} \begin{pmatrix} a \\ b \end{pmatrix} = 0 \qquad (6.167)$$

$$\text{and} \quad a^2 + b^2 = 1 \qquad (6.168)$$

From these coupled wavefunctions we construct the coupled differential equations which define the radial nuclear motion in this truncated representation of equation (6.14):

$$\begin{pmatrix} \int \phi^*_A <O|\mathcal{H}_{int}|O> \phi_A \, d\tilde{r}_g & \int \phi^*_A <O|\mathcal{H}_{int}|O> \phi_B \, d\tilde{r}_g \\ \int \phi^*_B <O|\mathcal{H}_{int}|O> \phi_A \, d\tilde{r}_g & \int \phi^*_B <O|\mathcal{H}_{int}|O> \phi_B \, d\tilde{r}_g \end{pmatrix} \begin{pmatrix} F_A \\ F_B \end{pmatrix}$$

$$= E \begin{pmatrix} F_A \\ F_B \end{pmatrix} \qquad (6.169)$$

where:

$$\int \phi_A^* < 0|\mathcal{H}_{int}| 0 > \phi_A d\underset{\sim}{r}_g = -\frac{1}{2\mu}\left[\frac{d^2}{dR^2} + \frac{2}{R}\frac{d}{dR} - \frac{J(J+1)}{R^2}\right]$$

$$+ a^2 U^{AD}_{1s\sigma_g} + b^2 U^{AD}_{1s\sigma_u} - \frac{1}{2\mu}\left[a\frac{d^2a}{dR^2} + b\frac{d^2b}{dR^2}\right]$$

$$- \frac{ab}{\mu_a R^2}\left[\int \phi^*_{1s\sigma_g}\left(RZ\frac{\partial}{\partial R} - \xi\eta X_0\right)\phi_{2p\sigma_u} d\underset{\sim}{r}_g\right.$$

$$\left. + \int \phi^*_{2p\sigma_u}\left(RZ\frac{\partial}{\partial R} - \xi\eta X_0\right)\phi_{1s\sigma_g} d\underset{\sim}{r}_g\right]$$

$$- \frac{1}{\mu_a R}\left(\frac{adb}{dR} - \frac{bda}{dR}\right)\int \phi^*_{1s\sigma_g} Z \phi_{2p\sigma_u} d\underset{\sim}{r}_g \qquad (6.170)$$

$$\int \phi_A^* < 0|\mathcal{H}_{int}|0 > \phi_B d\underset{\sim}{r}_g = ab\left(U^{AD}_{1s\sigma_g} - U^{AD}_{2p\sigma_u}\right)$$

$$- \frac{1}{\mu}\left(\frac{adb}{dR} - \frac{bda}{dR}\right)\left(\frac{1}{R} + \frac{d}{dR}\right) - \frac{1}{2\mu}\left(a\frac{d^2b}{dR^2} - b\frac{d^2a}{dR^2}\right)$$

$$+ \frac{1}{\mu_a R^2}\left[R\left(\int \phi^*_{1s\sigma_g} Z \phi_{2p\sigma_u} d\underset{\sim}{r}_g\right)\frac{d}{dR} + \int \phi^*_{1s\sigma_g} Z \phi_{2p\sigma_u} d\underset{\sim}{r}_g\right.$$

$$+ a^2 \int \phi^*_{1s\sigma_g}\left(RZ\frac{\partial}{\partial R} - \xi\eta X_0\right)\phi_{2p\sigma_u} d\underset{\sim}{r}_g$$

$$\left. - b^2 \int \phi^*_{2p\sigma_u}\left(RZ\frac{\partial}{\partial R} - \xi\eta X_0\right)\phi_{1s\sigma_g} d\underset{\sim}{r}_g\right] \qquad (6.171)$$

and similarly:

$$\int \phi_B^* < 0|\mathcal{H}_{int}|0 > \phi_B d\underset{\sim}{r}_g = -\frac{1}{2\mu}\left[\frac{d^2}{dR^2} + \frac{2}{R}\frac{d}{dR} - \frac{J(J+1)}{R^2}\right]$$

$$+ b^2 U^{AD}_{1s\sigma_g} + a^2 U^{AD}_{2p\sigma_u} - \frac{1}{2\mu}\left(a\frac{d^2a}{dR^2} + b\frac{d^2b}{dR^2}\right)$$

$$+ \frac{ab}{\mu_a R^2}\left[\int \phi^*_{1s\sigma_g}\left(RZ\frac{\partial}{\partial R} - \xi\eta X_0\right)\phi_{2p\sigma_u} d\underset{\sim}{r}_g\right.$$

$$\left. + \int \phi^*_{2p\sigma_u}\left(RZ\frac{\partial}{\partial R} - \xi\eta X_0\right)\phi_{1s\sigma_g} d\underset{\sim}{r}_g\right]$$

$$- \frac{1}{\mu_a R}\left(a\frac{db}{dR} - b\frac{da}{dR}\right)\int \phi^*_{1s\sigma_g} Z\phi_{2p\sigma_u} d\underset{\sim}{r}_g \qquad (6.172)$$

$$\int \phi_B^* <0|\mathcal{H}_{int}|0 > \phi_A d\underset{\sim}{r}_g = ab\left[U^{AD}_{1s\sigma_g} - U^{AD}_{2p\sigma_u}\right]$$

$$+ \frac{1}{\mu}\left(a\frac{db}{dR} - b\frac{da}{dR}\right)\left(\frac{1}{R} + \frac{d}{dR}\right) + \frac{1}{2\mu}\left(a\frac{d^2b}{dR^2} - b\frac{d^2a}{dR^2}\right)$$

$$- \frac{1}{\mu_a R^2}\left[R\left(\int \phi^*_{1s\sigma_g} Z\,\phi_{2p\sigma_u} d\underset{\sim}{r}_g\right)\frac{d}{dR} + \int \phi^*_{1s\sigma_g} Z\,\phi_{2p\sigma_u} d\underset{\sim}{r}_g\right.$$

$$+ b^2\int \phi^*_{1s\sigma_g}\left(RZ\frac{\partial}{\partial R} - \xi\eta X_0\right)\phi_{2p\sigma_u} d\underset{\sim}{r}_g$$

$$\left. - a^2\int \phi^*_{2p\sigma_u}\left(RZ\frac{\partial}{\partial R} - \xi\eta X_0\right)\phi_{1s\sigma_g} d\underset{\sim}{r}_g\right] \qquad (6.173)$$

In the above formulae we have extracted the centrifugal part of the adiabatic potentials $\left[J(J+1)/2\mu R^2\right]$ for clarity. We see that the only remaining problem in setting up (6.169) is the determination of the derivatives of (a,b) with respect to R. They were obtained numerically, by a piecewise six point polynomial approximation [144], tests are provided by:

$$\frac{ada}{dR} + \frac{bdb}{dR} = 0 \quad \text{and} \quad \frac{ad^2a}{dR^2} + \left(\frac{da}{dR}\right)^2 + \frac{bd^2b}{dR^2} + \left(\frac{db}{dR}\right)^2 = 0 \qquad (6.174)$$

The largest error, as defined by the quantities above, was 10^{-7}. Tests of the calculated electronic matrix elements of Z, $Z\,\partial/\partial R$ and $\xi\eta X_0$ are provided by the relationships (6.158),(6.159) and (6.160). As a further test these matrix elements have also been evaluated using the Jaffé expansion, exact agreement is found.

Equations (6.169) and (6.170) show that, neglecting the off diagonal terms, the nuclear motion for the ground state is governed by an effective potential:

$$U_A = \frac{J(J+1)}{2\mu R^2} + a^2\, U^{AD}_{1s\sigma_g} + b^2\, U^{AD}_{2p\sigma_u} - \frac{1}{2\mu}\left(ad^2a + bd^2b\right)$$

$$- \frac{ab}{\mu_a R^2}\left[\int \phi^*_{1s\sigma_g}\left(RZ\,\frac{\partial}{\partial R} - \xi\eta X_0\right)\phi_{2p\sigma_u}\,d\underset{\sim}{r}_g\right.$$

$$\left. + \int \phi^*_{2p\sigma_u}\left(RZ\,\frac{\partial}{\partial R} - \xi\eta X_0\right)\phi_{1s\sigma_g}\,d\underset{\sim}{r}_g\right]$$

$$- \frac{1}{\mu_a R}\left(adb - bda\right)\int \phi^*_{1s\sigma_g}\, Z\, \phi_{2p\sigma_u}\,d\underset{\sim}{r}_g \qquad (6.175)$$

While for the excited state we have:

$$U_B = \frac{J(J+1)}{2\mu R^2} + b^2\, U^{AD}_{1s\sigma_g} + a^2 U^{AD}_{2p\sigma_u} - \frac{1}{2\mu}\left(ad^2a + bd^2b\right)$$

$$+ \frac{ab}{\mu_a R^2}\left[\int \phi^*_{1s\sigma_g}\left(RZ\,\frac{\partial}{\partial R} - \xi\eta X_O\right)\phi_{2p\sigma_u}\,d\underset{\sim}{r}_g\right.$$

$$\left. + \int \phi^*_{2p\sigma_u}\left(RZ\,\frac{\partial}{\partial R} - \xi\eta X_O\right)\phi_{1s\sigma_g}\,d\underset{\sim}{r}_g\right]$$

$$- \frac{1}{\mu_a R}\left(a\frac{db}{dR} - b\frac{da}{dR}\right)\int \phi^*_{1s\sigma_g}\, Z\, \phi_{2p\sigma_u}\,d\underset{\sim}{r}_g \qquad (6.176)$$

At very large R :

$$a^2 = b^2 = \frac{1}{2} \quad \text{and} \quad U^{AD}_{1s\sigma_g} = U^{AD}_{2p\sigma_u} \qquad (6.177)$$

so that the ground state and excited state effective potentials are separated by:

$$\frac{1}{\mu_a R^2}\left[\int \phi^*_{1s\sigma_g}\left(RZ\,\frac{\partial}{\partial R} - \xi\eta X_O\right)\phi_{2p\sigma_u}\,d\underset{\sim}{r}_g\right.$$

$$\left. + \int \phi^*_{2p\sigma_u}\left(RZ\,\frac{\partial}{\partial R} - \xi\eta X_O\right)\phi_{1s\sigma_g}\,d\underset{\sim}{r}_g\right] \qquad (6.178)$$

These potentials go to the correct dissociation limits of $H^+ + D$ for the ground state and $H + D^+$ for the excited state, see figure 6.6.

Moving on to consider the off diagonal elements:

$$\int \phi^*_A < O|\mathcal{H}_{int}|O > \phi_B\, d\underset{\sim}{r}_g = C_{AB} + D_{AB}\,\frac{d}{dR} \qquad (6.179)$$

where $C_{AB} = ab\left(U^{AD}_{1s\sigma_g} - U^{AD}_{2p\sigma_u}\right) - \frac{1}{\mu R}\left(a\frac{db}{dR} - b\frac{da}{dR}\right)$

$$- \frac{1}{2\mu}\left(a\frac{d^2b}{dR^2} - b\frac{d^2a}{dR^2}\right) + \frac{1}{\mu_a R^2}\left[\int \phi^*_{1s\sigma_g}\, Z\, \phi_{2p\sigma_u}\,d\underset{\sim}{r}_g\right.$$

$$\left. + a^2 \int \phi^*_{1s\sigma_g}\left(RZ\,\frac{\partial}{\partial R} - \xi\eta X_O\right)\phi_{2p\sigma_u}\,d\underset{\sim}{r}_g\right.$$

$$- b^2 \int \phi^*_{2p\sigma_u} \left(RZ \frac{\partial}{\partial R} - \xi\eta X_O \right) \phi_{1s\sigma_g} d\underset{\sim}{r}_g \Bigg] \tag{6.180}$$

$$\text{and} \quad D_{AB} = - \frac{1}{\mu} \left(\frac{adb}{dR} - \frac{bda}{dR} \right) + \frac{1}{\mu_a R} \int \phi^*_{1s\sigma_g} Z \, \phi_{2p\sigma_u} d\underset{\sim}{r}_g \tag{6.181}$$

$$\int \phi^*_B < O | \mathcal{H}_{int} | O > \phi_A \, d\underset{\sim}{r}_g = C_{BA} + D_{BA} \frac{d}{dR} \tag{6.182}$$

C_{BA} and D_{BA} can be extracted from (6.173). We see that:

$$D_{BA} = - D_{AB} \tag{6.183}$$

while consideration of (6.167) reveals that:

$$C_{BA} = - C_{AB} \tag{6.184}$$

No further progress can be made by considering the electronic coupling alone.

The various results of the electronic calculations described above are presented in tables 6.4 (H), 6.5 (a,b), 6.6 (U_A,U_B) and 6.7 (C_{AB},D_{AB}), and in figures 6.6 (U_A,U_B), 6.7 (H), 6.8 (a,b) and 6.9 (C_{AB},D_{AB}). Figure 6.8 is particularly interesting, as it reveals a very rapid switch in character of the electronic wavefunction from a symmetrical 'molecular' electronic distribution ($a \sim 1$, $b \sim 0$), to a wavefunction resembling the dissociation products ($a \sim b \sim 1/\sqrt{2}$). At large R the Born-Oppenheimer electronic wavefunction is well described by the linear combination of atomic orbital approximation:

$$\phi_{1s\sigma_g} \sim \frac{1}{\sqrt{2}} \left[\phi_{1s}(D) + \phi_{1s}(H) \right] \tag{6.185}$$

$$\phi_{2p\sigma_u} \sim \frac{1}{\sqrt{2}} \left[\phi_{1s}(D) - \phi_{1s}(H) \right] \tag{6.186}$$

so that:

$$\phi_A = \phi_{1s}(D) \quad \text{and} \quad \phi_B = \phi_{1s}(H), \; R \longrightarrow \infty \tag{6.187}$$

TABLE 6.4

Hermitian Electronic Coupling Term Between $1s\sigma_g$ and $2p\sigma_u$

R (Bohrs)	H ($\times 10^{-3}$ Hartrees)
1.0	-0.1132364441
2.0	-0.0797243057
3.0	-0.0703978223
4.0	-0.0675003868
5.0	-0.0670593002
6.0	-0.0673249298
7.0	-0.0676122136
8.0	-0.0677911362
9.0	-0.0678900972
10.0	-0.0679452596
11.0	-0.0679775275
12.0	-0.0679974299
13.0	-0.0680102864
14.0	-0.0680189145
15.0	-0.0680248902
16.0	-0.0680291399
17.0	-0.0680322314
18.0	-0.0680345250
19.0	-0.0680362562
20.0	-0.0680375831
30.0	-0.0680422336
∞	-0.0680433708

TABLE 6.5

Mixing Coefficients Arising From Diagonalisation of the Electronic Coupling Between $1s\sigma_g$ and $2p\sigma_u$

R (Bohrs)	a	b
1.0	1.000000	0.127564(-3)*
2.0	1.000000	0.183146(-3)
3.0	1.000000	0.335866(-3)
4.0	1.000000	0.670891(-3)
5.0	0.999999	0.142147(-2)
6.0	0.999995	0.315317(-2)
7.0	0.999974	0.724181(-2)
8.0	0.999854	0.170647(-1)
9.0	0.999162	0.409264(-1)
10.0	0.995128	0.985950(-1)
11.0	0.973834	0.227262
12.0	0.903116	0.429397
13.0	0.808917	0.587923
14.0	0.750853	0.660470
15.0	0.724787	0.688973
16.0	0.714104	0.700040
17.0	0.709850	0.704353
18.0	0.708176	0.706035
19.0	0.707522	0.706691
20.0	0.707268	0.706946
30.0	0.707107	0.707107
∞	$1/\sqrt{2}$	$1/\sqrt{2}$

* The number in brackets indicates the exponent eg. 0.127564(-3) = 0.127564×10^{-3}

TABLE 6.6

Effective Potentials and Parallel Transition Moment for the Ground State and First Excited State of HD^+

R (Bohrs)	U_A (Hartrees)	U_B (Hartrees)	Transition Moment (electron charge.Bohr)
1.0	-0.4515133351	0.4361673332	0.7728507512
2.0	-0.6024398490	-0.1671340737	1.049942507
3.0	-0.5773909976	-0.3677903007	1.432686461
4.0	-0.5459128141	-0.4452997414	1.870908089
5.0	-0.5242394791	-0.4770632843	2.488599158
6.0	-0.5117790928	-0.4904274510	2.879027789
7.0	-0.5053978312	-0.4960612301	3.403968856
8.0	-0.5023710127	-0.4983979278	3.923654925
9.0	-0.5009948770	-0.4993351837	4.427097845
10.0	-0.5003761097	-0.4996866470	4.857201940
11.0	-0.5000848481	-0.4997909521	4.897714756
12.0	-0.4999555890	-0.4998007810	3.767331312
13.0	-0.4999338283	-0.4997983197	1.998168277
14.0	-0.4999217959	-0.4997860467	0.8899571950
15.0	-0.4999089468	-0.4997729498	0.3787124125
16.0	-0.4998987748	-0.4997551366	0.1587560782
17.0	-0.4998911997	-0.4997551366	0.6595897588(-1)
18.0	-0.4998855527	-0.4997494838	0.2720767422(-1)
19.0	-0.4998812870	-0.4997452145	0.1115265045(-1)
20.0	-0.4998780179	-0.4997419427	0.4545999745(-2)
30.0	-0.4998665711	-0.4997304866	0.4631603148(-6)
∞	-0.4998637781	-0.4997276913	0.0

TABLE 6.7

Vibronic Coupling Terms Between the Ground State and First Excited State of HD^+

R (Bohrs)	C_{AB} (Hartrees)	$D_{AB}(d/dR)$ (Hartrees.Bohr)
1.0	0.7801247797(-4)	0.8145386956(-4)
2.0	0.1903927180(-4)	0.6208827064(-4)
3.0	0.4407236376(-5)	0.4066155491(-4)
4.0	-0.1702941492(-6)	0.2519990474(-4)
5.0	-0.1761364091(-5)	0.1423948748(-4)
6.0	-0.2487039442(-5)	0.6253611909(-5)
7.0	-0.3776298495(-5)	-0.6850480444(-6)
8.0	-0.7395985381(-5)	-0.9977028438(-5)
9.0	-0.1664841521(-4)	-0.2846521338(-4)
10.0	-0.3686353360(-4)	-0.7010160334(-4)
11.0	-0.5480303176(-4)	-0.1469800816(-3)
12.0	0.9992249585(-6)	-0.1830978661(-3)
13.0	0.3242942153(-4)	-0.1106387488(-3)
14.0	0.1798069013(-4)	-0.4796999625(-4)
15.0	0.7616406527(-5)	-0.1927362063(-4)
16.0	0.3074464448(-5)	-0.7613562682(-5)
17.0	0.1225033654(-5)	-0.2988345853(-5)
18.0	0.4848282183(-6)	-0.1167937907(-5)
19.0	0.1908975257(-6)	-0.4548478399(-6)
20.0	0.7483680787(-7)	-0.1765863239(-6)
30.0	0.8407618722(-11)	-0.1216539078(-10)
∞	0.0	0.0

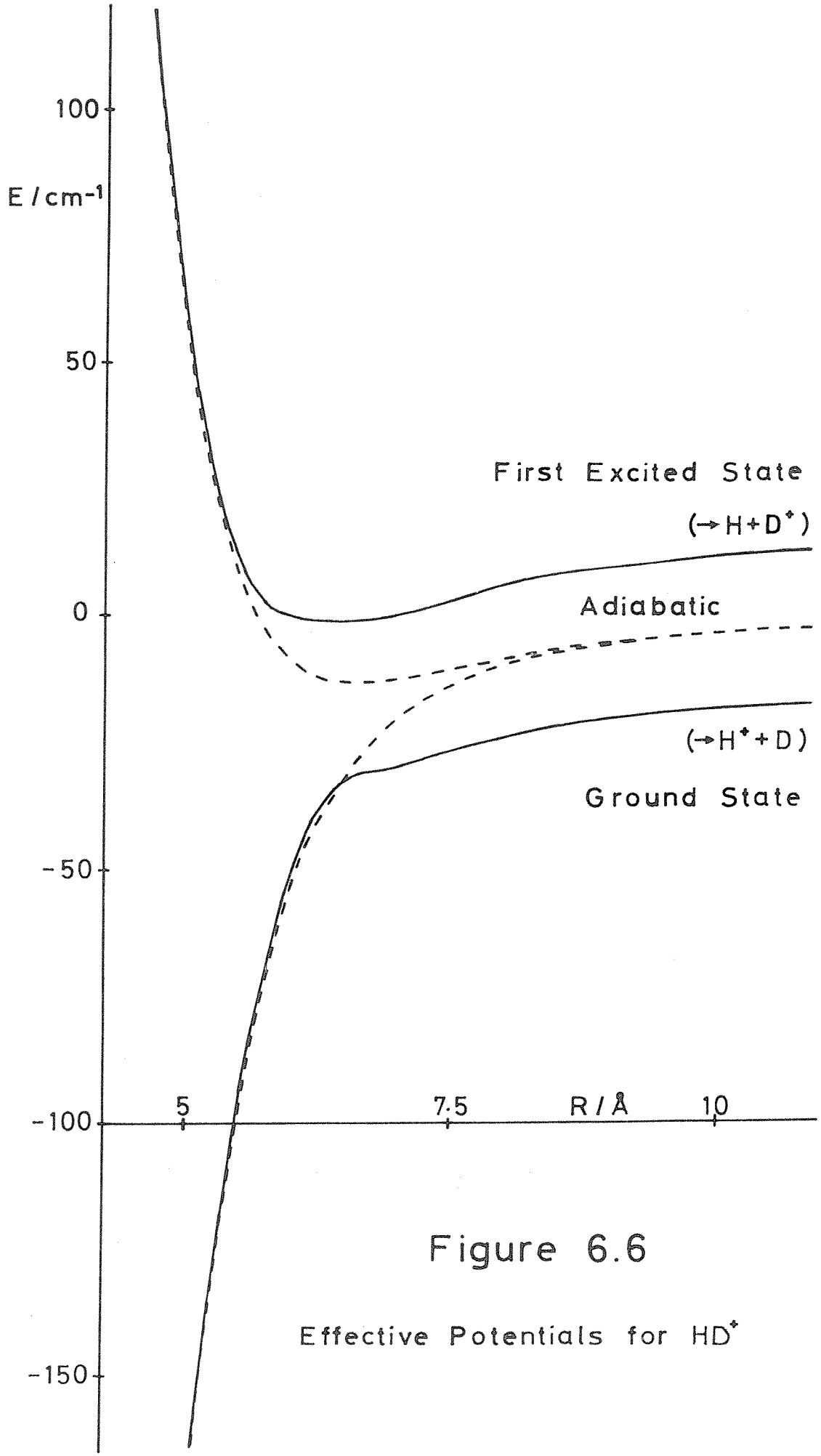

Figure 6.6

Effective Potentials for HD^+

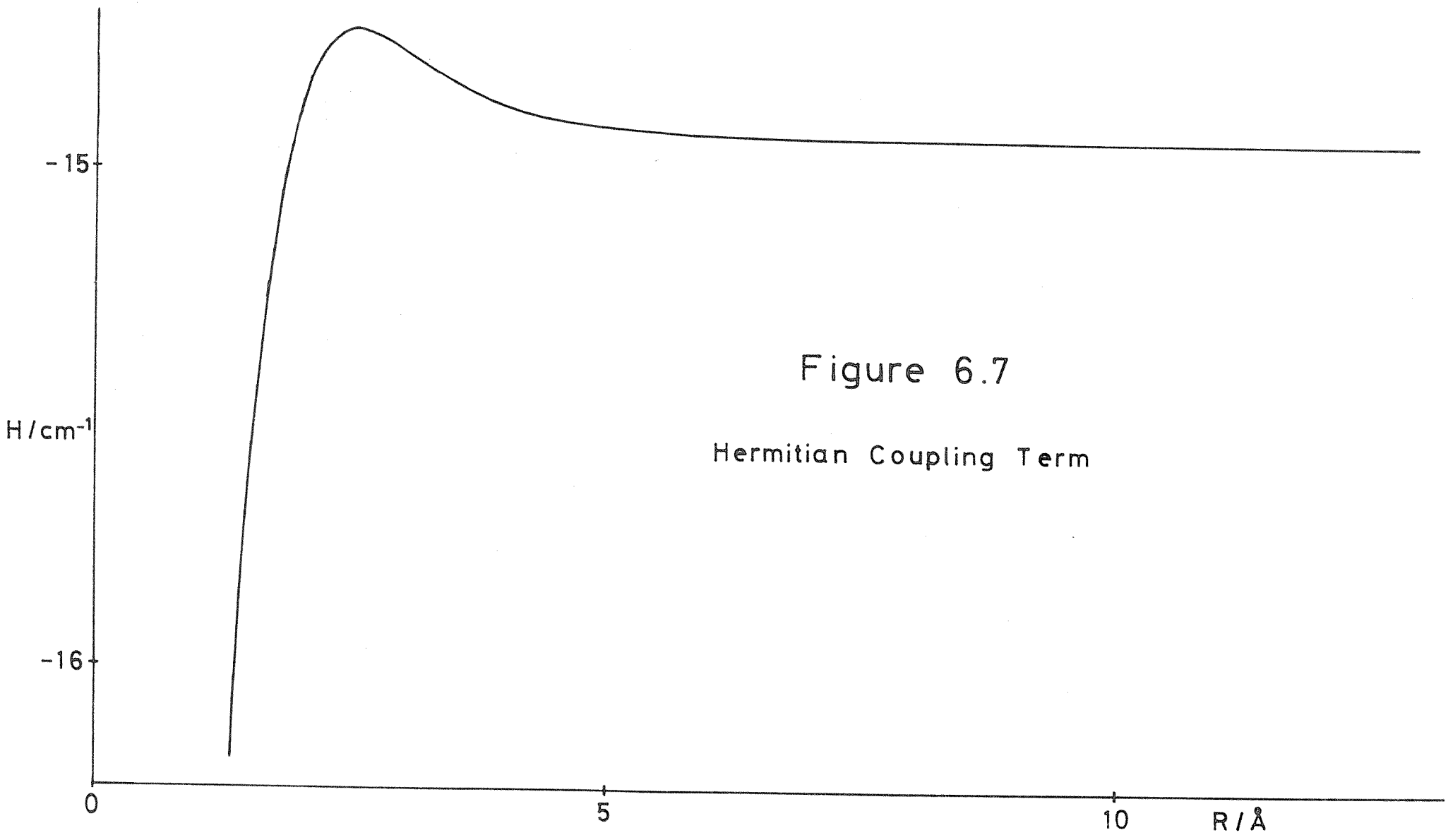

Figure 6.7

Hermitian Coupling Term

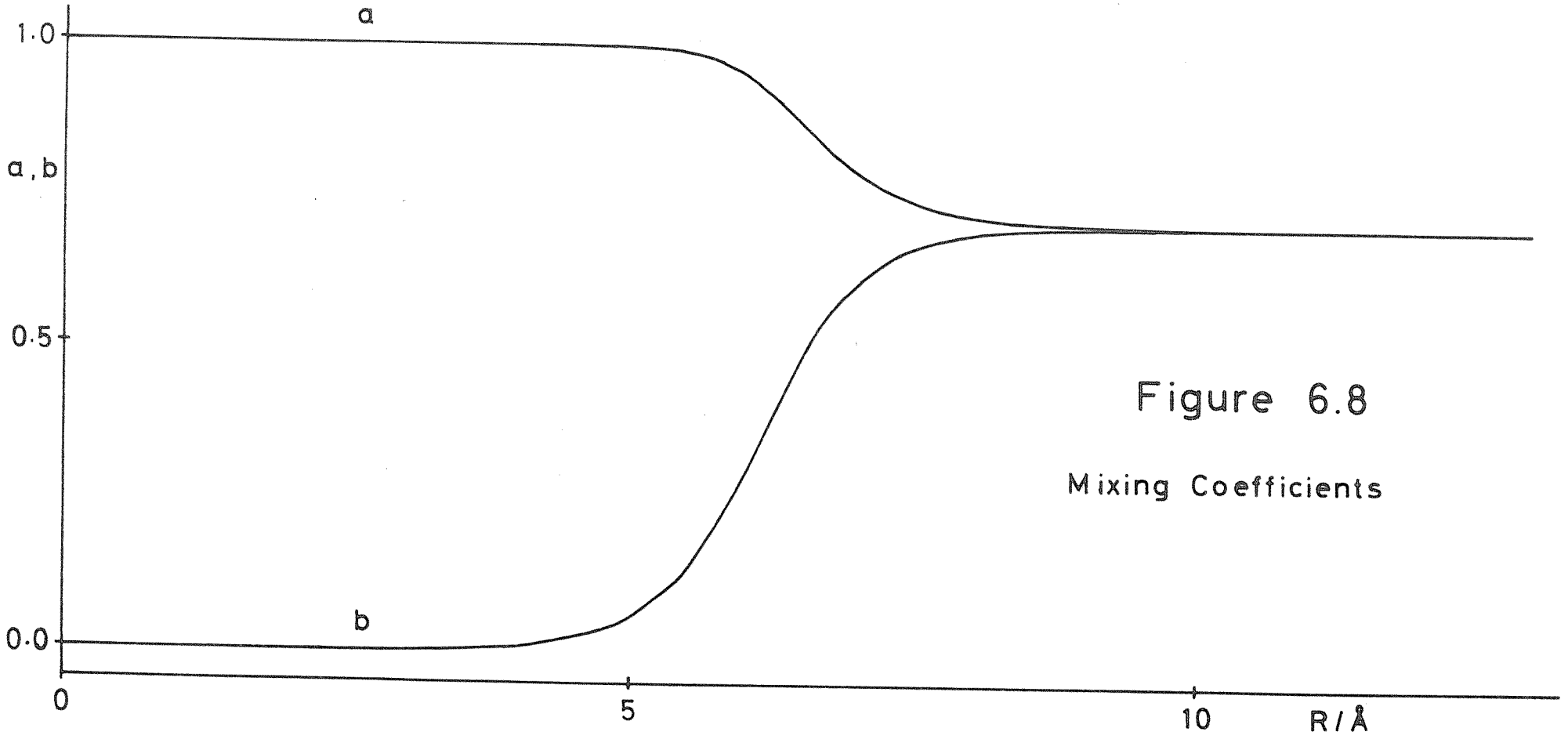

Figure 6.8

Mixing Coefficients

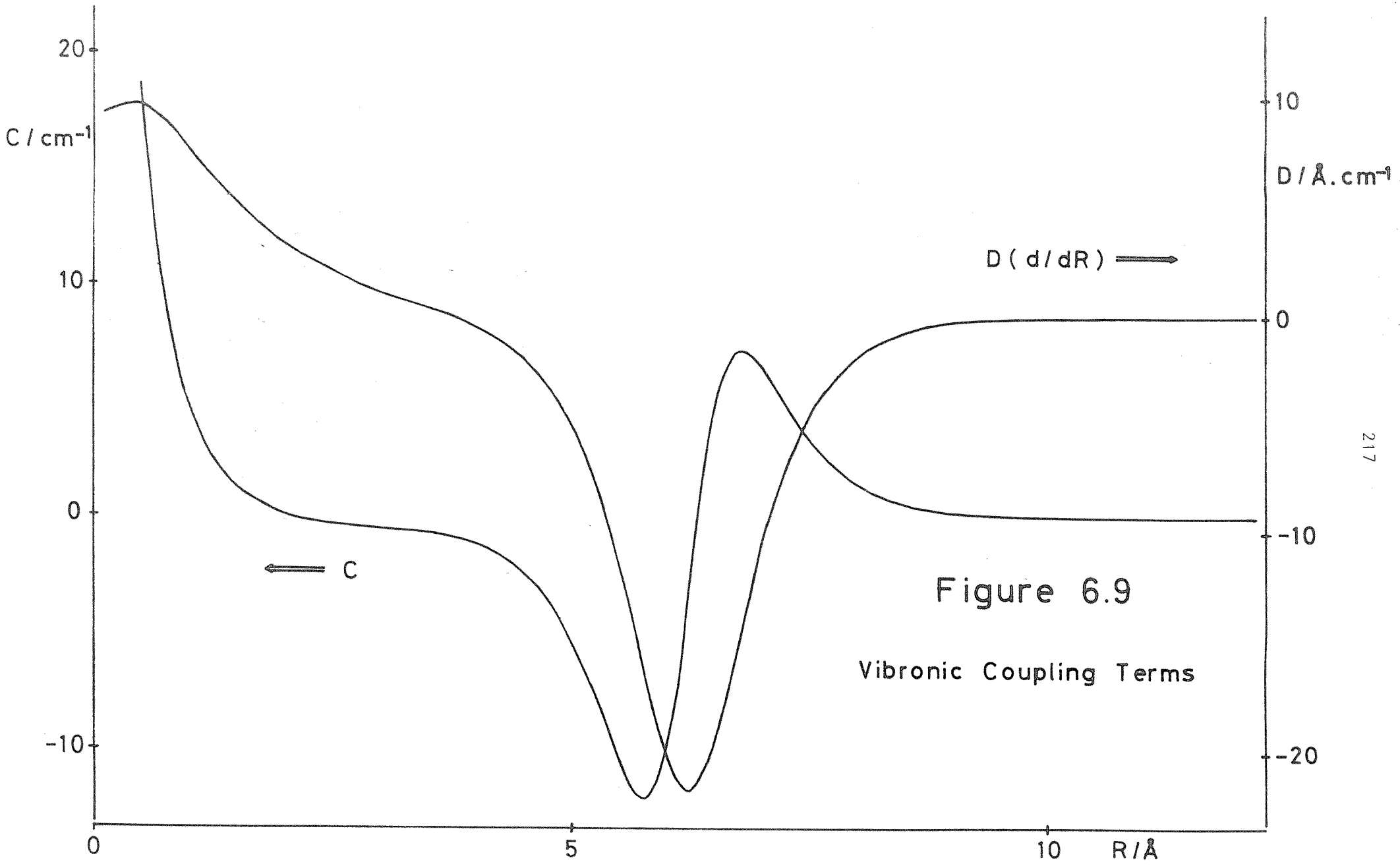

Figure 6.9

Vibronic Coupling Terms

and the correct limiting behaviour is obtained.

Finally we have used (a,b) to evaluate the electronic transition moment between the coupled states:

$$\left| \int \phi_A^* \, \underset{\sim}{r}_g \, \phi_B d\underset{\sim}{r}_g \right| = \left| (a^2 - b^2) \int \phi^*_{1s\sigma_g} \underset{\sim}{r}_g \phi_{2p\sigma_u} d\underset{\sim}{r}_g \right| \qquad (6.188)$$

The values are presented in table 6.6 and figure 6.4. We see that the physically unrealistic behaviour at large R has been removed, as we anticipated. We also note that there is an electronic contribution to the transition moment within each of the coupled states:

$$\left| \int \phi_A^* \, \underset{\sim}{r}_g \phi_A \, d\underset{\sim}{r}_g \right| = \left| \int \phi_B^* \, \underset{\sim}{r}_g \phi_B d\underset{\sim}{r}_g \right| = \left| ab \int \phi^*_{1s\sigma_g} \underset{\sim}{r}_g \phi_{2p\sigma_u} d\underset{\sim}{r}_g \right| \qquad (6.189)$$

6.12 Calculation of the Vibration-Rotation Energy Levels.

The Born-Oppenheimer, adiabatic and our coupled states approximations all require the solution of a radial Schrödinger equation of the form:

$$\left\{ -\frac{1}{2\mu} \left[\frac{d^2}{dR^2} + \frac{2}{R} \frac{d}{dR} - \frac{J(J+1)}{R^2} \right] + U_s(R) \right\} F_{vJ}(R) = E_{vJ} F_{vJ}(R) \qquad (6.190)$$

to obtain the radial functions $F_{vJ}(R)$, and the energy levels E_{vJ}. $U_s(R)$ is the effective potential for nuclear motion appropriate to the approximation, see equation (6.37), (6.39) or (6.175). Some simplification of (6.190) is achieved by writing:

$$\chi_{vJ}(R) = \frac{1}{R} F_{vJ}(R) \qquad (6.191)$$

for:

$$\left\{ -\frac{d^2}{dR^2} + \frac{J(J+1)}{R^2} + 2\mu \, U_s(R) - 2\mu \, E_{vJ} \right\} \chi_{vJ}(R) = 0 \qquad (6.192)$$

$\chi_{vJ}(R)$ is also more convenient for evaluating expectation values of electronic matrix elements:

$$\Omega_{vJ} = \int F_{vJ}(R)\Omega(R)F_{vJ}(R)R^2dR \qquad (6.193)$$

$$= \int \chi_{vJ}(R)\Omega(R)\chi_{vJ}(R)dR \qquad (6.194)$$

It is usually called the vibrational wavefunction.

Various algorithms have been developed for solving (6.192), we use the Numerov-Cooley algorithm [142], as implemented by Professor R.J.LeRoy [141]. The required effective potentials for HD^+ were calculated on a grid spacing of 0.05 Bohrs from 0.2 to 30 Bohrs. To obtain the fine grid required for numerical solution of (6.192) these points were interpolated by a cubic spline [197] to a spacing of 0.005 Å. The R range was extended to 20 Å using $(A + B/R^4 + C/R^6)$. Values for the fundamental constants required were taken from [105]. Tests of the calculations were provided by comparing the results of an adiabatic calculation on H_2^+ with the tabulation of Hunter, Yau and Pritchard [127], no differences of more than 0.1 cm^{-1} were detected.

Vibration-rotation energy levels for v = 0-22 and J = 0-10 of the ground state of HD^+ are presented in tables 6.8 (Born-Oppenheimer), 6.9 (adiabatic) and 6.10 (coupled states). Table 6.11 contains the nonadiabatic calculations of Wolniewicz & Poll [48]. The energy levels are given relative to the dissociation limit appropriate to the approximation. The absolute energies (relative to infinitely separated nuclei and electron) of these dissociation limits in atomic units are -0.5 Born-Oppenheimer, -0.499795735 adiabatic, and -0.499863778 coupled states $(H^+ + D)$. We believe that the nonadiabatic results of Wolniewicz and Poll are quoted relative to this last limit, although this is not made clear in their paper [48]. Comparing first the adiabatic and Born-Oppenheimer results, the adiabatic levels lie further below the dissociation limit than the corresponding level in the Born-Oppenheimer potential, a reflection of the slight increase in D_e due to the adiabatic corrections. Introduction of the $1s\sigma_g - 2p\sigma_u$ coupling immediately decreases D_e by about 14.9 cm^{-1}. Comparing our coupled states calculations with the adiabatic results shows that with the coupling the low vibrational levels are now about 14.9 cm^{-1} closer

TABLE 6.8

Dissociation Energies of the Bound Vibration-Rotation Levels of the Ground State of HD^+ from the Born-Oppenheimer Potential

v	J = 0	1	2	3	4	5	6	7	8	9	10
0	21528.445	21484.565	21397.068	21266.475	21093.552	20879.301	20624.938	20331.872	20001.681	19636.091	19236.945
1	19614.843	19572.967	19489.468	19364.848	19199.846	18995.427	18752.760	18473.205	18158.279	17809.644	17429.074
2	17797.444	17757.511	17677.889	17559.062	17401.742	17206.859	16975.542	16709.097	16408.990	16076.820	15714.295
3	16073.387	16035.344	15959.493	15846.300	15696.454	15510.850	15290.577	15036.897	14751.221	14435.091	14090.155
4	14440.185	14403.986	14331.814	14224.120	14081.568	13905.023	13695.536	13454.324	13182.750	12882.302	12554.570
5	12895.716	12861.322	12792.752	12690.444	12555.036	12387.367	12188.450	11959.461	11701.718	11416.659	11105.819
6	11438.215	11405.595	11340.567	11243.551	11115.169	10956.228	10767.710	10550.753	10306.629	10036.732	9742.547
7	10066.276	10035.407	9973.873	9882.082	9760.635	9610.314	9432.069	9227.003	8996.349	8741.456	8463.766
8	8778.851	8749.716	8691.645	8605.034	8490.463	8348.693	8180.644	7987.385	7770.114	7530.140	7268.866
9	7575.255	7547.848	7493.226	7411.773	7304.055	7170.807	7012.925	6831.449	6627.543	6402.481	6157.632
10	6455.185	6429.506	6378.336	6302.048	6201.192	6076.484	5928.797	5759.143	5568.658	5358.588	5130.268
11	5418.729	5394.790	5347.095	5276.007	5182.062	5065.961	4928.555	4770.834	4593.911	4399.006	4187.431
12	4466.397	4444.219	4400.042	4334.222	4247.283	4139.911	4012.941	3867.346	3740.218	3524.762	3300.275
13	3599.148	3578.765	3538.175	3477.727	3397.938	3299.482	3183.182	3049.997	2901.012	2737.420	2560.515
14	2818.431	2799.891	2762.986	2708.060	2635.623	2546.345	2441.041	2320.668	2186.306	2039.153	1880.514
15	2126.238	2109.607	2076.518	2027.314	1962.505	1882.759	1788.894	1681.872	1562.785	1432.851	1293.408
16	1525.159	1510.523	1481.424	1438.210	1381.394	1311.651	1229.815	1136.867	1033.931	922.274	803.301
17	1018.448	1005.921	981.043	944.170	895.828	836.716	767.697	689.798	604.211	512.296	415.598
18	610.077	599.807	579.453	549.388	510.166	462.528	407.403	345.909	279.375	209.363	137.731
19	304.671	296.858	281.436	258.809	229.590	194.608	154.924	111.865	67.096	22.788	
20	106.904	101.814	91.869	77.543	59.575	39.005	17.281				
21	16.897	14.731	10.684	5.353							
22	0.791	0.365									

All energies in cm^{-1}

TABLE 6.9

Dissociation Energies of the Bound Vibration-Rotation Levels of the Ground State of HD^+ from the Adiabatic Potential

v	J = 0	1	2	3	4	5	6	7	8	9	10
0	21530.852	21486.990	21399.528	21268.986	21096.132	20881.965	20627.701	20334.748	20004.683	19639.231	19240.234
1	19617.727	19575.868	19492.401	19367.828	19202.889	18998.547	18755.971	18476.519	18161.709	17813.200	17432.765
2	17800.747	17760.829	17681.236	17562.452	17405.189	17210.377	16979.142	16712.791	16412.789	16080.732	15718.330
3	16077.050	16039.020	15963.195	15850.042	15700.247	15514.706	15294.508	15040.912	14755.330	14439.303	14094.476
4	14444.150	14407.962	14335.814	14228.155	14085.649	13909.161	13699.740	13458.604	13187.113	12886.755	12559.120
5	12899.926	12865.542	12796.993	12694.715	12559.349	12391.729	12192.871	11963.948	11706.278	11421.297	11110.542
6	11442.613	11410.002	11344.992	11248.004	11119.656	10960.759	10772.291	10555.390	10311.329	10041.499	9747.386
7	10070.806	10039.944	9978.426	9886.658	9765.240	9614.956	9436.754	9231.735	9001.133	8746.295	8468.663
8	8783.456	8754.328	8696.270	8609.677	8495.131	8353.390	8185.375	7992.154	7774.924	7534.994	7273.765
9	7579.880	7552.478	7497.866	7416.427	7308.728	7175.502	7017.647	6836.199	6632.323	6407.294	6162.476
10	6459.773	6434.097	6382.935	6306.657	6205.814	6081.122	5933.452	5763.817	5573.352	5363.300	5134.999
11	5423.223	5399.286	5351.595	5280.513	5186.576	5070.483	4933.087	4775.375	4598.459	4403.560	4191.990
12	4470.740	4448.563	4404.387	4338.568	4251.631	4144.261	4017.291	3871.694	3708.563	3529.100	3334.603
13	3603.282	3582.899	3542.307	3481.856	3402.063	3303.600	3187.291	3054.095	2905.094	2741.481	2564.550
14	2822.299	2803.757	2766.847	2711.913	2639.465	2550.173	2444.851	2324.454	2190.063	2042.875	1884.192
15	2129.780	2113.145	2080.047	2030.831	1966.004	1886.235	1792.342	1685.284	1566.153	1436.168	1296.663
16	1528.313	1513.671	1484.561	1441.328	1384.487	1314.712	1232.836	1139.838	1036.844	925.116	806.060
17	1021.152	1008.616	983.722	946.825	898.450	839.294	770.221	692.257	606.592	514.585	417.777
18	612.261	601.981	581.606	551.509	512.244	464.551	409.356	347.778	281.141	211.006	139.227
19	306.264	298.439	282.990	260.323	231.048	195.994	156.220	113.049	68.142	23.658	
20	107.839	102.733	92.754	78.377	60.377	39.672	17.823				
21	17.182	14.999	10.916	5.531							
22	0.815	0.383									

All energies in cm^{-1}

TABLE 6.10

Dissociation Energies of the Bound Vibration-Rotation Levels of the Ground State of HD^+ from the Effective Coupled States Potential

v	J = 0	1	2	3	4	5	6	7	8	9	10
0	21515.923	21472.061	21384.599	21254.057	21081.203	20867.036	20612.772	20319.819	19989.755	19624.303	19225.305
1	19602.799	19560.939	19477.472	19352.900	19187.960	18983.618	18741.043	18461.590	18146.781	17798.272	17417.837
2	17785.819	17745.900	17666.308	17547.524	17390.261	17195.448	16964.213	16697.863	16397.861	16065.804	15703.402
3	16062.122	16024.092	15948.267	15835.114	15685.319	15499.778	15279.580	15025.985	14740.403	14424.375	14079.549
4	14429.223	14393.035	14320.887	14213.228	14070.722	13894.234	13684.813	13443.676	13172.186	12871.828	12544.193
5	12884.999	12850.615	12782.066	12679.789	12544.422	12376.802	12177.944	11949.021	11691.352	11406.371	11095.616
6	11427.687	11395.076	11330.066	11233.077	11104.730	10945.832	10757.365	10540.464	10296.403	10026.573	9732.460
7	10055.881	10025.019	9963.500	9871.732	9750.315	9600.030	9421.828	9126.809	8986.207	8731.370	8453.739
8	8768.531	8739.403	8681.345	8594.752	8480.206	8338.465	8170.451	7977.230	7760.000	7520.070	7258.841
9	7564.957	7537.554	7482.942	7401.504	7293.804	7160.579	7002.724	6821.276	6617.401	6392.371	6147.554
10	6444.851	6419.175	6368.013	6291.753	6190.892	6066.200	5918.531	5748.896	5558.431	5348.380	5120.079
11	5408.303	5384.366	5336.675	5265.593	5171.656	5055.564	4918.168	4760.456	4583.541	4388.642	4177.072
12	4455.823	4433.645	4389.470	4323.651	4236.714	4129.344	4002.375	3856.778	3693.648	3514.185	3319.688
13	3588.368	3567.985	3527.393	3466.943	3387.149	3288.687	3172.379	3039.183	2890.182	2726.571	2549.641
14	2807.390	2788.848	2751.938	2697.004	2624.557	2535.265	2429.944	2309.548	2175.158	2027.971	1869.290
15	2114.878	2098.243	2065.146	2015.930	1951.104	1871.336	1777.444	1670.387	1551.259	1421.276	1281.774
16	1513.423	1498.782	1469.672	1426.440	1369.600	1299.827	1217.953	1124.958	1021.967	910.244	791.193
17	1006.283	993.748	968.855	931.959	883.587	824.435	755.366	677.408	591.750	499.752	402.957
18	597.432	587.154	566.782	536.688	497.429	449.743	394.558	332.992	266.371	196.255	124.492
19	291.516	283.692	268.247	245.585	216.317	181.268	141.491	98.299	53.325	8.707	
20	92.935	87.810	77.791	63.351	45.232	24.548	3.177				
21	7.665	6.201	3.660	0.665							
22	0.235										

All energies in cm^{-1}, relative to the $H^+ + D$ limit.

TABLE 6.11

Dissociation Energies of the Bound Vibration-Rotation Levels of the Ground State of HD^+ from the Nonadiabatic Calculations of Wolniewicz & Poll [48]

v	J = 0	1	2	3	4	5
0	21516.073	21472.214	21384.755	21254.220	21081.374	20867.218
1	19603.079	19561.222	19477.759	19353.192	19188.262	18983.931
2	17786.217	17746.300	17666.712	17547.935	17390.680	17195.878
3	16062.630	16024.601	15948.781	15835.634	15685.848	15500.318
4	14429.831	14393.645	14321.502	14213.849	14071.351	13894.873
5	12885.697	12851.315	12782.772	12680.500	12545.142	12377.533
6	11428.466	11395.857	11330.851	11233.870	11105.530	10946.644
7	10056.731	10025.871	9964.357	9872.595	9751.186	9600.912
8	8769.444	8740.318	8682.264	8595.677	8481.139	8339.409
9	7565.920	7538.520	7483.912	7402.480	7294.788	7161.573
10	6445.854	6420.181	6369.022	6292.750	6191.915	6067.234
11	5409.332	5385.397	5337.710	5266.634	5172.705	5056.623
12	4456.863	4434.688	4390.517	4324.703	4237.774	4130.414
13	3589.404	3569.022	3528.435	3467.990	3388.204	3289.752
14	2808.402	2789.862	2752.956	2698.028	2625.588	2536.304
15	2115.845	2099.212	2066.118	2016.908	1952.088	1872.329
16	1514.323	1499.682	1470.576	1427.349	1370.515	1300.749
17	1007.086	994.552	969.661	932.769	884.401	825.255
18	598.111	587.833	567.462	537.369	498.111	450.426
19	292.063	284.239	268.794	246.131	216.862	181.817
20	93.603	88.498	78.521	64.148	46.113	25.455
21	2.93	0.74				

All energies in cm^{-1}

Radiative and Relativistic corrections are included.

to the dissociation limit; their absolute energies are virtually unchanged. For higher vibrational levels the shifts relative to the dissociation limit are smaller. In particular although v = 22 in the adiabatic potential lies above the $H^+ + D$ limit, we find that using our effective potential it is moved to below this limit. Finally we compare the results of our coupled states treatment with the full nonadiabatic calculations of Wolniewicz & Poll. Their levels are consistently below ours, as one would anticipate, since the nonadiabatic shifts for the ground state must all be negative. However, our estimate for the position of v = 21 lies more than 4 cm^{-1} below that of Wolniewicz & Poll. This supports our view that the second order treatment is inadequate for the $1s\sigma_g - 2p\sigma_u$ coupling. We also note that we have succeeded in locating one more vibrational level than Wolniewicz & Poll, but it must be regarded with caution as it lies so close to the dissociation limit. In table 6.12 we compare the various theories with the available experimental data [46,53,54]. As one would anticipate the full nonadiabatic treatment gives the best agreement, the Born-Oppenheimer the poorest, with the adiabatic and coupled states approximations being intermediate and virtually identical. The effects of the $1s\sigma_g - 2p\sigma_u$ coupling are only severe for the very highest levels. Introduction of the coupling changes the predicted 21-17 adiabatic band origin from 1003.970 cm^{-1} to 998.618 cm^{-1}; Wolniewicz & Poll's value is 1004.156 cm^{-1} [48]. Experiments to locate v = 21, see chapter three, are clearly highly desirable and important.

Our coupled states treatment is incomplete, since we have neglected the effects of the vibronic coupling between the ground state and first excited states. This coupling is strongest at about 12 Bohrs, where the form of the electronic wavefunction is changing from molecular to atomic. We expect its effects, a lowering of the energies of the vibrational levels of the ground state, to be greatest for the highest vibrational levels. The estimate of the 21-17 band origin given above should thus be regarded as an upper bound. We intend to estimate the additional shifts by perturbation theory. This requires an infinite summation over the vibrational continuum of the excited state, the direct summation method of Hutson & Howard [201] provides an efficient method for performing such calculations. Eventually we would like to see our coupled states approximation used as the starting point for

TABLE 6.12

Comparison of Experimental Wavenumbers for HD^+ with Theoretical Calculations

Transition	Experiment	Experiment-			
(v',J')-(v",J")	(cm^{-1})	Born-Oppenheimer	Adiabatic	Coupled States	Nonadiabatic[e] (cm^{-1})
(1,0)-(0,1)	1869.134[a]	-0.588	-0.129	-0.128	-0.001
(1,1)-(0,2)	1823.533[a]	-0.568	-0.127	-0.127	0.000
(1,2)-(0,3)	1776.459[b]	-0.548	-0.126	-0.126	-0.002
(2,1)-(1,0)	1856.778[a]	-0.554	-0.120	-0.121	-0.001
(3,1)-(2,0)	1761.616[a]	-0.484	-0.111	-0.111	0.000
(3,2)-(2,1)	1797.522[a]	-0.496	-0.112	-0.111	0.003
(3,3)-(2,2)	1831.083[b]	-0.506	-0.111	-0.111	0.005
(3,1)-(2,2)	1642.108[a]	-0.437	-0.108	-0.108	-0.003
(17,1)-(14,0)	1813.853[c]	1.343	0.170	0.211	0.001
(17,2)-(14,1)	1820.209[c]	1.361	0.174	0.216	0.008
(17,3)-(14,2)	1820.201[c]	1.385	0.179	0.222	0.014
(17,4)-(14,3)	1813.645[c]	1.413	0.182	0.228	0.018
(17,5)-(14,4)	1800.359[c]	1.452	0.188	0.237	0.026
(17,6)-(14,5)	1780.145[c]	1.497	0.193	0.246	0.030[f]
(17,0)-(14,1)	1782.773[c]	1.330	0.168	0.208	-0.003
(18,1)-(16,0)	926.4895[d]	1.137	0.157	0.220	0.000
(18,2)-(16,1)	932.2237[d]	1.154	0.159	0.224	0.004
(18,3)-(16,2)	933.2129[d]	1.177	0.161	0.229	0.006
(18,4)-(16,3)	929.2471[d]	1.203	0.163	0.236	0.009
(18,5)-(16,4)	920.1001[d]	1.234	0.164	0.243	0.011
(18,6)-(16,5)	905.5191[d]	1.271	0.163	0.250	0.007[f]
(18,7)-(16,6)	885.2183[d]	1.312	0.160	0.257	-0.011[f]
(18,0)-(16,1)	901.5648[d]	1.119	0.155	0.215	-0.006
(18,1)-(16,2)	882.7312[d]	1.114	0.151	0.213	-0.012
(17,8)-(15,7)	1078.8532[d]	1.192	0.161	0.216	-0.054[f]

a) from reference [46]

b) from J.J.Spezeski, Ph.D. Thesis, University of Yale

c) from chapter four

d) from reference [53]

e) from reference [48]

f) required extrapolation, using B, D and H from a fit to the data of [48]

a nonadiabatic treatment of HD^+ of the type described by Wolniewicz & Poll. We have just learnt that Wolniewicz has performed these calculations [202], but we do not yet have the full details. His revised prediction for the 21-17 band origin is 996.882 cm^{-1}.

6.13 Discussion and Conclusions.

The above material demonstrates that although theoreticians have studied the properties of the hydrogen molecular ion for more than fifty years our understanding is still far from complete. Our own calculations are very much in their early stages. We intend to explore not only the calculations of accurate energies for the highest vibration-rotation levels of HD^+, but also to tackle the problem of calculating other properties of this ion. In particular we wish to investigate the hyperfine interactions, as these provide a sensitive probe of the electronic structure. Will the effects of mixing $2p\sigma_u$ into $1s\sigma_g$ affect the hyperfine structure for v = 21, and what will the splitting look like on a 21-17 transition?

We have not mentioned the behaviour of the excited state in the coupled states treatment. There is still a small minimum in the potential, which supports four bound vibration-rotation levels, see table 6.13. These levels are metastable because they can predissociate through the vibronic coupling with the continuum of the ground state. It might be possible to find predissociated transition to these levels, their lifetimes may be evaluated from the vibronic coupling terms. The existence of these levels has previously been noted in a theoretical investigation of $H^+ + D$ scattering, where they appear as Feshbach resonances lying between the $H^+ + D$ and $H + D^+$ dissociation limits [203].

TABLE 6.13

Dissociation Energies of the Bound Vibration-Rotation Levels of the First Excited State of HD^+ from the Effective Coupled States Potential.

v	J = 0	1	2	3
0	5.840	4.975	3.304	0.987

All energies in cm^{-1}; relative to the $H + D^+$ limit, this limit lies 29.868 cm^{-1} above the $H^+ + D$ limit.

CHAPTER 7

CONCLUSIONS

Our primary purpose in obtaining the results described in this thesis has been to test and extend our ideas and theories of the dynamics of molecules. We have studied molecular ions largely as a matter of convenience, rather than because of any intrinsic merit there may be in studying ions. The advantages of ions revolve around the ease with which we can manipulate them through the interaction of their net charge with electric and magnetic fields. The work presented in this thesis powerfully demonstrates the range and quality of information that can readily be obtained for ions by exploiting these capabilities.

Our studies have focused on one of the most challenging areas in molecular physics, the behaviour of molecules near their dissociation limits. The results we have obtained illustrate both the extent and the limitations of our present understanding. Even for the simplest molecule, the hydrogen molecular ion, we have some way to go before we can claim to have a complete understanding of its dynamics. As we move to more complicated systems, such as H_3^+, we can at present only offer a semiquantitative description. Our studies of H_3^+ are particularly exciting, because of the uniquely detailed view the results can be conceived to offer of an elementary chemical reaction:

$$H^+ + H_2 \rightarrow (H_3^+) \rightarrow H^+ + H_2 \qquad (7.1)$$

Future investigations by ourselves and other workers will extend and refine the ideas and results presented in this thesis. We can also expect that exciting results will continue to be obtained for other molecular ions, through the use of ion beams and by the various other techniques described in chapter one. We have found that virtually

every molecular ion we have been able to form exhibits infrared photofragmentation. We take this to indicate that it is the norm for ions formed via electron bombardment to be created in energy levels right up to and above their dissociation limits. All such ions are potential candidates for investigation by the methods described in chapter two. Extensive studies of CH^+ and $HeNe^+$ are presently underway on our instrument, giving new insights into the behaviour of molecules near dissociation.

Several challenges still remain for the experimentalist. Beams of negative ions can be formed, but so far a high resolution spectrum of only one negative molecular ion C_2^- [204] has been observed. The difficulty is that for most negative ions only the ground electronic state may be stable with respect to electron detachment. However, infrared vibration-rotation spectroscopy should still be possible, and the occurrence of transitions might be detected through the electrons and/or fast neutrals formed by subsequent photodetachment. It is likely that some negative ions will photodissociate, so that sequential two photon photodissociation may be a feasible technique. The Doppler tuning methods are also potentially applicable to beams of fast neutral molecules formed by neutralisation of ion beams [172]. It is probable that highly vibrationally excited neutral molecules can be generated in this way. This would allow the extension of Doppler-tuned spectroscopy to neutral molecules near their dissociation limits, once suitable detection schemes have been devised. There continue to be steady developments in other instrumental techniques for studying molecular ions, notably ion cyclotron resonance [205, 206]. Coupled with the use of tunable lasers, these instruments should have considerable potential in the spectroscopic study of molecular ions.

To conclude, although the spectroscopy of molecular ions using ion beams is still very much in its infancy, its contributions to molecular physics are already considerable. Further exciting developments and results are eagerly awaited. It has been a great privilege to have contributed to the application of these methods to the infrared spectroscopy of molecular ions near their dissociation limits.

REFERENCES

[1] a "Molecular Ions, Geometric and Electronic Structures", ed. J. Berkowitz & K.-O. Groeneveld, Plenum Press (1983).

b "Molecular Ions, Spectroscopy, Structure and Chemistry", ed. T. A. Miller & V. E. Bondybey, North Holland (1983).

c J. T. Moseley & J. Durup, Ann. Rev. Phys. Chem. 32 (1981), 53.

d R. J. Saykally & R. C. Woods, Ann. Rev. Phys. Chem. 32 (1981), 403.

e J. T. Moseley, J. Phys. Chem. 86 (1982), 3282.

[2] L. B. Knight, Jr. & J. Steadman, J. Chem. Phys. 77 (1982), 1750.

[3] T. A. Miller & V. E. Bondybey, Phil. Trans. Roy. Soc. Lond. A 307 (1982), 617.

[4] T. A. Miller, Ann. Rev. Phys. Chem. 33 (1982), 257.

[5] H. G. Dehmelt & K. B. Jefferts, Phys. Rev. 125 (1962), 1318.

[6] C. B. Richardson, K. B. Jefferts & H. G. Dehmelt, Phys. Rev. 165 (1968), 80.

[7] K. B. Jefferts, Phys. Rev. Lett. 20 (1968), 39.

[8] K. B. Jefferts, Phys. Rev. Lett. 23 (1969), 1476.

[9] R. D. Ray & P. R. Certain, Phys. Rev. Lett. 38 (1977), 824.

[10] R. P. McEachran, C. J. Veenstra & M. Cohen, Chem. Phys. Lett. 59 (1978), 275.

[11] R. C. Woods, Far. Disc. Chem. Soc. 71 (1981), 57.

[12] N. D. Piltch, P. G. Szanto, T. G. Anderson, C. S. Gudeman, T. A. Dixon & R. C. Woods, J. Chem. Phys. 76 (1982), 3385.

[13] R. C. Woods, R. J. Saykally, T. G. Anderson, T. A. Dixon & P. G. Szanto, J. Chem. Phys. 75 (1981), 4256.

[14] P. G. Szanto, T. G. Anderson, R. J. Saykally, N. D. Piltch, T. A. Dixon & R. C. Woods, J. Chem. Phys. 75 (1981), 4261.

[15] C. S. Gudeman, N. H. Haese, N. D. Piltch & R. C. Woods, Astrophys. J. Lett. 246 (1981), L47.

[16] C. S. Gudeman & R. C. Woods, Phys. Rev. Lett. 48 (1982), 1344.

[17] R. C. Woods, C. S. Gudeman, R. L. Dickman, P. F. Goldsmith, G. R. Huguenin, W. M. Irvine, Å. Hjalmarson, L.-Å. Nyman & H. Olofsson, Astrophys. J. 270 (1983), 583.

[18] A. Carrington, D. R. J. Milverton & P. J. Sarre, Molec. Phys. 35 (1978), 1505.

[19] F. C. de Lucia, E. Herbst, G. M. Plummer & G. A. Blake, J. Chem. Phys. 78 (1983), 2312.

[20] K. V. L. N. Sastry, P. Helminger, E. Herbst & F. C. de Lucia, Astrophys. J. Lett. 250 (1981), L91.

[21] K. V. L. N. Sastry, E. Herbst & F. C. de Lucia, J. Chem. Phys. 75 (1981), 4169.

[22] K. V. L. N. Sastry, P. Helminger, E. Herbst & F. C. de Lucia, Chem. Phys. Lett. 84 (1981), 286.

[23] G. A. Blake, P. Helminger, E. Herbst & F. C. de Lucia, Astrophys. J. Lett. 264 (1983), L69.

[24] W. C. Bowman, E. Herbst & F. C. de Lucia, J. Chem. Phys. 77 (1982), 4261.

[25] F. C. van den Heuvel & A. Dynamus, Chem. Phys. Lett. 92 (1982), 219.

[26] K. M. Evenson, R. J. Saykally, D. A. Jennings, R. F. Curl, Jr. & J. M. Brown in "Chemical and Biochemical Applications of Lasers", Volume V, ed. C. B. Moore, Academic Press (1980), 95.

[27] R. J. Saykally & K. M. Evenson, Phys. Rev. Lett. 43 (1979), 515.

[28] D. Ray, K. G. Lubic & R. J. Saykally, Molec. Phys. 46 (1982), 217.

[29] F. Bien, J. Chem. Phys. 69 (1978), 2631.

[30] T. Oka, Phys. Rev. Lett. 45 (1980), 531.

[31] T. Oka, Phil. Trans. R. Soc. Lond. A303 (1981), 543.

[32] G. D. Carney & R. N. Porter, Phys. Rev. Lett. 45 (1980), 537.

[33] P. Bernath & T. Amano, Phys. Rev. Lett. 48 (1982), 20.

[34] M. Wong, P. Bernath & T. Amano, J. Chem. Phys. 77 (1982), 693.

[35] P. B. Davies, P. A. Hamilton, W. Lewis-Bevan & M. Okumura, J. Phys. E: Sci. Instrum. 16 (1983), 289.

[36] N. N. Haese, F.-S. Pan & T. Oka, Phys. Rev. Lett. 50 (1983), 1575.

[37] C. S. Gudeman, M. H. Begemann, J. Pfaff & R. J. Saykally, Phys. Rev. Lett. 50 (1983), 727.

[38] C. S. Gudeman, M. H. Begemann, J. Pfaff & R. J. Saykally, J. Chem. Phys. 78 (1983), 5837.

[39] V. Špirko & P. R. Bunker, J. Mol. Spec. 95 (1982), 226.

[40] S. Carter, N. C. Handy & B. T. Sutcliffe, Molec. Phys. 49 (1983), 745.

[41] P. Rosmus, H.-J. Werner & M. Grimm, Chem. Phys. Lett. 92 (1982), 250.

[42] J. W. Brault & S. P. Davis, Phys. Scrip. 25 (1982), 268.

[43] M. A. Smith, V. M. Bierbaum & S. R. Leone, Chem. Phys. Lett. 94 (1983), 398.

[44] A. Carrington, Proc. R. Soc. Lond. A 367 (1979), 433.

[45] S. L. Kaufman, Opt. Commun. 17 (1976), 309.

[46] W. H. Wing, G. A. Ruff, W. E. Lamb, Jr. & J. J. Spezeski, Phys. Rev. Lett. 36 (1976), 1488.

[47] D. M. Bishop & L. M. Cheung, Phys. Rev. A 16 (1977), 640.

[48] L. Wolniewicz & J. D. Poll, J. Chem. Phys. 73 (1980), 6225.

[49] D. E. Tolliver, G. A. Kyrala & W. H. Wing, Phys. Rev. Lett. 43 (1979), 1719.

[50] J.-T. Shy, J. W. Farley, W. E. Lamb, Jr. & W. H. Wing, Phys. Rev. Lett. 45 (1980), 535.

[51] J.-T. Shy, J. W. Farley & W. H. Wing, Phys. Rev.A 24 (1981), 1146.

[52] D. M. Bishop & L. M. Cheung, J. Mol. Spec. 75 (1979), 462.

[53] A. Carrington & J. Buttenshaw, Molec. Phys. 44 (1981), 267.

[54] A. Carrington, J. Buttenshaw & R. A. Kennedy, Molec. Phys. 48 (1983), 775.

[55] A. Carrington, J. Buttenshaw, R. A. Kennedy & T. P. Softley, Molec. Phys. 44 (1981), 1233.

[56] A. Carrington, R. A. Kennedy, T. P. Softley, P. G. Fournier & E. G. Richard, Chem. Phys. (accepted).

[57] A. Carrington, J. A. Buttenshaw, R. A. Kennedy & T. P. Softley, Molec. Phys. 45 (1982), 747.

[58] A. Carrington, J. A. Buttenshaw & R. A. Kennedy, Molec. Phys. 45 (1982), 753.

[59] G. Herzberg & A. Lagerqvist, Can. J. Phys. 46 (1968), 2363.

[60] A. E. Douglas & G. Herzberg, Can. J. Res. 20 (1942), 71.

[61] F. J. Grieman, B. H. Mahan, A. O'Keefe & J. S. Winn, Far. Disc. Chem. Soc. 71 (1981), 191.

[62] B. H. Mahan & A. O'Keefe, J. Chem. Phys. 74 (1981), 5606.

[63] D. H. Katayama & J. A. Welsh, J. Chem. Phys. 75 (1981), 4224.

[64] J. A. Coxon & S. C. Foster, J. Mol. Spec. 93 (1982), 117.

[65] M. A. Johnson, J. Rostas & R. N. Zare, Chem. Phys. Lett. 92 (1982), 225.

[66] S. D. Rosner, T. D. Gaily & R. A. Holt, Phys. Rev. A 26 (1982), 697.

[67] D. L. Cooper & W. G. Richards, J. Phys. B : At. Mol. Phys. 14 (1981), L 127.

[68] D. A. Ramsay & P. J. Sarre, J. Chem. Soc. Far. II 78 (1982), 1331.

[69] A. Carrington & D. A. Ramsay, Phys. Scr. 25 (1982), 272.

[70] I. Dabrowski & G. Herzberg, J. Mol. Spec. 73 (1978), 183.

[71] I. Dabrowski, G. Herzberg & K. Yoshino, J. Mol. Spec. 89 (1981), 491.

[72] R. P. Tuckett, A. R. Dale, D. M. Jaffey, P. S. Jarrett & T. Kelly, Molec. Phys. 49, 475 (1983).

[73] A. J. Capel, J. H. D. Eland & R. F. Barrow, Chem. Phys. Lett. 82 (1981), 496.

[74] M. Tsuji, S. Shimada & Y. Nishimura, Chem. Phys. Lett. 89 (1982), 75.

[75] A. Carrington, D. R. J. Milverton, P. G. Roberts & P. J. Sarre, J. Chem. Phys. 68 (1978), 5659.

[76] J. C. Hansen, C. H. Kuo, F. J. Grieman & J. T. Moseley, J. Chem. Phys. 79 (1983), 1111.

[77] A. Carrington, P. G. Roberts & P. J. Sarre, Molec. Phys. 35 (1978), 1523.

[78] P. C. Cosby, J.-B. Ozenne, J. T. Moseley & D. L. Albritton, J. Mol. Spec. 79 (1980), 203.

[79] J. C. Hansen, J. T. Moseley & P. C. Cosby, J. Mol. Spec. 98 (1983), 48.

[80] J. C. Hansen, J. T. Moseley, A. L. Roche & P. C. Cosby, J. Chem. Phys. 77 (1982), 1206.

[81] F. J. Grieman, J. T. Moseley, R. P. Saxon & P. C. Cosby, Chem. Phys. 51 (1980), 169.

[82] H. Helm, P. C. Cosby & D. L. Huestis, J. Chem. Phys. 73 (1980), 2629.

[83] P. C. Cosby & H. Helm, J. Chem. Phys. 76 (1982), 4720.

[84] R. N. Zare, Mol. Photochem. 4 (1972), 1.

[85] C. Pernot, J. Durup, J.-B. Ozenne, J. A. Beswick, P. C. Cosby & J. T. Moseley, J. Chem. Phys. 71 (1979), 2387.

[86] A. Tabaché-Fouhaillé, J. Durup, J. T. Moseley, J.-B. Ozenne, C. Pernot & M. Tadjeddine, Chem. Phys. 17 (1976), 81.

[87] H. Helm, P.C. Cosby, M. M. Graff & J. T. Moseley, Phys. Rev. A 25 (1982), 304.

[88] M. M. Graff, J. T. Moseley & E. Roueff, Astrophys. J. 269 (1983), 796.

[89] M. M. Graff, J. T. Moseley, J. Durup & E. Roueff, J. Chem. Phys. 78 (1983), 2355.

[90] P. C. Cosby & H. Helm, J. Chem. Phys. 75 (1981), 3882.

[91] H. Helm & P. C. Cosby, J. Chem. Phys. 77 (1982), 5396.

[92] C. P. Edwards, C. S. Maclean & P. J. Sarre, Chem. Phys. Lett. 87 (1982), 11.

[93] C. P. Edwards, C. S. Maclean & P. J. Sarre, J. Chem. Phys. 76 (1982), 3829.

[94] R. Frey, R. Kakoschke & E. W. Schlag, Chem. Phys. Lett. 93 (1982), 227.

[95] S. Abed, M. Broyer, M. Carré, M. L. Gaillard & W. Larzillière, Chem. Phys. 74 (1983), 97.

[96] J. Lerme, S. Abed, R. A. Holt, M. Larzillière & M. Carré, Chem. Phys. Lett. 96 (1983), 403.

[97] S. P. Goss, J. D. Morrison & D. L. Smith, J. Chem. Phys. 75 (1981), 757.

[98] W. C. Lineberger & T. A. Patterson, Chem. Phys. Lett. 13 (1972), 40.

[99] P. L. Jones, R. D. Mead, B. E. Kohler, S. D. Rosner & W. C. Lineberger, J. Chem. Phys. 73 (1980), 4419.

[100] A. Carrington, J. Buttenshaw & P. G. Roberts, Molec. Phys. 38 (1979), 1711.

[101] G. H. Dunn, Phys. Rev. 172 (1968), 1.

[102] G. Guelachvili, D. de Villeneuve, R. Farrenq, W. Urban & J. Vergés, J. Mol. Spec. 98 (1983), 64.

[103] C. Freed, L. C. Bradley & R. G. O'Donnell, IEEE J. Quant. Elec. QE-16 (1980), 1195.

[104] W. Rindler, "Introduction to Special Relativity", Oxford (1982).

[105] E. R. Cohen & B. N. Taylor, J. Phys. Chem. Ref. Data 2 (1973), 663.

[106] H. Winter & M. Gaillard, J. Phys. B : At. Mol. Phys. 10 (1977), 2739.

[107] C. S. Willett, "Introduction to Gas Lasers: Population Inversion Mechanisms", Pergamon (1974).

[108] C. Freed, IEEE J. Quant. Elec. QE-18 (1982), 1220.

[109] R. P. Morgan, J. H. Beynon, R. H. Bateman & B. N. Green, Int. J. Mass Spec. Ion Phys. 28 (1978), 171.

[110] J. H. Beynon, J. A. Hopkinson & G. R. Lester, Int. J. Mass Spec. Ion Phys. 1 (1968), 343.

[111] B. A. Huber, T. M. Miller, P. C. Cosby, H. D. Zeman, R. L. Leon, J. T. Moseley & J. R. Peterson, Rev. Sci. Instrum. 48 (1977), 1306.

[112] J. Schopman & J. Los, Physica 48 (1970), 190.

[113] D. M. Bishop, S.-K. Shih, C. L. Beckel, F.-M. Wu & J. M. Peek, J. Chem. Phys. 63 (1975), 4836.

[114] a G. Herzberg & Ch. Jungen, J. Mol. Spec. 41 (1972), 425.

b S. Takezawa & Y. Tanaka, J. Chem. Phys. 56 (1972), 6125.

c S. Takezawa & Y. Tanaka, J. Mol. Spec. 54 (1975), 379.

[115] J. E. Pollard, D. J. Trevor, J. E. Reutt, Y. T. Lee & D. A. Shirley, J. Chem. Phys. 77 (1982), 34.

[116] W. B. Peatman, J. Chem. Phys. 64 (1976), 4093.

[117] J. G. Maas, N.P.F.B. van Asselt & J. Los, Chem. Phys. 8 (1975), 37.

[118] A. G. Brenton, J. H. Beynon, E. G. Richard & P. G. Fournier, J. Chem. Phys. 79 (1983), 1834.

[119] N.P.F.B. van Asselt, J. G. Maas & J. Los, Chem. Phys. 5 (1974), 429; 11 (1975), 253.

[120] P. R. Bunker, Chem. Phys. Lett. 27 (1974), 322.

[121] M. Tadjeddine & G. Parlant, Molec. Phys. 33 (1977), 1797.

[122] N. H. Rich, J. W. C. Johns & A. R. W. McKellar, J. Mol. Spec. 95 (1982), 432.

[123] P. Fournier, B. Lassier-Govers & G. Comtet in "Laser-Induced Processes in Molecules", ed. K. L. Kompa & S. D. Smith, Springer-Verlag (1979), 247.

[124] G. Herzberg, "Spectra of Diatomic Molecules", Van Nostrand Reinhold (1950).

[125] A. Dalgarno, T. N. L. Patterson & W. B. Somerville, Proc. Roy. Soc. Lond A 259 (1960), 100.
Errata: W. B. Somerville, Mon. Not. R. Astr. Soc. 139 (1968), 163.

[126] R. A. Frosch & H. M. Foley, Phys. Rev. 88 (1952), 1337.

[127] G. Hunter, A. W. Yau & H. O. Pritchard, At. Data Nucl. Data Tab. 14 (1974), 11.

[128] a D. M. Brink & G. R. Satchler, "Angular Momentum", Oxford (1968).

b A. R. Edmonds, "Angular Momentum in Quantum Mechanics", Princeton (1974).

[129] P. G. Roberts, Ph.D. Thesis, Southampton (1980).

[130] D. R. Bates & G. Poots, Proc. Phys. Soc. (Lond.) A 66 (1953), 784.

[131] J. M. Peek, A.-R. H.-Attar & C. L. Beckel, J. Chem. Phys. 71 (1979), 5382.

[132] W. Kołos, Int. J. Quant. Chem. 10 (1976), 217.

[133] W. Kołos & J. M. Peek, Chem. Phys. 12 (1976), 381.

[134] R. J. Le Roy & W. K. Liu, J. Chem. Phys. 69 (1978), 3622.

[135] D. M. Bishop & L. M. Cheung, Adv. Quant. Chem. 12 (1980), 1.

[136] P. G. Fournier, G. Comtet, R. W. Odom, R. Locht, J. G. Maas, N.P.F.B. van Asselt & J. Los, Chem. Phys. Lett. 40 (1976), 170.

[137] R. Locht, J. G. Maas, N.P.F.B. van Asselt & J. Los, Chem. Phys. 15 (1976), 179.

[138] J. Schopman, P. G. Fournier & J. Los, Physica 63 (1973), 518.

[139] F. Schneider, U. Havemann, L. Zülicke, V. Pacák, K. Birkinshaw & Z. Herman, Chem. Phys. Lett. 37 (1976), 323.

[140] W. Roberge & A. Dalgarno, Astrophys. J. 255 (1982), 489.

[141] R. J. Le Roy, Univ. of Waterloo Chem. Phys. Res. Rep. CP - 110 (1978).

[142] J. W. Cooley, Math. Comp. 15 (1961), 363.

[143] M. S. Child, "Molecular Collision Theory", Academic Press (1974).

[144] M. Abramowitz & I. A. Stegun, "Handbook of Mathematical Functions", Dover (1968).

[145] R. J. Le Roy & R. B. Bernstein, J. Chem. Phys. 54 (1971), 5114.

[146] M. S. Child, Spec. Per. Rep. Chem. Soc., Mol. Spec. 2 (1974), 466.

[147] I. Dabrowski & G. Herzberg, Trans. N.Y. Acad. Sci. 38 (1977), 14.

[148] R. I. Price, Chem. Phys. 31 (1978), 309.

[149] M. Konrad & F. Linder, J. Phys. B : At. Mol. Phys. 15 (1982), L405.

[150] J. J. Thomson, Phil. Mag. 21 (1911), 225.

[151] J. A. Burt, J. L. Dunn, M. J. McEwan, M. M. Sutton, A. E. Roche & H. I. Schiff, J. Chem. Phys. 52 (1970), 6062.

[152] E. Herbst & W. Klemperer, Astrophys. J. 185 (1973), 505.

[153] R. N. Porter, Ber. Buns. Ges. Phys. Chem. 86 (1982), 407.

[154] M. J. Gaillard, D. S. Gemmell, G. Goldring, I. Levine, W. J. Pietsch, J. C. Poizat, A. J. Ratkowski, J. Remillieux, Z. Vager & B. J. Zabransky, Phys. Rev. A 17 (1978), 1797.

[155] a C. E. Dykstra, A. S. Gaylord, W. D. Gwinn, W. C. Swope & H. F. Schaefer III, J. Chem. Phys. 68 (1978), 3951.

b C. E. Dykstra & W. C. Swope, J. Chem. Phys. 70 (1979),1.

[156] R. Schinke, M. Dupuis & W. A. Lester, Jr., J. Chem. Phys. 72 (1980), 3909.

[157] G. D. Carney & R. N. Porter J. Chem. Phys. 65 (1976), 3547.

[158] I. Dabrowski, Can. J. Phys. (to be published).

[159] R. Ahlrichs, C. Votava & C. Zirz, J. Chem. Phys. 66 (1977), 2771.

[160] M. Faubel & J. P. Toennies, Adv. At. Mol. Phys. 13 (1977), 229.

[161] E. Teloy in "Electronic and Atomic Collisions", ed. G. Watel, North Holland (1978), 591.

[162] D. Gerlich, U. Nowotny, Ch. Schlier & E. Teloy, Chem. Phys. 47 (1980), 245.

[163] J. Krenos, R. K. Preston, R. Wolfgang & J. C. Tully, J. Chem. Phys. 60 (1974), 1634.

[164] M. T. Bowers & A. J. Illies, personal communication.

[165] R. J. Le Roy & J. S. Carley, Adv. Chem. Phys. 42 (1980), 353.

[166] R. J. Le Roy, G. C. Corey & J. M. Hutson, Far. Disc. Chem. Soc. 73 (1982), 339.

[167] J. M. Hutson, C. J. Ashton & R. J. Le Roy, J. Phys. Chem. 87 (1983), 2713.

[168] D. E. Brinza, B. A. Swartz, C. M. Western & K. C. Janda, J. Chem. Phys. 79 (1983), 1541.

[169] A. S. Pine & W. J. Lafferty, J. Chem. Phys. 78 (1983), 2154.

[170] E. U. Condon, Phys. Rev. 41 (1932), 759.

[171] G. H. Dunn, J. Chem. Phys. 44 (1966), 2592.

[172] W. R. Gentry, D. J. McClure & C. H. Douglass, Rev. Sci. Instrum. 46 (1975), 367.

[173] S. L. Anderson, F. A. Houle, D. Gerlich & Y. T. Lee, J. Chem. Phys. 75 (1981), 2153.

[174] M. Quack, Molec. Phys. 34 (1977), 477.

[175] E. E. Marinero, C. T. Rettner & R. N. Zare, Phys. Rev. Lett. 48 (1982), 1323.

[176] E. E. Marinero, C. T. Rettner, R. N. Zare & A. H. Kung, Chem. Phys. Lett. 95 (1983), 486.

[177] H. Rottke & K. H. Welge, Chem. Phys. Lett. 99 (1983), 456.

[178] R. Kosloff & D. Kosloff, J. Chem. Phys. 79 (1983), 1823.

[179] A. Carrington & R. A. Kennedy in "Gas Phase Ion Chemistry", Vol. 3 ed. M. T. Bowers, Academic Press (1984).

[180] M. Born & K. Huang, "Dynamical Theory of Crystal Lattices", Oxford (1954), Appendix VIII.

[181] E. A. Hylleraas, Z. Phys. 71 (1931), 739.

[182] G. Jaffé, Z. Phys. 87 (1934), 535.

[183] G. Hunter & H. O. Pritchard, J. Chem. Phys. 46 (1967), 2146.

[184] D. M. Bishop & R. W. Wetmore, Molec. Phys. 26 (1973), 145.

[185] L. Wolniewicz & J. D. Poll, J. Mol. Spec. 72 (1978), 264.

[186] G. Hunter & H. O. Pritchard, J. Chem. Phys. 46 (1967), 2153.

[187] D. M. Bishop, Molec. Phys. 28 (1974), 1397.

[188] E. A. Colbourn & P. R. Bunker, J. Mol. Spec. 63 (1976), 155.

[189] W. Kołos & L. Wolniewicz, Rev. Mod. Phys. 35 (1963), 473.

[190] S. K. Luke, G. Hunter, R. P. McEachran & M. Cohen, J. Chem. Phys. 50 (1969), 1644.

[191] J. W. Gonsalves & R. E. Moss, Chem. Phys. Lett. 62 (1979), 534.

[192] D. M. Bishop, J. Chem. Phys. 66 (1977), 3842.

[193] J. I. Gersten, J. Chem. Phys. 51 (1969), 3181.

[194] D. M. Bishop & L. M. Cheung, J. Phys. B : At. Mol. Phys. 11 (1978), 3133.

[195] D. M. Bishop & L. M. Cheung, J. Chem. Phys. 75 (1981), 3155.

[196] W. H. Wing in "Laser Spectroscopy III", ed. J. L. Hall & J. L. Carlsten, Springer-Verlag (1977), 69.

[197] S. D. Conte & C. de Boor, "Elementary Numerical Analysis", McGraw-Hill (1980).

[198] J. M. Peek, J. Chem. Phys. 43 (1965), 3004.

[199] R. S. Mulliken, J. Chem. Phys. 7 (1939), 20.

[200] E. Teller & H. L. Sahlin in "Physical Chemistry", Vol. V ed. H. Eyring, Academic Press (1970), 13.

[201] J. M. Hutson & B. J. Howard, Molec. Phys. 41 (1980), 1113.

[202] L. Wolniewicz, personal communication (1983).

[203] J. P. Davis & W. R. Thorson, Can. J. Phys. 56 (1978), 996.

[204] U. Hefter, R. D. Mead, P. A. Schulz & W. C. Lineberger, Phys. Rev. A 28 (1983), 1429.

[205] T. A. Lehman & M. M. Bursey, "Ion Cyclotron Resonance Spectrometry", Wiley (1976).

[206] P. R. Kemper & M. T. Bowers, Int. J. Mass Spec. Ion Phys. 52 (1983), 1.

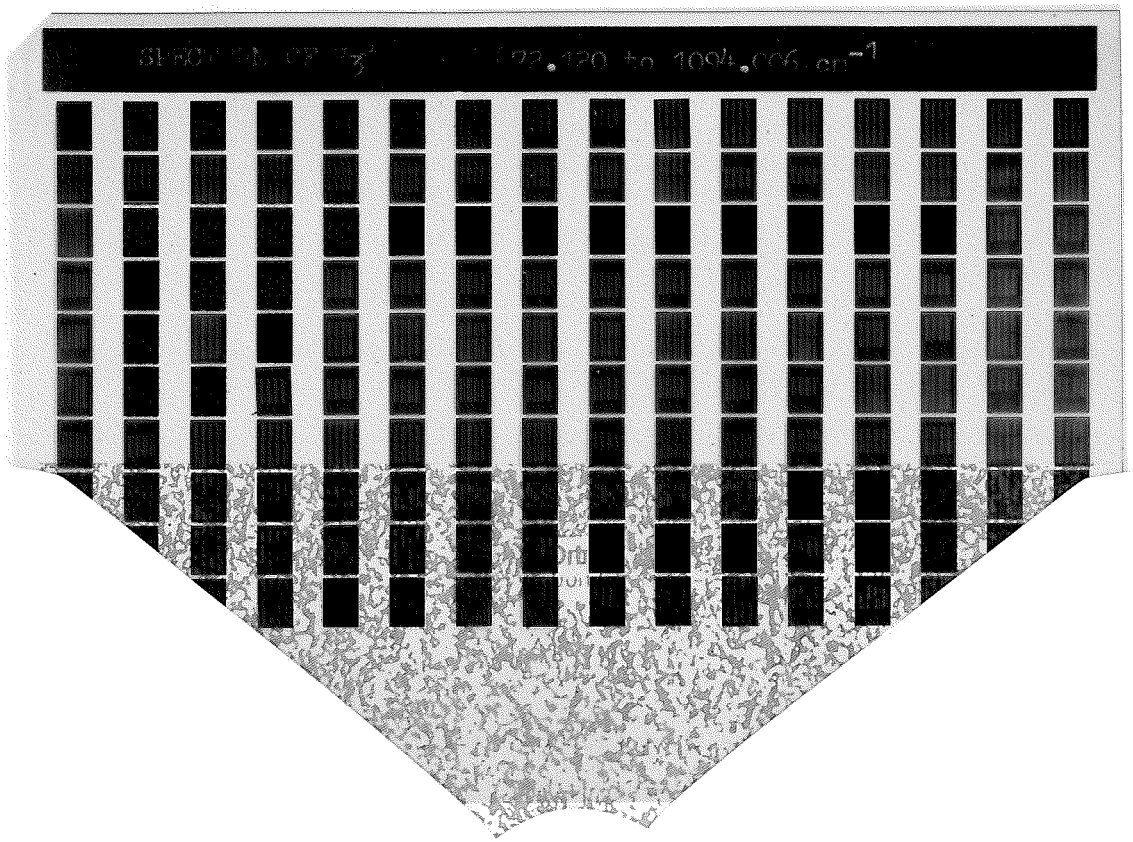

Table 5.1